UNIVERSITY OF CALIFORNIA
RIVERSIDE

Smart Optical Materials by Nanoscale Magnetic Assembly

A Dissertation submitted in partial satisfaction
of the requirements for the degree of

Doctor of Philosophy

in

Chemistry

by

Zhiwei Li

December 2019

Dissertation Committee:
Dr. Yadong Yin, Chairperson
Dr. Ming Lee Tang
Dr. Pingyun Feng

The Dissertation of Zhiwei Li is approved:

Committee Chairperson

University of California, Riverside

Acknowledgments

I would like to express my sincere gratitude to my advisor, Prof. Yadong Yin, for his academic advice, continued patience, and financial support during my graduate study at University of California, Riverside. As a mentor, he patiently guides me to explore the wonders of nanoworld. As a good friend, he helps me to understand the real world.

I am very grateful to other committee members, Prof. Ming Lee Tang, and Prof. Pingyun Feng, for their valuable comments and suggestions on my dissertation. Special thanks are also directed to Prof. Eric L. Chronister and Prof. Elaine D Haberer for their constructive comments in my career development. I appreciate the granted access to beamtime of advanced light source from Prof. Chenhui Zhu at Lawrence Berkeley National Laboratory, electron tomography analysis from Prof, Huolin Xin at UC Irvine and help in biological imaging from Prof. Zhuang Liu at Soochow University.

I appreciate all the contributions and helps from many collaborators: Dr. Mingsheng Wang, Dr. Wenjing Xu, Dr. Yaocai Bai, Dr. Xiaojing Wang, Dr. Ji Feng, Feng Tian, Dr. Jinxing Chen, Dr. Yiding Liu, Dr. Wenshou Wang, Dr. Le He, and many past and current members of Yin group: Fan Yang, Rashed Aleisa, Dr. Yoon Jae Lee, Dr. Anirban Das, Qingsong Fan, Chaolumeng Wu, Dr. Yongqiang Wang, Dr. Aiwei Tang, Dr. Dawei Wang, Dr. Shichuan Li, Dr. Chunyu Zhou, Dr. Mingfu Gong, Dr. Aiqin Gao, Dr. Yun Liu, Dr. Shuai Zhou, Lan Peng, Dr. Panpan Xu, Dr. Wenwen Yin, Bo Li, Dr. Xiaojun Zeng, Dr. Zhouhui Xia, Dr. Zhenyuan Liu et al. I would also like to thank the undergraduate and high school students who have worked and are working with me right now: Jianbo Jin, Chang Qian, Xiaoxia Zheng, Zhecun Guan, Lydia Xu, Jaskirat Sandhu, and Audrey Hoang.

I would like to thank Dr. Krassimir N. Bozhilov, Dr. Mathias Rommelfanger, and Dr. Michael Pigeon in CFAMM for their patient assistance; Dr. Dan Borchardt for his help in using optical facilities in Chemistry department. I thank Dr. Kevin Simpson for his guidance during my teaching in general chemistry and Dr. Rena Hayashi for her help in organic chemistry.

I am very grateful to my family for their selfless love and support. I want to take this opportunity to thank my parents, Hongwu Li and Ru Li, my sister, Qing Li, my parents-in-law, Xiuding Sun and Yujin Sun for their continued encouragement. Special thanks are directed to my wife, Fengfeng sun, for her contributions in this dissertation. Additional thanks are for Jessie Li and Jeffery Li.

Dedication

To my wife Fengfeng and two little ones, Jessie and Jeffery.

ABSTRACT OF THE DISSERTATION

Smart Optical Materials by Nanoscale Magnetic Assembly

by

Zhiwei Li

Doctor of Philosophy, Graduate Program in Chemistry
University of California, Riverside, December 2019
Dr. Yadong Yin, Chairperson

The nanoscale magnetic assembly has been demonstrated as a simple yet reliable strategy for preparing responsive optical materials, including photonic and plasmonic nanostructures. Compared with other assembly approaches, the magnetic assembly provides various smart optical materials without the need for complicated surface or property engineering. It enables remote, reversible, accurate, and instant control over orientational and/or positional orders of nanoparticles, whose secondary structures represent open platforms for creating integrated devices and advanced materials.

This dissertation covers a set of concepts and working principles of smart optical materials through the nanoscale magnetic assembly. In the first part, extending magnetic assembly to nanostructures with reduced symmetry represents a simple and effective strategy to create responsive photonic crystals with emerging crystal structures and novel optical tunability. This is achieved by controlling the easy axis of magnetization in different nanostructures. The systematical studies of the force dynamics by using finite element analysis appreciate the critical role of shape anisotropy in magnetic assembly: it decouples the favorable magnetic bonding between interacting colloids from any of their geometric

axes, thus generating preferential 1D [110] photonic chains, 2D centered rectangular photonic sheet, and 3D body-centered tetragonal photonic crystals in the magnetic assembly of nanocubes, nanoplates, and nanorods, respectively.

In the second part, a space-confined, seed-mediated growth is used for preparing hybrid magnetic-plasmonic nanostructures. It demonstrates that combining the conventional seeded growth with new nanostructure engineering produces a robust and versatile synthetic strategy for preparing smart materials, opening the door to many hybrid materials with various size, shape, and chemical composition. In this strategy, a secondary nanostructure is grown in a pre-designed gap between a core and a phenolic shell, rather than a hollow interior in conventional seeded growth. This strategy produces hybrid Fe_3O_4 and Au nanorods with coupled magnetic and plasmonic anisotropy. Their extinction spectra, perceived colors, and photothermal conversion can be reversibly, rapidly tuned by changing the direction of applied magnetic fields. Fixing the orientational order of the hybrid nanorods in the polymer matrix can be easily achieved by applying magnetic fields during lithography, which creates mechanochromic films with programmable colorimetric changes in response to linear and nonlinear mechanical perturbations. Relying on the high deformability of phenolic resin, this strategy is further advanced to producing conformal plasmonic coating at a hard-soft interface without the need of creating a space. This new growth mode enables efficient and cost-effective production of core-shell structures, for example, Fe_3O_4@Au nanoparticles. The plasmonic coupling of Au shell can be tuned by assembling Fe_3O_4@Au into plasmonic chains.

In the third part, by taking advantage of the new growth methodology, we propose a background-free bioimaging strategy on the basis of magnetic modulation and fast Fourier transform. It is demonstrated that the interface-confined growth supports a smooth deposition of metal atoms to small seeds: while the deformability of phenolic shell affords enough space for conformal metal coating, its elasticity can suppress the radical growth of metal structures. Thus, thin Au shells are coated on superparamagnetic Fe_3O_4 nanorods, and their physical properties, like extinction spectra, photothermal conversion, and photoacoustic signals, are tunable by external magnetic fields. Switching the directions of applied magnetic fields during imaging creates bright and deactivated imaging modes with enhanced and suppressed imaging signals from Fe_3O_4@Au nanorods, respectively. A data processing based on either pixel subtraction or fast Fourier transform is applied to remove noises from any biological and synthetic backgrounds. It has potentials to remarkably enhance the contrast and specificity of optical bioimaging in the two tissue optical transparency windows.

Table of Contents

List of Tables

List of Figures

Figure 3.11. Programming the mechanochromic response by magnetic alignment. (a) Extinction spectra of plasmonic film at different rotational angles. Insert shows its corresponding colors. (b) The design principles of mechanochromic response of plasmonic films upon pressing and stretching. (c) Extinction spectra of the plasmonic films under different pressures with cAuNRs aligned along 30° to the surface normal. (d) Intensity changes of longitudinal modes when the plasmonic films were subject to different pressures. (e) Color contour of intensity changes of the film extinction (ΔE) upon stretching. The stretching angle (labeled on the right y-axis), α, is defined as the angle between stretching directions and the long axes of cAuNRs collectively aligned inside the films. (f) Summary of intensity changes of cAuNRs under different strains. Arrows in inset indicate the slopes of mechanochromic response. (g) Anisotropic mechanochromic response of the plasmonic films enabled by magnetic alignment. (h) Orientation-dependent mechanochromic response of plasmonic films enabled by magnetically aligning cAuNRs along pre-designated directions.

Figure 3.12. Motion-active plasmonic films. (a) Schematics of the specific arrangement of cAuNRs in the plasmonic film. (b) Top views of the plasmonic films under different rotation angles. (c) The transverse excitation of cAuNRs under different transverse phase angles (ϕ_T). (d) Top views of the plasmonic films under different bending angles. (e) Schematics showing the in-plane 45° arrangement of cAuNRs inside the plasmonic film at top (top) and side view (bottom). (f) Schematics of left-handed twist (top) and right-handed twist states (bottom). The twisting angle is set at 540°. (g) Digital images of the plasmonic film at initial (top panel), left-handed (middle panel) and right-handed twisting states (bottom panel). The polarization direction and orientation of cAuNRs are illustrated by red and black arrows correspondingly. (h) Dependence of transverse excitation on localized rotation angle and y-coordinates by analyzing the superposition of intensity of transverse and longitudinal resonances to the overall lineshape. Insets: a picture of the twisted plasmonic film and the helical configuration of cAuNRs. (i) CD spectra of pure polymer and plasmonic films under twisted configuration. (j) Electric filed distribution (at 800 nm) and Poynting vectors (at 630 nm), *S*, on the surface of cAuNRs under a twisted configuration. In the side view, the numbers under and above the cAuNRs are γ and ϕ_T, respectively. The arrows and colors indicate the strength of transverse and longitudinal modes, respectively.

Figure 3.13. Mechanochromic devices. Top views of the plasmonic films under (a) rotation and (b) bending. The angles above the images are rotation angles. And, numbers below the images in (a) indicate the excitation angle of longitudinal modes (α) of cAuNRs imbedded in the regions with same colors. In (a), the plasmonic film was rotated in a left-handed manner. In (b), negative bending angle indicates bending backwards while positive angles indicate bending forwards. (c) The scheme of the mechanochromic devices. The top plasmonic film will expand upwards or downwards when subject to positive or negative

Chapter 1 Overview of Nanoscale Magnetic Assembly

1.1 Introduction

Nanoscience is a multifaced, interdisciplinary study of matter on the scale of nanometers. When the dimension of materials is reduced to nanometers, they have distinct physical and chemical properties compared with their bulk phases. Therefore, the latest three decades have witnessed the booming development of nanoscience and technology, within which nanomaterials, as referred to colloidal particles or colloids in a more general sense, are central. Nanostructures have been existing in nature long before their extensive explorations in scientific labs. DNA double helix carries the genetic information for all organisms in macromolecular structures of a few nanometers width. The specific binding between base pairs has been developed as reliable approaches in nanostructures synthesis and self-assembly. Natural precious opal-a mineraloid-exhibit iridescent colors due to the diffraction of light by periodic silica nanostructures some 100 nm to 350 nm in diameter. Living creatures are master in taking advantage of the intriguing properties of nanostructures. For example, the wings of a number of butterflies and feathers of peacocks exhibit iridescent coloration based on the interaction of light with biological nanostructures just ten nanometers, such as scales and hairs. Another interesting example is chameleon, which exhibits reversible color changes during camouflage, social interaction, and temperature variation through the active tuning of a lattice of guanine nanocrystals within its superficial skin layer of dermal iridophores.[1-2] Since the oldest chameleon was described back to Middle Paleocene (about 58.7–61.7 mya), it was long thought that chameleons change color relying on the pigment-containing organelles. It had not been realized until

2014 that they actually diffract different colors by changing the periodicity of highly ordered nanostructures within their skin. Nowadays, scientists refer these kinds of periodic nanostructures that diffract light at a particular wavelength as photonic crystals and have successfully developed a number of biomimetic strategies to prepare synthetic photonic nanostructures.

After decades' development, it has been widely accepted that colloidal synthesis and assembly are of equal importance in nanoscience. Preparing and assembling matters of nanometers length scale in nanoscale precision is critical to fulfilling the visions of nanotechnology: scientists are devoting tremendous efforts in making functional nanostructures and then assemble them in a logical way for portable, faster, cheaper, and smarter real-world devices. In these two research aspects, there exist two general methodologies, engineers' top-down and chemists' bottom-up approaches.[3] While the top-down methods produce nanostructures by breaking down a bulk phase lithographically or mechanically, bottom-up approaches pay attention to synthesizing nanostructures through underlying chemical and physical transformations. Compared with top-down methods, bottom-up approaches have many advantages. They can produce beautiful and useful nanostructures with a narrow size distribution, well-defined morphology, and complex chemical composition of the desired combination of elements. The state of art colloidal synthesis has enabled numbers of colloidal particles with complex morphologies, including hollow, hybrid, core/shell, yolk/shell, Janus, highly faceted, high entropy nanostructures et al.[4-10]

In **Chapter 1**, we will introduce a set of concepts in nanoscale magnetic assembly. As magnetic interactions between nanoparticles and particles with external magnetic fields are of particular importance in assembly dynamics and kinetics, in **Section 1.2**, we start with an overview of magnetic particles, their magnetization properties in an external magnetic field, and forces that direct their movements and collective phase behaviors in the magnetic field. In **Section 1.3**, the general concepts in photonic crystals and current achievements based on magnetic assembly of colloidal particles are provided. We elucidate the systematical, well-documented studies of magnetic assembly of nanospheres and their interesting properties in serving as building blocks of responsive photonic crystals. In the fourth part (**Section 1.4**), we introduce the localized surface plasma resonance of plasmonic particles and previous efforts in preparing responsive plasmonic nanostructures in response to external stimuli. In the end, we conclude this chapter with current challenges (**Section 1.5**) in preparing smart nanomaterials. Based on these considerations, the motivation and scope of this dissertation (**Section 1.6**) are depicted following the discussion of current challenges.

1.2 Nanoscale Magnetic Assembly

1.2.1 Magnetic Nanoparticles

In a general sense, magnetic nanoparticles refer to a set of particles possessing magnetic properties, including paramagnetic, ferromagnetic and diamagnetic ones.[11] They have been extensively exploited because of their instant, reversible, and remote response to an applied magnetic field.[12-16] Paramagnetic and superparamagnetic nanoparticles have zero net magnetic dipole moment under the absence of an external magnetic field. The magnetic moments in a single or multiple magnetic domain thermally fluctuate at room temperature, resulting in zero magnetization without external magnetic fields. In external magnetic fields, they will be magnetized and thus have a parallel magnetic moment to the external field direction. Ferromagnetic nanoparticles have spontaneous magnetic dipole moments even under the absent of a magnetic field. They have a high susceptibility to external magnetic fields and thus a high saturated magnetization in the magnetization curve. Common ferromagnetic materials include metallic ion, nickel, cobalt, their alloys and compounds of rear earth metals.[17] Some nanoparticles of metal oxides are reported as ferromagnetic when they have a considerably large magnetic domain. For magnetic nanoparticles composed of small iron oxide clusters, the superparamagnetic-ferromagnetic transition will occur when the size of crystal size is over ca. 30 nm.[18] As in most cases, the magnetism of nanoparticles is referred to their magnetic properties at room temperature. A blocking temperature (T_B) is introduced to accurately describe the magnetic phase of nanoparticles. It is defined as the temperature when the zero-field cooled (ZFC) magnetization approaches the maximum. In the case of sufficiently small nanoparticles or

nanoparticles with sufficiently small magnetic domains, the magnetization will thermally fluctuate. The time between two random flip directions is defined as Néel relaxation time (τ_N). When the ZFC curve approaches the maximum, the measurement time (τ_M) is equal to τ_N, which determines the transition from the blocked state to the superparamagnetism state. At a given temperature that is lower than T_B, it is under blocked state. That is, if the T_B of nanoparticles is large than room temperature, they are empirically described as ferromagnetic. If the T_B is smaller than room temperature, nanoparticles are paramagnetic. When ferromagnetic nanoparticles are exposed to an external magnetic field, their magnetic properties will be enhanced with a parallel moment to the direction of the external field. In the case of diamagnetic nanoparticles, however, an external magnetic field will create an induced magnetic field with opposite moment direction. Therefore, diamagnetic nanoparticles experience repulsion force in an external magnetic field rather than attraction force that paramagnetic and ferromagnetic particles do.

In paramagnetic nanospheres, their magnetization is isotropic under applied magnetic fields. In other words, they respond to the magnetic field identically no matter which direction the field is applied. For nanoparticles that are synthesized in well-prepared conditions, particularly particles of nonspherical shape or perfect crystallinity, there exist one or more preferential directions, called easy axis, for their magnetic moments under a directional magnetic field. It takes low energy to get magnetized along easy axis than that along other axes. This phenomenon is recognized as magnetic anisotropy. Magnetocrystalline anisotropy originates from the spin-orbit interaction, whose first-order and second-order contribution comes from coupling between orbital motion of electrons

and crystal electric field, the mutual interaction of magnetic dipoles, respectively. Also, particles may have anisotropic magnetic properties because of their nonspherical shapes, like the cube, plate, and rod. Nonspherical nanoparticles have associated anisotropic demagnetizing field in an applied magnetic field, creating one or more easy axes. Previous results have demonstrated that the easy axis of nonspherical nanoparticles normally is parallel to one of their longest geometric axes. For example, the easy axis of nanocubes is along their body diagonal direction. Nanorods and nanoplates have preferential magnetization along the long and in-plane radical directions, respectively. Based on the classical formula of Néel–Arrhenius equation, $E_B=T_B k_B \ln(t_0/\tau_0)$,[19] we can estimate the magnetic anisotropy energy if the interparticle interactions and the polycrystalline character of nanostructures are not taken into consideration. In this equation, k_B is the Boltzmann constant (1.38064852×10^{-23} J/K), t_0 the time scale of measurement and τ_0 the microscopic jump time (10^{-9} to 10^{-11} s). If the interparticle interaction is taken into account, the Vogel-Fulcher law is better to describe the magnetic anisotropy energy: $E_B=(T_B-T_0)k_B\ln(t_0/\tau_0)$, where T_0 is introduced to calibrate the effect of interparticle interaction.[20] Under this scenario, the magnetic anisotropy energy and the magnetic anisotropy constant should be smaller than the values estimated by Néel–Arrhenius equation.

1.2.2 Mechanism of Magnetic Assembly

The magnetic assembly is a process, where magnetic nanoparticles obtain orientational and/or positional order under an applied magnetic field. Both superparamagnetic and ferromagnetic nanoparticles will be magnetized with an induced magnetic dipole parallel to the field direction when subjected to an external magnetic field.[21-23] If nanoparticles are

separated far away from one another, they will only experience a packing force due to the coupling between the induced dipole and the external field. In a uniform external magnetic field, the packing force exerts magnetic torques on colloidal nanoparticles with anisotropic magnetic properties, such as shape anisotropy and magnetocrystalline anisotropy. In a non-uniform magnetic field, it drives the movement of magnetic nanoparticles along the field gradients into aggregates.[24] When two magnetic colloidal nanoparticles get closer, the dipole-dipole interaction becomes important as it determines the "bonding" manner between building blocks and hence the positional order, crystal structures, physical and chemical properties of the assemblies.[25-27]

For magnetic nanospheres in a uniform magnetic field, there will be an induced dipole moment, **m**, along the direction of the applied fields. The magnitude of the moment is determined by MV, where V is the volume and M the magnetization of the particle. For a nanoparticle with a volume magnetic susceptibility of χ under the auxiliary magnetic field H, the associated magnetization can be further expressed as χH. The dipole-dipole interaction between colloidal particles can be quantitatively described by a general formula. As shown in the inset of **Figure 1.1a**, the induced magnetic field H_1 by the dipole moment of the primary nanosphere (illustrated by the black dashed circle) at another dipole with a separation of d can be expressed as $\mathbf{H_1} = [3(\mathbf{m}\cdot\mathbf{r})\mathbf{r}-\mathbf{m}]/d^3$, where r is the unit vector along the connecting line between the centers of the two nanospheres. The dipole-dipole coupling energy is then calculated as the dot product of the magnetic dipole and the induced magnetic fields: $U(\Theta, d) = \mathbf{m}\cdot\mathbf{H_1} = (3\cos^2\Theta-1)m^2/d^3$, where Θ is the angle between the direction of $\mathbf{H_1}$ and the connecting line. The dipole coupling energy is a function of both

the angle and separation, whose partial differential against d and Θ defines the normal ($\mathbf{F_N}$) and tangent ($\mathbf{F_T}$) components of the force exerted on the second nanosphere, respectively:

$$\boldsymbol{F}_{\boldsymbol{N},(\Theta,\boldsymbol{d})} = \frac{\boldsymbol{\partial U}(\Theta,\boldsymbol{d})}{\boldsymbol{\partial d}} = \frac{\mathbf{3(1-3}\boldsymbol{cos}^{\mathbf{2}}\Theta)\boldsymbol{m}^{\mathbf{2}}}{\boldsymbol{d}^{\mathbf{4}}}\mathbf{r} \quad (1)$$

$$\boldsymbol{F}_{\boldsymbol{T},(\Theta,\boldsymbol{d})} = \frac{\boldsymbol{\partial U}(\Theta,\boldsymbol{d})}{\boldsymbol{\partial}\Theta} = \frac{\mathbf{-3sin(2}\Theta)\boldsymbol{m}^{\mathbf{2}}}{\boldsymbol{d}^{\mathbf{3}}}\Theta \quad (2)$$

where **r** and **Θ** are the corresponding unit radial and angular vectors. These two equations predict that the magnetic force exerted by the second nanosphere (illustrated by the red dashed circle in the inset of **Figure 1.1a**) is dependent on the geometric configuration of the two nanospheres. The normal component of the magnetic forces is zero as the critical angle equals 54.74°. It is negative when Θ is between 0° and 54.74°, suggesting an attraction between the two particles. To further illustrate the magnetic interactions, we can calculate the magnetic force between the two nanospheres using finite element method (COMSOL Multiphysics). The geometry of the simulation is illustrated in the insert in **Figure 1.1a** for two nanospheres (100 nm in diameter) separated by 40 nm. As shown in **Figure 1.1a**, the magnetic force calculated from the finite element method is of high consistency with the analytical solution of equations (1) and (2). The force transits from attraction to repulsion at the critical angle where its normal component equals zero. At this critical point, the second nanosphere experience a net magnetic force along the tangent direction. An equilibrium is established when Θ is zero, resulting in a nanochains of nanoparticles with the long axis parallel to the directions of the applied fields. The local magnetic fields at different assembly configuration are illustrated in **Figures 1.1b** and **1.1c**. When Θ is zero, the field strength is greatly enhanced, giving rise to the strongest attraction force. At the critical point, the normal components of the magnetic force vanish as the force

vector is perpendicular to the connecting line of the two nanospheres. At 90^{o}, however, the field strength decreases to the minimum, suggesting the presence of strong repulsion. Under this scenario, the perpendicular alignment is not energetically favorable (left panel in **Figure 1.1d**). However, the strong coupling between neighboring nanospheres at 0^{o} can significantly lower the magnetic potential energy, giving rise to an equilibrium state and preferential parallel alignment (right panel in **Figure 1.1d**).

Similar to the 1D nanochains, magnetic nanorods also preferentially align parallel to the external magnetic fields. As plotted in **Figure 1.1e**, the magnetic fields are significantly localized at the two ends of the long axis of the nanorods, indicating the strong coupling between the rods with external fields. In the case of perpendicular alignment (**Figure 1.1f**), however, the maximum field strength at the two ends of the short axis is much weaker. Therefore, the coupling between nanorods at parallel alignment and the applied fields is obviously stronger than that at perpendicular alignment. And, the difference increases with the aspect ratios of the nanorods. To the contrary, in the case of nanosphere, the line profile of the field strength is identical as it has isotropic magnetic properties due to the spherical geometry. The difference of the coupling states can be visualized in the magnetic field distribution in **Figure 1.1g**. Under parallel alignment, the magnetic fields exhibit significant localized effect, giving rise to stronger coupling with applied fields and lower magnetic potential energy over other orientation configurations. The above discussion suggests that the long axis of the anisotropic nanostructures, such as 1D nanochains and nanorods, align preferentially parallel to the applied magnetic fields, which provides a reliable and efficient way to control the orientation of anisotropic nanostructures in

colloidal dispersions and hence the electric, magnetic, optical, mechanical and chemical properties of the assemblies and devices via magnetic fields.

For very thin flat magnetic ellipsoids, the induced magnetic moment can be expressed as $m=\chi HV$, where χ is volume susceptibility, H is the magnetic field, and V is the volume.[28] In turn, it couples to the external magnetic field by the de-magnetization field with opposite direction. The associated de-magnetization energy can be simplified as

$$E_{demag} = \frac{1}{2}\mu_0 m^2 sin^2\theta \quad (3)$$

where μ_0 is the permeability of free space and Θ is the angle between the field direction and the long axis of ellipsoids.[29] Basically, it predicts an energetically favored orientation when Θ equals 0, which means an automatic parallel alignment.

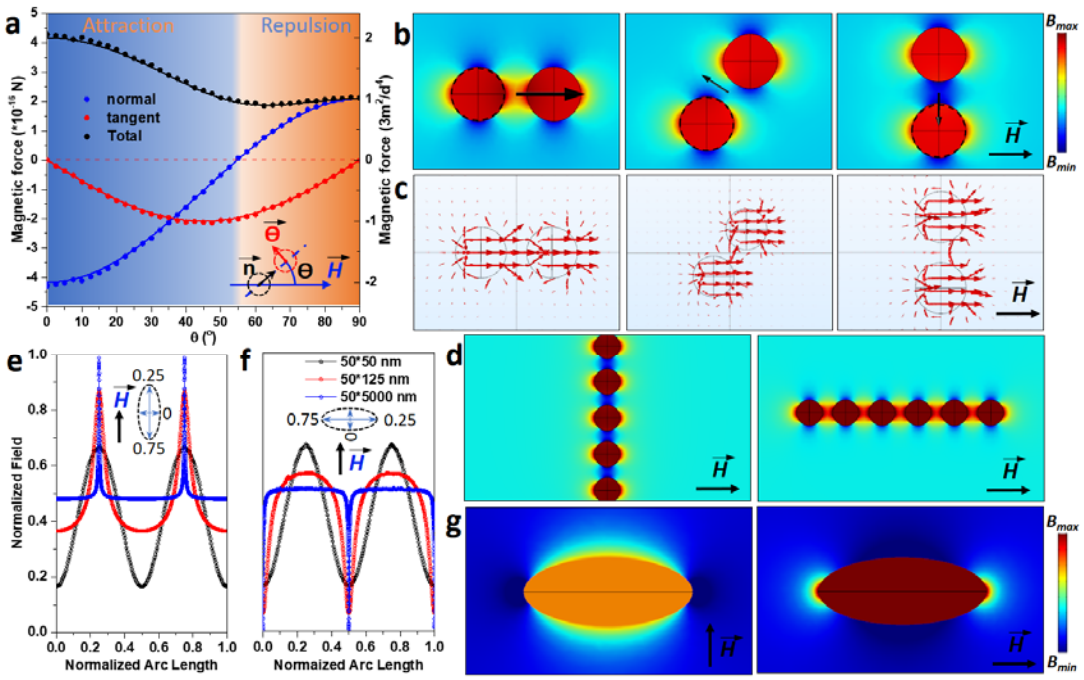

Figure 1.1. (a) Plot of magnetic force and its normal, tangent components between two magnetic nanospheres. The data represented by dots is calculation by simulation, while the data for solid line is the analytical solution of equation (1) and (2). (b) Magnetic field distribution and (c) magnetic force between two magnetic nanospheres at the angle of 0° (left), 55° (middle) and 90° (right). The black arrows in (b) indicate the magnetic force of the nanosphere highlighted by dashed circles. (d) Magnetic field distribution of assembled nanochains from nanospheres with perpendicular (left) and parallel alignment (right). Normalized field strength of nanospheres and nanorods with the long axis parallel (e) and perpendicular (f) to field directions. (g) Magnetic field distribution of nanorods (aspect ratio = 2.5) with short (left) and long (right) axis parallel to external magnetic fields. Copyright © 2019 WILEY-VCH Verlag GmbH & Co. KGaA, Weinheim.[30]

1.3 Magnetic Assembly for Responsive Photonic Crystals

1.3.1 Photonic Crystals

In analogy to controlling the behavior of electrons in semiconductors, the propagation of an electromagnetic wave can be regulated by photonic crystals due to the similarities between the Schrödinger's equation and the wave equation. The periodic dispersion of refractive indices within photonic crystals creates forbidden gaps, which exclude any photonic bands in optical frequencies. Manipulation of the structure-dependent optical dispersion correlation allows the design of photonic crystals for various fascinating applications, such as photonic pigments or inks, waveguides, refractive materials, superlens, zero or negative index metamaterials, and sensors. Responsive photonic crystals (RPCs) capable of exhibiting optical changes upon external stimuli have attracted ever-increasing attention due to their fast response to stimuli, high reversibility, and strong optical output. Through such materials, the application of external stimuli is dynamically transduced into optical changes which, if occurs in the visible spectrum, can be observed in the form of color shift or intensity change.

The fundamental physical principle that determines the constructive and destructive interference of light can be described by Bragg's law.[31] In the case of a dielectric mirror, it can be expressed under normal incidence as [32]

$$m\lambda = 2(n_1 d_1 + n_2 d_2) \quad (4)$$

where n and d indicate the refractive index and periodicity, respectively. Subscript 1 and 2 denote the layers with low and high refractive indices, and m is the diffraction order. Constructive interference occurs when m is an integer and light intensity at the

corresponding wavelength is then enhanced. When it is a half-integer, however, destructive interference occurs. More specifically, quantitative description of reflectance, *R*, can be expressed as:

$$R = [\frac{n_0 - n_s(n_1/n_2)^{2N}}{n_0 + n_s(n_1/n_2)^{2N}}]^2 \quad (5)$$

where n_0 and n_s are the refractive indices of surroundings and substrates, respectively. *N* is the number of bilayers inside the dielectric mirror.[33] The corresponding bandwidth for reflection centered at λ_0 can be calculated by:

$$\Delta\lambda_0 = \frac{4\lambda_0}{\pi}\arcsin(\frac{n_2 - n_1}{n_2 + n_1}) \quad (6)$$

As predicted from these equations, the wavelength where reflection occurs is determined by the refractive indices and periodicity while reflectance and bandwidth are solely dependent on refractive indices. A general form[34] can be derived if taking the incident angle, Θ, and the average refractive index, n_{eff}, into account:

$$m\lambda = 2d(n_{eff}^2 - \sin^2\Theta)^{1/2} \quad (7)$$

$$n_{eff}^2 = \sum n_i^2 \phi_i \quad (8)$$

where n_i and ϕ_i are the refractive indices and volume fraction of component *i* of the photonic system. Taking planar colloidal crystals as an example, they have face-centered-cubic (*fcc*) close-packed structures with the (111) plane parallel to the substrate surface during the drying process.[35] Under this scenario, *d* in the generalized equation indicates the distance between close-packed planes and its correlation with the distance between adjacent nanoparticles, *D*, can be deduced as:

$$d_{hkl} = \frac{D\sqrt{2}}{\sqrt{h^2 + k^2 + l^2}} \quad (9)$$

where *h*, *k,* and *l* are the indices of Miller planes.[36] For (111), $d_{111}= (2/3)^{0.5}D$. Finally, for a light incident relative to the normal of (111) plane of *fcc* close-packed photonic crystals, the diffraction correlation can be degenerated as:

$$2 \quad m\lambda = \sqrt{\frac{8}{3}}D(\sum n_i^2 \phi_i - \sin^2\Theta)^{1/2} \tag{10}$$

Specifically, strategies that are employed for engineering RPCs may include: i) tuning the periodicity of photonic crystals; ii) tuning the effective refractive indices of the system; iii) controlling the orientation of photonic crystals relative to incident light. These predictions are frequently modified by the presence of synergistic changes of more than one parameter induced by a single stimulus.

1.3.2 Magnetic Assembly of Nanospheres

The first version of magnetically responsive photonic crystals was reported back in 1994,[37] where 1D chain structures were assembled from uniform emulsion droplets containing concentrated ferrofluids. This strategy, however, suffered from the poor stability of emulsion and limited compatibility. In 2007, we prepared colloidal nanocrystal clusters (CNCs) of magnetite (Fe_3O_4) using a high-temperature hydrolysis reaction. The size of CNCs is tunable between 30 and 180 nm by simply controlling the hydrolysis kinetics. They are superparamagnetic due to the small size of the primary crystal units (~ 10 nm) as shown in **Figure 1.2a**.[18] The substantial negative charges on the surface, rendered by the capping ligands, provide strong electrostatic repulsive force to balance the dipole-dipole attraction.[38] Under an external magnetic field, they self-assemble into 1D nanochains with well-defined and tunable interparticle distance (**Figure 1.2b**).[39] When the field was weak, uniform red color was observed in the colloidal dispersion due to the relatively large

interparticle distance. As the field strength increased gradually, the digital images in **Figure 1.2c** showed continuously blue-shift to final purple color. Such a color shift originated from a roughly linear correlation between interparticle distance and wavelength of reflected light (**Figure 1.2d**). This magnetic field-responsive variation in distance shifts the reflection peak accordingly, which is evidenced by the reflection spectra in **Figure 1.2e**. Directly applying this strategy to a system involving nonpolar organic solvents is problematic since the surface charges are significantly suppressed. Further surface engineering was needed to overcome this barrier by, for example, the introduction of reverse micelles to promote charge separation.[27]

The dynamic equilibrium between forces of different physical origins could induce far-reaching influences on the structural complexity as well as optical tunability of the assembled entities, especially under the scenario where the concentration of colloidal nanoparticles, as well as the strength of the external magnetic field, are so high that inter-chain interactions become effective. Phase transitions can be observed by assembling CNCs in high concentration and strong magnetic field.[40] Under this scenario, the rearrangement between nanochains into zigzag multi-chains and further 2D planar photonic structures is energetically favored to occur.

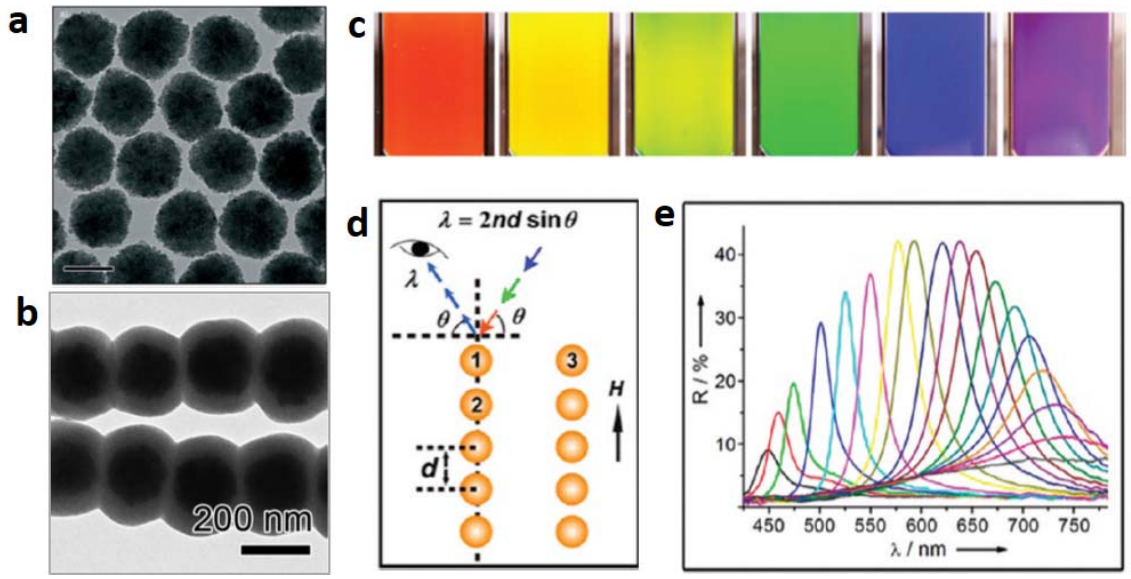

Figure 1.2. TEM images of (a) CNCs and (b) 1D chain-like assembly of CNCs. Scale bar: 100 nm. (c) Digital photos of an aqueous dispersion of CNCs encapsulated in a capillary tube under magnetic fields with increasing strengths from left to right. (d) Scheme of Bragg diffraction from the 1D chain-like structures. (e) Dependence of the reflection spectra at normal incidence of the colloidal crystals on the distance of the sample from the magnet. Diffraction peaks blue-shift (from right to left) as the distance decreases from3.7 to 2.0 cm with step size of 0.1 cm. The average diameter of the CNCs in this sample is 120 nm. [41]

Further increase in the colloidal concentration and strength of the magnetic field gives rise to a high-crystalline 3D phase.[42] Blue-shift occurred on the assembled 3D photonic crystals by enhancing the strength of the magnetic field (**Figure 1.3a-e**). The corresponding phase transitions of photonic crystal structures were captured by small-angle X-ray scattering (SAXS), as shown in **Figure 1.3f-i**. Debye-Scherrer diffraction rings were observed without a magnetic field, indicating that CNCs self-assembled into non-close-packed *fcc* structures with polycrystallinity governed by the dynamic interactions of hard steric repulsions, soft electrostatic repulsions, and van de Waals attractions. When further increasing the field strength, a transition to well-ordered single-crystalline hexagonal structures was observed. The phase transition between the 2D hexagonal planer structures to a rather disordered 3D close-packed structures was reported at the top and bottom of a capillary containing the colloidal dispersion, respectively, due to the sediment-induced concentration gradients.[43] Other types of crystal structures such as the body-centered tetragonal (*bct*) phase were reported in magnetic assembled photonic crystals.[44]

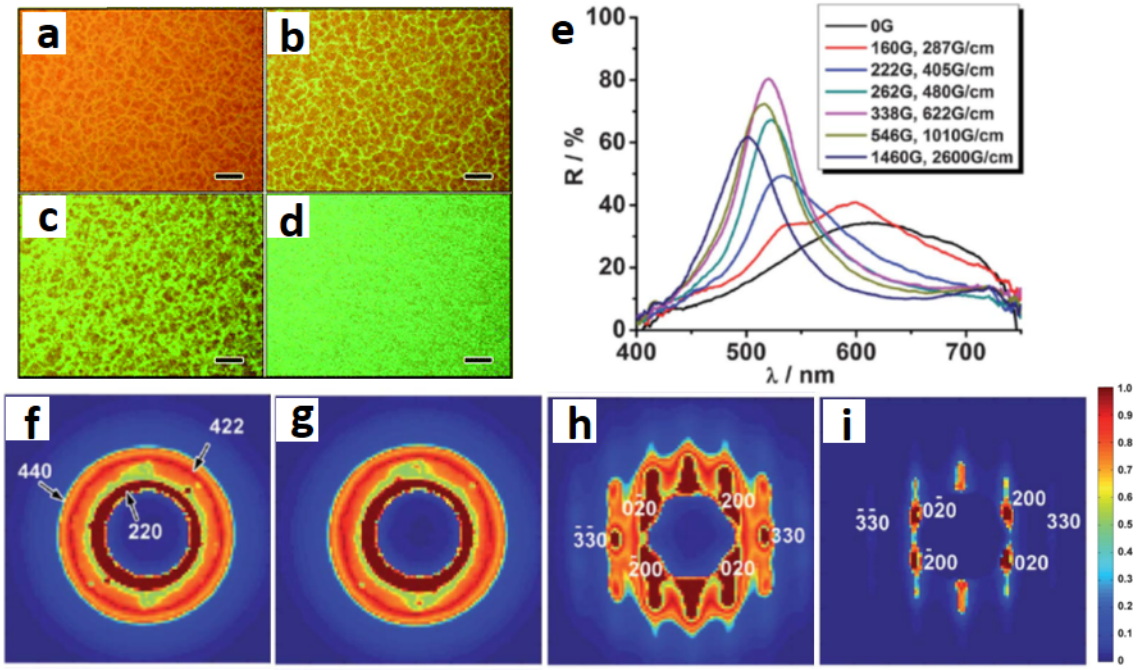

Figure 1.3. Dark-field optical microscopy images of CNCs@SiO_2 aqueous dispersion under magnetic field strengths of (a) 0 G, (b) 120 G, (c) 200 G, and (d) 500 G. The scale bars: 20 mm. (e) Reflectance spectra of CNCs@SiO_2 aqueous sample in response to the external magnetic fields. Small angle X-ray diffraction patterns of a 160 nm CNCs@SiO_2 in acetonitrile sample under magnetic field strengths of (f) 0 G, (g) 100 G, (h) 900 and (i) 1600 G. Copyright © 2012 Royal Society of Chemistry.[42]

The magnetic assembly and tuning strategy can be extended to packing nonmagnetic building blocks into RPCs by utilizing ferrofluids as the magnetic media.[45] Under the external magnetic field, as shown in **Figure 1.4a**, nonmagnetic particles such as polystyrene (PS) microbeads act as magnetic "holes," whose induced magnetic moment is equal to the total moment of the replaced ferrofluids but with the opposite direction.[46] Therefore, they experience magnetic interactions similar to the CNC case as shown in **Figure 1.4b**, and assemble from a random dispersion into 1D chains (observed in dark field as isolated green spots) and then labyrinth-like 2D structures in an enhancing magnetic field. When exposed to a strong magnetic field with high gradient, the PS beads become more concentrated locally over time due to the strong packing force and eventually form 3D photonic crystals with strong reflectance up to 83% (**Figure 1.4c** and **1.4d**). The time-dependent enhancement of the reflectance is due to the increased particle concentration of PS beads, the overall thickness of the assembled film, and the improved long-range order of the 3D assemblies.

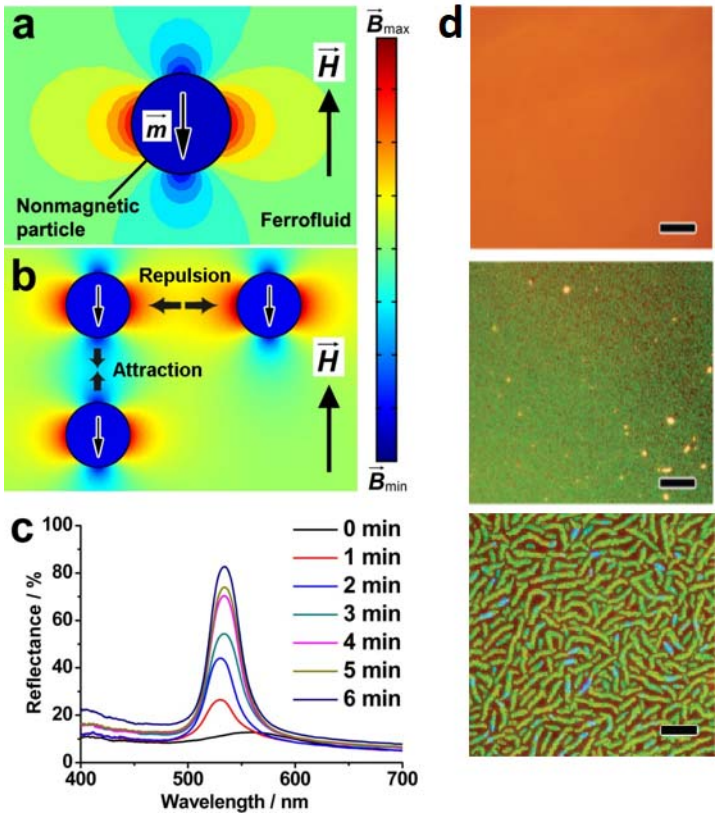

Figure 1.4. (a) Magnetic field distribution around a nonmagnetic particle with a dipole moment in the opposite direction of the external magnetic field. (b) The interparticle dipole-dipole force is repulsive or attractive depending on different particle configurations. The color bar on the right shows the strength of the magnetic field. (c) Time-dependent reflection spectra of mixed polystyrene beads and ferrofluid aqueous solution in response to a fixed magnetic field of 2530 G with a gradient of 2500 G/cm. The volume fractions are 4% for both PS and Fe_3O_4. (d) Optical microscope images showing the assembly of 185 nm PS beads in a ferrofluid with volume fractions of 3% for PS and 2% for Fe_3O_4. Field strength from left to right: 0 G and 0 G/cm; 300 G and 580 G/cm; 1500 G and 2670 G/cm. Scale bars: 20 μm. Copyright © 2010 American Chemical Society.[45]

1.3.3 Magnetic Assembly of Anisotropic Nanostructures

The anisotropic shape of the building blocks provides additional freedom to not only regulate their assembly behavior by controlling the forces of similar magnitude yet distinct physical origins but also tailor the collective optical properties of the assembled entities.[47] In the case of ellipsoidal γ-phased Fe_2O_3@SiO_2 core-shell particles whose easy magnetization was along the long axis, they could self-assemble into well-orientated photonic crystals under the help of a magnetic field. By maintaining the field direction during convective self-assembly, 3D photonic crystals were formed with both orientational and positional orders after evaporating water,[48] producing strong but untunable diffraction colors. Using ferromagnetic Fe@SiO_2 nanoellipsoids (**Figure 1.5a, 1.5b, and 1.5c**) as the anisotropic building blocks, a new class of magnetic RPCs was demonstrated by controlling the orientation of nanoellipsoids via external magnetic fields.[49] In a highly concentrated dispersion, these nanoellipsoids spontaneously self-assembled into face-centered orthorhombic (*fco*) lattices as driven by the interparticle electrostatic repulsion. Contrary to the scenario in 1D magnetic nanochains, the optical diffraction was not affected significantly by the field strength but highly dependent on the direction of the applied magnetic field (**Figure 1.5d and 1.5e**). As shown in **Figure 1.5f**, the diffraction peaks continuously blue-shifted from ~730 nm to ~510 nm during varying the field from vertical to the horizontal direction, which was induced by the decrease in the effective optical pathway. When subjected to a complex magnetic field generated by a linear Halbach array, a rainbow pattern containing red, green and blue stripes, was displayed in response to the

periodical distribution of field orientations (**Figure 1.5g**). The magnetic tuning was fast (within seconds) and entirely reversible.

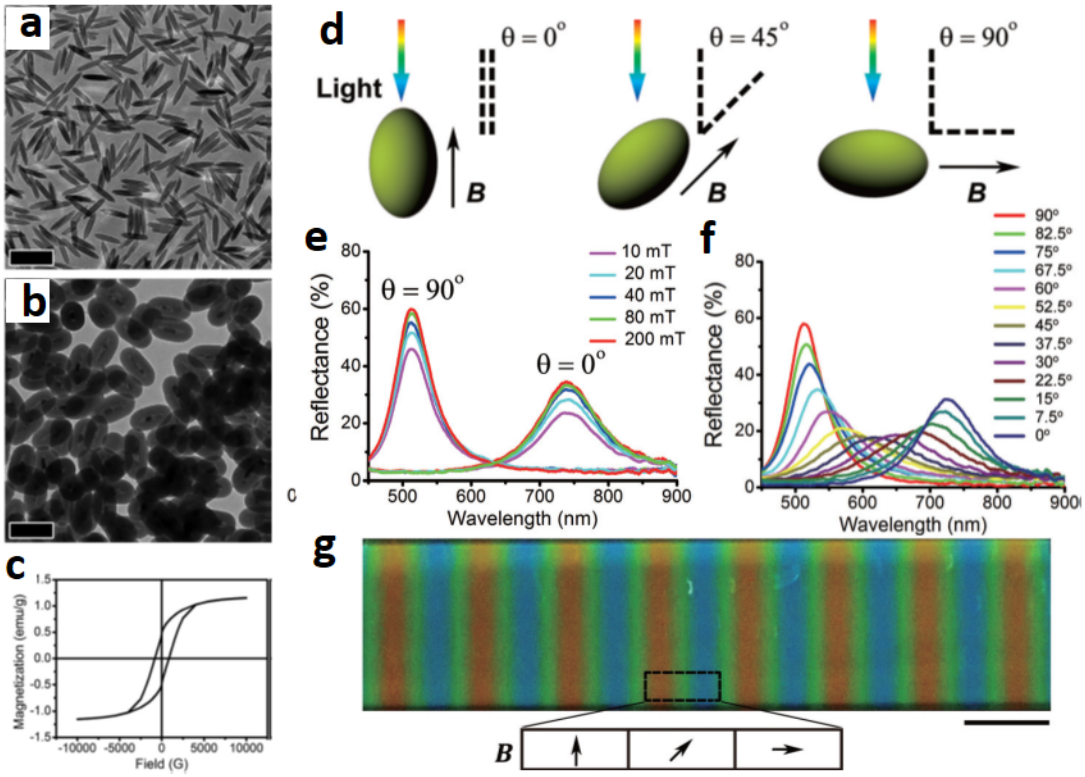

Figure 1.5. TEM images of (a) FeOOH and (b) FeOOH@SiO_2 after reduction. Scale bars: 200 nm. (c) The corresponding magnetic hysteresis loops. (d) Schematic representation of the alignment of nanoellipsoids under magnetic fields. Reflection spectra of photonic structures under magnetic fields with (e) varying strengths and (f) varying directions with respect to the direction of light. (g) Digital photo showing the photonic response under a non-ideal linear Halbach array. The scale bar corresponds to 5mm. Copyright © 2015 WILEY-VCH Verlag GmbH & Co. KGaA, Weinheim.[49]

1.4 Magnetic Assembly for Responsive Plasmonic Nanostructures

1.4.1 Surface Plasmon Resonance

Plasmonic nanostructures are another class of important optical nanomaterials with the capability of modulating the propagation of light via surface plasmon resonance (SPR).[50] SPR originates from the collective oscillation of conductive electrons within nanostructures under excitation of the electromagnetic wave.[51] Generally, SPR is either localized within the subwavelength scale (localized surface plasmon resonance, LSPR) or propagating along the surface of planar interfaces as surface plasmon polariton (SPP). The excited states of electrons relax to their ground states by transferring their oscillating energy into either the collective vibration of lattices as phonon through a photothermal effect or re-emitting light as strong scattering. Despite the structural diversities of plasmonic nanomaterials and associated complex physical transitions of SPR, their lineshapes are mostly invariably the sum of spectral intensities from several independent resonances. Therefore, most spectra of plasmonic nanostructures are symmetric against the peak maximum. The asymmetric features, however, do exist in certain well-designed plasmonic assembly, such as the Au four-member rings[52] and sphere-rod nanohybrids,[53] due to the constructive and destructive interferences between a narrow discrete resonance and a broad spectral profile, which creates unexpected minimum close to the initial maximum and is named as Fano resonance. During the last three decades, the basic science of plasmonic optics has been extensively studied, and the potential applications of plasmonic nanostructures have been widely explored in many disciplines, including optics, catalysis, chemistry, biology, and medicine.

It is well-established that the photon-electron coupling is dependent on the dielectric function and conductive electron distribution of nanostructures, through the variation in shape, size, morphology and chemical compositions, as well as their surroundings.[54] Therefore, many efforts have been exerted on tailoring the optical properties of plasmonic nanostructures by synthetically controlling their sizes and morphologies with nanometer precision. Tuning the dielectric surroundings of plasmonic nanostructures, including the solvent, capping ligands and coating materials, was first proposed as a promising approach towards responsive plasmonic nanostructures. Though the line shape of plasmonic structures bears similarity of spectral maximum, they can originate from different resonance modes, such as the transverse and longitudinal modes of metallic nanorods,[55] multipoles of large Au nanospheres[56] and coupling effect between individual resonances.[57] Accordingly, active manipulation of the separation between plasmonic nanostructures and orientation of anisotropic metallic nanomaterials, together with control over the dielectric surroundings, have been utilized to induce changes in their spectral profiles and perceived colors and creates new opportunities in various fields such as sensing, catalysis, and photoelectronic devices.

The analytical solution of Mie theory can be used to characterize plasmonic resonance by extinction cross section (ECS), which is basically the sum of absorption (ACS) and scattering cross section (SCS), and then define the overall profile of various plasmonic resonances. For a homogeneous dielectric surrounding with wavelength-independent relative permittivity, ε_m, the extinction cross section of a metallic nanoparticle with

considerably small size parameter, q (q=a/λ, where a is the radius of nanoparticles and λ is the wavelength of incident light), can be simplified as

$$\sigma_{ECS} = \frac{18\pi V \varepsilon_m^{2/3} \varepsilon_2(\lambda)}{\lambda[\varepsilon_1(\lambda)+2\varepsilon_m]^2+\lambda[\varepsilon_2(\lambda)]^2} \quad (11)$$

where V is the volume of the nanoparticle; ε_1 and ε_2 are the real and imaginary parts of the complex relative permittivity of the metal, respectively. This expression predicts a resonant spectral maximum when $\varepsilon_m=0.5[\varepsilon_1-(4\varepsilon_1^2+3\ \varepsilon_2^2)^{0.5}]$, which can be deduced as $\varepsilon_m=-0.5\varepsilon_1$ considering the small imaginary part of the relative permittivity, ε_2. In the Drude model, this expression has a more efficient form, $\lambda_{LSPR}=\lambda_P(2\varepsilon_m+1)^{0.5}$, where λ_{LSPR} and λ_P are the resonant wavelengths of metallic nanoparticles and their bulk counterparts. Therefore, the resonant wavelength monotonically increases as a function of the relative permittivity of surroundings. A similar dependence of longitudinal plasmonic resonance for anisotropic nanorods can be raised by prolate nanosphere approximation with the formula as $\lambda'_{LSPR}=\lambda_P[\varepsilon_\infty+(1/P-1)\ \varepsilon_m]^{0.5}$, where ε_∞ is high-frequency relative permittivity of metal and *P* is shape-dependent depolarization along the long axis of the nanorods. This equation suggests another type of responsive plasmonics that operates via perturbing the *P* term. Experimentally, this has been achieved by orientational control of nanorods using external stimuli such as magnetic or electric fields. The third type of responsive plasmonic nanostructures can be constructed if the dielectric properties of plasmonic nanostructures can be modulated by external stimuli including light and chemicals. According to the formula approximation of nanorods, the shift of resonant wavelength is predicted to be proportional to the change in the electron density according to the relation: $\Delta\lambda=-$

$\lambda'_{LSPR}\Delta N/2N$, where N is the electron density and ΔN its change in response to external stimuli.

The active interference between plasmonic resonance from neighboring particles can remarkably reconfigure the localized electric field distribution, hence induces unusual optical phenomena. The plasmonic coupling can either induce a significant shift in the resonance wavelength without affecting the intrinsic symmetry of the components or unexpectedly induce asymmetric spectral maximum and minimum by Fano resonance. The separation-dependent coupling can first be interpreted as the dielectric effect of the surroundings which induces remarkable spectral changes once the particles are close enough to "couple" with each other. However, the coupling induced spectral evolution depends not solely on separation but also on the morphology of nanostructures to be coupled, implying that this far-reaching effect has deep physical origins. Therefore, a hybridization model was proposed to understand the coupling behaviors. Taking the dipolar coupling between Au nanospheres as an example, the interaction energy, given as $V \propto p_1 p_2 / r^3$ (p_1, p_2: magnitudes of dipole moment; r: interparticle distance) between two adjacent nanospheres is sufficiently strong to induce spectral splitting of initial resonance into two: red- and blue-shifted ones corresponding to the bonding and antibonding hybridized modes. In the low-frequency mode, the dipoles of the two Au nanospheres are aligned along the longitudinal direction and couple mutually, forming bright bonding mode in the far field. For high-energy resonance, the two initial dipoles are anti-aligned and cancel out, resulting in zero net dipole moment and forming a dark anti-bonding resonance mode. Quantitative studies have uncovered the roughly exponential dependence of

plasmonic shift on interparticle distance as $\Delta\lambda/\lambda=Ae^{-d/(s\tau)}$, where A is the maximum shift, d the edge-edge distance, and τ the decay length of the electric field.[58]

1.4.2 Magnetically Responsive Plasmonic Nanostructures

In 1912, Richard Gans extended the Mie theory to a more general form for ellipsoidal particles of any aspect ratios. The absorption cross section can be expressed as:

$$\sigma_{ABS} = \frac{\omega}{3c}\varepsilon_m^{3/2} V \sum_j \frac{(1/P_j^2)\varepsilon_2(\lambda)}{(\varepsilon_1(\lambda)+\left(\frac{1-P_j}{P_j}\right)\varepsilon_m)^2+\varepsilon_2^2(\lambda)} \quad (12)$$

where j indicates individual anisotropic plasmonic resonance mode and includes one longitudinal and two identical transverse values for nanorods. P_j can be interpreted as depolarization factor for each principal axis of nanorods (P_{long} and P_{trans} for longitudinal and transverse mode, respectively), which induces anisotropic values of ε_1 and ε_2, and can be expressed as:

$$P_{long} = \frac{1-e^2}{e^2}\left[\frac{1}{2e}\ln\left(\frac{1+e}{1-e}\right)-1\right] \quad (13)$$

$$P'_{trans} = P''_{trans} = \frac{1-P_{long}}{2} \quad (14)$$

where e is the morphological factor with the dependence on the particle aspect ratio R: $e=(1-1/R^2)^{0.5}$. **Equation 13** predicts two distinct peaks, one originating from the transverse plasmonic mode and the other from the longitudinal mode. The space-differentiated coupling correlation between conductive electrons in anisotropic plasmonic nanostructures and the electric field of light is highly dependent on the orientation of the nanostructures concerning the electric field, with the transverse mode of electron oscillation along the short axis and the longitudinal mode along the long axis. Based on this property, new types of active plasmonics were recently demonstrated by controlling the orientation of

plasmonic nanostructures by various means, such as the electric[59] and magnetic fields, mechanical force,[60] and electrospinning process.[61]

Relying on the high affinity between Au surface and amino groups, Au nanorods were attached to the surface of Fe_3O_4@SiO_2 nanorods modified with aminosilane with parallel manner (**Figure 1.6a**).[62] The nano-hybrids can be aligned along specific directions by external magnetic field, which provided an opportunity for selective excitation of two modes of Au nanorods. As shown in **Figure 1.6b and 1.6c**, only the longitudinal plasmonic resonance was observed when the field direction was parallel to the z-axis, and consequently, the colloidal dispersion was green. Gradually varying the field direction to y-axis suppressed the longitudinal mode instantly and instead enhanced transverse mode. A response of 200 Hz (in millisecond scale) with a 6% modulation to the laser intensity at 650 nm was demonstrated. This strategy was later extended to modulate the scattering of Au microplates by attaching small γ-Fe_2O_3 nanoparticles[63] Block nanocomposites with integrated plasmonic and magnetic segments represent another type of magnetically responsive plasmonics, as demonstrated by block Ni-Au nanorods synthesized by electrochemical deposition in porous alumina templates.[64] By controlling their orientations magnetically, the strongest scattering peak shifted by more than 100 nm. During magnetic manipulation, however, irreversible aggregation of nanorods occurred due to the strong magnetic interaction and poor surface modification, which degrades the optical performance. In addition, a combination of top-down lithography and bottom-up assembly was reported to construct magnetic-plasmonic nanocomposites.[65] Particularly, $Zn_{0.2}Fe_{2.8}O_4$ and Au nanocrystals were assembled in rod-shaped templates. Subsequent ligand exchange

by thiocyanate fuses Au nanocrystals together,[66] forming porous 3D networks with high mechanical stability. The assembled nanorods with notable monodispersity (**Figure 1.6d**) exhibited a superparamagnetic response to an external magnetic field. In **Figure 1.6e and 1.6f**, the transmission at 2600 nm was modulated from 20% to 50% when the rods were re-aligned from parallel to perpendicular to polarization direction.

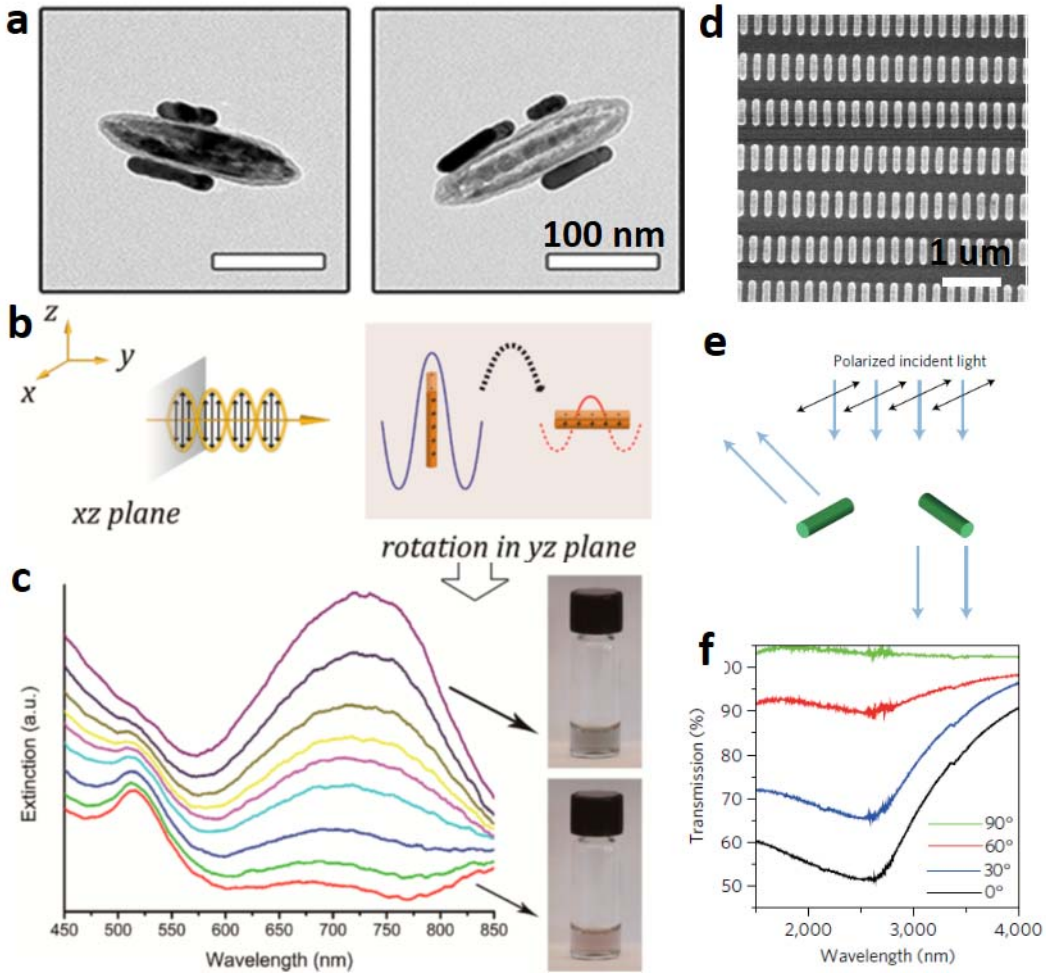

Figure 1.6. (a) TEM images of the as-assembled structures; scale bar: 100 nm. (b) Scheme showing the plasmon excitation of AuNRs under polarized light. (c) Spectra of a dispersion of the hybrid nanostructures under a magnetic field. The inset shows digital images of the dispersion. (d) SEM images of hybrid nanorod arrays. (e) Schematic of the modulated light transmission by controlling the orientation of the hybrid nanorods (green). (f) Transmission spectra of the hybrid nanorod array as a function of the polarization angle. Copyright © 2013 American Chemical Society.[62]

1.5 Challenges

The latest three decades have witnessed significant progress in smart nanomaterials, including both the development of conceptually novel sensitive materials and the advancements of existing platforms to solve practical problems. Standing on the shoulders of giants, we are on the right time to sum up those fascinate achievements and to devote to solving the next-generation challenges. Regarding the responsive photonic nanostructures, the challenges in fundamental research lie in the assembly of anisotropic building blocks into RPCs and exploration of new optical opportunities. We have demonstrated the unique optical tunability by varying the direction of the magnetic field instead of strength when ellipsoidal nanoparticles were magnetically assembled into 3D photonic crystals. More generally, the symmetry-breaking in shapes of nanomaterials gives rise to magnetic anisotropy, whose easy axis will in turn couple with the shape anisotropy, forming photonic crystals with unique structural complexity and diversity. These, however, call for synthesis approaches towards highly uniform anisotropic nanomaterials with a suitable size between 100 and 500 nm. The requirements of monodispersity of anisotropic building blocks are much higher than the case of nanospheres since any size and shape variance could ruin the structural uniformity and degrade the optical performance. From practical points of view, the challenges come from the large-scale synthesis of colloidal building blocks as well as producible assembly of high-quality photonic crystals. We believe that the developments in colloidal synthesis and even-increasing research interests in RPCs represent several critical efforts towards their commercialization to meet the strong market demands in specific areas, like pressure sensors and photonic inks, papers.

The main challenges in responsive plasmonics are the controllable assembly of metallic nanoparticles into well-defined structures and tunable excitation of their plasmonic resonance. To this end, several approaches have been developed for the assembly of plasmonic nanoparticles into either 1D or branched chains. For example, relying on the DNA,[67-68] hard templates[69-71] and molecular clusters,[72] nanoparticles can be well regulated into pre-designed structures. By controlling the electrostatic interactions via ionic strength,[73] temperature[74] and solvents,[75] metallic nanoparticles self-assembled into branched chain-like structures with continuous shifted plasmonic coupling. Coupled magnetic and plasmonic nanostructures are promising units for constructing responsive materials. Even though assembly approaches towards magneto-plasmonic nanostructures have been reported, it is still highly desirable to develop colloidal synthesis approaches that are compatible with conventional wet-chemistry methods, like templated synthesis or ligand-directed growth of metallic nanomaterials. To achieve this purpose, we have outlined several criteria based on the previous researches, including comparable small features to minimize resonant scattering, feasible control over the size and shape, strong magnetic susceptibility for assembly or orientation control by an external field and enhanced stability and dispersibility of colloidal nanocomposites.

1.6 Scope of this dissertation

This dissertation summarizes my efforts in designing smart optical materials through nanoscale magnetic assembly. It can be divided into three highly relevant parts: (i) magnetic assembly of anisotropic nanostructures into responsive photonic crystals; (ii) space-confined, seed-mediated growth of hybrid magnetic-plasmonic nanostructures for programmable optical devices; (iii) unconventional confined growth of Fe_3O_4@Au nanorods for background-free optical biological imaging.

Chapter 2 represents a systematic study on the magnetic assembly of a set of anisotropic nanostructures, including nanocubes, nanoplates, and nanorods, into responsive photonic crystals. By gradually reducing the shape symmetry of building blocks from nanocubes to nanoplates and nanorods, we have developed 1D, 2D, and 3D photonic crystals, respectively. The potential of magnetic assemble is first demonstrated in magnetic nanocubes to produce [110] photonic chains, whose diffraction and structural color can be tuned by changing the direction of the applied magnetic field, rather than the field strength in the cases using magnetic nanospheres as building blocks. By further reducing the symmetry of building blocks plates, 2D centered rectangular photonic crystals are produced due to the overlapped packing of nanoplates along the radical direction and the resulted force symmetry-breaking along another orthogonal radical direction. In the last part, it is demonstrated that body-centered tetragonal photonic crystals can be prepared if uniform nanorods with easy magnetization along long axis is used as building blocks. The fixed crystals are useful to serve as photonic pigment, whose structural colors can be tuned across the whole visible spectrum by simply changing the directions of applied magnetic

fields. This work underpins the shape anisotropy of nanostructures as a critical role in preparing emerging photonic crystals with new assembly behaviors, novel optical properties, and flexible response to external stimuli. It provides insightful understandings about the magnetic interactions between anisotropic nanostructures.

Chapter 3 introduces a set of concepts in space-confined, seed-mediated growth of plasmonic nanostructures and the large-scale production of high-quality hybrid nanostructures by combining the confined growth concept with nanostructure engineering in colloidal synthesis. By using hybrid magnetic-plasmonic nanorods as examples, a general approach toward hybrid nanostructures has been demonstrated on Au, Ag, and Cu. A well-defined gap between magnetic core and phenolic shell is created for seeded growth of the secondary nanorods, instead of using hollow nanostructures as templates in conventional confined growth. Thanks to the coupled magnetic and plasmonic anisotropy in hybrid nanorods, their physical properties, including optical extinction, perceived color, and photothermal conversion can be rationally, reversibly tuned by changing the directions of applied magnetic fields. The instant, remote, and reversible magnetic orientational control enables a number of emerging applications. Fixing the orientation of coupled nanorods in polymer matric by lithography enables the rational design of a number of mechanochromic films with programmable, reversible colorimetric response to linear and nonlinear mechanical perturbations. If Fe_3O_4 nanospheres are used as initial templates, superparamagnetic Au shells are synthesized with well-defined plasmonic properties. A new scheme of magnetically responsive plasmonic chains is further demonstrated with promising applications in smart windows and displays.

Chapter 4 describes an unconventional confined seeded growth of plasmonic nanostructures on magnetic nanorods. This synthetic method takes advantage of highly deformable, permeable phenolic shells. It enables smooth deposition of metallic atoms at the hard-soft interfaces between Fe_3O_4 and phenolic resin. While the deformability of phenolic resin affords enough space for the conformal coating of metallic layer, its elasticity limits the growth of metal along radical direction. One advantage of this new growth concept is that it can produce metal shells with controllable thickness on compact nanostructures. As thus, Au shells of few nanometers can be successfully synthesized with pronounced plasmonic resonance. Controlling the orientation of core/shell nanorods by external magnetic fields enables reliable modulation of a number of their physical properties, including optical extinction and photothermal conversion. A background-free biological imaging technique is proposed in cognition of the unique synthesis method with large-scale production and reversibly tunable physical properties of nanostructures. In this demonstration, imaging signals are actively, reversibly modulated by applying magnetic field of different directions during imaging. Signal noises from any biological and synthetic backgrounds can be completely removed by pixel subtraction or fast Fourier transform. The unconventional synthesis method, tunable properties of core-shell nanorods, and reliable data processing can remarkably enhance the image contrast and specificity of multimodal bioimaging.

1.7 References

1. Teyssier, J.; Saenko, S. V.; Van Der Marel, D.; Milinkovitch, M. C., Photonic crystals cause active colour change in chameleons. *Nat. Commun.* **2015,** *6*, 6368.

2. Li, Z.; Yin, Y., Creating Chameleon-like Smart Actuators. *Matter* **2019,** *1* (3), 550-551.

3. Murphy, C. J., Nanocubes and nanoboxes. *Science* **2002,** *298* (5601), 2139-2141.

4. Wang, X.; Feng, J.; Bai, Y.; Zhang, Q.; Yin, Y., Synthesis, properties, and applications of hollow micro-/nanostructures. *Chem. Rev.* **2016,** *116* (18), 10983-11060.

5. Li, X.; Zhu, J.; Wei, B., Hybrid nanostructures of metal/two-dimensional nanomaterials for plasmon-enhanced applications. *Chem. Soc. Rev.* **2016,** *45* (11), 3145-3187.

6. Li, Z.; Yin, S.; Cheng, L.; Yang, K.; Li, Y.; Liu, Z., Magnetic targeting enhanced theranostic strategy based on multimodal imaging for selective ablation of cancer. *Adv. Funct. Mater.* **2014,** *24* (16), 2312-2321.

7. Liu, J.; Qiao, S. Z.; Chen, J. S.; Lou, X. W. D.; Xing, X.; Lu, G. Q. M., Yolk/shell nanoparticles: new platforms for nanoreactors, drug delivery and lithium-ion batteries. *Chem. Commun.* **2011,** *47* (47), 12578-12591.

8. Lattuada, M.; Hatton, T. A., Synthesis, properties and applications of Janus nanoparticles. *Nano Today* **2011,** *6* (3), 286-308.

9. Zhou, Z. Y.; Huang, Z. Z.; Chen, D. J.; Wang, Q.; Tian, N.; Sun, S. G., High-Index Faceted Platinum Nanocrystals Supported on Carbon Black as Highly Efficient Catalysts for Ethanol Electrooxidation. *Angew. Chem. Int. Ed.* **2010,** *49* (2), 411-414.

10. Yao, Y.; Huang, Z.; Xie, P.; Lacey, S. D.; Jacob, R. J.; Xie, H.; Chen, F.; Nie, A.; Pu, T.; Rehwoldt, M., Carbothermal shock synthesis of high-entropy-alloy nanoparticles. *Science* **2018,** *359* (6383), 1489-1494.

11. Papaefthymiou, G. C., Nanoparticle magnetism. *Nano Today* **2009,** *4* (5), 438-447.

12. Li, Z.; Wang, M.; Zhang, X.; Wang, D.; Xu, W.; Yin, Y., Magnetic Assembly of Nanocubes for Orientation-Dependent Photonic Responses. *Nano Lett.* **2019,** *19* (9), 6673-6680.

13. Li, Z.; Wang, C.; Cheng, L.; Gong, H.; Yin, S.; Gong, Q.; Li, Y.; Liu, Z., PEG-functionalized iron oxide nanoclusters loaded with chlorin e6 for targeted, NIR light induced, photodynamic therapy. *Biomaterials* **2013,** *34* (36), 9160-9170.

14. Yin, S.; Li, Z.; Cheng, L.; Wang, C.; Liu, Y.; Chen, Q.; Gong, H.; Guo, L.; Li, Y.; Liu, Z., Magnetic PEGylated Pt 3 Co nanoparticles as a novel MR contrast agent: in vivo MR imaging and long-term toxicity study. *Nanoscale* **2013,** *5* (24), 12464-12473.

15. Reiss, G.; Hütten, A., Magnetic nanoparticles: applications beyond data storage. *Nature Mater.* **2005,** *4* (10), 725.

16. Frey, N. A.; Peng, S.; Cheng, K.; Sun, S., Magnetic nanoparticles: synthesis, functionalization, and applications in bioimaging and magnetic energy storage. *Chem. Soc. Rev.* **2009,** *38* (9), 2532-2542.

17. Keng, P. Y.; Shim, I.; Korth, B. D.; Douglas, J. F.; Pyun, J., Synthesis and self-assembly of polymer-coated ferromagnetic nanoparticles. *Acs Nano* **2007,** *1* (4), 279-292.

18. Ge, J.; Hu, Y.; Biasini, M.; Beyermann, W. P.; Yin, Y., Superparamagnetic magnetite colloidal nanocrystal clusters. *Angew. Chem., Int. Ed.* **2007,** *46* (23), 4342-4345.

19. Demortiere, A.; Panissod, P.; Pichon, B.; Pourroy, G.; Guillon, D.; Donnio, B.; Begin-Colin, S., Size-dependent properties of magnetic iron oxide nanocrystals. *Nanoscale* **2011,** *3* (1), 225-232.

20. Lartigue, L.; Innocenti, C.; Kalaivani, T.; Awwad, A.; Sanchez Duque, M. d. M.; Guari, Y.; Larionova, J.; Guérin, C.; Montero, J.-L. G.; Barragan-Montero, V., Water-dispersible sugar-coated iron oxide nanoparticles. An evaluation of their relaxometric and magnetic hyperthermia properties. *J. Am. Chem. Soc.* **2011,** *133* (27), 10459-10472.

21. Erb, R. M.; Son, H. S.; Samanta, B.; Rotello, V. M.; Yellen, B. B., Magnetic assembly of colloidal superstructures with multipole symmetry. *Nature* **2009,** *457* (7232), 999.

22. Ge, J.; He, L.; Hu, Y.; Yin, Y., Magnetically induced colloidal assembly into field-responsive photonic structures. *Nanoscale* **2011,** *3* (1), 177-183.

23. Kraftmakher, Y., Magnetic field of a dipole and the dipole–dipole interaction. *European journal of physics* **2007,** *28* (3), 409.

24. Erb, R. M.; Sebba, D. S.; Lazarides, A. A.; Yellen, B. B., Magnetic field induced concentration gradients in magnetic nanoparticle suspensions: Theory and experiment. *J. Appl. Phys.* **2008,** *103* (6), 063916.

25. Sacanna, S.; Philipse, A., Preparation and properties of monodisperse latex spheres with controlled magnetic moment for field-induced colloidal crystallization and (dipolar) chain formation. *Langmuir* **2006,** *22* (24), 10209-10216.

26. Ge, J.; Goebl, J.; He, L.; Lu, Z.; Yin, Y., Rewritable photonic paper with hygroscopic salt solution as ink. *Adv. Mater.* **2009,** *21* (42), 4259-4264.

27. Ge, J.; He, L.; Goebl, J.; Yin, Y., Assembly of magnetically tunable photonic crystals in nonpolar solvents. *Journal of the American Chemical Society* **2009,** *131* (10), 3484-3486.

28. BECKER, R.; EINSTEIN, A.; INFELD, L.; EINSTEIN, A., GRIFFITHS, DJ Introduction to Electrodynamics. Upper Saddle River (New Jersey): Prentice Hall: 1999.

29. Wang, M.; Yin, Y., Magnetically responsive nanostructures with tunable optical properties. *J. Am. Chem. Soc.* **2016,** *138* (20), 6315-6323.

30. Li, Z.; Yang, F.; Yin, Y., Smart Materials by Nanoscale Magnetic Assembly. *Adv. Funct. Mater.* **2019**, 1903467.

31. Joannopoulos, J. D.; Johnson, S. G.; Winn, J. N.; Meade, R. D., *Photonic crystals: molding the flow of light*. Princeton university press: 2011.

32. Fowles, G. R., *Introduction to modern optics*. Courier Corporation: 1975.

33. Bonifacio, L. D.; Lotsch, B. V.; Puzzo, D. P.; Scotognella, F.; Ozin, G. A., Stacking the nanochemistry deck: structural and compositional diversity in one-dimensional photonic crystals. *Advanced Materials* **2009,** *21* (16), 1641-1646.

34. Asher, S. A.; Holtz, J.; Liu, L.; Wu, Z., Self-assembly motif for creating submicron periodic materials. Polymerized crystalline colloidal arrays. *Journal of the American Chemical Society* **1994,** *116* (11), 4997-4998.

35. Norris, D. J.; Arlinghaus, E. G.; Meng, L.; Heiny, R.; Scriven, L., Opaline Photonic Crystals: How Does Self-Assembly Work? *Advanced Materials* **2004,** *16* (16), 1393-1399.

36. Aguirre, C. I.; Reguera, E.; Stein, A., Tunable colors in opals and inverse opal photonic crystals. *Advanced Functional Materials* **2010,** *20* (16), 2565-2578.

37. Calderon, F. L.; Stora, T.; Monval, O. M.; Poulin, P.; Bibette, J., Direct measurement of colloidal forces. *Physical review letters* **1994,** *72* (18), 2959.

38. Hu, Y.; He, L.; Yin, Y., Charge Stabilization of Superparamagnetic Colloids for High-Performance Responsive Photonic Structures. *Small* **2012,** *8* (24), 3795-3799.

39. He, L.; Wang, M.; Ge, J.; Yin, Y., Magnetic assembly route to colloidal responsive photonic nanostructures. *Accounts of chemical research* **2012,** *45* (9), 1431-1440.

40. Zhang, Q.; Janner, M.; He, L.; Wang, M.; Hu, Y.; Lu, Y.; Yin, Y., Photonic labyrinths: Two-dimensional dynamic magnetic assembly and in situ solidification. *Nano letters* **2013,** *13* (4), 1770-1775.

41. Li, Z.; Yin, Y., Stimuli-Responsive Optical Nanomaterials. *Adv. Mater.* **2019,** *31* (15), 1807061.

42. He, L.; Malik, V.; Wang, M.; Hu, Y.; Anson, F. E.; Yin, Y., Self-assembly and magnetically induced phase transition of three-dimensional colloidal photonic crystals. *Nanoscale* **2012,** *4* (15), 4438-4442.

43. Malik, V.; Petukhov, A. V.; He, L.; Yin, Y.; Schmidt, M., Colloidal crystallization and structural changes in suspensions of silica/magnetite core–shell nanoparticles. *Langmuir* **2012,** *28* (41), 14777-14783.

44. Pal, A.; Malik, V.; He, L.; Erné, B. H.; Yin, Y.; Kegel, W. K.; Petukhov, A. V., Tuning the colloidal crystal structure of magnetic particles by external field. *Angewandte Chemie International Edition* **2015,** *54* (6), 1803-1807.

45. He, L.; Hu, Y.; Kim, H.; Ge, J.; Kwon, S.; Yin, Y., Magnetic assembly of nonmagnetic particles into photonic crystal structures. *Nano Lett.* **2010,** *10* (11), 4708-4714.

46. Liu, J.; Mao, Y.; Ge, J., The magnetic assembly of polymer colloids in a ferrofluid and its display applications. *Nanoscale* **2012,** *4* (5), 1598-1605.

47. Li, H.; Li, C.; Sun, W.; Wang, Y.; Hua, W.; Liu, J.; Zhang, S.; Chen, Z.; Wang, S.; Wu, Z., Single-Stimulus-Induced Modulation of Multiple Optical Properties. *Adv. Mater.* **2019,** *31* (23), 1900388.

48. Ding, T.; Song, K.; Clays, K.; Tung, C. H., Fabrication of 3D Photonic Crystals of Ellipsoids: Convective Self-Assembly in Magnetic Field. *Adv. Mater.* **2009,** *21* (19), 1936-1940.

49. Wang, M.; He, L.; Xu, W.; Wang, X.; Yin, Y., Magnetic assembly and field-tuning of ellipsoidal-nanoparticle-based colloidal photonic crystals. *Angew. Chem., Int. Ed.* **2015,** *54* (24), 7077-7081.

50. Jiang, N.; Zhuo, X.; Wang, J., Active plasmonics: principles, structures, and applications. *Chem. Rev.* **2017,** *118* (6), 3054-3099.

51. Schasfoort, R. B., *Handbook of surface plasmon resonance*. Royal Society of Chemistry: 2017.

52. Shafiei, F.; Monticone, F.; Le, K. Q.; Liu, X.-X.; Hartsfield, T.; Alù, A.; Li, X., A subwavelength plasmonic metamolecule exhibiting magnetic-based optical Fano resonance. *Nature nanotechnology* **2013,** *8* (2), 95-99.

53. Shafiei, F.; Wu, C.; Wu, Y.; Khanikaev, A. B.; Putzke, P.; Singh, A.; Li, X.; Shvets, G., Plasmonic nano-protractor based on polarization spectro-tomography. *Nature Photonics* **2013,** *7* (5), 367-372.

54. Anker, J. N.; Hall, W. P.; Lyandres, O.; Shah, N. C.; Zhao, J.; Van Duyne, R. P., Biosensing with plasmonic nanosensors. *Nature materials* **2008,** *7* (6), 442-453.

55. Murphy, C. J.; Gole, A. M.; Hunyadi, S. E.; Stone, J. W.; Sisco, P. N.; Alkilany, A.; Kinard, B. E.; Hankins, P., Chemical sensing and imaging with metallic nanorods. *Chemical Communications* **2008,** (5), 544-557.

56. Gao, C.; Vuong, J.; Zhang, Q.; Liu, Y.; Yin, Y., One-step seeded growth of Au nanoparticles with widely tunable sizes. *Nanoscale* **2012,** *4* (9), 2875-2878.

57. Jain, P. K.; El-Sayed, M. A., Plasmonic coupling in noble metal nanostructures. *Chem. Phys. Lett.* **2010,** *487* (4-6), 153-164.

58. Jain, P. K.; Huang, W.; El-Sayed, M. A., On the universal scaling behavior of the distance decay of plasmon coupling in metal nanoparticle pairs: a plasmon ruler equation. *Nano Letters* **2007,** *7* (7), 2080-2088.

59. Kim, D.-Y.; Kang, D.-G.; Lee, M.-H.; Kim, J.-S.; Lee, C.-R.; Jeong, K.-U., A photo-responsive metallomesogen for an optically and electrically tunable polarized light modulator. *Chemical Communications* **2016,** *52* (87), 12821-12824.

60. Fu, L.; Liu, Y.; Wang, W.; Wang, M.; Bai, Y.; Chronister, E. L.; Zhen, L.; Yin, Y., A pressure sensor based on the orientational dependence of plasmonic properties of gold nanorods. *Nanoscale* **2015,** *7* (34), 14483-14488.

61. Zhang, H.; Hu, Z.; Ma, Z.; Gecevičius, M.; Dong, G.; Zhou, S.; Qiu, J., Anisotropically enhanced nonlinear optical properties of ensembles of gold nanorods electrospun in polymer nanofiber film. *ACS applied materials & interfaces* **2016,** *8* (3), 2048-2053.

62. Wang, M.; Gao, C.; He, L.; Lu, Q.; Zhang, J.; Tang, C.; Zorba, S.; Yin, Y., Magnetic tuning of plasmonic excitation of gold nanorods. *J. Am. Chem. Soc.* **2013,** *135* (41), 15302-15305.

63. Goebl, J.; Liu, Y.; Wong, S.; Zorba, S.; Yin, Y., Magnetically tunable colloidal micromirrors. *Nanoscale Horizons* **2016,** *1* (1), 64-68.

64. Geryak, R.; Geldmeier, J.; Wallace, K.; Tsukruk, V., Remote giant multispectral plasmonic shifts of labile hinged nanorod array via magnetic field. *Nano letters* **2015,** *15* (4), 2679-2684.

65. Zhang, M.; Magagnosc, D. J.; Liberal, I.; Yu, Y.; Yun, H.; Yang, H.; Wu, Y.; Guo, J.; Chen, W.; Shin, Y. J., High-strength magnetically switchable plasmonic nanorods assembled from a binary nanocrystal mixture. *Nature nanotechnology* **2017,** *12* (3), 228.

66. Fafarman, A. T.; Hong, S.-H.; Caglayan, H.; Ye, X.; Diroll, B. T.; Paik, T.; Engheta, N.; Murray, C. B.; Kagan, C. R., Chemically tailored dielectric-to-metal transition for the design of metamaterials from nanoimprinted colloidal nanocrystals. *Nano Lett* **2013,** *13* (2), 350-357.

67. Ding, B.; Deng, Z.; Yan, H.; Cabrini, S.; Zuckermann, R. N.; Bokor, J., Gold nanoparticle self-similar chain structure organized by DNA origami. *Journal of the American Chemical Society* **2010,** *132* (10), 3248-3249.

68. Warner, M. G.; Hutchison, J. E., Linear assemblies of nanoparticles electrostatically organized on DNA scaffolds. *Nature Materials* **2003,** *2* (4), 272.

69. Yin, Y.; Lu, Y.; Gates, B.; Xia, Y., Template-assisted self-assembly: a practical route to complex aggregates of monodispersed colloids with well-defined sizes, shapes, and structures. *Journal of the American Chemical Society* **2001,** *123* (36), 8718-8729.

70. Xia, Y.; Yin, Y.; Lu, Y.; McLellan, J., Template-assisted self-assembly of spherical colloids into complex and controllable structures. *Advanced Functional Materials* **2003,** *13* (12), 907-918.

71. Lu, Y.; Yin, Y.; Li, Z.-Y.; Xia, Y., Synthesis and self-assembly of Au@ SiO_2 core− shell colloids. *Nano Letters* **2002,** *2* (7), 785-788.

72. Zhang, X.; Lv, L.; Ji, L.; Guo, G.; Liu, L.; Han, D.; Wang, B.; Tu, Y.; Hu, J.; Yang, D., Self-assembly of one-dimensional nanocrystal superlattice chains mediated by molecular clusters. *J. Am. Chem. Soc.* **2016,** *138* (10), 3290-3293.

73. Han, X.; Goebl, J.; Lu, Z.; Yin, Y., Role of salt in the spontaneous assembly of charged gold nanoparticles in ethanol. *Langmuir* **2011,** *27* (9), 5282-5289.

74. Liu, Y.; Han, X.; He, L.; Yin, Y., Thermoresponsive assembly of charged gold nanoparticles and their reversible tuning of plasmon coupling. *Angewandte Chemie International Edition* **2012,** *51* (26), 6373-6377.

75. Liao, J.; Zhang, Y.; Yu, W.; Xu, L.; Ge, C.; Liu, J.; Gu, N., Linear aggregation of gold nanoparticles in ethanol. *Colloids and Surfaces A: Physicochemical and Engineering Aspects* **2003,** *223* (1-3), 177-183.

Chapter 2 Magnetic Assembly of Anisotropic Nanostructures into Responsive Photonic Crystals

2.1 Introduction

Colloidal crystals are ordered secondary superstructures of colloidal particles, whose repeating subunits are commonly much larger than that of their analogous atomic and molecular crystals.[1-3] Because the spatial configuration of matter and surface ligands in colloidal crystals – which controls many physical and chemistry properties – could be easily tailored in a nanometer precision within up to centimeter length scale by adjusting not only the chemical composites, sizes, and shapes of the subunits but also the ways of symmetry they self-assembled in the crystals,[4] colloidal self-assembly has produced a variety of intriguing materials with desired functions in photonics,[4-5] biomaterials, structural materials,[6] and catalysis.[7] Compared with the accessible nanocrystals of diverse shapes, the assembly of either spherical colloids or highly faceted particles has been dominated by entropic processes that involves depletion, hydrophobic forces, and polymer "elasticity", producing densely packed colloidal crystals with maximum hard contact areas and highest packing density.[8] Recent theoretical simulations and experimental self-assembly at multiscale have demonstrated this widespread bonding manner in many entropy-dominated crystal assemblies.[9]

To break the entropic symmetry in colloidal assembly, sole or joint underlying microscopic interactions have been applied on interacting colloids for exploiting more complex superstructures, including specific binding between biomolecules (particularly DNA),[10-13] van der Waals forces of ligand molecules,[1, 14] magnetic forces,[15-16] and electrostatic

forces.[3, 17-18] These approaches require sophisticated engineering of subunits properties while producing limited new functions due to the homogeneity of surface properties and/or energy-driven similar tendency of maximizing surface contact area.[1, 19] Few examples on directed assembly of emerging superstructures, so far in 1D or 2D form, has only been reported on micro colloids, which involves highly anisotropic surface interactions between subunits through pre-designed engineering of Janus particles.[20-23]

In this chapter, we report the use of magnetic interaction as directing driving force to assemble anisotropic nanostructures into responsive photonic crystals. As described in Chapter 1, magnetic assembly of nanospheres has been developed for producing photonic crystals with 1D, 2D, and 3D orders. Among these well-established structures, 1D photonic crystals are particularly useful in various practical applications. They have numbers of advantages in the synthesis and further property engineering in combination with lithography. These also exist several limitations that hinder their further exploration in practical applications. Therefore, it is still highly desirable to discovery emerging photonic crystals with new crystal structures and novel photonic properties. By gradually reducing the shape symmetry of building blocks from nanocubes to nanoplates and nanorods, we have developed 1D, 2D, and 3D photonic crystals, respectively. This work underpins the shape anisotropy of nanostructures as a critical role in preparing emerging photonic crystals with new assembly behaviors, novel optical properties, and flexible response to external stimuli. It provides insightful understandings about the magnetic interactions between anisotropic nanostructures.

2.2 Materials and Methods

Materials. Potassium ferricyanide, HCl and NH4OH were purchased from Fisher Scientific. Tetraethylorthosilicate (TEOS, 98%), diethylene glycol (DEG, reagent grade), ethyl alcohol (EG, denatured), polyvinylpyrrolidone (PVP, Mw=40000) and 2-Hydroxy-2-methylpropiophenone (97%) as photoinitiator were purchased from Sigma-Aldrich. Acrylamide (AM) and N, N′-Methylenebisacrylamide (BIS) were obtained from Fluka. Ethanol (proof 200) was purchased from Decon Labs. Polyacrylic acid (PAA, MW=1800), iron chloride hexahydrate ($FeCl_3 \cdot 6H_2O$), tetraethyl orthosilicate ($C_8H_{20}O_4Si$, TEOS) were bought from Sigma-Aldrich. Ethylene glycol (EG) and diethylene glycol (DEG) was from Acros Organics. Ammonium hydroxide ($NH_3 \cdot H_2O$) were purchased from Fisher Scientific. All chemicals are used directly without further purification.

Synthesis of PB nanocubes. PB nanocubes with an edge length of about 200 nm were synthesized according to a reported method. 113.14 mg potassium ferricyanide and 3 g PVP (Mw. =40000) were added into 40 mL of 0.01 M HCl. The solution was magnetically stirred for 30 min and then heated at 80 ºC for 20 hours. The obtained PB nanocubes were dispersed in 6 mL DI water.

Synthesis of FeOOH nanorods. The synthesis of nanorods with different aspect ratios was achieved by hydrolysis of $FeCl_3$ in aqueous solution[24]. The details about the concentration and reaction temperature are summarized in **Table. 2.1**. The synthesis of FeOOH nanorods with small aspect ratios was carried out at room temperature without addition of HCl. Due to relative low temperature, it takes about 3 months for the formation of uniform FeOOH nanorods. To synthesize FeOOH nanorods with larger aspect ratios, we added HCl to the

solution and raised the reaction temperature to 87ºC. The reactions were kept at this temperature for 25.5 hours. Notably, this hydrolysis method can be easily scaled up without significant change in size and aspect ratios. Take the rods with aspect ratios of 4.6 (#F2) or example, the total volume was 4 L during room-temperature hydrolysis. During the reaction, the formed FeOOH nanorods precipitated to the bottom of the reaction containers. After removing the supernatants, the FeOOH nanorods were washed by water three times and then dispersed in 400 mL of water, which served as stock solutions.

PAA modification. For PAA modification, 3 mL of the stock solution with theoretical concentration of 90 mg/mL was added into 120 mL of PAA solution (43.2 mg) and stirred for 8 hrs. Excess PAA was removed by centrifugation and washing with water for three time. The FeOOH-PAA was further dispersed in 9 mL of water for SiO_2 coating.

SiO_2 coating. 3 mL of the above colloidal dispersion of PB was added to the mixture of 10 mL of DI water and 70 mL of ethanol, which was then sonicated for ~10 min for better dispersion. Consequently, 3 mL of ammonia and 55 μL of TEOS were added. The mixture was magnetically stirred overnight. The obtained PB@SiO_2 was washed by DI water three times and finally concentrated in ~50 μL of DI water for following polyol reduction. For nanorods, in a typical coating process, 3 mL of FeOOH-PAA dispersion was added into a flask. The mixture was sonicated for 3 min to fully disperse the rods after 1 mL of ammonia solution was added. Then, 20 mL of ethanol was added to the dispersion. To control the thickness of silica, we added different volumes of TEOS to the mixture. Taking #F2 for an example, 30 μL and 100 μL of TEOS were added into the mixture for thickness of 20.5 and 44.2 nm, respectively, after 30 min reaction. For a thicker silica (~ 72.8 nm), two

batches of 130 μL TEOS was added to the mixture each 30 min to prevent the formation of free silica nanoparticles. Half an hour later after the second addition, the FeOOH@SiO_2 nanorods were precipitated by centrifugation and further washed three times by water.

Polyol reduction. After silica coating, the PB@SiO_2 was concentrated into about 50 μL in DI water, which was then injected into 25 mL of DEG at 300 ºC under nitrogen protection. Reduction typically took 12 hours under continuous nitrogen flow. Afterward, the products were washed by DI water three times. Magnetic nanorods were synthesized by reduction of FeOOH@SiO_2 nanorods in high-temperature calcination[25]. FeOOH@SiO_2 nanorods was dried in crucibles and placed in tubular furnace. The system was de-gassed for 10 min by forming gas (5% H_2 and 95% N_2). The reduction occurred at 360ºC for 2 hours. After cooling down to room temperature, the prepared Fe_3O_4@SiO_2 nanorods were fully dispersed in water by sonication and then washed by water for three times. To further increase the surface charges and facilitate the fixation of colloidal crystals by silica coating, the Fe_3O_4@SiO_2 nanorods were modified by PAA (20mL, 5 mg/mL) overnight.

Magnetic assembly of anisotropic nanostructures. Fe_3O_4@SiO_2 nanocubes were dispersed in 3 mL of ethanol with the concentration of ~ 20mg/mL. The dispersion was then exposed to a magnet (2000 G) for 20 seconds. After removing the magnet, NH_4OH (20 μL) and TEOS (6 μL) were added sequentially. The dispersion was then vortexed gently for 30 minutes. The obtained nanochains were washed by ethanol three times.

Simulation of magnetic and electric field distribution of nanocubes. The magnetic field distribution was simulated by a finite-element method performed on COMSOL Multiphysics. Background magnetic field was set parallel to the x-axis with the filed

strength of 1mT. Three typical assembly modes were modulated as [100], [110], and [111]. The magnetization of nanocubes was set as 12006 A/m at the applied field strength of 1 mT based on the magnetization curve in Figure 1d. The magnetic susceptibility of surroundings was 1. The electric field distribution was simulated by a finite-element method performed on COMSOL Multiphysics as well. The Fe_3O_4@SiO_2 nanocubes were modulated with a length of 250 nm. The cross-section of a nanochain with 27 nanocubes aligned along their [110] direction inside was constructed (**Figure S7**). The average refractive indices were 2.2 for domains of nanocubes and 1.333 for domains of water. A Gauss beam, S-polarized, was incident from the top with the pre-designed wavelength (wl), spot radius (w0) of 12000 nm. Its Rayleigh range was dependent on the incident wavelength with the formula of π*w0^2/wl.

Computing the interactions between nanorods. In the classic approximation of electrostatic interactions, only the monopole of the multipolar expansions is used to calculate the force between two neighbouring colloids[26]. This approach is reliable for isotropic particles, like nanospheres, or anisotropic particles with considerable separations. For colloidal crystals of nanorods in hard contact bonding, a more accurate analysis is desired as understand the screened Coulomb electrostatic force is critical to identify the thermodynamic equilibrium position of the assemblies. To this end, we divided the surface of each rod into 5000 surface elements, each of which serves as point charge. The screened Coulomb electrostatic force between each pairs of surface elements is calculated by

$$F_{C,ij} = k_e \frac{q_{ij}^2}{r_{ij}^2}, \tag{10}$$

where q_{ij} is the charge carried by the surface element i and j, r_{ij} is the distance between element i and j. k_e is Coulomb constant (k_e=9.0×10^9 N·m_2/C_2). The electrostatic repulsion force is expressed as a vector sum of individual interacting elements across the whole surface of pair rods:

$$F_C = \sum_{1,1}^{n,n} \overrightarrow{F_{c,ij}}. \quad (11)$$

The overall force is decomposed into two orthogonal components along the surface normal and tangent directions. Then, an angle, α, is defined as the angle between the overall force vector and the short axis of rods to represent the directions of the electrostatic repulsion force. For comparison, another angle, Θ, is defined as the angle between the connecting line of the two interacting rods and the short axis. Under this scenario, α will be equal to Θ if the electrostatic repulsion force is along the center-to-center. We first identified the thermodynamic equilibrium position of two nanorods by analyzing the pair magnetic interactions and then mapping their spatial force fields. The geometry of nanorods is an ellipsoid characterized by two parameters, the length l and the width w. To precisely mimic the conformal coating of SiO_2 with a thickness (t), a geometric domain (dashed red line in **Figure. 3A**) is created by epitaxial extension of the ellipsoidal surface along surface normal with a constant value of t. In our simulation, the trajectory of the second rod was defined by two sweet parameters, β and T. β is the azimuth angle for an arbitrary dot with a coordinate of (x, y) on the ellipsoid and t represents the silica thickness that is defined by the distance between the dot with azimuth of β to the hard contact point of the two rods along the surface normal. The critical azimuth is identified in the simulation on the basis of the criteria: the tangent components of the magnetic attraction force between the two

rods disappears. Under this scenario, the magnetic attraction is along surface normal and balanced by the normal electrostatic and steric repulsion forces due to the hard contact of the two rods.

In the following sections, the calculation of critical angles (ϕ_{CA}) and the unit cell parameters of *bct* crystals is derived. For a nanorod with length of L and width of W, the semidiameter at the azimuth of β can be calculated by the following equation.

$$r = \sqrt{\frac{1}{\frac{cos^2\beta}{(W/2)^2} + \frac{1}{\frac{sin^2\beta}{(L/2)^2}}}} \tag{12}$$

The angle between the surface normal and the Y-axis can be expressed as

$$\alpha = arctan(-\frac{\frac{L^2}{W^2}}{\tan(\beta)}) + \pi/2. \tag{13}$$

And the coordinates, (x_1, y_1), for the second rod can be expressed as

$$x_1 = 2 \times (r \times \cos(\beta) + T \times \cos(\alpha)) \tag{14}$$

$$y_1 = 2 \times (r \times \sin(\beta) + T \times \sin(\alpha)). \tag{15}$$

Therefore, the parameters, a and c, of the colloidal crystals are calculated by the following equations.

$$a_{bct} = 2\sqrt{2}y_1 = 2\sqrt{2} \times (r \times \sin(\beta) + T \times \sin(\alpha)) \tag{16}$$

$$c_{bct} = 2x_1 = 4 \times (r \times \cos(\beta) + T \times \cos(\alpha)) \tag{17}$$

And, the critical angle is derived based on the following expression:

$$\phi_{CA} = \arctan\frac{x_1}{y_1} = arctan\frac{(r\times\cos(\beta)+T\times\cos(\alpha))}{(r\times\sin(\beta)+T\times\sin(\alpha))}. \tag{18}$$

Based on this expression, it is found that the critical angle is determined by the aspect ratio of the initial FeOOH rods (L/W), the thickness of silica (T) and the theoretical critical azimuth (β).

The computation of the force was achieved by solving the equation in Comsol Multiphysics. First, the x (F_x), y (F_y) and z (F_z) components of magnetic forces between two nanorods were resolved by sweeping the secondary nanorod along a pre-designed trajectory. Then the three components were exported from Comsol. The overall magnetic forces (F_{total}) and their tangent (F_{tang}), normal (F_{norm}) components were calculated based on the following equations, respectively:

$$F_{total} = \sqrt{F_x^2 + F_y^2 + F_z^2} \tag{19}$$

$$F_{norm} = F_x sin\alpha + F_y cos\alpha \tag{20}$$

$$F_{tang} = F_x cos\alpha - F_y sin\alpha. \tag{21}$$

Printing color by lithography. Fe_3O_4@SiO_2 nanocubes were dispersed in hydrogel precursor containing AM (250 mg), BIS (14 mg), photoinitiator (3 μL) in EG (1 mL), which was then loaded between a glass substrate and a coverslip. A pre-designed photomask was placed above the devices, and then permanent magnet was applied parallelly to the surface of the cover glass. The polymerization was initiated by UV lamp with a wavelength of 254 nm and took 90 seconds totally.

Characterization. TEM images were taken on a Tecnai T12 transmission electron microscope operating at 120 kV. The magnetic properties of cubic Fe_3O_4@SiO_2 were measured using a Lakeshore vibrating sample magnetometer equipped with 736 VSM controller, Model 142A, Model 642 Electromagnet power supply, and Model EM4 HV

electromagnet. Optical diffraction spectra were measured by the Ocean Optics HR2000CG-UV-NIR spectrometer with a six-around-one reflection/backscattering probe. The angle between the incident light and the surface of the capillary was set at 30o. A home-made goniometer was used to precisely measure the angles between reflected light and the capillary surface. Dark-filed optical microscopic images were acquired by using A Zeiss AXIO Imager optical microscope. An X-ray diffractometer (XRD, EMPYREAM, PANalytical, Cu-Kα radiation) was used to characterize the crystals phases of nanocubes after reduction. Dynamic light scattering (DLS) measurement was conducted in Delsa NanoC Particle Analyzer from Beckman Coulter. TEM images were taken on Tecnai 12 transmission electron microscope operating at 120 kV. Diffraction spectra were measured by Ocean Optics HR2000 CG-UV-NIR high-resolution spectrometer. Optical microscopic images were acquired by ZEISS microscopy. SEM images was taken on scanning electron microscopy NovaNanoSEM 450 operating at 10 kV. The magnetization curve was measured at room temperature (RT) on a squid magnetometer.

2.3 Magnetic Assembly of Nanocubes into 1D Photonic Chains

Colloidal assembly has been developed as a reliable bottom-up approach toward the fabrication of photonic crystals with rich structural diversities and well-controlled optical properties.[2, 7, 27-33] In principle, the collective properties of assemblies can be tailored by not only changing the physical properties of colloidal particles but also modulating the way they "bond" in the periodic structures.[4, 6, 16, 34-35] In practice, however, most current research activities only produce close-packed assemblies due to the high symmetry of interacting forces. For example, polyhedral nanocrystals with shape varying from cubes to cuboctahedra, and octahedra were predicted to assemble in a close-packed face-to-face manner.[9, 19] Similar phase behavior was also observed in the nanoscale assembly of plates and rods.[36-38] As a result, this simple phase behavior greatly hinders the advancement of colloidal assembly in preparing photonic structures with more complex configurations. Introducing forces of different symmetries represents one of the promising approaches to overcome this limitation. Specifically, this purpose can be achieved by magnetic assembly of anisotropic building blocks whose magnetization does not correspond to any of the geometric axis favoring close packing. It has been long recognized that magnetic assembly is capable of not only assembling colloidal nanoparticles into ordered structures but also manipulating the dynamic equilibrium between various forces for reversible photonic response.[5, 39-44] These are typically achieved by balancing the magnetic attractions against various repulsive forces, like electrostatic repulsion or steric hindrance.[42, 44] Although the magnetic assembly of nanospheres[45-46] and their applications in ink-free printing, sensors, anti-counterfeiting and rewritable pads[5, 45, 47-51] have been extensively studied, magnetic

assembly of anisotropic nanoparticles has not been fully explored due to the lack of uniform building blocks and practical ways to analyze the competing interactions featuring different symmetries.

Herein, using superparamagnetic nanocubes as the building blocks, we show that their assembly under external magnetic fields does not favor close packing and therefore produces unique magnetic-field-responsive photonic nanostructures that allow active tuning of their structural colors by changing the field direction. More specifically, we show that the competing effects between long-range Zeeman coupling and short-range dipole-dipole coupling in the magnetic assembly of magnetite (Fe_3O_4) nanocubes give rise to a unique edge-to-edge rather than the common face-to-face mode. The cubic shape is found to be critical in determining the overall assembly behavior: the longest axis along the corner-to-corner direction causes favorable magnetization, while close packing in a face-to-face manner produces the strongest interparticle coupling. The unique assembly behavior not only provides a well-defined model to study the dynamic magnetic interactions between nanocubes but also offers new opportunities in tuning the structural colors of the assemblies: the optical diffraction of the 1D chain-like assemblies of the nanocubes can be tuned significantly from visible to near-infrared (NIR) region by varying the directions of magnetic fields, rather than the field strength that the nanospheres assemblies rely on in the previously demonstrated case.[5, 32] This study sheds light on the dynamic interactions between anisotropic nanoparticles, provides a reliable way to modulate magnetic forces of different symmetries and also offers new opportunities for

designing unique stimuli-responsive photonic nanostructures for building novel optical devices.

To prepare uniform superparamagnetic nanocubes, we used a robust post-treatment method.[52] More specifically, Prussian Blue (PB) nanocubes with an edge length of 200 nm were synthesized according to reported method[53] and then coated with a layer of silica (~25 nm in thickness) by a typical sol-gel process, as shown in the Transmission Electron Microscopy (TEM) images in **Figures 2.1a** and **2.1b**.[54] The PB@SiO_2 was then converted into Fe_3O_4@SiO_2 by a high-temperature polyol reduction process.[52, 55-56] As shown in **Figure 2.1c**, small magnetite nanocrystals with a size of about 10 nm are formed inside cubic silica shells,[52, 57] which is further confirmed by the X-ray Diffraction (XRD) patterns. Notably, silica coating not only maintains the cubic shapes during thermal decomposition but also provides abundant negative surface charges to balance the magnetic dipole-dipole attractions in the following assembly process.[58] The size of Fe_3O_4@SiO_2 nanocubes was 344.8 ± 53.2 nm, indicating their good uniformity and dispersibility in water. The crystal domain is calculated to be 8.9 nm in size by Scherrer Equation, and its consistency with the TEM observation in **Figure 2.1c** implies that each small nanoparticle is a single crystal. The magnetic hysteresis loop in **Figure 2.1d** confirms the superparamagnetic nature of the building blocks with a coercivity of 2.5 G, which is consistent with the tiny small crystal domain of the as-formed magnetite. The saturated magnetization of Fe_3O_4@SiO_2 is 32.5 emu/g and comparable to that of the superparamagnetic nanospheres that have been used for constructing magnetically responsive photonic crystals in our previous research.[46]

To facilitate the observation of the assembly behavior of Fe_3O_4@SiO_2 nanocubes under different magnetic fields, we placed a permanent magnet beneath the sample stage of a dark-field optical microscope. Before exposing to a magnetic field, the samples were well-dispersed in both water and ethanol without any apparent aggregates. Under the external magnetic field, linear chain-like structures were observed with parallel alignment to the field directions, which is similar to the assembled structures in the case of nanospheres.[47, 59-60] However, unlike the photonic chains of nanospheres which display bright structural colors under a vertical magnetic field, the diffraction of assemblies of nanocubes was negligibly weak under the same condition.[45] In addition, the chains remained randomly orientated in ethanol after removing the magnets as the electrostatic repulsion was significantly suppressed in ethanol compared with water.[44, 61] With this unique feature, the chains were further fixed by binding the neighboring nanocubes with additional silica species produced from the hydrolysis of tetraethyl orthosilicate (TEOS) in their colloidal dispersions. TEM images in **Figure. 2.1e** clearly show that the majority of nanocubes tend to align along [110] directions, namely edge to edge manner, with few [100] (face to face) and [111] (corner to corner) defects.

It has been well-established that magnetic nanoparticles experience a packing force (coupling between the magnetic fields and induced dipoles) as well as dipole-dipole interactions under magnetic fields.[42, 62] Basically, the magnetic coupling energy is the dot product of magnetic dipole moment ($\boldsymbol{m}$) and the field ($\boldsymbol{H}$) where it is exposed, whose first derivative defines the corresponding force in the form of $\nabla(\boldsymbol{m}\cdot\boldsymbol{H})$. For 1D photonic nanochains, it can be expressed as $F=3(1-3\cos^2\Theta)\ m^2/d^4$, where d is the distance between

the adjacent nanoparticles and Θ is the angle between external field directions and the lines connecting two nanoparticles. These interactions also occur in the magnetic assembly of nanocubes, but along the preferential magnetization (easy axis), i.e., the [111] crystallographic direction due to the shape anisotropy.[63] Compared to other two primary axes, [100] and [110], the easy axis connects the diagonally opposite corners and is the physically longest, which could minimize the magnetic coupling potential by aligning a maximum number of dipoles within the attractive regime ($\Theta \in [0^o, 54.74^o]$). The correlation between the easy axis and the long primary axis of anisotropic nanoparticles also exists in nano ellipsoids and plates with preferential magnetization along the longitudinal and radial directions, respectively.[64-67] In **Figure 2.1f**, we show the simulated magnetic field distribution of 1D chains of nanospheres and nanocubes. The magnetic flux density is the largest at corners when nanocubes align along the [111] direction, suggesting the strongest coupling between magnetic fields and the induced dipoles. To the contrary, the dipole-dipole coupling approaches the maximum in face-face configurations as evidenced by obviously stronger magnetic fields between adjacent nanocubes. Experimentally, the competition between the two magnetic interactions gives rise to [110] assembly mode due to the minimization of the overall magnetic potential.[63] Notably, based on the force equation, it can be easily concluded that the strength of Zeeman coupling and dipole-dipole coupling increases as the strength of the external magnetic field. This is mainly due to the increase in the strength of both the external magnetic fields and the induced magnetic dipole moment in individual nanocubes before they reach saturated magnetization. Therefore, the two competing forces can maintain the same order of magnitude in a broad

range of field strength, which, in turn, facilitates the formation of nanocube chains with uniform orientation, good periodicity, and widely tunable structural colors. Compared with isotropic nanospheres, the shape anisotropy of nanocubes breaks the coupling symmetry of not only the Zeeman effect but also the dipole-dipole interactions. In other words, the assembly of nanocubes under a magnetic field is governed by the competing local and global forces of different symmetries, thus produces 1D chains with energy-favorable [110] assembly mode .

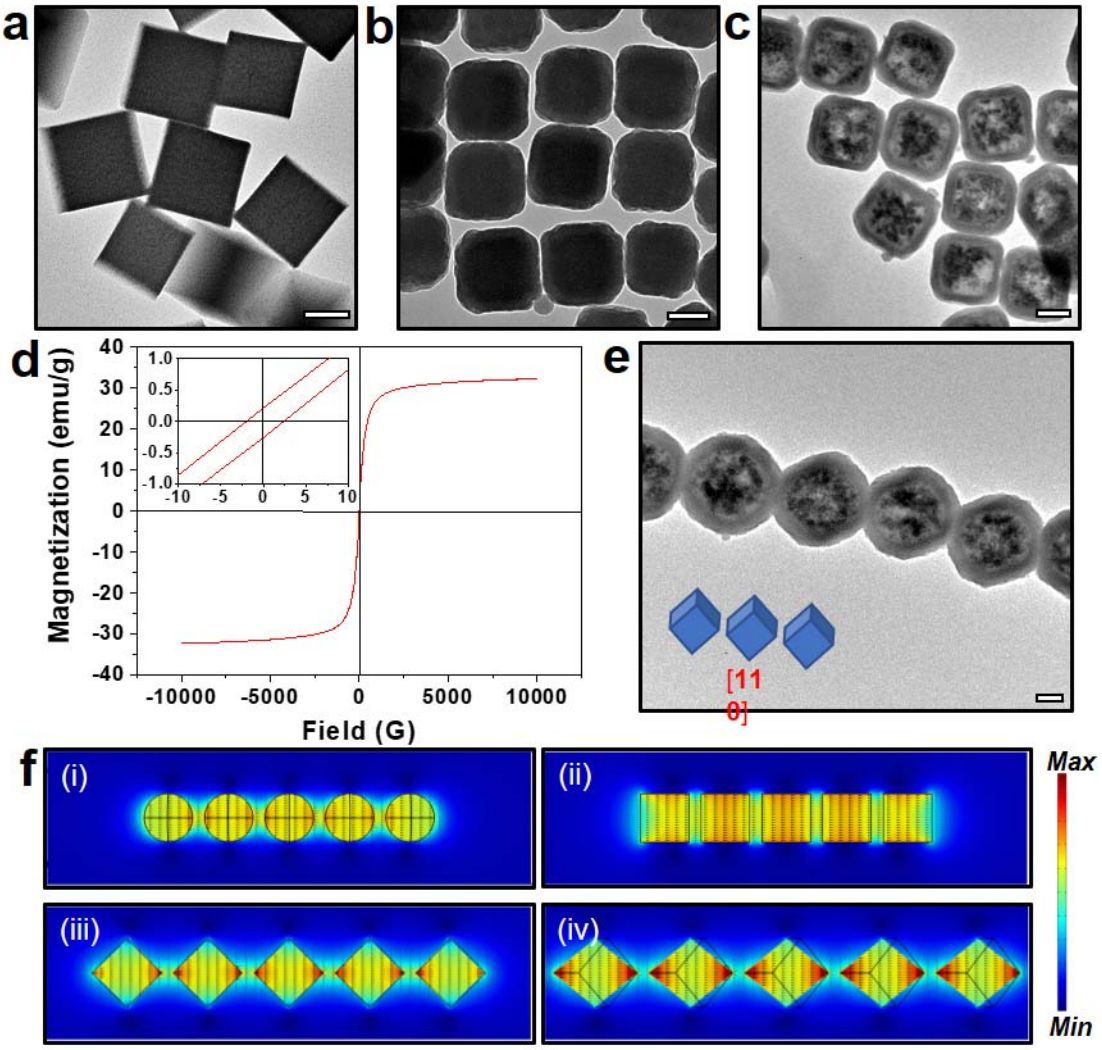

Figure 2.1. TEM images of (a) PB, (b) PB@SiO_2 and (c) Fe_3O_4@SiO_2 nanocubes. (d) Magnetic hysteresis loop of the Fe_3O_4@SiO_2. Inset: expanded low-field curve. (e) TEM image of assembled 1D chain-like structures fixed by additional silica coating. (f) Simulated magnetic field distribution of various chains of (i) nanospheres, and nanocubes assembled along the (ii) [100], (iii) [110] and (iv) [111] directions. Scale bars: 100 nm. Copyright © 2019 American Chemical Society.[15]

The specific [110] arrangements of nanocubes in 1D nanochains give rise to unique photonic properties, which are different from the cases of nanospheres. In our experiments, the z-y plane was set as the incident plane with an incident angle (α) of 30°， as illustrated in **Figure 2.2a**. The diffraction was found to be highly dependent on the viewing-angle (Θ) as demonstrated in **Figures 2.2b and 2.2c**. While the aqueous dispersion of magnetic nanocubes was gray without magnets, vivid and uniform structural colors were observed, which blue-shifted from red to orange, green, cyan and finally blue by changing the viewing angle from 20° to 70°. Further quantitative measurements indicated a quasi-linear correlation between the diffraction wavelength and viewing angle with a shift rate of ~ 6 nm per degree in diffraction wavelength. Such a dependence is theoretically confirmed by solving their collective scattering by the wave optics in COMSOL Multiphysics. As the refraction occurred at the air-water interface, the incident angle was calibrated as 48.2°. As shown in **Figures 2.2d and 2.2e**, the diffraction predicted by solving the wave equation is quite consistent with the measurement values. More practically, we systematically studied the diffractions of 1D chains by varying the directions of magnetic fields with fixed incidence and detection angles. As shown in **Figure 2.2f**, the reflection peak blue-shifted when magnetic fields were rotated from -10° to 55°. The measured reflection covers the whole visible spectra from 500 nm to 780 nm (**Figure 2.2g**). It is worth noting that the dependence of diffraction on the field strength is not as significant as the field direction. The tunable range by varying the field strength was much narrower (between 480 nm and 600 nm) and suffered from the broadening effect owing to the degradation of both positional and orientational orders when the magnet was far from the dispersion. To

interpret the physical origin of the unique optical performance, we started with a qualitative model based on ray optics, as shown in **Figure 2.2h**. The optical pathway of beams reflected by the adjacent faces is highly dependent on the reflection angle (Θ): a larger Θ results in a shorter optical pathway, which predicts blue-shift of diffraction peak and is consistent with the experimental observations.

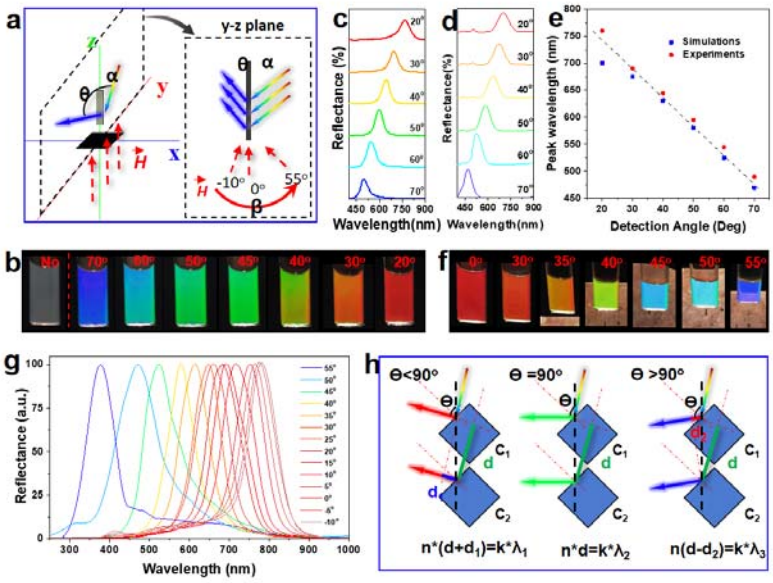

Figure 2.2. Tunable diffraction and structure colors in the colloidal dispersion under magnetic field. (a) Schematic illustration of the geometry for optical measurements. (b) Optical images of colloidal dispersion of Fe_3O_4@SiO_2 nanocubes in capillary without and with magnetic field under different viewing angles. Reflection spectra measured (c) and simulated (d) at different viewing angles (Θ). The incident angle, α, is set at 30°. (e) The correlation between peak position of reflection and detection angles. (f) Optical images of colloidal dispersions of Fe_3O_4@SiO_2 nanocubes in capillary under various directions (β) of magnetic fields. Note that the capillaries in the images were tilted slightly to get uniform structural colors in the colloidal dispersions. (g) The corresponding normalized reflection spectra measured by varying the directions of external magnetic field. (h) Qualitative ray-optic model predicting the difference of light pathway along three typical directions. Copyright © 2019 American Chemical Society.[15]

The viewing-angle-dependent diffraction of nanochains assembled from magnetic nanocubes and their obvious difference compared with photonic crystals based on magnetic nanospheres are fully revealed in **Figure 2.3**. When a colloidal dispersion of nanospheres was exposed to a vertical magnetic field, only green was observed along different viewing angles (**Figure 2.3a**). The diffraction of photonic nanochains based on nanospheres was mainly tunable by the field strength instead of the field direction as reported in our previous work.[45, 51] The dynamic equilibrium between the electrostatic repulsion and magnetic attraction between adjacent nanospheres makes the 1D photonic structures quite susceptible to field strength: the inter-particle distance and diffraction wavelength increase when field strength decreases. In the case of magnetic nanocubes, however, a continuous redshift of the structural color occurred in their colloidal dispersion under vertical magnetic fields when the viewing angles gradually decreased (**Figure 2.3b**). The geometry correlation between light incidence and diffraction is summarized in **Figure 2.3c**: larger viewing angle produces shorter diffraction wavelength. These observations clearly demonstrate that light will be diffracted along different directions through the colloidal dispersion owing to the shape anisotropy of nanocubes and their preferential [110] assembly manner under external magnetic fields.

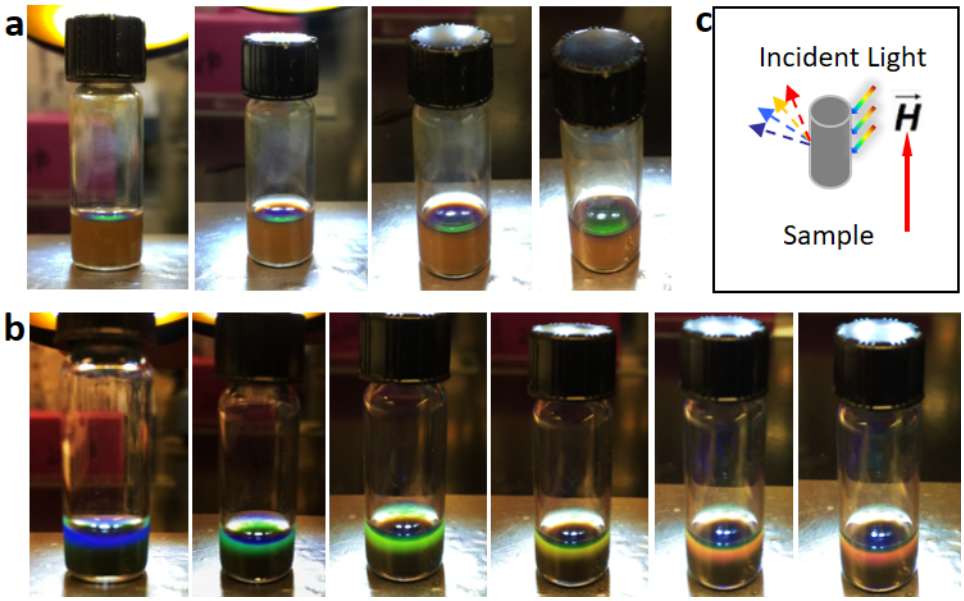

Figure 2.3. (a) Optical images showing structural color in the colloidal dispersion of CNCs exposed to vertical magnetic field. (b) Optical images showing structural color in the bulk solution of cubic Fe_3O_4@SiO_2 in glass vail. (c) Scheme showing the diffraction occurring in the colloidal dispersion of cubic Fe_3O_4@SiO_2 exposed to vertical magnetic field. Images in (a) and (b) were taking at different viewing angles. From left to right, viewing angles decreased gradually. Copyright © 2019 American Chemical Society.[15]

To quantitatively analyze the diffraction of the assembled chains, we simulated the light field distribution by a finite-element method (COMSOL Multiphysics). The modeling and symmetry of the assembled structure are illustrated in **Figure 2.4**. An S-polarized Gauss beam is incident from the top with an incident angle of 48.2º to the chain orientation, and nanocubes are aligned along their [110] direction with a separation of 30 nm. The electric field distribution and polar plots under incident light of different wavelengths are shown in **Figure 2.5**. With the incidence of a 400-nm light (**Figure 2.5a**), the diffracted beam is split to the right bottom with a large angle. When the incidence wavelength increases from 400 to 800 nm, it shifts from the bottom right to the top, as shown in **Figures 2.5b and 2.5c**. Polar plots in **Figures 2.5d to 2.5f** indicate that light is diffracted along 127º, 107 º and 75 º for incidence wavelength of 400, 600 and 800 nm, respectively.

$$-\nabla^2\vec{E} + \vec{\nabla}\left(\vec{\nabla}\vec{E}\right) - \frac{\omega^2}{C^2}\varepsilon\,(r)\vec{E} = \frac{\omega^2}{C^2}\varepsilon_0\vec{E}$$

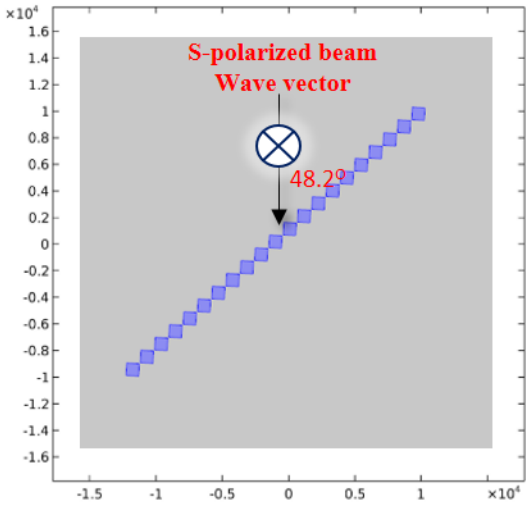

Figure 2.4. Modeling of light-field splitting by assembled nanochains in wave optics by solving the Maxwell' Equation. Copyright © 2019 American Chemical Society.[15]

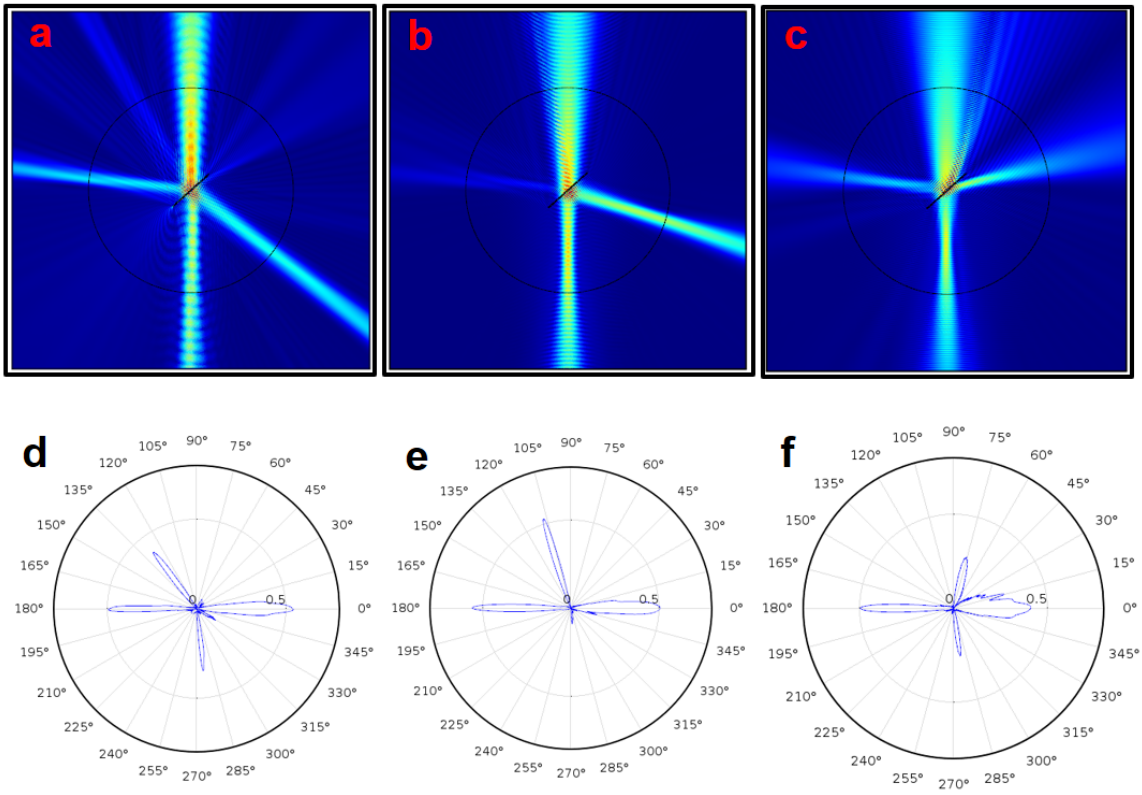

Figure 2.5. Simulation of light field split by the assembled chains along the [110] directions. Electric field distributions under incident light with wavelengths of (a) 400 nm, (b) 600 nm and (c) 800 nm. (d), (e) and (f) The corresponding polar plots. Copyright © 2019 American Chemical Society.[15]

Direct mapping of the split of the light field is realized by dark-field scattering. The colloidal dispersion of Fe_3O_4@SiO_2 nanocubes was sealed in a capillary with optical beam incident along the edge of the capillary. Without a magnet, only the random scattering of individual nanocubes in the colloidal solution was observed (**Figures 2.6a and 2.6c**). Under an external magnetic field, however, the formation of 1D nanochains induced distinct diffraction patterns with unique and continuous color strips. Two symmetric optical spectra from red to blue were observed once the magnetic field direction became parallel to light incidence (0^o configuration in the middle panel of **Figure 2.6b**). These observations directly confirmed the angle-dependent diffraction in our previous measurements: light with shorter wavelength will be diffracted along larger reflection angles. The spatial dispersion of diffracted light is highly dependent on the orientation of 1D nanochains. When the field direction of the magnet was switched along either counter- or clockwise direction, the diffraction patterns will shift accordingly with gradually attenuated intensity (**Figure 2.6b**). Relying on the spatially resolved diffraction spectra, we can intuitively visualize the diffracted light of different colors along specific directions. Taking the 0^o configuration as an example, the blue beam path was observed inside the capillary at the reflection angle of about 120^o. When it decreased to 60^o, the color shifted from blue to green, yellow, orange, and finally red, as suggested in **Figure 2.6d**.

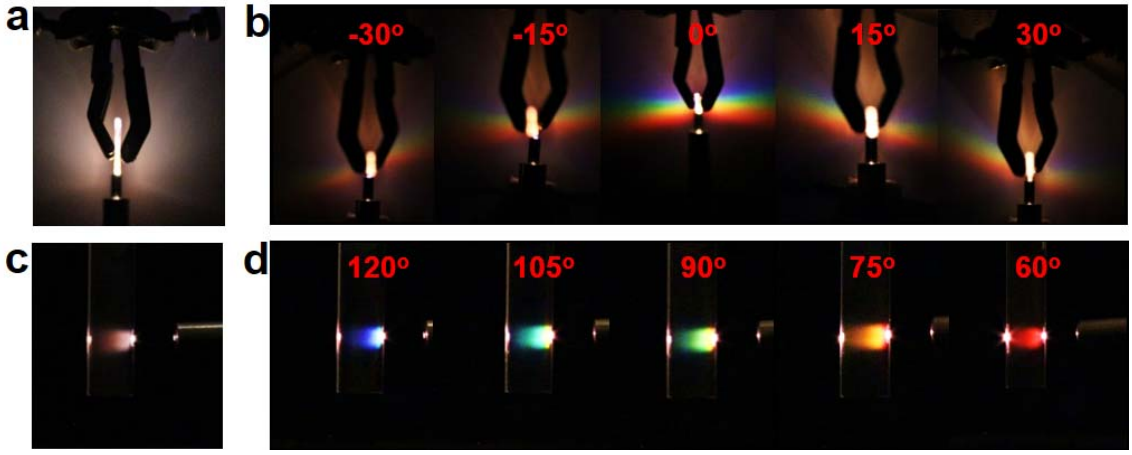

Figure 2.6. (a) Optical image of light scattered by colloidal dispersion without magnetic field. (b) Optical images of light scattered under different orientations of magnetic fields. (c) Side view of colloidal dispersion in capillary without magnetic field. (d) Side views of colloidal dispersion with magnetic field under different viewing angles (Θ). Copyright © 2019 American Chemical Society.[15]

Comparing with nanospheres assemblies, a unique feature of the nanocube assemblies is the strong dependence of their diffraction on the chain orientation, which offers excellent opportunities for designing photonic devices with novel functionalities not achievable by other means. In our previous work, when nanospheres are magnetically assembled in a thin film, the strongest diffraction is obtained along the chain direction (the field direction) which is typically perpendicular to the film surface. Since the intensity of the diffraction increases with the repeating units of the lattice, the film has to be thick enough (typically above 500 μm) to produce an easily perceptible color contrast. This is particularly a challenge for many applications that do not allow the incorporation of thick films, for example, anti-counterfeiting in banknotes which have a total thickness of ~100 μm. On the contrary, nanocubes can be assembled in the plane of the film with sufficient repeating units or chain length to exhibit high-intensity colors that are observable from outside the plane, making them ideal candidates for this type of anti-counterfeiting applications. As an example, here, we demonstrate printing of arbitrary patterns in thin films with the in-plane alignment of the nanocube assemblies by combining dynamic magnetic assembly and photolithography. As shown in **Figure 2.7a**, a mixture containing colloidal dispersion of magnetic nanocubes in ethylene glycol, acrylamide monomer, and photoinitiator was first sandwiched between a glass substrate and cover glass. A UV light was then illuminated through a photomask with pre-designed patterns while a magnetic field was applied horizontally (parallel to the cover glass surfaces). The nanochains in the uncovered areas are fixed in position, with parallel alignment to the film surfaces. The photomasks and magnets were then removed, followed by another UV exposure to polymerize the rest parts

of the films. To highlight the differences between the two cases, the process of fixing nanosphere-based chains is also schematically illustrated in **Figure 2.7b**. Notably, a vertical magnetic field was applied during UV exposure, which gave rise to the perpendicular orientation of nanochains to the film surfaces and thereby uniform backward diffractions.[47-48, 59] Under light illumination to the front surface, the as-made films containing nanocube chains did not display any apparent patterns against both dark (**Figure 2.7c**) and white (**Figure 2.7d**) backgrounds. Upon illumination at ~ 30° from the backside, a vividly blue butterfly came into view (**Figure 2.7e**). As expected, the same image could show different colors, from blue to red, depending on the viewing-angles. In addition, a color gradient covering the whole visible range was observed under the illumination of a point light source due to the variation in the incident angle, as shown in **Figure 2.7f**. By taking advantage of the in-plane alignment of the 1D nanocube assemblies, we were able to decrease the film thickness from the initial 1 mm to 80 μm and finally 10 μm. As shown in **Figures 2.7g and 2.7h**, they still exhibited pre-designed patterns with vivid structural colors, clearly demonstrating their significant advantage in applications where a small thickness (micrometer scale) is preferred. This process was able to produce any arbitrary images and letters by simply applying a pre-designed photomask during polymerization.

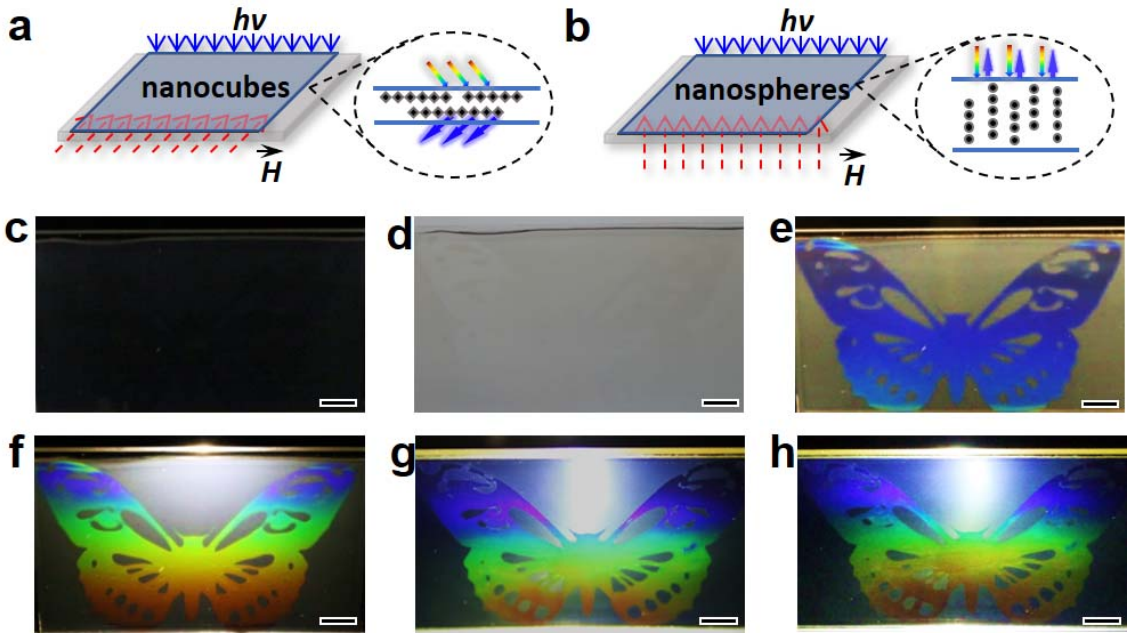

Figure 2.7. (a) Scheme showing the printing process based on the assembly of nanocubes. The orientation of nanochains assembled from nanocubes is parallel to the surface of the film and light will be diffracted through the film. (b) Scheme showing geometry of fixing nanochains based on nanospheres. Their orientation is perpendicular to the film surface and light will be diffracted backward. Optical images of the fabricated film under (c) dark and (d) bright backgrounds. (e) The same film under directional light illumination. Hydrogel films under the illumination of point light sources (dotted circle) with the film thickness of (f) 1 mm, (g) 80 μm, and (h) 10 μm. Scale bars: 5 mm. Copyright © 2019 American Chemical Society.[15]

The unique orientation-dependent photonic response of the nanocube assemblies allows one to create some "magic" patterns of structural colors to exhibit unusual optical effects that are not attainable using spherical building blocks, thereby offering many new opportunities for designing novel security devices. **Figure 2.8** demonstrates such an example. Using a photomask with the original pattern shown in **Figure 2.8a,** we fixed vertically aligned nanocubes in the black regions and horizontally aligned ones in the white regions of a polymer film. When the film was illuminated from the front and viewed against a dark background, no obvious structural color was observed as demonstrated in **Figure 2.8b**. When the light was illuminated from the backside, the film displayed the hidden pattern with an orientation-dependent contrast. As shown in **Figure 2.8c**, at the original orientation (0^o), only the regions with vertical photonic chains exhibited deep blue color, producing a positive image similar to the photomask. When the film was rotated 90^o counterclockwise, the orientation of the embedded nanochains in the black and white regions became horizontal and vertical, respectively, and the blue colors would be observed in the white regions, which was consistent with the images shown in **Figure 2.8d**. Interestingly, by comparing the printed images before and after 90^o rotation, we found that the film appeared to be rotated clockwise, which was opposite to the counterclockwise rotation in reality. Similarly, when the film was further rotated counterclockwise by 180^o (**Figure 2.8e)** and 270^o (**Figure 2.8f**), the patterns were perceived to further rotate clockwise. This optical effect is attributed to the unique orientation-dependent photonic response of the nanocube assemblies and their simultaneous change in the orientation and position when the film is rotated.

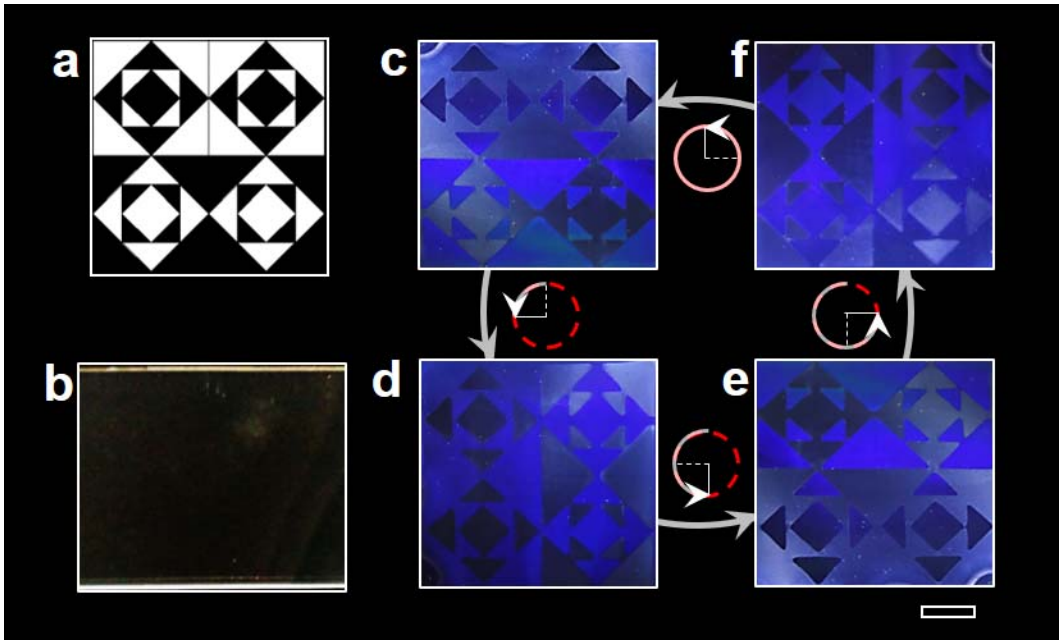

Figure 2.8. (a) Photomask used for printing the corresponding image in (c). The chains were fixed vertically in dark and horizontally in white areas. (b) Digital images of printed pattern under dark background. Digital images of the printed pattern under different orientations by rotating the film counterclockwise from (c) 0° to (d) 90°, (e) 180° and final (f) 270°. The complementary coloration occurred for each counterclockwise rotation of 90°, which produced an opposite visual effect of clockwise rotation. Scale bar: 5 mm. Copyright © 2019 American Chemical Society.[15]

2.4 Magnetic Assembly of Nanoplates into 2D Photonic Crystals

Hexagonal nanoplates are synthesized by solvothermal method.[68] The edge length is 100 nm and thickness is 30 nm (**Figure 2.9a**). A 37.5 nm silica is coated on the Fe_2O_3 nanoplates to increase the final thickness to 105 nm (**Figure 2.9b**), which is desirable for constructing photonic crystals with bandgap in the visible range. Silica layer also plays an important role in the following reduction as it can protect the overall plate-shape from being damaged at the high-temperature reduction. We first examined their magnetic assembly under optical microscope. As shown in **Figure 2.10**, nanoplates self-assembled into chain-like structures under a horizontal magnetic field. Interestingly, we observed blue color on the assembled structures. If the applied magnetic field was tilted from horizontal to perpendicular direction, the structural color changed from blue to green, and final red. At the vertical magnetic field, the cross sections of the assembled structures were observed, and they did not exhibit obvious diffraction of visible light.

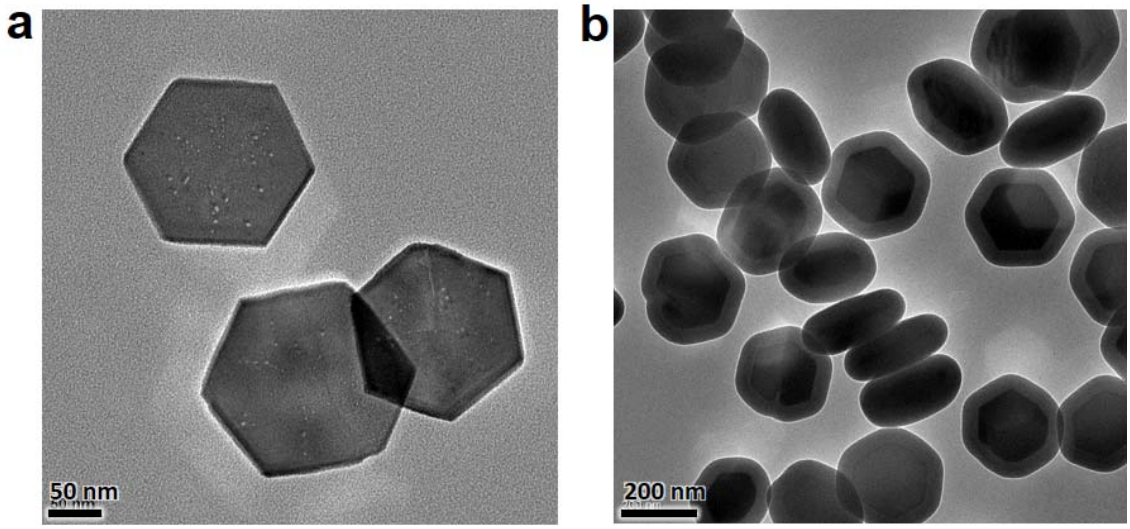

Figure 2.9. TEM images of (a) Fe_2O_3 nanoplates, (b) Fe_2O_3@SiO_2 nanoplates with the overall side thickness of 105 nm.

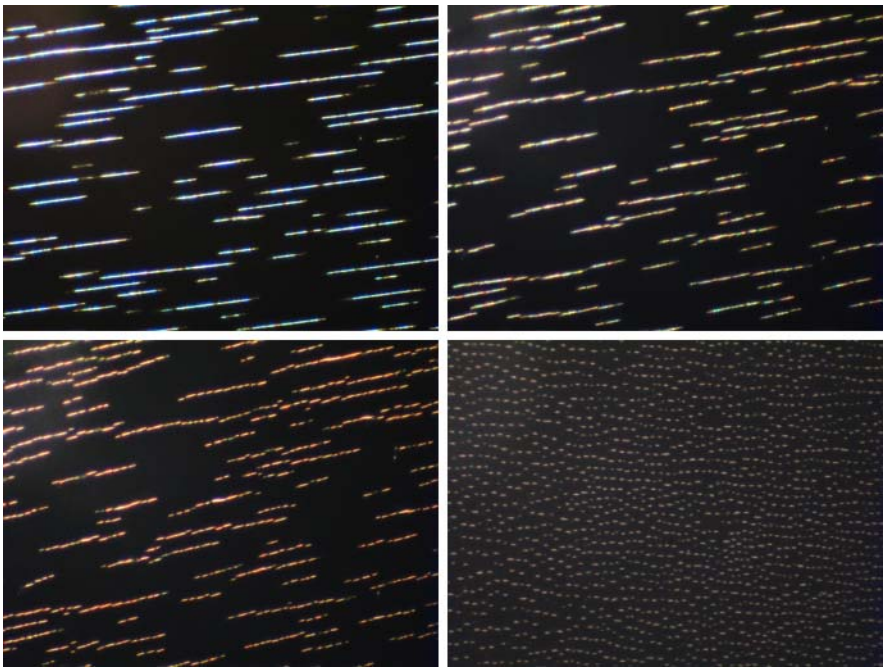

Figure 2.10. The optical images of magnetic nanoplates with overall side thickness of 105 nm while changing the direction of magnetic field.

The assembled photonic structures were fixed by additional silica coating and characterized by TEM. As shown in **Figure 2.11a**, we observed a preferential 2D packing of the nanoplates. The projection of the assembled structures along the radical direction of the nanoplates gives rise to a centered rectangular phase of the nanoplates. The assembled structures are illustrated in **Figure 2.11b**. Under an external magnetic field, nanoplates tend to be magnetized along their long axes due to their plate-shape induced magnetic anisotropy. It is interesting to point out that neighbouring plates self-assembled though a side-on manner instead of the intuitive end-on manner. This remarkable preferential bonding further results in a 2D centered hexagonal assembly as illustrated in **Figure 2.11b**. Another possible reason why nanoplates favor 2D photonic structures is because the formed 2D structures exert strong repulsion to the plates trying to approach the 2D structures from the side. As a result, there is no chance for free plates to find a thermodynamic position from side-on attachment.

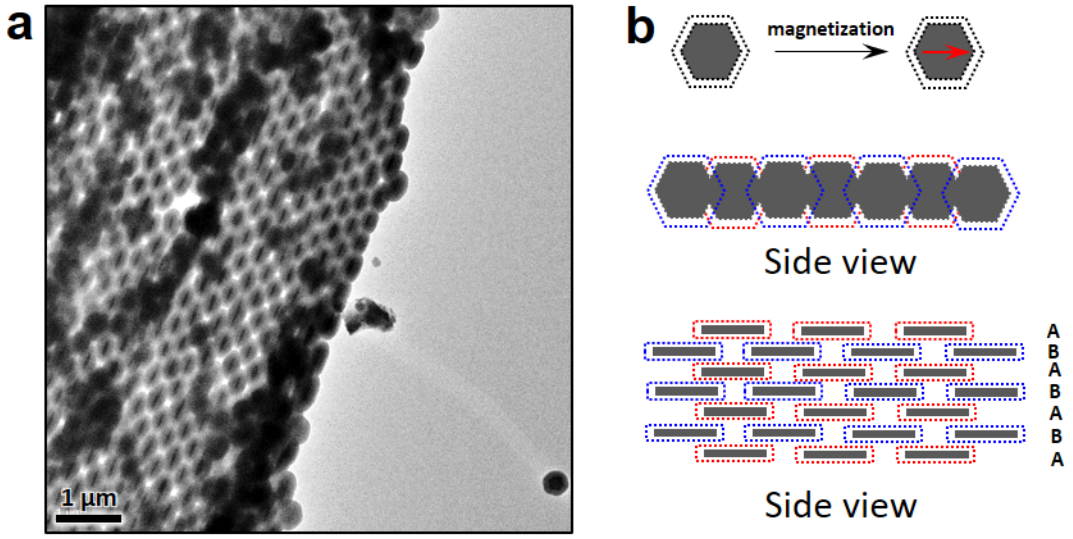

Figure 2.11. (a) TEM of the assembled 2D photonic crystals. (b) Schematic illustration of the 2D photonic crystals.

2.5 Magnetic Assembly of Nanorods into 3D Photonic Crystals

In this section, we establish a new type of superstructures, *bct* colloidal crystals, by breaking the entropic symmetry in colloidal assembly using magnetic forces. The anisotropic super-dipole interactions between magnetic nanorods create well-defined and size-sensitive attractive and repulsive surface "patches" on hard colloids. Our joint multi-dimensional simulation reveals that rod shape-induced magnetic anisotropy diverges the thermodynamic equilibrium from the two main axes of rods, producing superstructures in hard contact while maintaining minimum surface overlap, readily accessible surface areas, and interconnected porosity. Similar phase behavior has been observed in nanorods over a broad range of ARs and *bct* crystals can thus be created with tunable lattice constants and tailorable physical properties. The reduced symmetry of *bct* crystals generates anisotropic photonic bands that are determined by the crystal orientations. It enables us to actively tune the optical diffraction and structural colors of the assembled *bct* photonic crystals by simply changing the direction of applied magnetic fields.

Magnetic assembly of nanorods into *bct* colloidal crystals. FeOOH nanorods with different ARs (from 3 to 30) were synthesized by hydrolysis of $FeCl_3$ at desirable conditions (**Figures 2.12**). A layer of SiO_2 of controllable thickness was coated[54] and the FeOOH@SiO_2 rods were further reduced to magnetic nanorods by H_2 at elevated temperature (**Figure 2.13a**).[52] Due to the protection of silica layers, the rod-like morphology maintained after reduction. A transmission electron microscope (TEM) image in **Figure 2.13a** reveals the high uniformity and structural integrity of magnetic rods (FeOOH-II, 322×70 nm). Their assembly was carried out by sitting an aqueous dispersion

of rods on a permanent magnet. Silica precursor was introduced to fix the assembled crystals through a conformal coating of SiO_2[34]. During assembly process**,** brilliant green color was observed on stripe-like microstructures in the colloidal dispersion. A scanning electron microscope (SEM) image in **Figure 2.13b** shows that the rods self-assembled into 3D colloidal crystals under magnetic fields, whose equilibrium position offset from end-on close packing. In this crystal plane, neighbouring rods magnetically bond with a regular tip overlap. The colloidal crystals maintain a perfect order in a scale of hundreds of micrometers (**Figure 2.13c**). Due to the offset arrangement, the contact joints between neighbouring rods form 1D periodic structures with alternating high (black lines) and low mass density areas. As the colloidal assemblies are fixed by SiO_2, they can be readily transformed into lattices made of other colloids by post-assembly wet chemical process without affecting the structural integrity. For example, we prepared *bct* crystals of hollow SiO_2 nanorods by selectively etching away Fe_3O_4 cores (**Figure 2.13d**). The crystal structures maintained after Fe_3O_4 was complete etched, leaving hollow SiO_2 colloids in the primary *bct* lattices. After carefully examining the arrangement of rods in the crystals, a 3D rendering model and ball-stick bond diagram are illustrated in **Figure 2.13e**. In one unit cell, eight rods occupy the vertex sites with one in the middle, forming a *bct* lattice. Its length along a and c-axis are 210.6 nm and 513.9 nm, respectively. The angle between [111] and [110] is 30^o.

Table 2.1. The synthesis and characterization of FeOOH nanorods with different aspect ratios.

FeOOH #	HCl (M)	T (°C)	t	L (nm)	D (nm)	Aspect Ratio
F1	0	RT	3 m	288.10±15.06	91.59±7.27	3.16±0.24
F2	0			322.15±16.45	70.22±4.69	4.60±0.19
F3	0.02	87	25.5 h	381.40±50.34	52.05±8.79	7.44±1.05
F4	0.03			433.83±82.80	41.72±8.13	10.54±1.47
F5	0.04			600.63±50.26	32.88±4.14	18.14±3.05
F6	0.05			661.82±63.03	30.12±4.34	21.78±4.73
F7	0.06			819.24±88.80	27.35±3.49	30.26±3.91

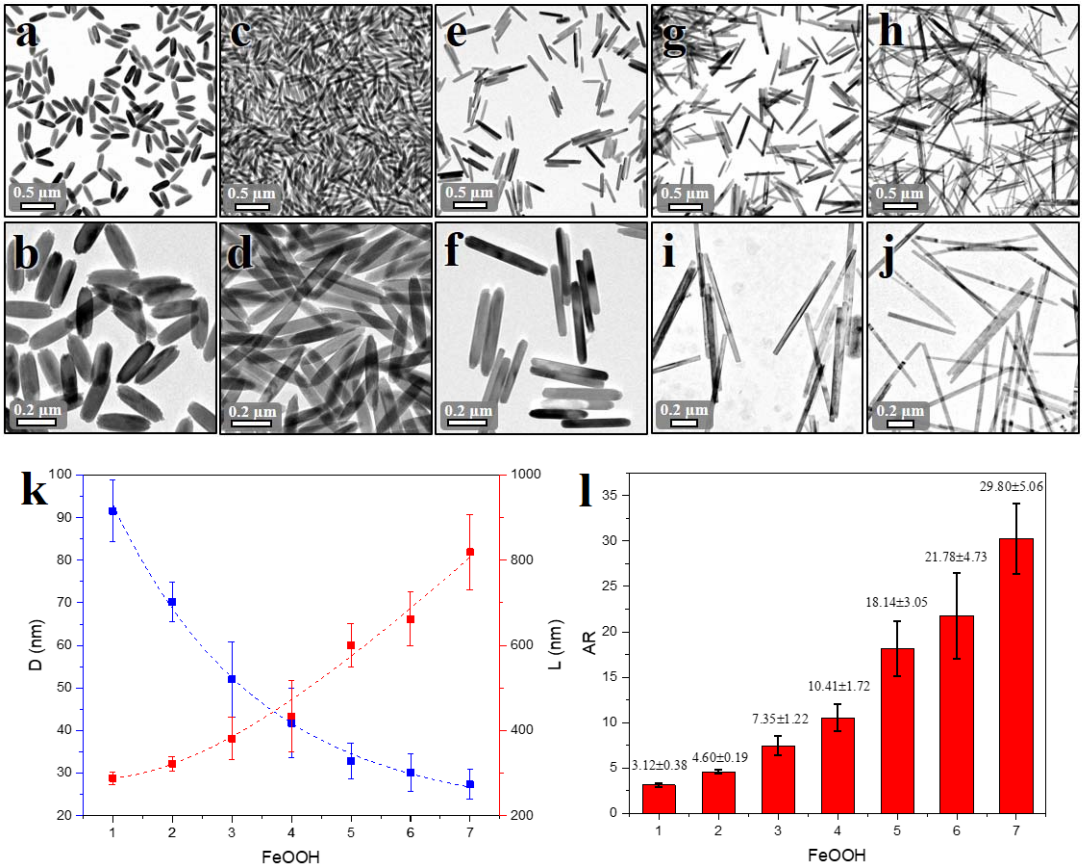

Figure. 2.12. TEM images of FeOOH nanorods with different aspect ratios. The FeOOH nanorods from #1 to #7 in **Table 2.1** are shown in a-b, c-d, e-f, g, h, i and j, respectively. (k, l) Summary of the average size of FeOOH nanorods with different aspect ratios.

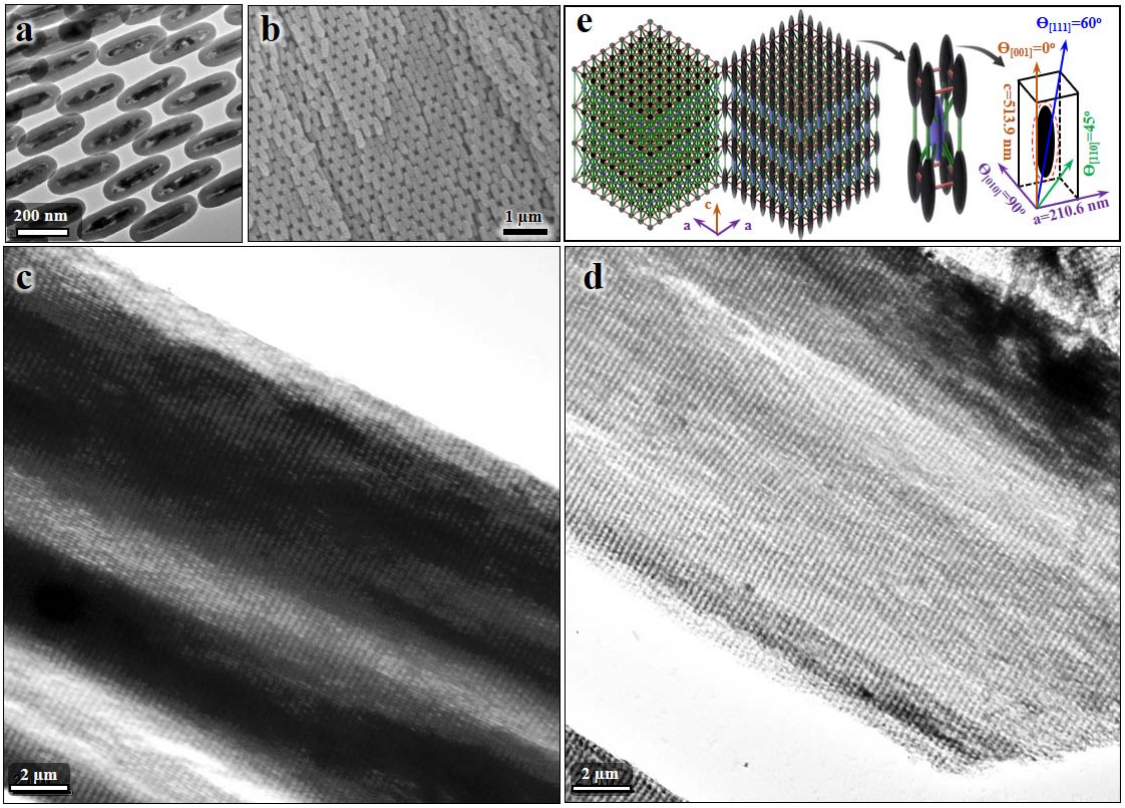

Figure 2.13 | Magnetic assembly of nanorods into *bct* colloidal crystals. (a) TEM image of Fe_3O_4@SiO_2 nanorods. (b) SEM image of *bct* crystals. (c) Schematics of *bct* crystals, primitive cell and its parameters. Low-magnification TEM images of *bct* crystals of (d) Fe_3O_4@SiO_2 nanorods and (e) hollow SiO_2 ellipsoids formed by post-assembly etching of Fe_3O_4 core.

In TEM images, we observed crystal projections along two typical crystallographic directions. In **Figure 2.14a,** the TEM image exhibits projection of a crystal along <100>, giving rise to well-packed rods in a centered rectangular phase. The apparent periodic cavity in the crystal indicates that the rods are not closely packed but remain hard contact. TEM image in **Figure 2.14b** is a projection of the superlattice along a small offset angle (~15º) from <100>, which compromises of two crystal planes. The crystal projection along their <110> (**Figures 2.14c and 2.14d**) indicates a layer-by-layer stacking of {110} crystal planes with apparent periodic nodes of overlapped rods. The arrangements of rods in {100} and {110} planes are illustrated in the 2D rendering of **Figure 2.14e**, suggesting rectangular and centered rectangular phases, respectively. In projection scenario, the lattice patterns (Ball-stick bond diagram in **Figure 2.14e**) along the two crystallographic directions appears opposite to rod arrangements and are clearly exhibited in TEM images.

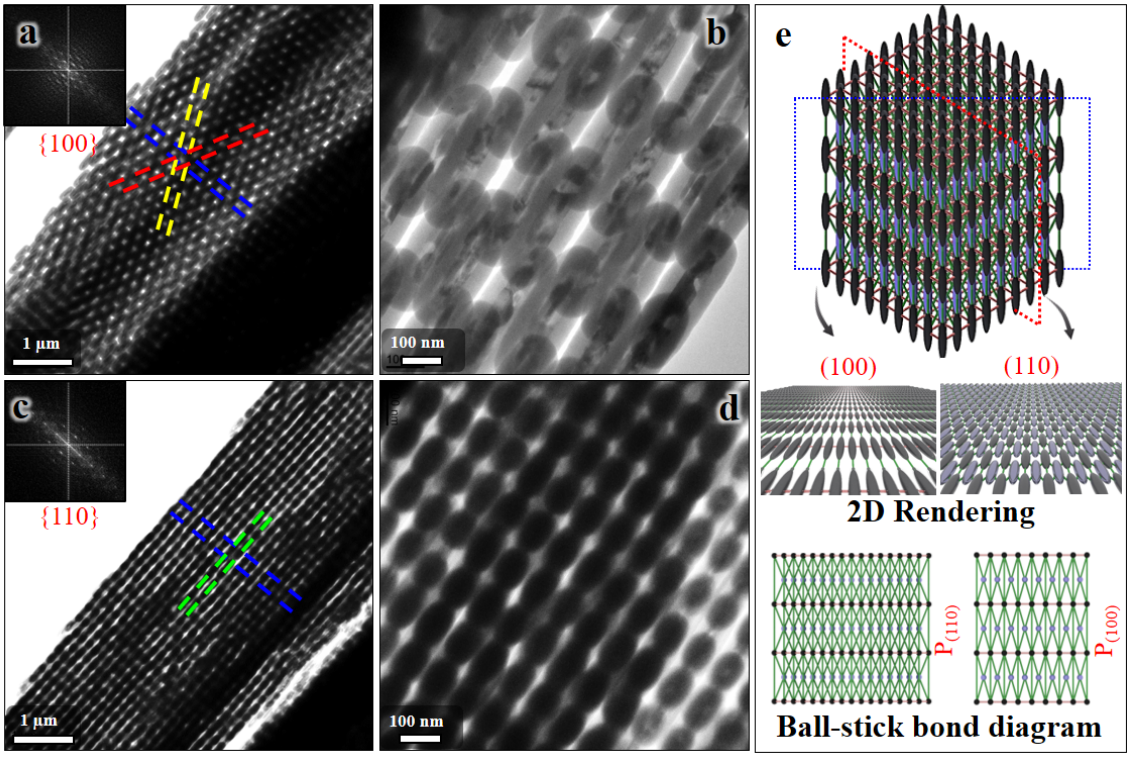

Figure 2.14. Magnetic assembly of nanorods into *bct* colloidal crystals. (a, b) {100} facets and (c, d) {110} facets. Inserts in E and G show the corresponding FFT. (e) Compute-generated models. The 3D reddening and ball-stick bond diagram of the *bct* colloidal crystal and its facets.

Structure characterization of the *bct* colloidal crystals. The positions of rods in the colloidal crystals was identified by imaging processing and mapped to a *bct* lattice in **Figure 2.15a**. The radical distribution of nanorods (r_{cc}) in **Figure 2.15b** demonstrates the excellent order of rods, which defines the lattice spacing (d) between facets of (110), (100), (101), and (001). The 3D arrangement of rods and the rotational symmetry of the *bct* crystals were systematically studied by electron tomography. In **Figure 2.15c**, we started with a projection of (110) facets, $P_{(110)}$, and acquired TEM images by continuously rotating the crystal along [001] and [110] crystallographic directions. The initial $P_{(110)}$ exhibits a layer-by-layer structures with a centered rectangular packing of rods in (110) (**Figure 2.15d**). When the crystal was tilted by $R_{[001]}$=45°, we observed a gradual evolution toward $P_{(100)}$, which exhibits rectangular arrangements of rods in (100). In the case of $R_{[110]}$, the initial $P_{(100)}$ was switched to $P_{(111)}$ when the tilting angle was 60°, thus resulting in a rectangular out-of-plane topography of rods (**Figure 2.15e**). Using nanorods with different sizes and ARs, we obtained a library of *bct* colloidal crystals with tunable lattice constants. In **Figure 2.15f**, projections of (100) facets of a *bct* crystal were observed for nanorods with ARs ranging from 2.25 to 18.5. Isotropic nanospheres instead favor chain-like structures due to the dipole-dipole attractions. In the phase diagram (inset in **Figure 2.15g**), nanorods of large ARs self-assembled into disordered fibers under magnetic fields due to their significant decrease in diameters and the segregation of magnetic cores after reduction. By carefully examining the lattice spacing, a quasi-linear correlation between the c/a and ARs (l/w) was identified (**Figure 2.15g**).

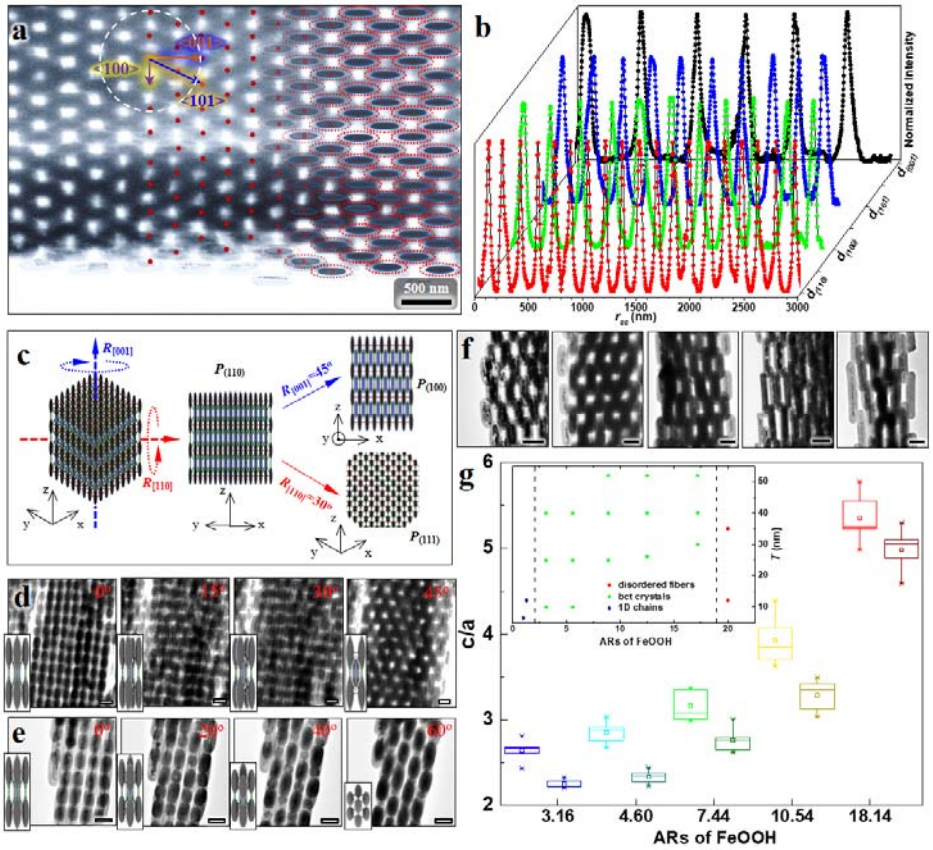

Figure 2.15. Structure characterization of *bct* colloidal crystals. (a) TEM image of the bct crystal showing the projection along {100} facets. Positions of rods are identified with image processing and mapped to a *bct* lattice. (b) Normalized distribution intensity of nanorods inside the crystals in (a) along different crystallographic directions. (c) Schematics of *bct* crystals under different orientation by rotating along given crystallographic directions. (d, e) TEM images of bct crystals under various orientation by rotating along [001] and [110], respectively. (f) TEM images of bct crystals assembled form magnetic nanorods with different sizes and aspect ratios. (g) The dependence of crystal structure (c/a) on the ARs of magnetic nanorods. Inset is the phase diagram.

Force dynamics and assembly mechanism. In our multi-scale computer simulations**,** a secondary rod is continuously swept along a well-define trajectory in tight placement with the primary rod (**Figure 2.16a**). Under a magnetic field, they will be magnetized with a parallel magnetic dipole moment. As in situ plotted in **Figure 2.16b** by using FeOOH-II as an example, their overall magnetic force evolves as t and Θ. For Fe_3O_4@SiO_2 colloids with abundant surface charges, the Coulomb electrostatic repulsion is major reaction force to magnetic attraction.[42] Its classic use involves multipolar expansions of an analytical equation, whose direction is mainly considered to be along the connecting line of interacting colloids within the Debye screening length. The monopole approximation is operational for isotropic, homogeneously charged spheres or anisotropic colloids with considerably large separation.[69] As colloids approach closer, their shape anisotropy becomes more effective. Instead, our finite element analysis points out that the force direction is highly dependent on interparticle separation and that, in closely packed assemblies, it gradually approaches the surfaces normal of interacting rods. Therefore, it is reasonable to propose that, at thermodynamic equilibrium, the tangent component of the magnetic attraction force will vanish to get rid of any relative translational shifts of two rods, leaving only normal force component that will be balanced by the electrostatic repulsion. To verify this hypothesis and identify the critical angles (ϕ_c), we decompose the overall magnetic force into tangent (F_{tang}) and normal components (F_{norm}). In **Figure 2.16c**, F_{norm} changes from negative to position values at Θ=43º, which separates a repulsion and attraction domain. This interaction motif drives neighbouring rods to assembly at their attractive patches into a geometric arrangement limited by their shape while avoiding

energetically unfordable hard contacts between repulsive middle patches. In the attraction regime, we specify a critical point at F_{tang}=0, where the magnetic attraction is along the surface normal. For example, at SiO_2 thickness of 50 nm, the ϕ_c was found to be 69°, which was very close to 63.5° measured from TEM images.

In **Figure 2.16d**, the tangent (left half) and normal (right half) components are mapped and vectorized by local arrows. For isotropic nanospheres, ϕ_c remains 90° due to the dipole-dipole attraction, resulting in end-on bonding and energetically favorable 1D chains. For nanorods, the force boundary shifts to small Θ regions as silica thickness is increased from 5 to 50 nm. Meanwhile, we observed a first decrease and then increase in ϕ_c (dashed blue line). To understand the deterministic role of ARs, we systematically analyzed ϕ_c for different magnetic rods and map their correlation in a 3D surface in **Figure 2.16e**. Nanorods favor offset packing with a well-defined ϕ_c, which finally degenerate to 90° as SiO_2 thickness increases (**Figure 2.16f**). It was also pointed out that ϕ_c mainly increased as ARs due to the geometric elongation of rods. The offset bonding between two rods initiated the nucleation of *bct* crystals as neighbouring rods will assemble at preferential crystalline sites (**Figure 2.17a**). Further qualitative thermodynamic analysis elucidates that it breaks lateral symmetry of rods, providing few energetically active sites for neighbouring rods to deposit. The crystal growth is driven by preferential in-plane tessellation of rods in {110} facets, instead of homogeneous 3D packing, as evidenced by contrast differences of TEM images along <100> and <110> crystallographic projections; the uniform contrast in TEM images of <110> projection (**Figures 2.17b-2.17d**) imply even, sequent rod packing in the exposed (110) facets. At this stage, out-of-plane deposition of rods is energetically

forbidden as it needs to overcome higher magnetic potential. In <100> (**Figures 2.17e-2.17g**) projections, we observed gradient contrast and thus a gradual decrease of crystal thickness from middle to crystal edge. These observations suggest a well-defined rectangular cross section of bct crystal grains (depicted in **Figure 2.17a**) as consequence of the preferential in-plane packing in (110) facets. The presence of a metastable intermediate of 2D sheet in our experiment demonstrates the proposed pathway of nucleation (**Figure 2.17h**), whose further growth into 3D crystals require higher dimension analysis of the reaction dynamics.

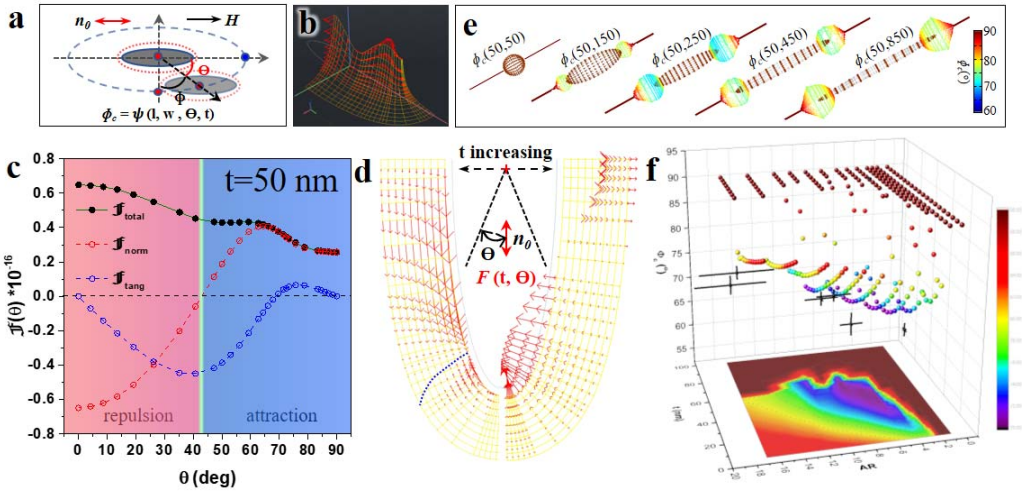

Figure 2.16. Assembly mechanism and force dynamics. (a) Schematics showing the geometry for calculating the pair interaction between two nanorods under horizontal magnetic fields. (b) Force filed of pair interaction between two magnetic nanorods by varying separation and angles (Θ) between $\boldsymbol{r_{cc}}$ and $\boldsymbol{n_0}$. (c) Plot of total force and its normal, tangent components against Θ. (d) Force field of the normal (left half) and tangent (right half) components of the pair interactions. (e) 3D mapping of critical angles (ϕ_c) for nanorods with different ARs. (f) Plot of the critical angles (ϕ_c) against SiO_2 thickness and ARs. (g) 3D force field of magnetic interactions experienced by one nanorod above the 2D assemblies. (h) Magnetic potential above the 2D assemblies at certain separations.

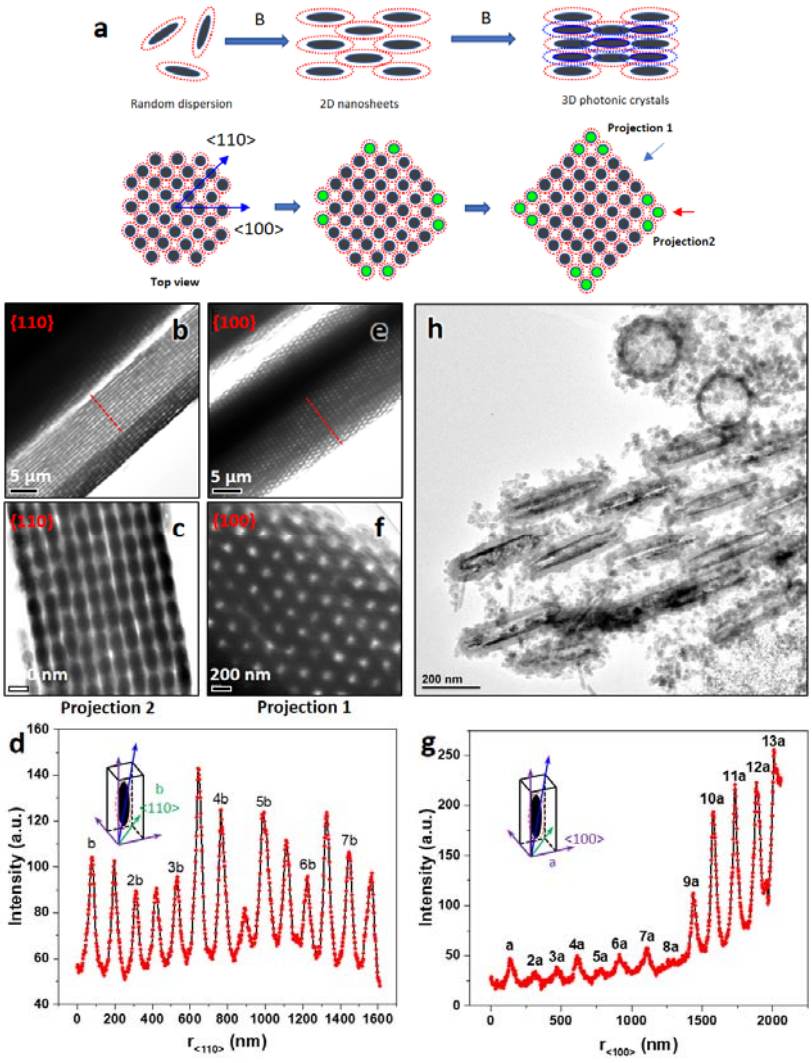

Figure 2.17. (a) The proposed assembly mechanism of the *bct* colloidal crystals. TEM images of the *bct* colloidal crystals under the {110} (b, c) and {100} (e, f) orientations. Translational orders of the *bct* crystals along the <110> (d) and <100> (g) crystalline directions. (h) TEM image of the 2D sheet-like structures at the early stage of magnetic assembly. The r is the center-to-center separation between nanorods along certain crystalline directions.

Therefore, we extended the force computation to a 3D model (**Figures 2.18a and 2.18b**). The force field in **Figure 2.18c** suggests a strong repulsion force (red arrows) when the rod overlaps bottom ones. Interestingly, we observe a gradual shift to downward attraction when the rod of interest moves to the positions above cavities (blue arrows). In the magnetic potential landscape (**Figure 2.18d**), we recognize periodic bonding sites above bottom cavities due to the localized low magnetic potential. The localized magnetic fields are mapped in **Figures 2.19** and **2.20**. And, the force dynamics and magnetic potential against position are plotted in **Figure 2.21**. From both force and energetic points of view, there exist four active binding sites above and below each rod in the 2D sheet, resulting in a total of 8 bonded rods shared by its neighbors. The assembly pathway can be proposed as follows: first, in external magnetic fields, monodisperse rods nucleate out of a dense fluidic phase due to the directionality of pair magnetic interactions, which acts as seed for preferential deposition of free rods to form small crystals; second, rods of orientational order preferentially bond to the exposed (110) facets in sequence, following a chain-growth polymerization scheme[70]; finally, the super-dipoles of the free-standing crystals can magnetically bond together, which is likely comparable to a step-growth polymerization process[21, 71], to form macroscopic crystals.

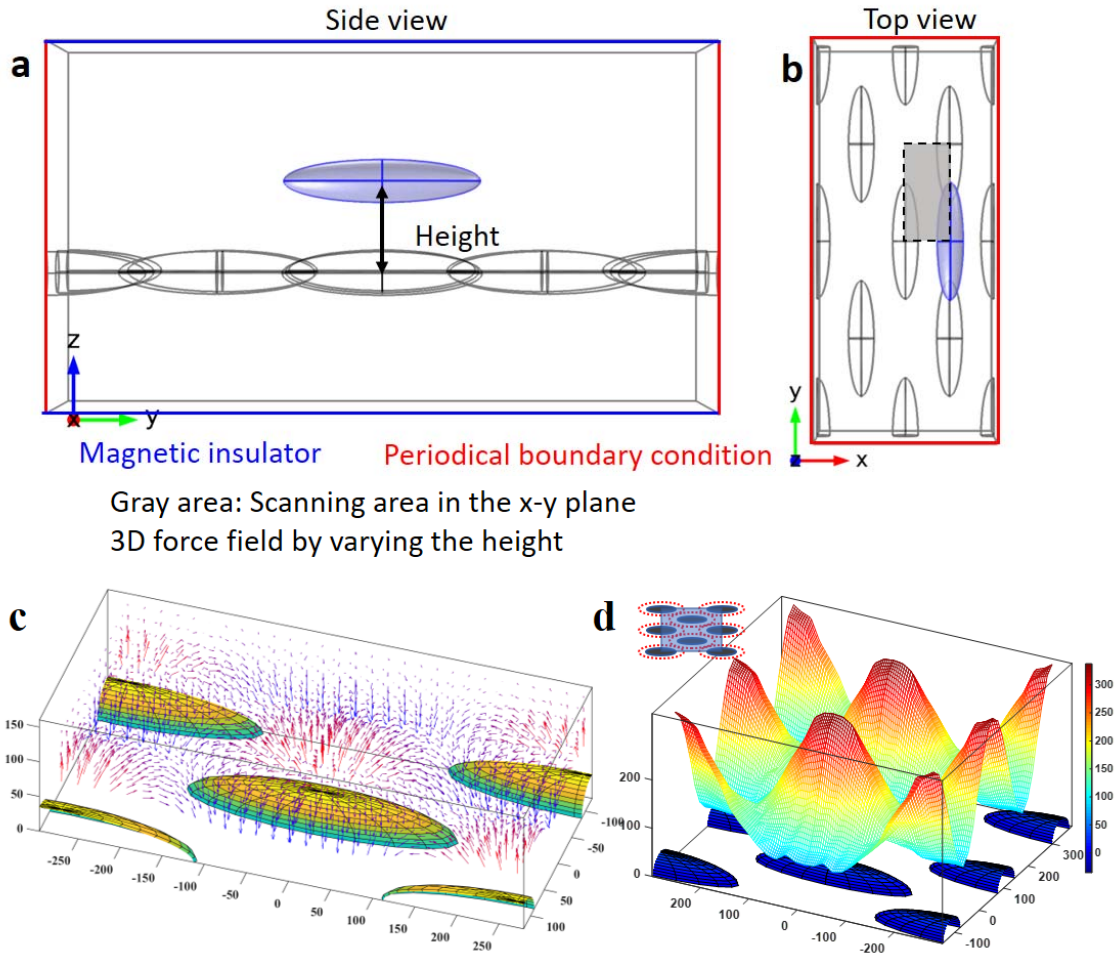

Figure 2.18. Assembly mechanism and force dynamics. Modeling of 3D assembly for calculating the force of nanorod above the 2D assemblies. In (a), a side view is provided. To search for the equilibrium point, the nanorod (gray) is placed above a 2D assembly. The searching area is highlighted in gray in (b). The boundaries highlighted in blue are defined as magnetic insulator. And, the boundaries highlighted in red meet the periodical boundary condition. (c) 3D force field of magnetic interactions experienced by one nanorod above the 2D assemblies. (d) Magnetic potential above the 2D assemblies.

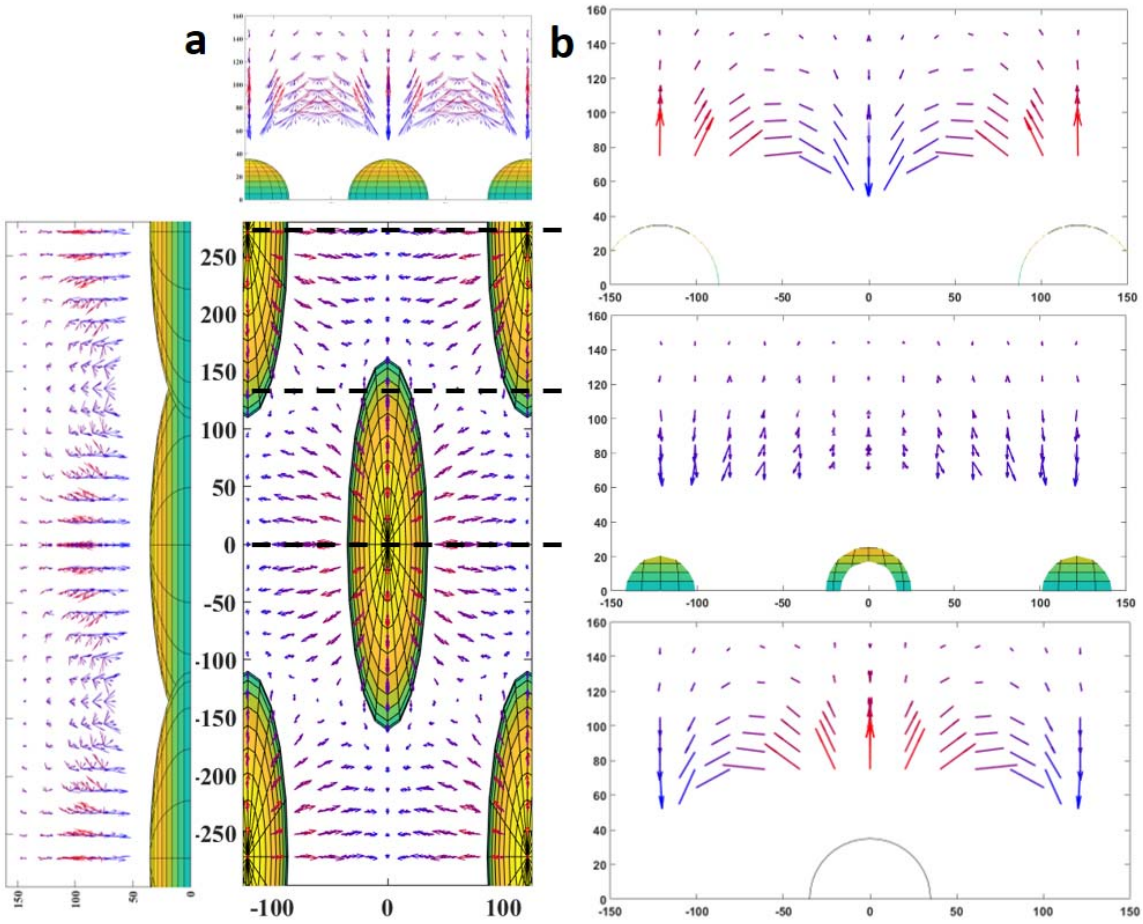

Figure 2.19. Force fields of simulated results during the formation of 3D colloidal crystals. (a) The force fields under different views. (b) The force fields in the three typical cross sections as highlighted in a.

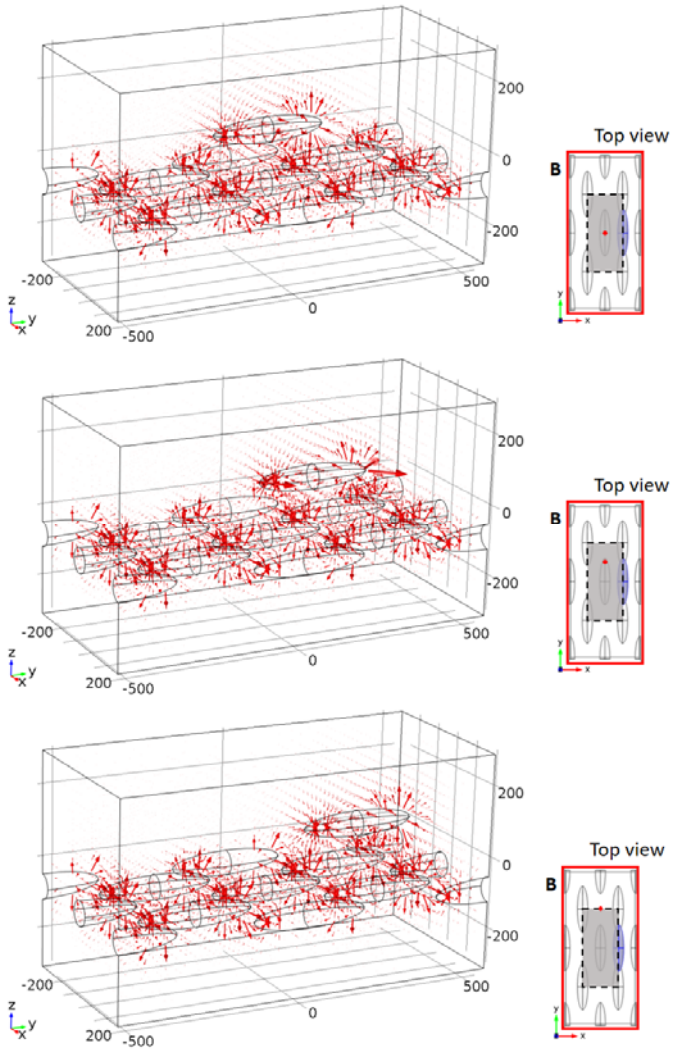

Figure 2.20. Magnetic field distribution of the assemblies when the nanorod is in different places. The center of the nanorod is labelled by the red dots in the right panels.

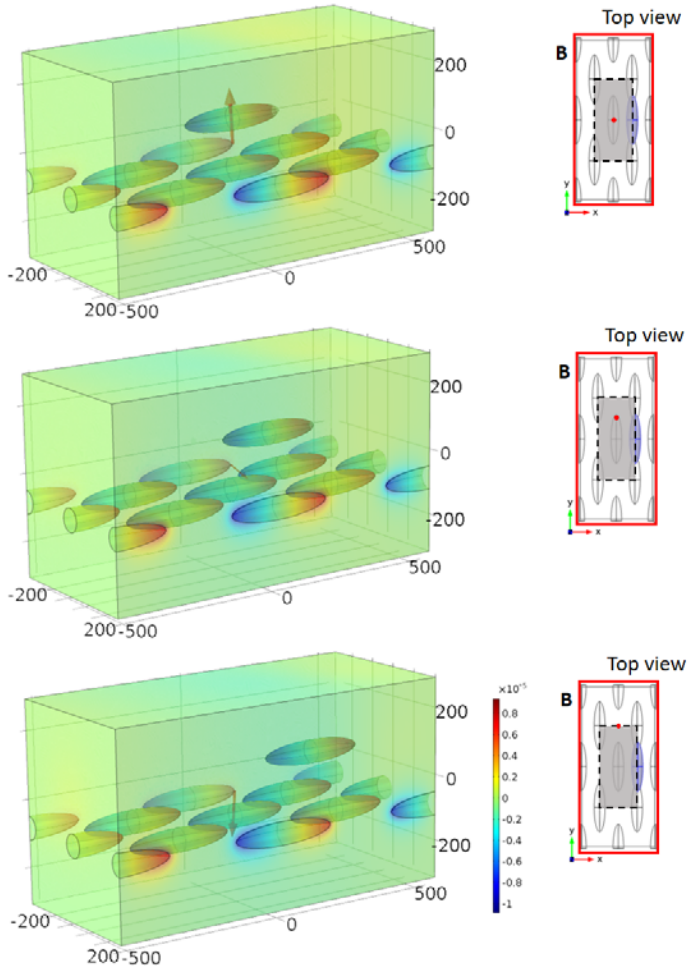

Figure 2.21. Magnetic scale potential (color-coded volume) and the force vector (red arrows) of the assemblies when the nanorod is in different places. The center of the nanorod is labelled by the red dots in the right panels.

Assembly kinetics. To resolve the assembly kinetics of nanorods under magnetic fields, we probe in real time the crystal formation by *in situ* synchrotron-based small-angle X-ray scattering (SAXS) (**Figure 2.22a**). The representative 2D SAXS patterns are shown in **Figure 2.22b**. At the initial stage (0 min), we observed a remarkable anisotropic diffuse scattering pattern due to the form factor of rods of purely orientational orders. Under a vertical magnetic field, the scattering features at horizontal direction is much larger than that at vertical direction, confirming the parallel alignment of rods to the fields. Starting at 33 min, clear diffraction peaks appeared as colloidal rods began to crystalize. We observed a well-defined rectangular diffraction pattern, which represents the reciprocal lattice of nanorods packed in real-space {110} facets. The perfect structures of the *bct* crystals are further confirmed by the high-order diffraction peaks. For example, the linear profiles in **Figures 2.23a** (horizontal) and **2.23b** (vertical) show a 9^{th} diffraction of {110} facets and 5^{th} diffraction of {001} facets, respectively. **Figure 2.23c** represents, with elapsed time, a contraction of the lattice under external magnetic fields with exponential superlattice densification. The assembly rate along both the a and c directions had initial ~ 4 nm/min and slowed down when approaching thermodynamic equilibrium at ~90 min. The considerably low assembly kinetics is expected to provide the rods with sufficient spatiotemporal degree of freedoms to anneal out defects and approach the thermodynamically equilibrium positions. We then quantified the local coordinates of the bonded rods using the diffraction peaks from corresponding facets. **Figure. 2.23d** show the evolution of local rods position in <111> crystallographic directions, indicating nearly linear contraction of the superlattices. The overall magnetic assembly was compiled and

depicted in **Figure 2.23e** with lattice shrinkage of 31.7% and 22.4% for a and c axis, respectively.

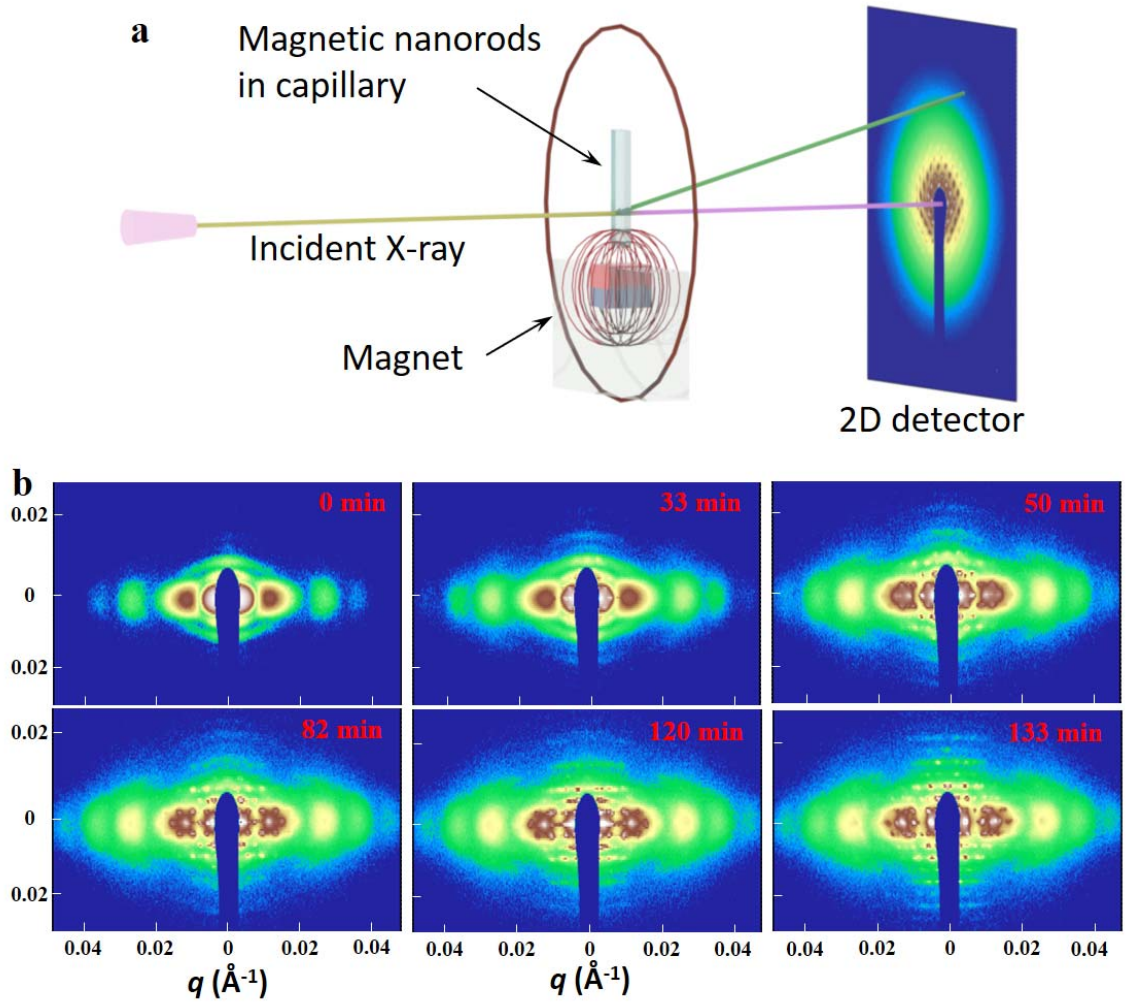

Figure 2.22. Assembly kinetics. (a) Schematic setup of the in situ measurement of SAXS patterns in real time. A home-made stage fixed with a permanent magnet was used for the measurement. The aqueous dispersion of magnetic nanorods was sealed in a flat capillary tube. (b) Temporal evolution of SAXS patterns during the in suit measurement of magnetic assembly of nanorods.

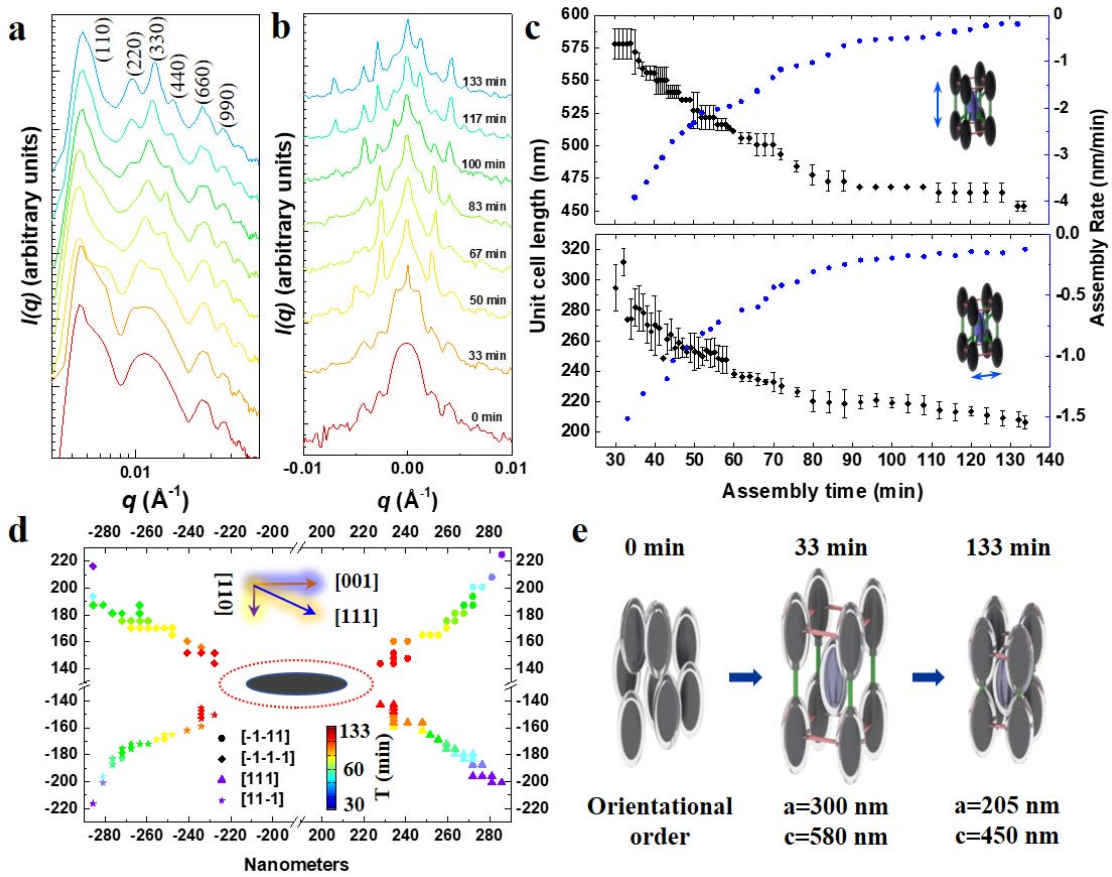

Figure 2.23. Assembly kinetics. (a, b) Representative linear profile of SAXS patterns along the horizontal and vertical directions, respectively. (c) Kinetics of the magnetic assembly of bct crystals along c axis (top) and a axis (bottom). (d) The trajectory of the magnetic nanorods during assembly process. (e) The depiction of the magnetic assembly and formation of bct crystals. a and b are based on facets of (110), (220), (330) and (440).

Shape anisotropy of rods breaks the band symmetry of the *bct* photonic crystals. The low symmetry of the *bct* crystals is found to support highly anisotropic photonic bands that are dependent on crystal orientation (**Figures 2.24 and 2.25**). In optical images in **Figure 2.26a**, we observed two typical structural colors diffracted from two types of facets: red from {100} and blue from {110} facets. The considerably uniform structural colors elucidate perfect ordering of rods into single crystal nature. At relatively high volume fraction (> 30%), crystals were packed densely, forming a continuous phase (**Figure 2.26b**). Their diffraction can be tuned from blue to cyan, green, yellow, orange and finally red by simply changing directions of magnetic fields (**Figure 2.26c**). Using geometric model in **Figure 2.26d**, it is expected that there exist isolated band gaps in the visible range. By readily changing the direction of applied magnetic field, we observed a steady redshift of diffraction peaks (**Figure 2.26e**), which is most likely due to the rotation of crystal grains from initial {100} to {110} facets by 45º along <001> directions. At off-angle incidence, diffraction was expected to occur at the band edge, thus attenuating the diffraction intensity.

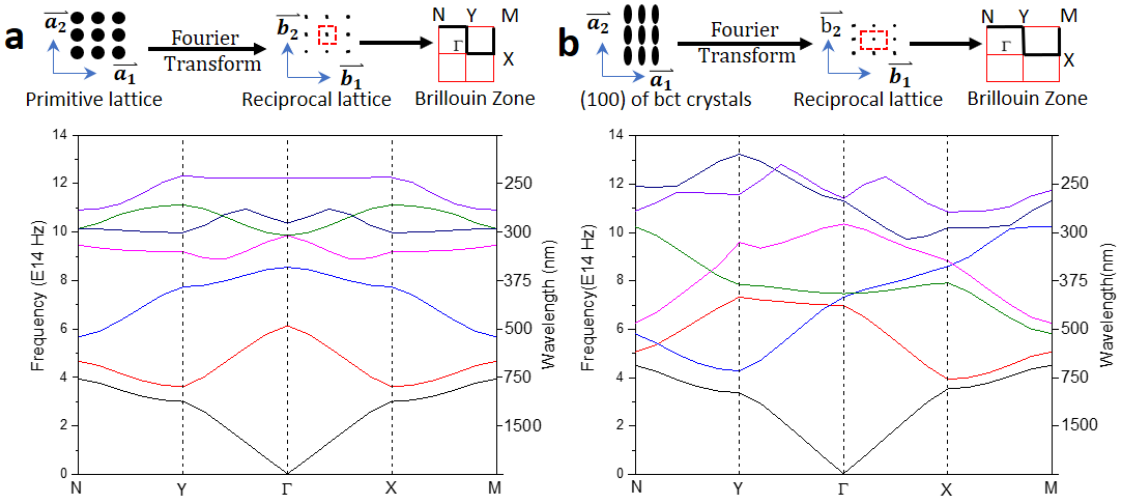

Figure 2.24. Shape anisotropy breaks the band symmetry of the photonic crystals. The photonic band structures of 2D lattices assembled from (a) nanospheres and (b) nanorods, respectively.

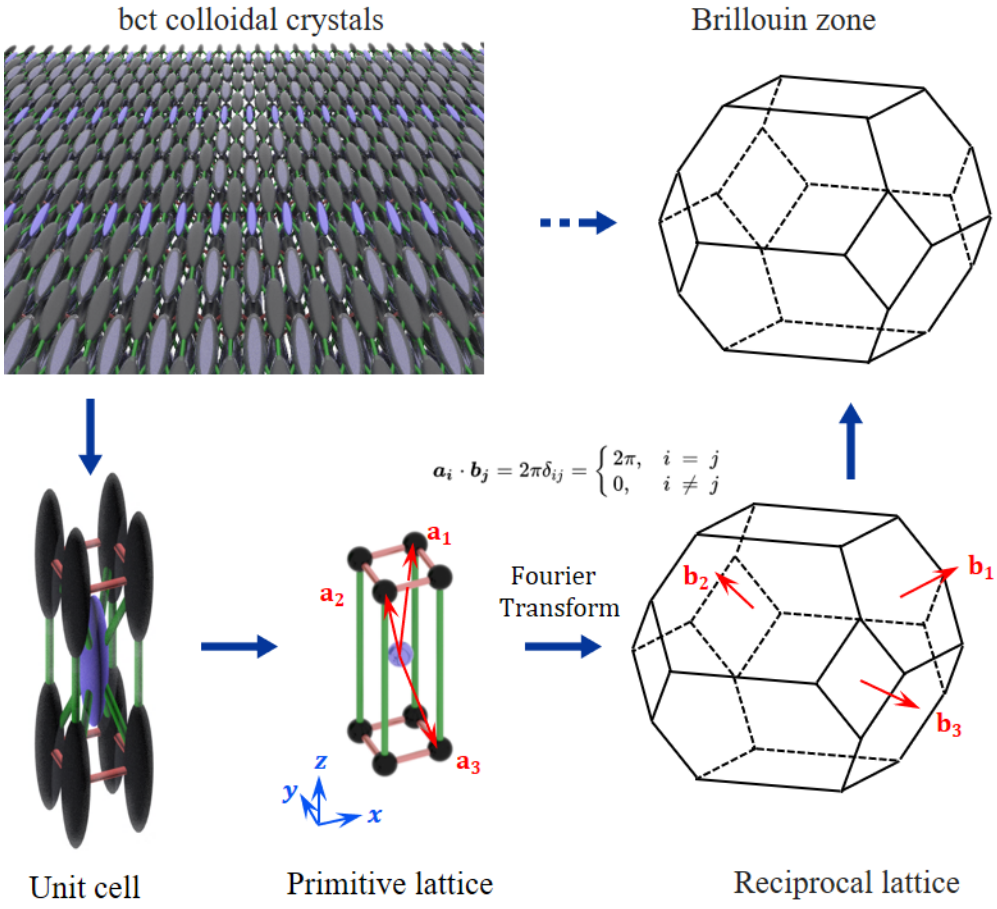

Figure 2.25. Constructing the irreducible Brillouin zone of *bct* colloidal crystals.

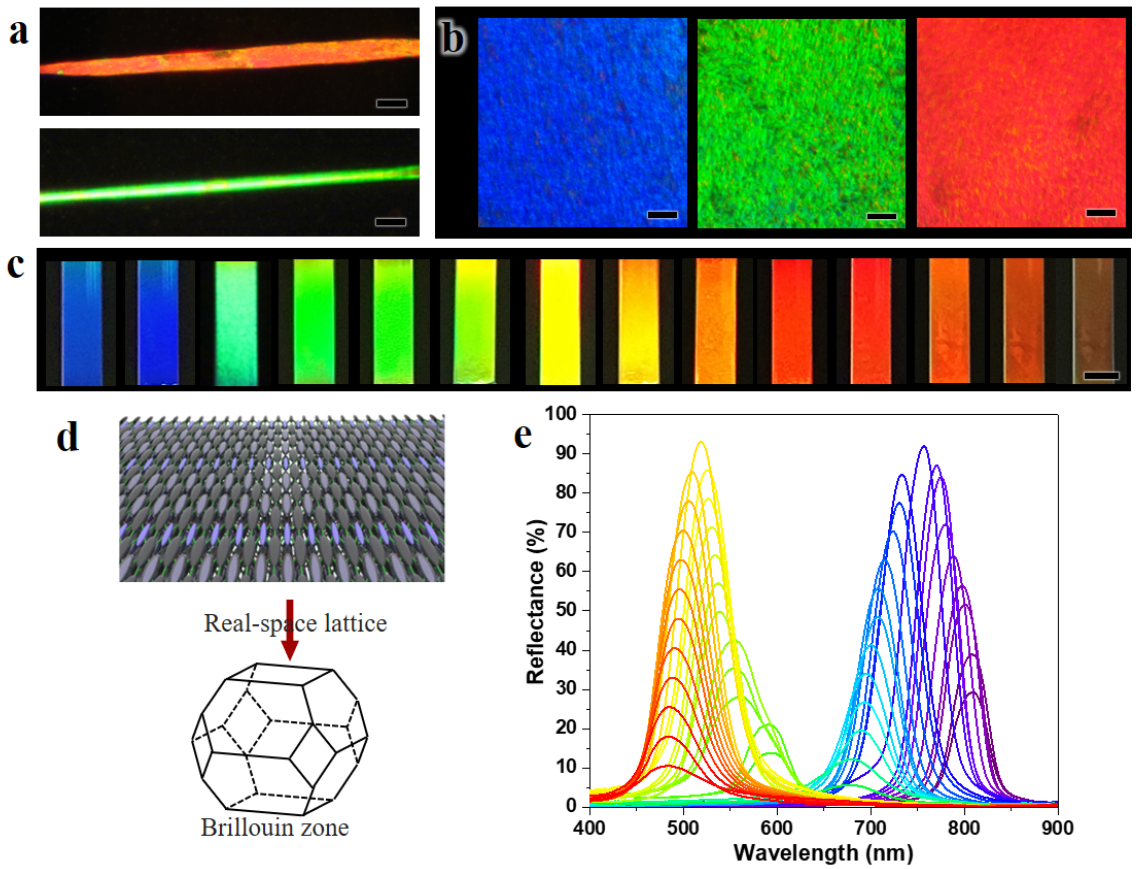

Figure 2.26. Shape anisotropy of rods breaks the band symmetry of the assembled *bct* photonic crystals. (a) Optical microscopic images of the bct crystals. (b) Optical microscopic images of bct crystals assembled from high volume fraction of magnetic nanorods. (c) Digital images of the photonic crystals in a capillary under different magnetic fields. (d) Schematic illustration of the 3D lattice and its brillouin zone. (e) Reflection spectra of the bct photonic crystals under different magnetic fields. Scale bars: 20 μm in (a) and (b); 5 mm in (c).

2.6 Magnetic Patterning of Nanorods into Photonic Structures

FeOOH nanorods (322 nm in length and 70 nm in width) are used as starting materials (**Figure 2.27a**). After silica coating, nanorods are reduced by H_2 at 360ºC and the final Fe_3O_4@SiO_2 with a silica of 40 nm (**Figure 2.27b**). In the synthesis, we observed an interesting size-confusing effect as shown in the size distribution in **Figure 2.27c** probably due to multiple washing steps that can remove small rods. Under magnetic fields, the magnetic nanorods self-assembled into 3D photonic crystals, which can be fixed by additional silica coating. The structures of the 3D photonic crystals are characterized by TEM. Similar to the results in previous chapter, it is found that the *bct* crystals exhibit two typical orientations: projection along <100> and <110> crystallographic directions in **Figures 2.28a** and **2.28b**, respectively. The perfect order of the 3D photonic crystal is first evidenced by the green structural color during the fixation of the photonic structures (**Figure 2.28c**). Interestingly, under optical microscope, single crystal can exhibit yellow and green colors under different rotation (**Figure 2.28d**). The different structure colors are expected to be the diffraction of light along different crystal facets. Besides, controlling the crystal orientation by a magnetic field provides much broader tunability of the structural colors. As shown in **Figure 2.28e**, the structural colors can be continuously tuned from blue at 0º to green, yellow, red at ~45º. When the crystals are aligned along vertical direction by magnetic fields, the structural color disappears because the photonic bandgap shifts to near-infrared region due to the relatively long rods.

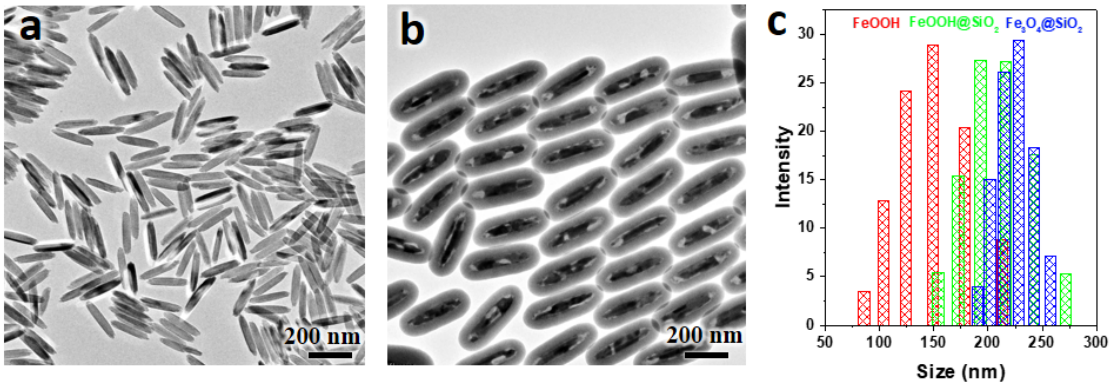

Figure 2.27. TEM images of (a) FeOOH nanorods and (b) Fe_3O_4@SiO_2 nanorods. (c) Size distribution of FeOOH, FeOOH@SiO_2, and Fe_3O_4@SiO_2 nanorods.

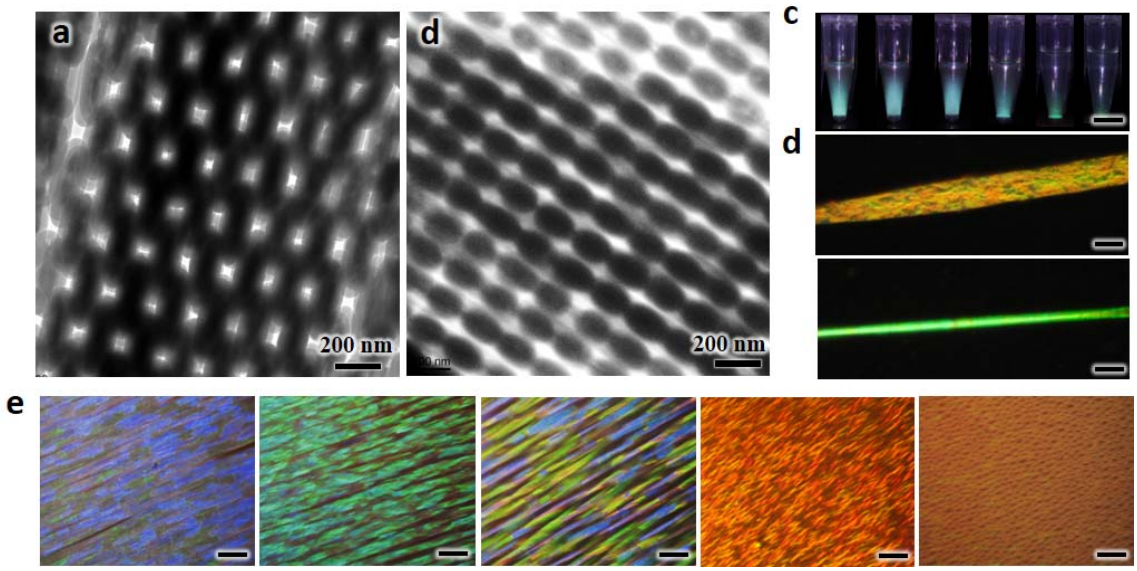

Figure 2.28. TEM images of (a) assembled *bct* crystals with (100) orientation and (b) (111) orientation. (c) Digital images of a colloidal dispersion during assembly process. (d) Optical microscopic images of a crystal under two typical orientations. (e) Optical microscopic images of the bct crystals under different magnetic fields. Scale bars: 2 mm in (c) and 20 μm in (d-e).

To investigate the assembly behavior of nanorods under pre-designed templates, we start with a simple 1D channels. The SEM image is shown in **Figure 2.29a**. It has well-defined 1-μm linear channels in a PDMS elastomer. The magnetic field distribution around the template is calculated by finite element analysis. In **Figures 2.29b** and **2.29c**, there is a remarkable enhancement of magnetic field localized in the gap than that above the template. Therefore, it is expected that nanorods will be trapped in the channel due to the large local gradient and strong packing force. To verify this, we added 10 μL of the rod dispersion on the template. The self-assembly of nanorods under the assistance of template is monitored under optical microscope. As shown in **Figure 2.29d**, we observed well-defined photonic structures, whose size, orientation, and geometry match well with the used template. Under a vertical magnetic field, nanorods in colloidal dispersion is gradually concentrated to the 1D channels, forming localized photonic structures and colors. One interesting feature of the template-assisted self-assembly is the high-resolution of the created photonic crystals inherited from the small feature of the template (**Figure 2.29e**).

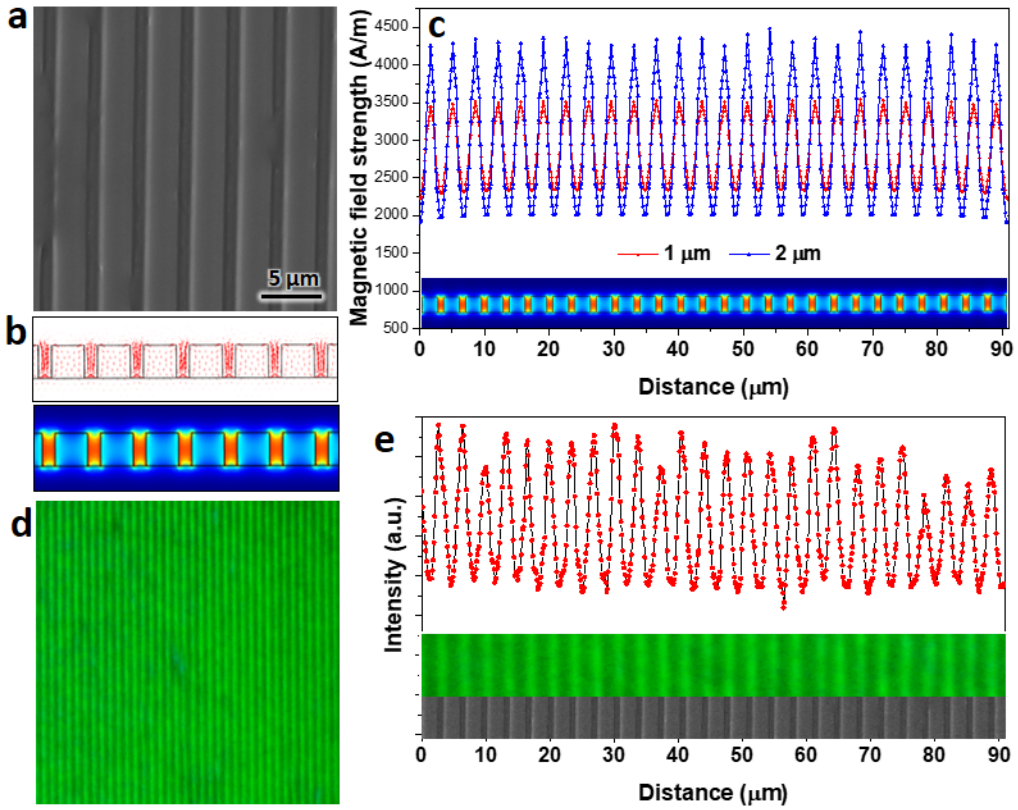

Figure 2.29. Magnetic patterning and assembly of nanorods. (a) SEM image of the PDMS template. (b) Magnetic field distribution around the template. (c) Linear profile of the magnetic field distribution at different distances from the channel bottom. (d) Optical microscopic images of the formed photonic structures under a vertical magnetic field. (e) Linear profile of the intensity of the photonic structures.

To demonstrate the versatility of this strategy, we extend the template-assisted self-assembly to other templates of different sizes and geometries. The enhancement of magnetic field at the gap areas is found over broad ranges of templates from 1D channels to 2D matrices (**Figure 2.30a**). One difference between large gap (right panel in **Figure 2.30a**) and small gap (left panel in **Figure 2.30a**) is that large one features significant decay in the filed enhancement from gap edge to center. It is therefore expected that nanorods will preferentially assembled at the gap edge rather than directly inheriting the template geometry. To verify this hypothesis, we created two templates. One has a 2D matrix of square gap (**Figure 2.30b**) while another has irregular geometry with variable gap size (**Figure 2.30c**). Interestingly, the formed photonic structures completely replicate the feature of the used templates, which is independent on the gap size and symmetry. This observation is consistent with the intuitive understanding in templates with small gap size but is controversial to that of large templates. Therefore, a different assembly pathway is proposed to explain the formation of photonic structures. Right after a vertical magnetic field is applied, nanorods are concentrated in the edge of the gap, forming small photonic crystals. As assembly proceeds, these small crystals may act as seed to magnetically attract more rods to grow into large ones. The nucleation and seeded growth of the local crystal occur in sequence and gradually fill all the gap space under a proper magnetic field.

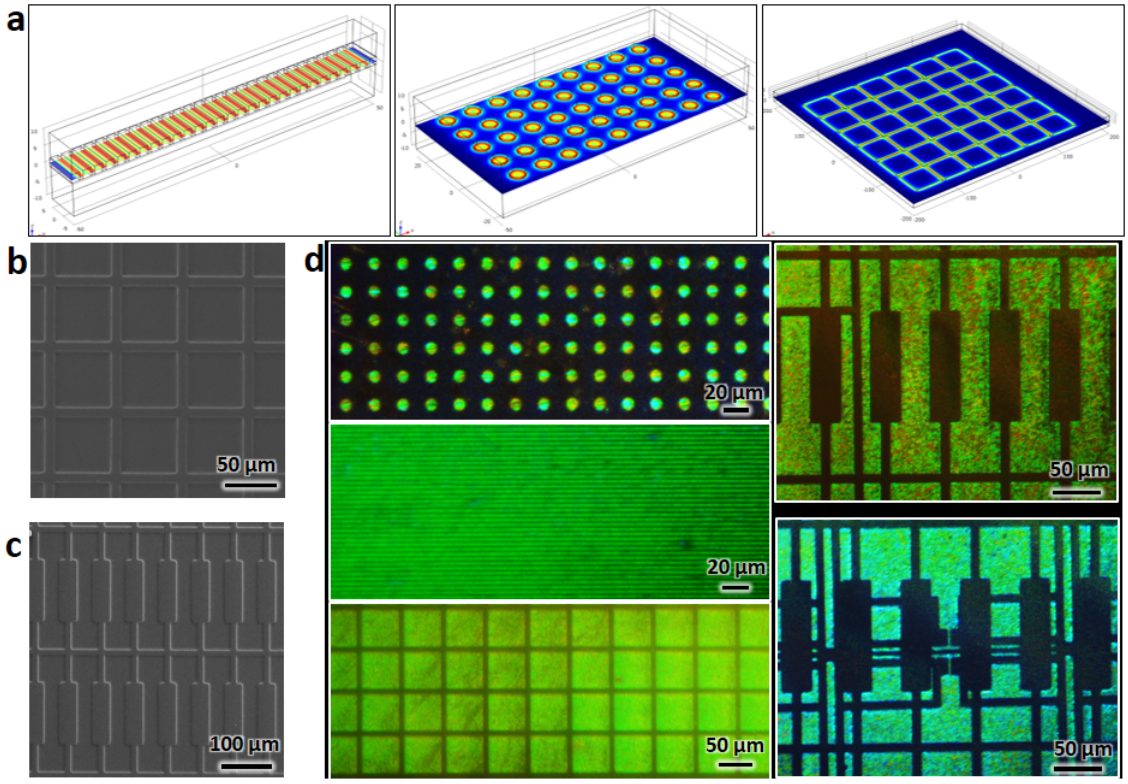

Figure 2.30. Different templates and structures. (a) Simulated magnetic field distribution on different templates. SEM images of (b) square lattice and (c) irregular templates. (d) Template-assisted assembly and patterning of various photonic structures.

The advantage of using anisotropic nanorods as building block is that they enable efficient control over the crystals orientation by changing the direction of applied magnetic field. In principle, it is possible to tune the colors of the assembled photonic structures using a magnetic field (**Figure 2.31a**). To this end, two templates containing squares of different sizes are used. As shown in **Figures 2.31b** and **2.31c**, the square templates have edge length of 50 μm and 20 μm, respectively. In a typical process, photonic structures are first assembled and localized in the template gaps under vertical magnetic field. Notably, photonic structures in vertical magnetic field (90^{o}) do not exhibit visible structural color due to the large bandgap long <001> crystallographic orientation. Because the magnetic field in the gap is only enhanced under a vertical external magnetic field, this step is critical to concentrate nanorods to form photonic structures. After that, the direction of applied magnetic field is carefully tilted from a vertical (90^{o}) to horizontal orientation (0^{o}). It is interesting to point out that the colors of the photonic structures changed from red to green and blue (**Figures 2.31d** and **2.31e**). The structures can be well maintained under various field directions. On the basis of template-assisted magnetic assembly of nanorods, various photonic patterns are created. As demonstrated in **Figure 2.32**, these photonic patterns can exhibit different structural colors by simply changing the direction of applied magnetic field.

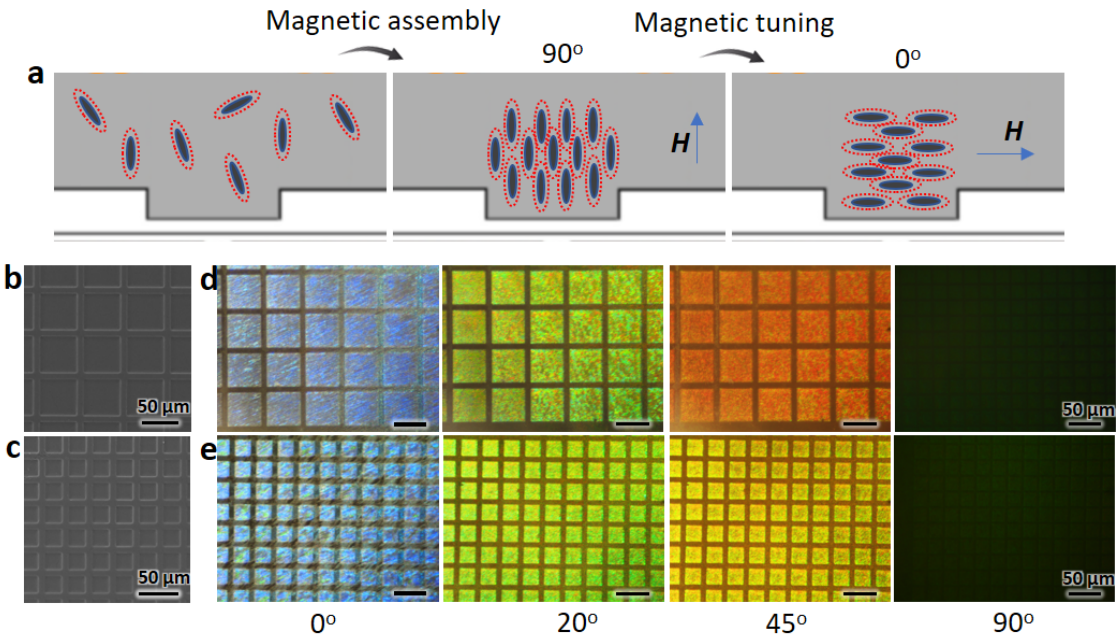

Figure 2.31. Tunable structural colors on templates. (a) Schematic illustration of the template-assisted assembly of tunable photonic structures. SEM images of (b) large and (c) small square templates. (d-e) The corresponding optical microscopic images of photonic structures under different magnetic fields.

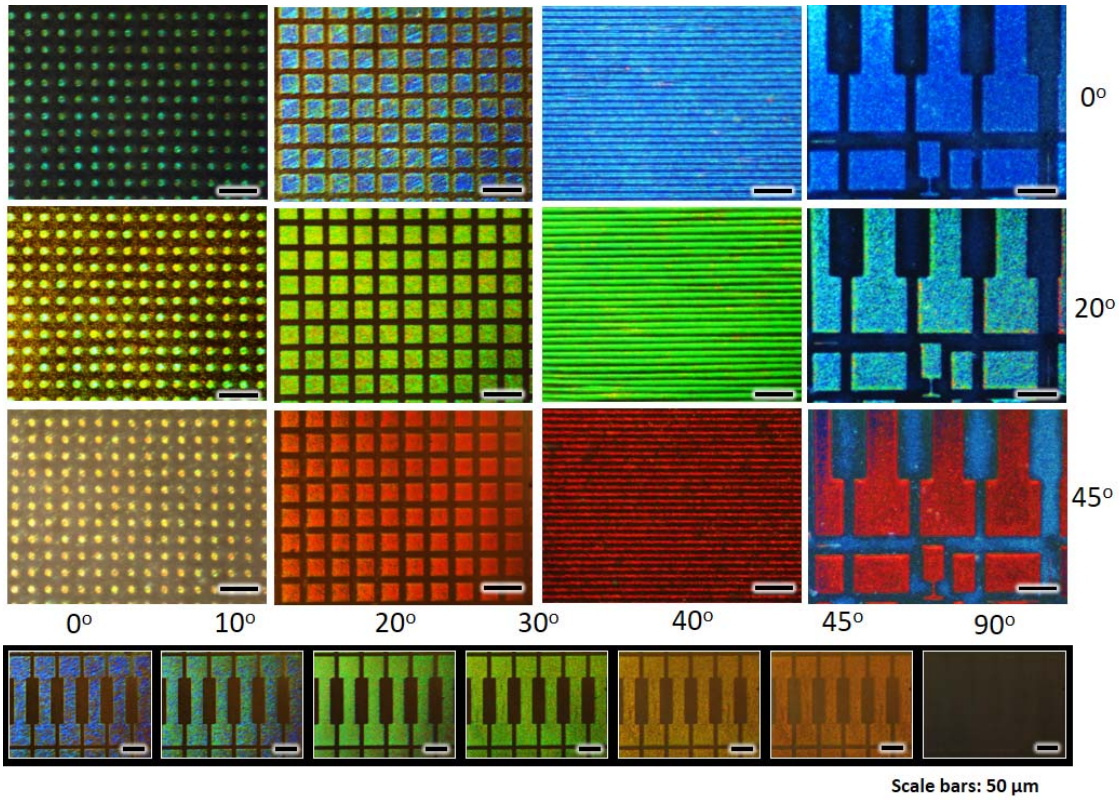

Figure 2.32. Photonic structures assembled and patterned from various templates.

2.7 Conclusion

In the first part, we report the edge-to-edge assembly of colloidal magnetite nanocubes along their [110] direction into 1D photonic structures under external magnetic fields as driven by the minimization of the competing dipole-dipole and Zeeman coupling energies originating from the shape anisotropy. The unique structure of the assemblies enables convenient tuning of the diffraction and structural color across the whole visible range by controlling the direction of the magnetic field, allowing them to operate differently from those assembled with magnetite nanospheres which display tunable optical properties dependent primarily on the field strength. The 1D nanocube assemblies exhibit bright structural colors at broad viewing-angles owing to their nonspherical shape, making them advantageous for building unique photonic devices by fixing the long-range periodic structures within the plane of a thin film while displaying the resulting structural colors out of the plane. This is a beneficial feature for many applications, such as anti-counterfeiting, where it is desirable to produce a structural color of sufficient intensity in a film having a minimum thickness. With the assistance of photolithography, we further demonstrate that predesigned patterns can be encrypted in a thin polymer film by controlling the orientation of the nanocube assemblies at designated locations. The encrypted patterns can only be observed by orienting them along a certain direction or by exposing them to light incident from a particular angle. Further, the unique orientation-dependent photonic response of the nanocube assemblies can be employed to create “magic” patterns whose rotation is perceived to be opposite to the actual rotation direction of the film. Such unusual optical effects are not achievable using nanosphere assemblies and are not easily cloned by other

fabrication methods, thereby providing many new ways for designing novel security devices. We believe this work highlights that the magnetic assembly strategy, when applied to nonspherical colloidal building blocks, can offer abundant opportunities in producing unique superstructures that can display interesting photonic properties.

The directional magnetic force has been long recognized in the assembly of colloidal particles, particularly of spheres, into multidimensional superstructures. So is the concession of its critical role in breaking the entropy-dominated phase symmetry. This is mainly because previous studies are focused on isotropic spheres or faceted crystals with high symmetry, in which the energetic process generates similar dense packing in magnetic force-mediated self-assembly. The second and third work in this chapter demonstrates the feasibility of extending the phase of colloidal crystals by magnetic assembly of highly anisotropic nanostructures, including nanorods and nanoplates. For nanoplates, they favor centered rectangular 2D packing due to the shape-induced magnetic anisotropy. For nanorods in external magnetic fields, their underlying and directional super-dipole interactions create attractive and repulsive surface patches. Our quasi-quantitative analysis identifies the critical roles of rod-like structures as it results in a size-specific thermodynamic equilibrium between magnetic dipole-dipole attraction and electrostatic repulsion. It decouples the preferential bonding from any of the two main axes of nanorods, producing non-close packing of rods while still featuring surface hard contact. As the underlying magnetic interactions is universal to magnetic rods and independent on surface chemistry, this assembly mechanism has been readily extended to produce various *bct* crystals on rods with a wide range of ARs. The unique tetragonal-phased 3D architectures

and fine-defined, interconnected porosity are expected to provide an alternative platform to modulate chemical transformations and physical processes in energy storage and conversion and photonics. In a more general sense, our work illuminates a new way to break the dense packing phase in the entropy-dominated colloidal assembly without the need of sophisticated surface chemistry and colloids engineering. Its simple generalization to colloidal crystals of highly anisotropic shape (cubes, plates) presents a promising direction for exploiting emerging colloidal crystal phase.

In the last part, we have developed a simply yet reliable template-assisted self-assembly approach toward responsive photonic structures. This strategy relies on the enhancement of a vertical magnetic field localized at well-defined regions when a template is immersed in the colloidal dispersion of magnetic nanorods that serve as magnetic medium. The enhancement of magnetic field is universal characters of many templates and therefore supports the formation of diverse photonic structures with brilliant structural colors. On the basis of anisotropic shape of nanorods, the orientation of the 3D photonic crystals can be readily tuned by simply changing the directions of applied fields, which enables the active modulation of the structural colors of the photonic patterns. Therefore, the combination of the template-assisted self-assembly with the unique optical properties of the 3D photonic crystals has great potentials in anticounterfeiting, encryption, sensing, and display.

2.8 References

1. Wang, T.; Zhuang, J.; Lynch, J.; Chen, O.; Wang, Z.; Wang, X.; LaMontagne, D.; Wu, H.; Wang, Z.; Cao, Y. C., Self-assembled colloidal superparticles from nanorods. *Science* **2012,** *338* (6105), 358-363.

2. Li, F.; Josephson, D. P.; Stein, A., Colloidal assembly: the road from particles to colloidal molecules and crystals. *Angew. Chem. Int. Ed.* **2011,** *50* (2), 360-388.

3. Xu, W.; Li, Z.; Yin, Y., Colloidal Assembly Approaches to Micro/Nanostructures of Complex Morphologies. *Small* **2018,** *14* (35), 1801083.

4. Li, Z.; Yin, Y., Stimuli-Responsive Optical Nanomaterials. *Adv. Mater.* **2019,** *31* (15), 1807061.

5. Ge, J.; Yin, Y., Responsive photonic crystals. *Angew. Chem. Int. Ed.* **2011,** *50* (7), 1492-1522.

6. Li, Z.; Yang, F.; Yin, Y., Smart Materials by Nanoscale Magnetic Assembly. *Adv. Funct. Mater.* **2019**, 1903467.

7. Whitesides, G. M.; Grzybowski, B., Self-assembly at all scales. *Science* **2002,** *295* (5564), 2418-2421.

8. Damasceno, P. F.; Engel, M.; Glotzer, S. C., Crystalline assemblies and densest packings of a family of truncated tetrahedra and the role of directional entropic forces. *Acs Nano* **2011,** *6* (1), 609-614.

9. Damasceno, P. F.; Engel, M.; Glotzer, S. C., Predictive self-assembly of polyhedra into complex structures. *Science* **2012,** *337* (6093), 453-457.

10. Macfarlane, R. J.; Lee, B.; Jones, M. R.; Harris, N.; Schatz, G. C.; Mirkin, C. A., Nanoparticle superlattice engineering with DNA. *Science* **2011,** *334* (6053), 204-208.

11. Park, S. Y.; Lytton-Jean, A. K.; Lee, B.; Weigand, S.; Schatz, G. C.; Mirkin, C. A., DNA-programmable nanoparticle crystallization. *Nature* **2008,** *451* (7178), 553.

12. Auyeung, E.; Li, T. I.; Senesi, A. J.; Schmucker, A. L.; Pals, B. C.; de La Cruz, M. O.; Mirkin, C. A., DNA-mediated nanoparticle crystallization into Wulff polyhedra. *Nature* **2014,** *505* (7481), 73.

13. Lin, H.; Lee, S.; Sun, L.; Spellings, M.; Engel, M.; Glotzer, S. C.; Mirkin, C. A., Clathrate colloidal crystals. *Science* **2017,** *355* (6328), 931-935.

14. Ye, X.; Chen, J.; Engel, M.; Millan, J. A.; Li, W.; Qi, L.; Xing, G.; Collins, J. E.; Kagan, C. R.; Li, J., Competition of shape and interaction patchiness for self-assembling nanoplates. *Nature chemistry* **2013,** *5* (6), 466.

15. Li, Z.; Wang, M.; Zhang, X.; Wang, D.; Xu, W.; Yin, Y., Magnetic Assembly of Nanocubes for Orientation-Dependent Photonic Responses. *Nano Lett.* **2019,** *19* (9), 6673-6680.

16. Singh, G.; Chan, H.; Baskin, A.; Gelman, E.; Repnin, N.; Král, P.; Klajn, R., Self-assembly of magnetite nanocubes into helical superstructures. *Science* **2014,** *345* (6201), 1149-1153.

17. Wang, M.; He, L.; Xu, W.; Wang, X.; Yin, Y., Magnetic assembly and field-tuning of ellipsoidal-nanoparticle-based colloidal photonic crystals. *Angew. Chem. Int. Ed.* **2015,** *54* (24), 7077-7081.

18. Leunissen, M. E.; Christova, C. G.; Hynninen, A.-P.; Royall, C. P.; Campbell, A. I.; Imhof, A.; Dijkstra, M.; Van Roij, R.; Van Blaaderen, A., Ionic colloidal crystals of oppositely charged particles. *Nature* **2005,** *437* (7056), 235.

19. Henzie, J.; Grünwald, M.; Widmer-Cooper, A.; Geissler, P. L.; Yang, P., Self-assembly of uniform polyhedral silver nanocrystals into densest packings and exotic superlattices. *Nature Mater.* **2012,** *11* (2), 131.

20. Chen, Q.; Bae, S. C.; Granick, S., Directed self-assembly of a colloidal kagome lattice. *Nature* **2011,** *469* (7330), 381.

21. Shah, A. A.; Schultz, B.; Zhang, W.; Glotzer, S. C.; Solomon, M. J., Actuation of shape-memory colloidal fibres of Janus ellipsoids. *Nature Mater.* **2015,** *14* (1), 117.

22. Chen, Q.; Whitmer, J. K.; Jiang, S.; Bae, S. C.; Luijten, E.; Granick, S., Supracolloidal reaction kinetics of Janus spheres. *Science* **2011,** *331* (6014), 199-202.

23. Smoukov, S. K.; Gangwal, S.; Marquez, M.; Velev, O. D., Reconfigurable responsive structures assembled from magnetic Janus particles. *Soft Matter* **2009,** *5* (6), 1285-1292.

24. Wang, X.; Feng, J.; Yu, H.; Jin, Y.; Davidson, A.; Li, Z.; Yin, Y., Anisotropically shaped magnetic/plasmonic nanocomposites for information encryption and magnetic-field-direction sensing. *Research* **2018,** *2018*, 7527825.

25. Li, Z.; Wang, M.; Zhang, X.; Wang, D.; Xu, W.; Yin, Y., Magnetic Assembly of Nanocubes for Orientation-Dependent Photonic Responses. *Nano Lett.* **2019**.

26. Mundoor, H.; Senyuk, B.; Smalyukh, I. I., Triclinic nematic colloidal crystals from competing elastic and electrostatic interactions. *Science* **2016,** *352* (6281), 69-73.

27. Yin, Y.; Lu, Y.; Gates, B.; Xia, Y., Template-assisted self-assembly: a practical route to complex aggregates of monodispersed colloids with well-defined sizes, shapes, and structures. *J. Am. Chem. Soc.* **2001,** *123* (36), 8718-8729.

28. Xia, Y.; Yin, Y.; Lu, Y.; McLellan, J., Template-assisted self-assembly of spherical colloids into complex and controllable structures. *Adv. Funct. Mater.* **2003,** *13* (12), 907-918.

29. Ozin, G. A.; Yang, S. M., The race for the photonic chip: colloidal crystal assembly in silicon wafers. *Adv. Funct. Mater.* **2001,** *11* (2), 95-104.

30. Lu, Y.; Yin, Y.; Xia, Y., Three-Dimensional Photonic Crystals with Non-spherical Colloids as Building Blocks. *Adv. Mater.* **2001,** *13* (6), 415-420.

31. Yin, Y.; Xia, Y., Self-assembly of monodispersed spherical colloids into complex aggregates with well-defined sizes, shapes, and structures. *Adv. Mater.* **2001,** *13* (4), 267-271.

32. Ge, J.; Hu, Y.; Yin, Y., Highly tunable superparamagnetic colloidal photonic crystals. *Angew. Chem. Int. Ed.* **2007,** *46* (39), 7428-7431.

33. Wang, Y.; Cui, H.; Zhao, Q.; Du, X., Chameleon-Inspired Structural-Color Actuators. *Matter* **2019,** *1*, 1-13.

34. Zhang, Q.; Janner, M.; He, L.; Wang, M.; Hu, Y.; Lu, Y.; Yin, Y., Photonic labyrinths: Two-dimensional dynamic magnetic assembly and in situ solidification. *Nano Lett.* **2013,** *13* (4), 1770-1775.

35. Batista, C. A. S.; Larson, R. G.; Kotov, N. A., Nonadditivity of nanoparticle interactions. *Science* **2015,** *350* (6257), 1242477.

36. Li, P.; Li, Y.; Zhou, Z. K.; Tang, S.; Yu, X. F.; Xiao, S.; Wu, Z.; Xiao, Q.; Zhao, Y.; Wang, H., Evaporative Self-Assembly of Gold Nanorods into Macroscopic 3D Plasmonic Superlattice Arrays. *Adv. Mater.* **2016,** *28* (13), 2511-2517.

37. Murphy, C. J.; Sau, T. K.; Gole, A. M.; Orendorff, C. J.; Gao, J.; Gou, L.; Hunyadi, S. E.; Li, T., *J. Phys. Chem. B*, **2005**, 109, (29), 13857-13870.

38. Li, H.; Li, C.; Sun, W.; Wang, Y.; Hua, W.; Liu, J.; Zhang, S.; Chen, Z.; Wang, S.; Wu, Z., Single-Stimulus-Induced Modulation of Multiple Optical Properties. *Adv. Mater.* **2019,** *31* (23), 1900388.

39. Xu, X.; Friedman, G.; Humfeld, K. D.; Majetich, S. A.; Asher, S. A., Superparamagnetic photonic crystals. *Adv. Mater.* **2001,** *13* (22), 1681-1684.

40. Erb, R. M.; Son, H. S.; Samanta, B.; Rotello, V. M.; Yellen, B. B., Magnetic assembly of colloidal superstructures with multipole symmetry. *Nature* **2009,** *457* (7232), 999.

41. Gates, B.; Xia, Y., Photonic crystals that can be addressed with an external magnetic field. *Adv. Mater.* **2001,** *13* (21), 1605-1608.

42. He, L.; Wang, M.; Ge, J.; Yin, Y., Magnetic assembly route to colloidal responsive photonic nanostructures. *Acc. Chem. Res.* **2012,** *45* (9), 1431-1440.

43. He, L.; Hu, Y.; Kim, H.; Ge, J.; Kwon, S.; Yin, Y., Magnetic assembly of nonmagnetic particles into photonic crystal structures. *Nano Lett.* **2010,** *10* (11), 4708-4714.

44. Ge, J.; He, L.; Goebl, J.; Yin, Y., Assembly of magnetically tunable photonic crystals in nonpolar solvents. *J. Am. Chem. Soc.* **2009,** *131* (10), 3484-3486.

45. Ge, J.; Hu, Y.; Yin, Y., Highly tunable superparamagnetic colloidal photonic crystals. *Angewandte Chemie* **2007,** *119* (39), 7572-7575.

46. Ge, J.; Hu, Y.; Biasini, M.; Beyermann, W. P.; Yin, Y., Superparamagnetic magnetite colloidal nanocrystal clusters. *Angew. Chem. Int. Ed.* **2007,** *46* (23), 4342-4345.

47. Ge, J.; Lee, H.; He, L.; Kim, J.; Lu, Z.; Kim, H.; Goebl, J.; Kwon, S.; Yin, Y., Magnetochromatic microspheres: rotating photonic crystals. *J. Am. Chem. Soc.* **2009,** *131* (43), 15687-15694.

48. Ge, J.; Goebl, J.; He, L.; Lu, Z.; Yin, Y., Rewritable photonic paper with hygroscopic salt solution as ink. *Adv. Mater.* **2009,** *21* (42), 4259-4264.

49. Xuan, R.; Wu, Q.; Yin, Y.; Ge, J., Magnetically assembled photonic crystal film for humidity sensing. *J. Mater. Chem.* **2011,** *21* (11), 3672-3676.

50. Zhao, Q.; Wang, Y.; Cui, H.; Du, X., Bio-inspired sensing and actuating materials. *J. Mater. Chem. C* **2019,** *7*, 6493-6511.

51. Kim, H.; Ge, J.; Kim, J.; Choi, S.-e.; Lee, H.; Lee, H.; Park, W.; Yin, Y.; Kwon, S., Structural colour printing using a magnetically tunable and lithographically fixable photonic crystal. *Nature Photon.* **2009,** *3* (9), 534.

52. Xu, W.; Wang, M.; Li, Z.; Wang, X.; Wang, Y.; Xing, M.; Yin, Y., Chemical transformation of colloidal nanostructures with morphological preservation by surface-protection with capping ligands. *Nano Lett.* **2017,** *17* (4), 2713-2718.

53. Hu, M.; Furukawa, S.; Ohtani, R.; Sukegawa, H.; Nemoto, Y.; Reboul, J.; Kitagawa, S.; Yamauchi, Y., Synthesis of Prussian blue nanoparticles with a hollow interior by controlled chemical etching. *Angewandte Chemie* **2012,** *124* (4), 1008-1012.

54. Lu, Y.; Yin, Y.; Mayers, B. T.; Xia, Y., Modifying the surface properties of superparamagnetic iron oxide nanoparticles through a sol− gel approach. *Nano Lett.* **2002,** *2* (3), 183-186.

55. Sun, Y.; Xia, Y., Large-scale synthesis of uniform silver nanowires through a soft, self-seeding, polyol process. *Adv. Mater.* **2002,** *14* (11), 833-837.

56. Sun, Y.; Xia, Y., Shape-controlled synthesis of gold and silver nanoparticles. *Science* **2002,** *298* (5601), 2176-2179.

57. Hu, M.; Belik, A. A.; Imura, M.; Mibu, K.; Tsujimoto, Y.; Yamauchi, Y., Synthesis of superparamagnetic nanoporous iron oxide particles with hollow interiors by using Prussian blue coordination polymers. *Chem. Mater.* **2012,** *24* (14), 2698-2707.

58. Wang, M.; He, L.; Xu, W.; Wang, X.; Yin, Y., Magnetic assembly and field-tuning of ellipsoidal-nanoparticle-based colloidal photonic crystals. *Angew. Chem. Int. Ed.* **2015,** *54* (24), 7077-7081.

59. Hu, Y.; He, L.; Yin, Y., Magnetically responsive photonic nanochains. *Angew. Chem. Int. Ed.* **2011,** *50* (16), 3747-3750.

60. Wang, M.; He, L.; Hu, Y.; Yin, Y., Magnetically rewritable photonic ink based on superparamagnetic nanochains. *J. Mater. Chem. C* **2013,** *1* (38), 6151-6156.

61. Ge, J.; Yin, Y., Magnetically tunable colloidal photonic structures in alkanol solutions. *Adv. Mater.* **2008,** *20* (18), 3485-3491.

62. Ge, J.; He, L.; Hu, Y.; Yin, Y., Magnetically induced colloidal assembly into field-responsive photonic structures. *Nanoscale* **2011,** *3* (1), 177-183.

63. Singh, G.; Chan, H.; Baskin, A.; Gelman, E.; Repnin, N.; Král, P.; Klajn, R., Self-assembly of magnetite nanocubes into helical superstructures. *Science* **2014**, 1254132.

64. Wang, M.; He, L.; Zorba, S.; Yin, Y., Magnetically actuated liquid crystals. *Nano Lett.* **2014,** *14* (7), 3966-3971.

65. Wang, M.; Gao, C.; He, L.; Lu, Q.; Zhang, J.; Tang, C.; Zorba, S.; Yin, Y., Magnetic tuning of plasmonic excitation of gold nanorods. *J. Am. Chem. Soc.* **2013,** *135* (41), 15302-15305.

66. Mao, Y.; Liu, J.; Ge, J., Tuning the transmittance of colloidal solution by changing the orientation of Ag nanoplates in ferrofluid. *Langmuir* **2012,** *28* (36), 13112-13117.

67. Bubenhofer, S.; Athanassiou, E.; Grass, R.; Koehler, F.; Rossier, M.; Stark, W. J., Magnetic switching of optical reflectivity in nanomagnet/micromirror suspensions: colloid displays as a potential alternative to liquid crystal displays. *Nanotechnology* **2009,** *20* (48), 485302.

68. Chen, L.; Yang, X.; Chen, J.; Liu, J.; Wu, H.; Zhan, H.; Liang, C.; Wu, M., Continuous shape-and spectroscopy-tuning of hematite nanocrystals. *Inorg. Chem.* **2010,** *49* (18), 8411-8420.

69. Lekkerkerker, H. N.; Tuinier, R., *Colloids and the depletion interaction*. Springer: 2011; Vol. 833.

70. Wang, H.; Chen, L.; Shen, X.; Zhu, L.; He, J.; Chen, H., Unconventional Chain-Growth Mode in the Assembly of Colloidal Gold Nanoparticles. *Angew. Chem. Int. Ed.* **2012,** *51* (32), 8021-8025.

71. Liu, K.; Nie, Z.; Zhao, N.; Li, W.; Rubinstein, M.; Kumacheva, E., Step-growth polymerization of inorganic nanoparticles. *Science* **2010,** *329* (5988), 197-200.

Chapter 3 Confined Growth of Hybrid Nanostructures for Smart Optical Materials

3.1 Introduction

Colloidal plasmonic particles, especially noble-metal Au and Ag, have attracted long-lasting research attention due to their unique plasmonic, photothermal and electric properties.[1-3] Among these well-established properties, the localized surface plasmon resonance (LSPR) has been demonstrated with great potentials in developing high-performance sensors,[4-5] catalysts[6] and smart optical devices[7-8] as it strongly depends on the chemical component, size, morphology, surrounding dielectric environment and, in some cases, the orientation of the plasmonic particles.[9-10] Previous studies have revealed that the shape and morphology of plasmonic nanoparticles are critical in determining the strength and wavelength of their LSPR.[11-14] Therefore, it has been of great interest in developing new solution-phase synthesis for plasmonic particles with controllable shape and tailorable plasmonic properties. In the case of Ag, for example, lots of research efforts have been exerted to reporting synthetic methods for plasmonic Ag particles with shapes varying from primary spheres to cubes, platelets, rods and wires with uniform size and tunable LSPR in a much broader spectrum.[15-18] From the application point of view, plasmonic nanostructures also play key roles in determining structure-dependent practical performances, including the active sites in photocatalysis and hot spots in surface-enhanced Raman scattering (SERS).[19-20] Therefore, it is of both fundamental importance and practical interest to develop new plasmonic nanostructures with tunable plasmonic properties in response to external stimuli and integrated functionalities.

In principle, the properties and structures of plasmonic nanoparticles can be tuned by controlling their shape evolution during the growth process. However, in most cases, it is impractical to quench the reactions at the seeded growth process, especially at the early stages when fast nucleation and growth occur simultaneously. Besides, metastable kinetic products are generally particles with a broad size distribution, nonuniform morphology, poor plasmonic activities and poor colloidal stability as the intermediate structures have large specific surface areas, energetic facets and crystal defects, which makes the analysis of their structure-dependent LSPR very difficult and adds additional limitations to further investigation of growth mechanism and their plasmon-based applications.[21] Instead of the "forward" growth methods, a "backward" structure reconstruction has been proven as an alternative approach to producing plasmonic nanoparticles with tunable LSPR.[20] In general, it involves two steps: the full growth of metal particles and then structural reconstruction under desired conditions. It was reported that plasmonic Ag particles were formed with highly tunable LSPR and enhanced colloidal stability by photoinduced reconstruction of triangular nanoplates to round nanoparticles.[21] Compared to Ag,[22] nanoparticles of Au, Pt or Pd have better chemical and structural stability and therefore require harsh conditions, like annealing at relatively high temperature or laser irradiation, to achieve and preserve their metastable structures. Previous studies have demonstrated the feasibility of reshaping Au nanorods into nanospheres by laser irradiation, but with morphological impurity and significant loss in the LSPR of intermediate Au nanorods.[23-24] By carefully manipulating the growth conditions in liquid-phase synthesis, it is possible to produce metallic nanostructures with high-energy facets, such as concave cubes and

icosahedra of Au and Pd.[25-27] Relatively high temperature was still required for "backward" reconstruction as the structures were stabilized by capping ligands.[28]

In **Section 3.3** of this chapter, we first report an unconventional templated method to synthesize hybrid Fe_3O_4/Au nanorods and then precise tuning of their plasmonic properties in mild and controllable conditions through "backward" structural reconstruction. Our synthetic strategy is based on the space-confined seed-mediated growth of metal nanostructures within well-defined gaps between Fe_3O_4 nanorods and polymer shells. Thanks to the unique synthesis and their perfect parallel alignment, the anisotropy of magnetic Fe_3O_4 nanorods and plasmonic Au nanorods couples mutually with each other, allowing for active regulation and selective excitation of plasmon bands of Au nanorods with a magnetic field. Using Fe_3O_4/Au hybrid nanorods as the active components, in **Section 3.4**, we demonstrate that the coupled magnetic and plasmonic anisotropy can enable effective control of their orientation and subsequently the plasmonic excitation through magnetic means, which was further confirmed by simulation and analytical solution derived from bra-ket notation. Based on the full understanding of the orientation-excitation correlation, we further developed plasmonic films with pre-designed mechanochromic responses under various mechanical perturbations, which are enabled by magnetically aligning hybrid nanorods along the desired directions in the defined locations of the polymer matrices. In **Section 3.5**, we report the confined growth of Au shell on magnetic nanoparticles with well-defined plasmon bands and dynamic tuning of their coupled resonant scattering by magnetic assemble of Fe_3O_4@Au core-shell particles into plasmonic chains. We first demonstrate by finite element analysis that shell structures of

Au have overwhelming advantages in terms of tuning range and scattering efficiency in place of Au nanospheres. To take advantages of these merits, we then propose an unconventional seed-mediated growth of Au shell with uniform morphology and well-controlled resonant frequency on magnetic nanoparticles. Relying on the strong magnetic susceptibility of core materials, we finally propose a new scheme to actively and reversibly tune the plasmonic coupling and resonant scattering of Au shell via the magnetic assembly of Fe_3O_4@Au nanoparticles into plasmonic chains, which allows for the rational design of the active transparent display and anti-counterfeiting devices. In **Section 3.6**, we provide a short summary of this chapter.

3.2 Materials and Methods

Materials. All chemicals are used directly without further purification. Ethanol was purchased from Decon Labs. Iron chloride (III) hexahydrate, tetraethyl orthosilicate (TEOS), polyacrylic acid (PAA, MW=1800), sodium hydroxide, polyvinylpyrrolidone (PVP, MW=10000), resorcinol (R), formaldehyde (F), 2-Hydroxy-2-methylpropiophenone, polyvinyl alcohol (PVA), 2-Hydroxy-2-methylpropiophenone and Tetrakis(hydroxymethyl)phosphonium chloride (THPC) were bought from Sigma-Aldrich. Ammonium hydroxide and hydrogen peroxide (H_2O_2) were purchased from Fisher Scientific. Chloroauric (III) acid trihydrate ($HAuCl_4 \cdot 3H_2O$) was from Acros Organics. Acrylamide (AM) and N,N'-Methylenebisacrylamide (BIS) was purchased from Fluka. Oleic acid sodium salt (NaOL) was purchased from TCI AMERICA. SYLGARD 184 silicone elastomer curing agent and SYLGARD 184 silicone elastomer base were purchased from Dow silicone corporation. 3-aminopropyl-triethoxysilane ($C_9H_{23}NO_3Si$,

APTES), L-Ascorbic acid (AA), were purchased from Sigma-Aldrich. Ammonium hydroxide ($NH_3 \cdot H_2O$) and potassium iodide (KI) were purchased from Fisher Scientific. Ethylene glycol (EG) and diethylene glycol (DEG) was from Acros Organics.

Synthesis of FeOOH nanorods. 10.8 g $FeCl_3 \cdot 6H_2O$ was dissolved in 400 mL of deionized water and heated to 87ºC in an oven for 18 hrs. After that, FeOOH precipitated at the bottom, and the supernatant was discarded. The precipitation was washed in deionized water three times at 11000rpm for 15 min and finally dispersed in 40 mL of DI water.

Silica coating on FeOOH nanorods and reduction. To form uniform SiO_2 coating, FeOOH was modified by PAA first. Typically, 216 mg of PAA (~1800) was dissolved in 600 mL of DI water, and 10 mL of FeOOH aqueous dispersion was added afterward. The solution was magnetically stirred overnight. FeOOH was recovered by centrifugation and washed with DI water three times at 11000rpm for 15 min. The PAA-modified FeOOH was dispersed in 12 mL of DI water. For silica coating, 4 mL of FeOOH dispersion was concentrated into 2 mL and added to 40 ml of ethanol followed by 250 μL ammonium solution (28%). 125 μL TEOS was added for 4 nm SiO_2 coating or 250 μL TEOS was added twice with a one-hour interval for 8 nm SiO_2 coating. To achieve 12 nm SiO_2 coating, 2 mL FeOOH dispersion was added in a 20 ml of ethanol followed by 250 μL ammonium solution and 150 μL TEOS twice with a one-hour interval. The mixture was magnetically stirred overnight. Afterward, FeOOH@SiO_2 was centrifugated out at 14500rpm for 10 min and washed with ethanol once and water three times. FeOOH@SiO_2 was reduced to magnetic nanorods in DEG at 220ºC. 15 mL of DEG was heated to 220ºC under nitrogen, to which 250 μL FeOOH@SiO_2 aqueous solution was injected. The reduction was kept for

6 hrs under nitrogen protection. The final product was washed by ethanol and water three times and dispersed in 12 mL ethanol.

APTES modification. Typically, the dispersion of magnetic nanorods in ethanol was added into 50 mL ethanol. Then it was heated to 80oC and 200 μL APTES was added quickly. The surface modification usually took 5 hrs under nitrogen protection. Afterward, the product was washed by ethanol four times and dispersed in 12 mL of ethanol. The protonation of the amino group rendered the nanorods positively charges, which were capable of attracting the negatively charged Au seeds through electrostatic interaction.

Synthesis of CNCs. Colloidal particles of CNCs with tunable size were synthesized based on our previously reported method.[29] The reaction was carried in the solution phase at elevated temperature. A stock solution was prepared by dissolving 50 mmol NaOH in 20 mL of DEG, which was heated at 120oC for 1 hour under the protection of nitrogen. The solution was kept at 70oC as a stock solution. In a typical synthesis, PAA (4 mmol) and FeCl3 (0.4 mmol) were dissolved in DEG (17 mL) and the mixture was heated to 22oC for 30 min under the protection of nitrogen. A certain amount of stock solution was injected rapidly. The mixture was heated at 220oC for another one hour. The volumes of stock solution were 1.7, 1.75 and 1.8 mL for the synthesis of CNCs with an average diameter of 70, 125 and 150 nm, respectively. The obtained CNCs were washed by deionized water several times and dispersed in 20 mL of water.

PEI modification. For PEI modification, 5mL (0.25 batch) of an aqueous solution of CNCs was added into 30 mL of PEI solution (20mg/mL, Mw=800) under sonication. The mixed solution was agitated by vortex overnight. To get rid of magnetic field-induced

aggregation, magnetic stirring was not suggested during PEI modification. After that, CNCs were washed with water for three times and then dispersed in 5 mL of water.

Au seed preparation. THPC (12 μL) and NaOH (250 μL, 2M) were added into 45 mL water. After stirring for 5 min, 2 mL of $HAuCl_4$ was added. The Au seeds (Aus) solution was stocked in dark for further attachment.

Au seed attachment. To 30 mL of Au seed solution, 5 mL of CNCs solutions after PEI modification was added slowly under sonication. The mixed solution was agitated for about one hour. Excess Au seed was removed by centrifugation. Au seed was attached to the surface of CNCs due to the electrostatic interactions, forming CNCs/Aus nanoparticles. They were further washed by water three times and then dispersed in 10 mL of water.

RF coating. PVP modification was first carried out before RF coating. In a typical process, a 10 mL solution of CNCs/Aus was added into 30 mL of PVP solution (5 mg/mL) under sonication. The solution was agitated by vortex overnight. The solution was washed by water three times to remove excess PVP. Finally, they were dispersed in 28 mL of water for RF coating. In a based-catalyzed step-growth polymerization, 20 mg R and 28 μL of F were added in sequence. 100 μL of ammonia solution (2.8%) was added into the solution. The reaction was first sonicated for 1 hour and then transferred into a 50 mL round bottom flask. The reaction was kept at 100ºC for 3 hours in order to further condense RF resins and increase their cross-linking ratios. After cooling down to room temperature, the solution was washed three times by water. Then obtained CNCs/Aus@RF was finally dispersed in 2 mL of water.

Confined growth of cAuNRs. The seeded growth was carried out based on work reported previously.[30] Typically for growth of concave AuRNs to the full length, chemicals were added into 2 mL of Milli Q water in the following sequence, 500 μL of PVP (20mg/mL, MW=10000), 33 μL of KI (0.2M), 33 μL of AA (0.1M), 5 μL of $HAuCl_4$(0.25M) and finally 25 μL of seed solution. The growth usually took ~5 min. If decreasing the amount of AA, KI and $HAuCl_4$ proportionally, concave AuRNs with different aspect ratio were achieved.

Seed-mediated growth of Au shell. In a typical process, 500 μL of PVP (50mg/mL, Mw=40000), 100 μL of NaOL (10 mM), 20 μL of $HAuCl_4$ (0.25 M) and 50 μL of H_2O_2 were added into 7.5 mL of deionized water in sequence. Then, 25 μL of CNCs/Aus@RF solution was added. The reaction occurred at room temperature for 30 min. The product was washed by deionized water three times and dispersed in deionized water for characterization.

Preparation of PVA-Au composite film. PDMS film served as a transparent substrate for the PVA-plasmonic composite films. Silicone elastomer curing agent and silicone elastomer base were thoroughly mixed with a mass ratio of 1 to 10. The mixture was placed at ambient conditions for 2 hours to remove the air bubble inside the viscous solution. Then, it was cured at 60^{o}C for two hours. 10% PVA solution was first prepared by dissolving PVA into deionized water under sonication. Then a certain amount of PVA solution was added into the Au shell solution with a final concentration of about 0.005 mg/mL. The obtained mixture solution was spin-casted on a PDMS substrate. To form a

uniform thin PVA film, the PDMS substrate was first treated by plasma for 20 min. The casted film was dried in a vacuum at room temperature.

Preparation of hydrogel-plasmonic composite film. 2-Hydroxy-2-methylpropiophenone serves as a photoinitiator. AM is monomer and BIS is the cross-linking agent. In a typical process, 250 mg of AM, 14 mg of BIS and 3 μL of 2-Hydroxy-2-methylpropiophenone were added in 1mL of DEG. Au shell was first precipitated by centrifugation and then dispersed in the DEG solution. The mixture solution was sandwiched between glass slides and then was exposed to UV light (254 nm) for 1 min. To create a pattern based on lithography, the photomask was placed above the cover glass. After the first exposure, it was removed and a magnetic field with the different direction was applied, followed by another UV exposure. The magnetic alignment was achieved by placing the mixture into the center of two identical permanent magnets. The field strength was measured to be 25 mT (250 G).

Characterization. TEM images were taken on Tecnai 12 transmission electron microscope operating at 120 kV. Ultraviolet-visible-near infrared (UV-Vis-NIR) spectra were measured by Ocean Optics HR2000 CG-UV-NIR high-resolution spectrometer. The same instrument was used for in-situ spectra to monitor the growth dynamics. All spectra were taken on an aqueous dispersion of nanoparticles. For measuring the spectra under polarized light, a commercial polarizer was introduced right in front of the sample. Meanwhile, a magnet was applied to the aqueous suspension at about 1 cm (~ 25 mT). Optical microscopic images were acquired by ZEISS microscopy. Circular dichroism (CD) spectra were measured using Jasco J-815 CD spectrophotometer. SEM images was taken on

scanning electron microscopy NovaNanoSEM 450 operating at 10 kV. Dynamic light scattering (DLS) and zeta potential measurement were conducted in Delsa NanoC Particle Analyzer from Beckman Coulter. The magnetization curve was measured at room temperature (RT) on a squid magnetometer and zero-field-cooling and field-cooling (ZFC/FC) curve was measured at 75 Oe from 10 K to 300 K.

3.3 Space-confined Seeded Growth and Reconstruction of Hybrid Nanorods

The Fe_3O_4 nanorods engrave a surface concavity on Au nanorods due to their templating effect, which, in turn, induces an unconventional transverse plasmon band at long wavelength. The uniqueness of surface concavity lies in that it brings Au nanorods to a metastable state, thus enabling the systematical study of structural reconstruction of Au at mild conditions. More importantly, the cavity plasmon band provides a reliable way to monitor the structural evolution and LSPR band shift of Au nanorods during aging. The migration of Au atoms within confined space and the LSPR of Au intermediates could also be elegantly tuned by controlling the swelling of polymer shells in different solvents, providing additional ways to tailor the structural intermediates and plasmonic properties.

The initial FeOOH nanorods are 110 nm in length and 20 nm in width. After silica coating, the FeOOH@SiO_2 was converted into magnetic nanorods by polyol reduction at 220ºC. Small Au seeds were prepared by rapidly adding $HAuCl_4$ to the solution of sodium hydroxide and tetrakis(hydroxymethyl)phosphonium chloride (THPC). In the reaction, THPC serves as a capping ligand as well as a strong reducing agent. The nucleation occurred in an extremely fast fashion under alkaline conditions,[31] which produced small Au particles of ~2 nm. The fast nucleation was evidenced by the immediate color change of the solution to dark brown, which also indicated the small feature of seeds as no red color of large Au nanoparticles was observed. The produced Au seeds are negatively charged due to the presence of large amounts of organophosphorus compounds on the surface.[10, 32] To immobilize negatively charged Au seeds through electrostatic interactions, nanorods were modified with 3-aminopropyltriethoxysilane (APTES). We further coated

the nanorods with resorcinol phenol (RF) resins by base-catalyzed step-growth polymerization to enable the confined growth of the secondary metals, followed by high-temperature condensation to increase the crosslinking ratios.[33-34] Simultaneously, we observed that SiO_2 layers were etched away under basic conditions, forming well-defined gaps between Fe_3O_4 nanorods and RF shells.

In the seeded growth step, the first key point is to minimize self-nucleation by maintaining the reduction at a considerable low rate. To this end, KI as a stronger coordination halide to Au^{3+} was introduced, which reduces the reduction potential from initial +0.93 V of $AuCl_4^-$ to +0.56 V of AuI_4^-. Besides, polyvinylpyrrolidone (PVP) was added to further suppress the self-nucleation by stabilizing the atomic monomers.[35] PVP also serves as a surfactant and prevents the final particles from aggregation.[36] In a typical seeded growth process, the growth solution was prepared by sequentially adding PVP, KI, ascorbic acid (AA) and $HAuCl_4$ to water. The solution turned quickly from brown to the colorless state after adding $HAuCl_4$. In the reaction, the chloride was first replaced by iodide and the formation of intermediate AuI_4^- was evidenced by the brown color right after adding $HAuCl_4$.[37-38] Shortly, the complex AuI_4^- was further reduced to AuI_2^- as the solution turned colorless.[39] Previous study revealed that AA is good reducing agent for $AuCl_4^-$ due to the high reduction potential of the Au-chloride complex.[30] The produced AuI_2^- has a low reduction potential of +0.58 V, thus also preventing the reaction from self-nucleation. Another key point for the seeded growth of Au nanorods is to minimize the deposition of Au atoms on multiple seeds. As revealed in most previous literature,[10, 40] the reduced Au atoms were homogeneously deposited on each seed and the final metal nanostructures

formed as the fusion of multiple Au grains, resulting in plasmonic structures with a rough surface and poor crystallinity. As predicted by Mie theory, the produced plasmonic structures exhibited broad bandwidths and dominant scattering effects due to significant damping of surface plasmons by crystalline grain boundaries.[41-42] To get rid of these frustrations, we carefully induced Ostwald ripening relying on the presence of I^- and dissolved oxygen in the growth solution (**Figure 1a**). In an acidic condition, the oxidative etching of small Au seeds could occur as follow:

$$6I^- + O_2 + 4H^+ = 2I_3^- + 2H_2O \quad (1)$$

$$2Au + I_3^- + I^- = 2AuI_2^- \quad (2)$$

In addition to coordination agent, the previous study suggested that KI was oxidized to tri-iodide ion under the presence of oxygen (**Reaction 1**), which, in turn, dissolved metallic Au by oxidative etching (**Reaction 2**).[39] To confirm the Ostwald ripening pathway, we added KI to Au seed solution at ambient conditions. Interestingly, the solution turned to bright red with an obvious plasmonic peak at ~ 520 nm, indicating the formation of large Au nanoparticles. It is worth noting that the THPC in the Au seed solution served as the reducing agent in this reaction. As a comparison, we also added H_2O_2 to the Au seed solution. Conversely, there was no obvious decay of the dark brown color of the seed after the same incubation time. In general, H_2O_2 has been recognized as a good etchant due to its powerful oxidizing strength. In the previous study, for example, H_2O_2 was used as an etchant to facilitate the formation of Ag nanoplates.[16] However, the ripening of Au seeds under the presence of dissolved oxygen and I^- was much faster than that of H_2O_2 due to the strong coordination between Au^+ and iodide.

The scheme of the unconventional templated synthesis is depicted in **Figure 3.1a**. After RF coating, a clear gap was observed, and small Au seeds were homogeneously attached to the inner surface of RF shells (**Figure 3.1b**). The TEM image after seeded growth is shown in **Figure 3.1c** and uniform Au nanorods are formed with a unique surface concavity (cAuNRs) due to the presence of eccentric Fe_3O_4 nanorods. The space-confined seed-mediated growth of secondary metallic nanorods can be monitored by TEM images. PVP was added to the growth solution before quick centrifugation to stabilize Au monomers and effectively stop the reaction. At 1 min, multiple Au seeds on the inner surface of RF shells disappeared due to the Ostwald ripening and only one seed within each gap grow isotropically into large nanospheres. After reaching the diameter of the gap, they began growing one-dimensionally with unique surface concavity because of the confinement of RF shell, forming anisotropic cAuNRs with perfect parallel alignment to the initial magnetic rods. By controlling the thickness of SiO_2 layers, we further synthesized cAuNRs with different diameters. The TEM images of cAuNRs using silica thickness of 3 nm and 12 nm are shown in **Figures 3.1d** and **3.1e**, respectively. In addition to the similar surface concave, all the Au nanorods have the same length as the initial gaps, indicating the good confinement of RF shells. The hybrid nanostructures were further evidenced by the elementary mapping in **Figure 3.1f**. Elemental signals of Au and Fe were heterogeneously distributed within each rod, suggesting good structural uniformity and parallel alignment of the Fe_3O_4 and Au nanorods. To monitor the seeded growth, we measured the extinction spectra of cAuNRs in real-time (**Figure 3.1g**). The gradual redshift of the plasmon bands indicated the successive one-dimensional growth of cAuNRs. In the colloidal dispersion,

we observed a color change from light yellow to dark blue and finally brown (**insets in Figure 3.1g**). Notably, an abnormal plasmon band emerged at 625 nm when seeded growth proceeded for ~5 min, whose intensity increased gradually with slight blueshift. As shown in **Figure 3.1h**, both the longitudinal and the second transverse plasmon bands can be tuned by the gap size. The longitudinal plasmon band blue-shifted because of a decrease in aspect ratios as gap size increased from 3 nm to 12 nm. Similarly, the second transverse band also blue-shifted from 625 nm to 590 nm. This shift could be ascribed to the changes in the sharpness of the surface concavity. When the gap size is larger, the cAuNRs feature more rounded morphology, which gives rise to a blueshift of the plasmon band. It is important to point out that the thickness of the RF shell plays a key role in confining the seeded growth of Au nanorods. Au nanorods with irregular shape and nonuniform size were produced in the case of a thin RF shell of ~10 nm. The real-time spectra exhibited a blueshift in the longitudinal plasmon band in the later stages of seeded growth due to weak confinement of thin RF shells.

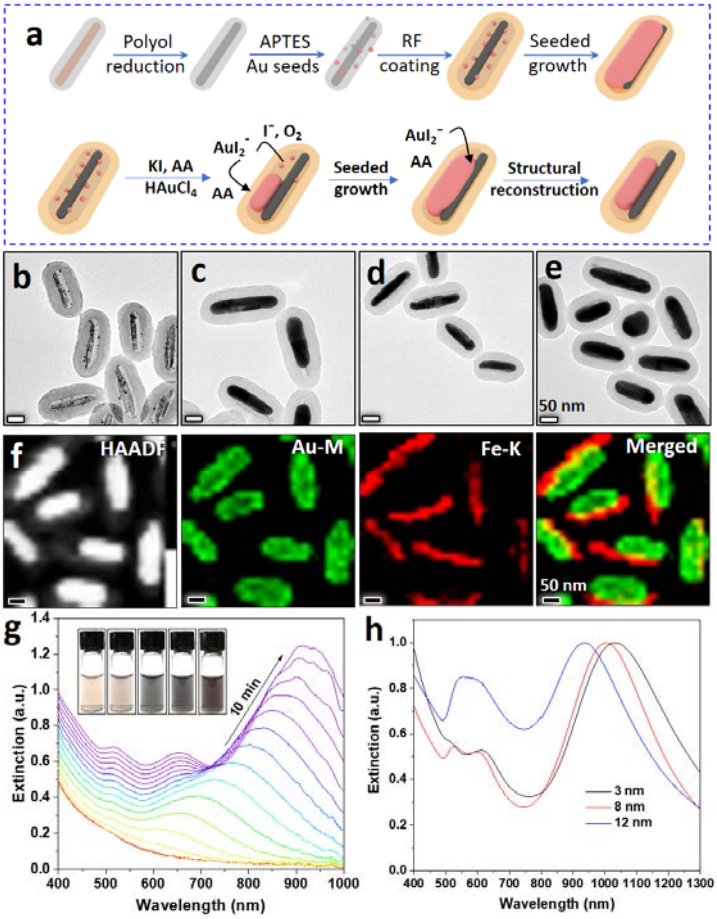

Figure 3.1. (a) Schematic illustration of the space-confined growth and reconstruction of cAuNRs. (b) TEM image of Fe_3O_4@gap/Aus@RF. (c)-(e) TEM images of hybrid nanorods after seeded growth within nano gaps of different thicknesses: (c) 8 nm, (d) 3 nm and (e) 12 nm. (f) High-angle annular dark-field (HAADF) image (left panel) and EDS mapping images of the hybrid structures (right three panels). (g) Real-time extinction spectra of hybrid nanorods during seeded growth with a time interval of 40 s. Insets show digital pictures of the colloidal dispersion during seeded growth (from left to right: 0, 1, 2.5, 5 and 10 min). (h) Extinction spectra of hybrid nanorods after seeded growth within nano gaps of different thicknesses.

To analyze the unconventional plasmon band at 625 nm, we calculated the extinction (ECS), scattering (SCS) and absorption cross-sections (ACS) of the cAuNRs synthesized by templating against 8 nm SiO_2 using finite element method. The 3D model of cAuNRs is illustrated in **Figure 3.2** and their geometry parameters are estimated from TEM images. In our simulation, the rod was parallel to the light incidence and their optical cross-sections under different rotations were calculated considering the symmetry-breaking of the surface concavity (**insets of Figure 3.3a**). It was found that the transverse plasmon band of cAuNRs was highly dependent on the rotation of cAuNRs relative to light polarization. At 90^o where the polarization is parallel to the connecting line of Au rod and surface concavity, only classic transverse band at 520 nm is observed (**Figure 3.3a**). When the angle is reduced to 0^o, another transverse band at 625 nm appears with gradually increased intensity (**Figure 3.3a**). Also, the second transverse band induces the dominant scattering effect as the magnitude of SCS in **Figure 3.3b** is much higher than that of ACS in **Figure 3.3c**. Therefore, It is reasonable to conclude that the surface concavity of cAuNRs does not change the classic transverse plasmon band of Au nanorods, but created another plasmon band with dominant scattering effects and rotation-dependent absorption, scattering and extinction (**Figure 3.3d**). We then analyzed this unconventional plasmon mode by mapping the surface energy flux (Poynting vector) and localized electric field distribution of cAuNRs excited at 615 nm. As suggested by **Figure 3.3e**, the scattering is highly localized on the surface concavity, giving rise to a well-defined cavity plasmon band.

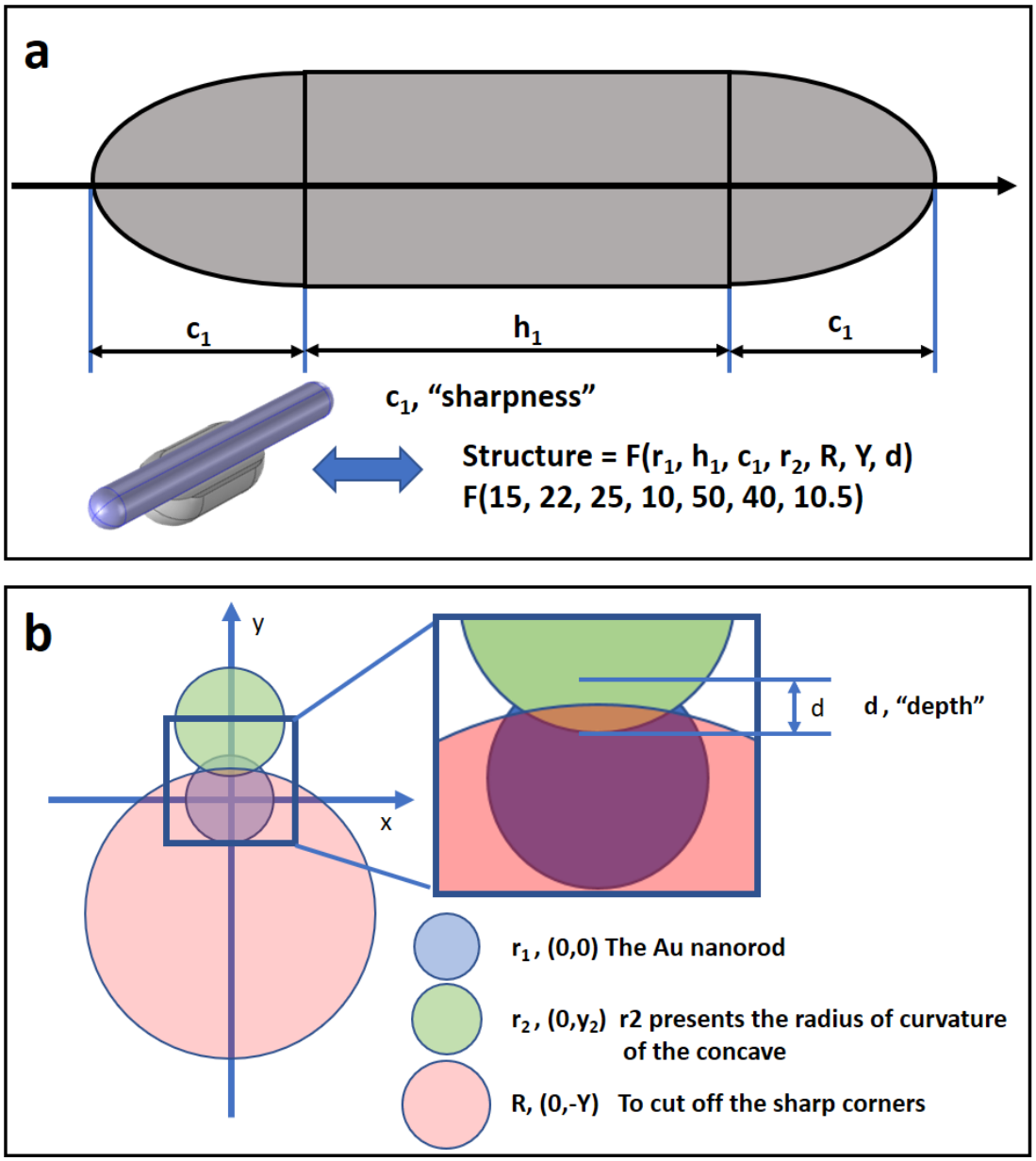

Figure 3.2. (a) Defining the geometry parameters of the cAuNRs. (b) Schematic illustration showing the modeling of cAuNRs.

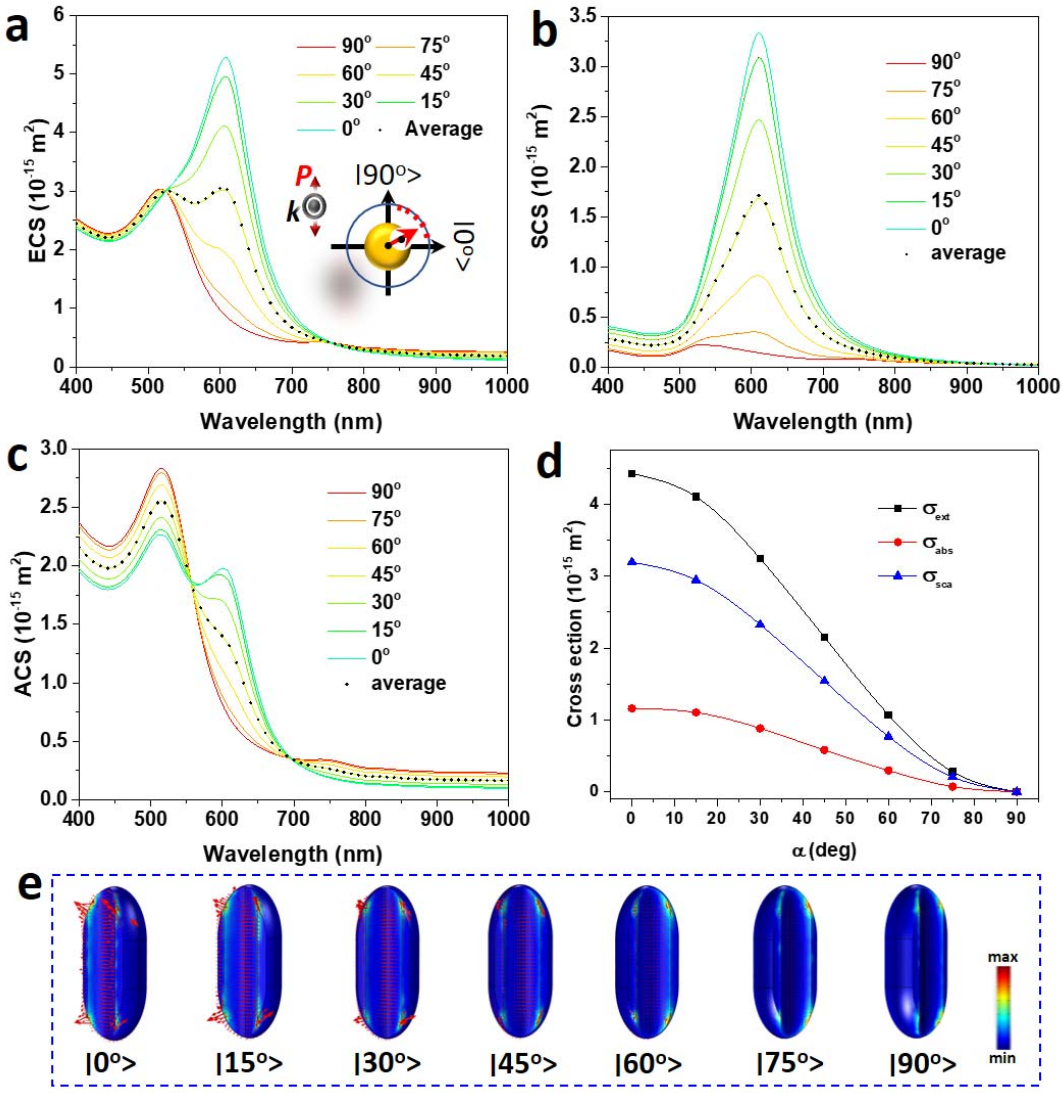

Figure 3.3. Calculated (a) extinction, (b) scattering and (c) absorption cross sections of cAuNRs by finite element method. The geometry of the simulation is shown in inset of (a). (d) Summary of the optical cross sections of cAuNRs under different rotation. (e) Poynting vector and localized electric field distribution of cAuNRs under different rotations excited at 610 nm.

We then studied the curvature effect by using FeOOH nanorods with different diameters as templates. In the experiment, we carefully increased their diameter from 25 nm to 35 nm, and finally, 70 nm while maintaining gap sizes by templating against SiO_2 of ~ 20 nm (**Figures 3.4a, 3.4b**, and **3.4c**). As shown in **Figures 3.4a and 3.4b**, the narrow magnetite nanorods created small concavity along the long axis of Au nanorods while the other parts could still be observed eccentrically. In the case of thicker magnetic nanorods, the surface concavity was more pronounced with smaller surface curvature. In an extreme case of thick magnetic nanorods (70 nm) but thin SiO_2 layers (5 nm) in **Figure 3.4d**, the seeded growth confined within the narrow space gave rise to a half shell-like Au structures. In the spectra, we observed a redshift from 670 nm to 870 nm of the cavity mode as the diameter of magnetic nanorods increased from 25 nm to 70 nm. The presence of a surface cavity by seeded growth of Au within confined space will damp the resonant frequency of the transverse mode. As the size of the surface cavity increased, more damping effects will be exerted on the oscillation of conductive electrons with electromagnetic fields, thus resulting in the redshift of the cavity plasmon mode.

It is worth mentioning that the cAuNRs prepared by the unconventional templated synthesis is far from thermodynamic equilibrium but in a state favored by reduction kinetics. On one hand, previous studies of metallic nanostructures featuring surface concaves,[25, 28, 43] like Ag, Au, and Pd, have revealed that there existed high-index facets in the local concavity, which provided active sites for catalysis.[26] The sharp edges of the concave structures, especially in the case of Ag, also provided additional sites for SERS due to their strong LSPR.[44] On the other hand, for metallic nanostructures with surface

concavity in conventional colloidal synthesis, morphological reconstruction usually requires high energy input or harsh conditions, which makes directive observation of the structure evolution and plasmon band shift quite difficult. By taking advantage of the many merits of unconventional templated synthesis as well as the surface concave structures and cavity plasmon band, we then demonstrated that the hybrid nanorods are an ideal model to study the surface reconstruction of Au materials and the structure-dependent physical properties.

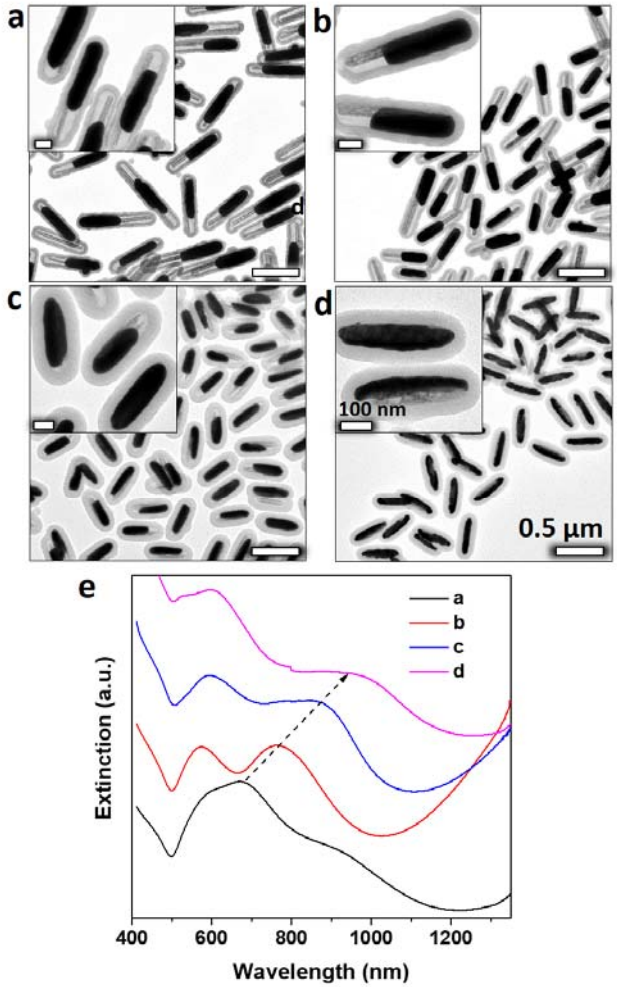

Figure 3.4. (a-d) TEM image of hybrid nanorods by using FeOOH of different sizes as templates. (e) The corresponding extinction spectra of hybrid nanorods after seeded growth.

We used small FeOOH nanorods (110 nm×20 nm) with silica of 8 nm for the real-time measurement of band shift since the produced cAuNRs had plasmon bands within 1000 nm. It was found that cAuNRs became fatter with a smoother surface when comparing their TEM images before (**Figure 3.5a**) and after (**Figure 3.5b**) aging for 24 hours in water at 60ºC. Due to the confinement of RF shells and the templating effect of Fe_3O_4 nanorods, surface concavity could be observed at the Au-Fe_3O_4 interfaces (**Figure 3.5c**). After cAuNRs were aged, the interface became clearer and more regular. Under the side-by-side configuration, the boundary between Au and Fe_3O_4 could be easily distinguished in **Figure 3.5d**, indicating the shallowing of the surface concavity. As a result, both longitudinal and cavity bands gradually blue-shifted. As the formation of high-energy surface curvature was partially induced by the confinement of RF shells, we further studied the plasmon band shift of cAuNRs in different solvents. **Figure 3.5e** indicates the extinction spectra of cAuNRs when they were aged in dimethylformamide (DMF) at 60ºC. The plasmon band of longitudinal mode shifted from 950 nm to 700 nm. Meanwhile, the cavity plasmon band blue-shifted until disappearance, leaving only the classic transverse band at 550 nm. It has been generally accepted that the rounded effect of sharp edges of plasmonic nanoparticles, particularly of Ag and Au, is responsive for the shift in plasmon bands but commonly with small magnitudes. For example, there would be only a 60 nm shift in the plasmon band of Ag nanoprisms with comparable sharpness and thickness,[45-46] which is much smaller than the 250 nm shift in our experiments. Instead, as suggested by the previous study,[21, 44] the significant change in the aspect ratios was the main reason for the large shift in the plasmon band. This explanation is also supported by the clear morphological changes in the TEM

images before and after aging. In the case of water and ethanol, however, the shift in the two bands was smaller, with only a 150-nm shift in the longitudinal mode as summarized in **Figure 3.5f**. Compared with previous studies on the thermal-induced reconstruction, the temperature is the main factor that determines the aging kinetics.[28] In our experiment, however, we revealed that the shift of plasmon bands of cAuNRs was also dependent on solvents. The previous study had demonstrated that polar solvent, especially DMF, can easily swell the RF reins and dissolve short chains due to the polar nature of the RF oligomers, which will make the shell softer and more porous.[47] As a result, the migration of Au atoms from the most energetic areas, like concave edges, is much easier. The etching effect was evidenced by the dramatic decrease in the contrast of RF shell after aging, which, in turn, weakens the confinement of RF shells and produces thick cAuNRs with small aspect ratios. By controlling solvents instead of temperature in the "backward" aging approach, we conclude that the structural reconstruction within confined spaces provides elegant control over the morphological and optical properties of plasmonic Au.

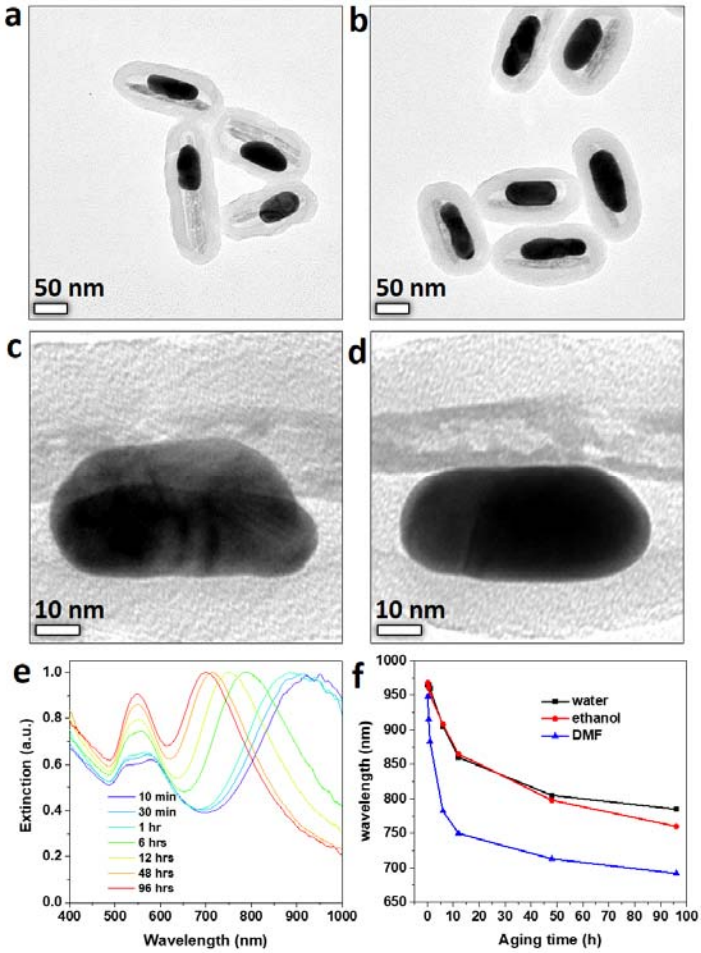

Figure 3.5. (a-d) TEM image of hybrid nanorods (a) before and (b) after aging. Enlarged TEM images exhibiting the concavity of cAuNRs. (c) before and (d) after aging. (e) The extinction spectra of cAuNRs during aging at 60ºC. (f) The peaks shift of plasmon band during aging.

To further depict the cavity band and structure-dependent LSPR of cAuNRs upon aging, we carried out a numerical simulation based on the finite element method. The initial cAuNRs are modeled with sharp tips and concave edges, followed by a gradual decrease in the concave depth and aspect ratios to mimic the morphological evolution of cAuNRs observed from TEM images. Notably, the 3D model was deliberately designed with a constant volume considering the negligible mass loss during structural reconstruction. Instead, the surface area decreased significantly due to the disappearance of energetic shape corners. Then, the longitudinal and transverse bands were calculated by placing cAuNRs with their long axis parallel to electric fields and the incident light, respectively. We observed a continuous blueshift in both the longitudinal and cavity plasmon bands. In the most reported cases, the extinction was measured in the colloidal dispersion of plasmonic nanostructures with random orientation, whose spectral profile is the superposition of all possible excitation states. In the numerical simulation, however, the extinction of a single rod with well-defined geometry and specific excited state will be calculated. To solve these frustrations, we utilized a magnetic alignment approach for selective excitation of plasmon bands of cAuNRs by taking advantage of the preferential parallel alignment of Fe_3O_4 nanorods along magnetic fields. To verify the feasibility, we first measured the extinction spectra of cAuNRs after aging by applying magnetic fields in different directions. At 90^o where the direction of the applied magnetic field was parallel to the polarization, the only longitudinal mode was excited as the transverse band at 535 nm disappeared. Conversely, when rotating the magnetic field to 0^o, we observed a gradual decrease of the longitudinal band to a state where only transverse mode was excited. Based on these measurements with

applied magnetic fields, we then measured the transverse (left panel in **Figure 3.6a**) and longitudinal plasmon bands (right panel in **Figure 3.6a**) of cAuNRs during aging under linearly polarized light. The longitudinal plasmon band had a blueshift from 725 nm to 675 nm when cAuNRs were aged for 2 days at 60ºC. Meanwhile, the cavity band at 600 nm blue-shifted until it overlapped with the classic transverse band at 535 nm. It is worth mentioning that the experimental shifts of plasmon bands were consistent with our simulation results (**Figure3.6b** and **3.6c**), indicating that the dynamic structure of cAuNRs and the associated plasmonic properties during aging can be fully revealed by our model. Furthermore, the Poynting vectors and the localized electric fields were plotted in **Figure 3.6d**. It is interesting to point out that the scattering is mainly localized on the concavity of the cAuNRs in all cases due to the presence of sharp edges.

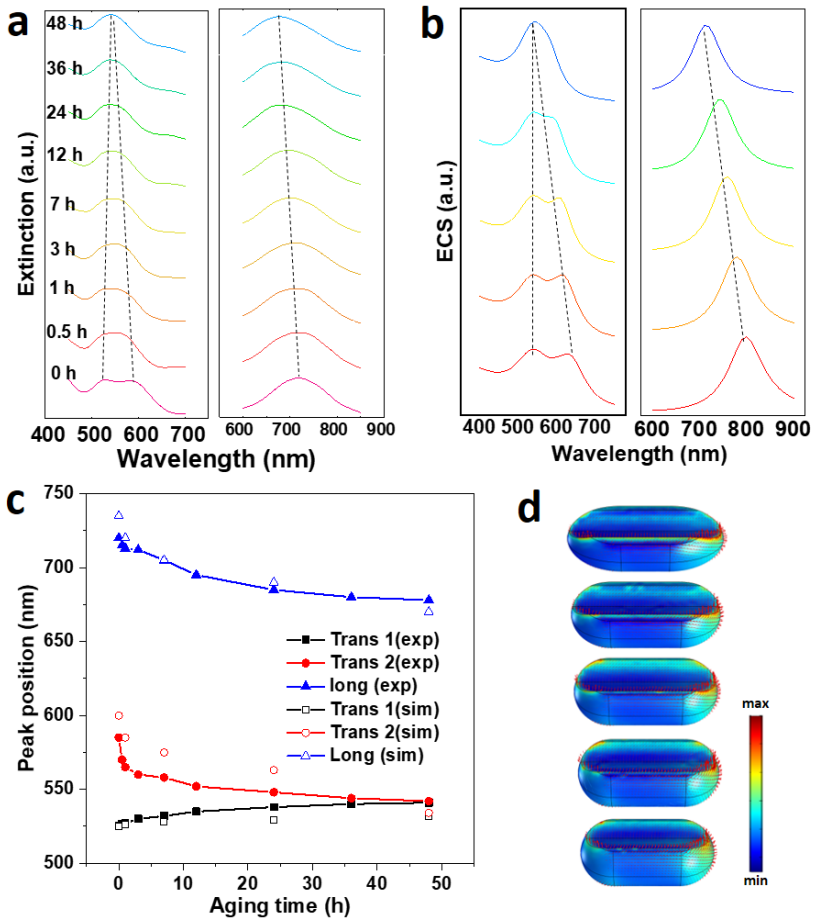

Figure 3.6. (a) Experimental extinction spectra of cAuNRs during aging at 60ºC for different times. (b) Simulated ECS of cAuNRs during surface reconstruction. Left and right panels represent the transverse and longitudinal modes, respectively. (c) Summary of peak shift of cAuNRs plasmon bands over aging time. (d) The scattering (red arrows) of cAuNRs over aging. The localized electric fields are represented by surface color.

By etching away magnetic nanorods, we further demonstrated that the "backward" aging process provides a reliable method to produce short Au nanorods with pronounced LSPR. It has been widely accepted that short nanorods featuring both strong LSPR and colloidal stability remains challenging in most well-established solution-phase synthesis as it commonly involves fast nucleation-growth process and quenching the reaction at the non-equilibrium stage turned out to be impractical and only produced metallic nanostructures with broad size distribution and limited plasmonic activity. Current reported approaches include oxidative etching[48] and photochemical synthesis,[49] which are still suffering from low yield, high cost and complex redox reaction involved. By taking advantage of the space-confined post-aging process, we provided a practical way for the synthesis of short Au nanorods with pronounced LSPR. To this end, the aging of cAuNRs was carried out in acidic environments at high temperatures (**Figure 3.7a**). More specifically, oxalic acid-etched away the magnetic nanorods, providing plenty of room for morphological reconstruction. As shown in **Figure 3.7b**, Fe_3O_4 nanorods were completely etched away within 1 h, leaving uniform Au nanorods inside, and the longitudinal plasmon band had shifted to 650 nm (**Figure 3.7c**), which was much faster than aging in the presence of Fe_3O_4 nanorods. In the spectra, Au nanorods exhibited two strong peaks at 545 nm and 650 nm. As shown in **Figure 3.7d**, Au of regular rod shape was formed by additional seeded growth, leading to the shift of the longitudinal mode to 925 nm. Notably, the real-time spectra (**Figure 3.7e**) only featured one transverse mode at 545 nm, further demonstrating that the band at 625 nm originated from the LSPR of surface concavity.

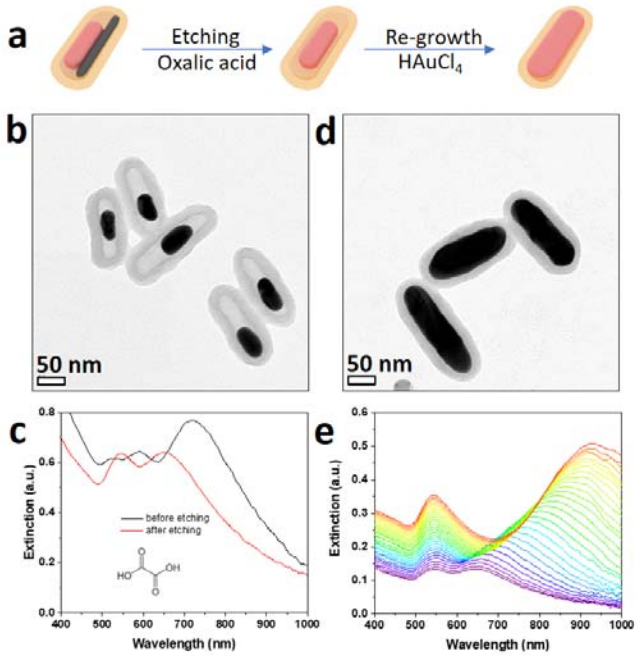

Figure 3.7. (a) Scheme illustrating the seeded growth of Au nanorods after etching the Fe_3O_4 nanorods by oxalic acid. (b) TEM images of Au nanorods after etching away Fe_3O_4 nanorods. (c) Extinction spectra of nanorods before and after etching. (d) TEM images of Au nanorods after additional seeded growth. (e) Real-time extinction spectra of Au nanorods during seeded growth.

One overwhelming advantage of templated synthesis over ligand-directed synthesis is that it does not require specific capping ligands to regulate the local growth kinetics of the metallic nanostructures. Therefore, the plasmon band can be easily tailored more flexibly and practically. To this end, we carried out successive growth-aging experiments to study the optical properties of cAuNRs. As shown in **Figures 3.8a**, **b**, and **c**, the length of the cAuNRs first decreased during the first aging process and then increased during additional seeded growth. In terms of the extinction spectra (**Figure 3.8d**), we observed a gradual blueshift of the longitudinal plasmon band, as well as the disappearance of the concave band as the aspect ratios of cAuNRs, decreased from 2.25 to 1.6 during aging. Afterward, the aged cAuNRs were used as a seed for further growth of Au within the remaining gaps. **Figure 3.8e** reveals a continuous redshift of the longitudinal plasmon band of cAuNRs. Interestingly, the cavity band of cAuNRs recovered with a clear peak at 600 nm, consistent with the peak position in **Figure 3.8d**. These spectrum results confirm the growth process of cAuNRs within the remaining gaps, which, in turn, demonstrates the good structural and chemical stability of RF shells in aqueous solutions. When the cAuNRs were subject to aging conditions again, similar blueshift of the two bands at longer wavelength was observed (**Figure 3.8f**), suggesting the occurrence of structural reconstruction of cAuNRs. In **Figure 3.8g**, the changes in aspect ratios were consistent with the peak shifts of the longitudinal plasmon band.

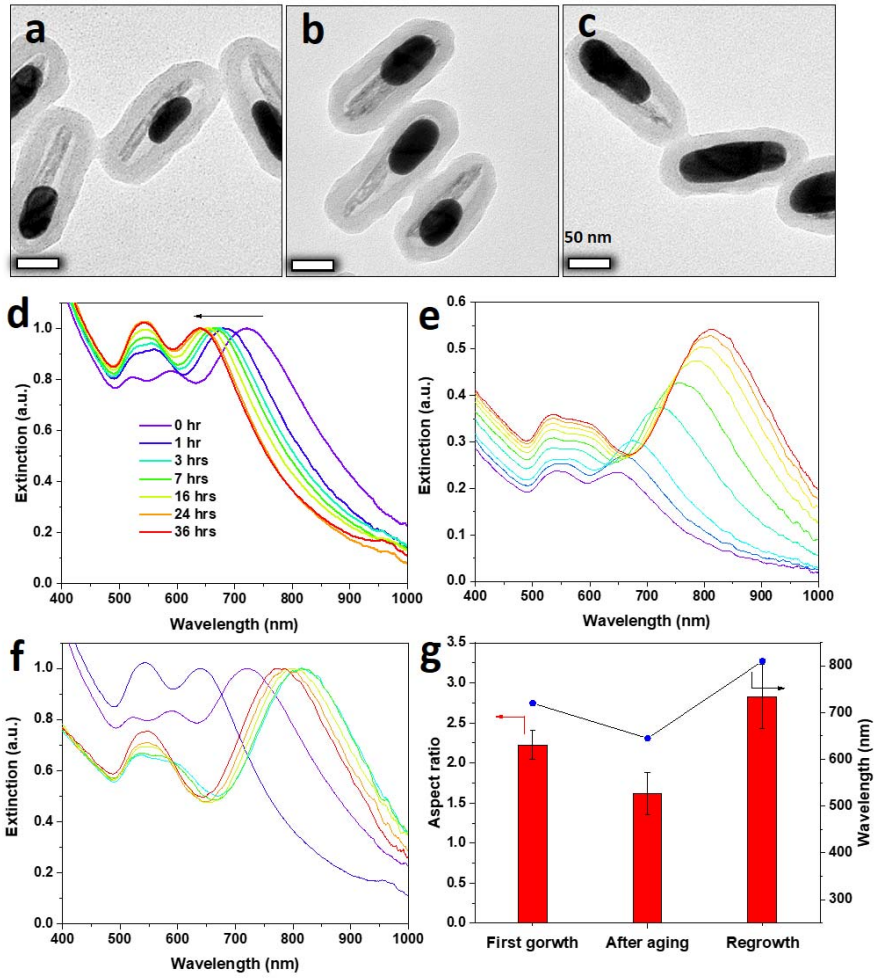

Figure 3.8. (a-c) TEM image of hybrid nanorods (a) before and (b) after aging and (c) after second seeded growth. (d) The corresponding extinction spectra of hybrid nanorods during the first aging. (e) The extinction spectra of hybrid nanorods after additional seeded growth. (f) The extinction spectra of hybrid nanorods after second aging. (g) Summary of the aspect ratios and peak positions of longitudinal modes during the sequential seeded growth and aging process.

3.4 Coupling Magnetic and Plasmonic Anisotropic in Hybrid Nanorods for Mechanochromic Films

Engineering mechanochromic systems with programmable colorimetric responses is a crucial challenge to develop high-performance robotic devices. Most current systems rely on photonic bandgap structures,[50-52] fluorescence,[53] and plasmonic resonance,[5, 54] thus limited in providing precise colorimetric responses to complex (linear and angular) mechanical motions and also lack the flexibility of large-scale programmable device fabrication. The spatially differentiated photon-electron resonance of anisotropic plasmonic nanostructures[2, 55] offers excellent opportunities to achieve colorimetric responses and enables a variety of fascinating applications such as diffraction-unlimited optics,[56] laser writing,[57] negative/zero-index metamaterials,[58] optical modulator,[59] and photothermal conversion.[60-61] Almost all of these explorations are, however, based on a small number of units that are either fabricated on solid substrates by advanced lithography[59, 62-65] or carefully chosen from those chemically synthesized and then randomly deposited on substrates.[59, 66-68] Selective excitation of multiple plasmonic nanorods has been achieved via incorporation into liquid crystals (LCs),[69-71] where orientational control could be realized by applying electric fields. Such a system may find applications in electrochromic displays,[72-73] but also shares the limitations of conventional LC devices. Through mechanical stretching of polymer matrices or masked metal evaporation, colloidal plasmonic nanoparticles were also made into oriented arrays to display polarization-dependent coloration.[74-76] Such systems, however, have limited

flexibility in precise orientational control in the exact locations and matrices desired for fabricating complex mechanochromic devices.

Magnetic-plasmonic hybrid nanostructures represent a class of smart nanomaterials that have profound impacts on not only biomimetic devices but also bioimaging, sensing, and information encryption.[40, 77-78] They have been mainly produced by co-assembly of plasmonic and magnetic nanomaterials,[79-81] and for practical applications, significant improvement is still desired in the dimensional control, structural stability, and the precision of alignment.[82] To this end, direct colloidal synthesis of multi-component nanostructures with high colloidal stability and tunable physical properties is of great interest for fabricating unique mechanochromic devices. Here, we report the development of magnetic-plasmonic hybrid nanorods with excellent control in morphology and dimension through an unconventional colloidal synthesis approach. The plasmonic nanorods were grown alongside the magnetic ones through a seed-mediated process confined within highly permeable polymer shells, producing compact hybrid nanorods with perfect structural alignment, coupled magnetic-plasmonic properties, and excellent colloidal stability. This versatile approach represents a new platform that allows the design of a wide range of high-quality complex nanostructures.

The space-confined seed-mediated growth of magnetic-plasmonic hybrid nanorods is depicted in **Figure 3.9a**. FeOOH nanorods were synthesized by a high-temperature hydrolysis reaction[83-84] and then reduced to Fe_3O_4 by a polyol process with the protection of a silica shell (**Figure 3.9b**).[85] The blocking temperature and the magnetic anisotropy constant of Fe_3O_4@SiO_2 nanorods were found to be 190 K (below RT) and 1.8 kJ/m^3 (one

order lower than magnetocrystalline anisotropy constant), indicating superparamagnetism with a dominant shape anisotropy. After immobilizing Au seeds through electrostatic interaction,[10] the nanorods were overcoated with a layer of resorcinol phenol (RF) resin,[86-87] whose crosslinking was enhanced by further heating at 100 ºC.[88-89] Meanwhile, the silica interlayer was etched by base,[90] producing magnetic nanorods@voids@RF nanostructure with small Au seeds dispersed homogeneously within the RF shells, as evidenced in **Figure 3.9c**.

The seeded growth of Au was carried out using our previously developed procedure[30]. Interestingly, once a small amount of $HAuCl_4$ was added, only one isotropic Au nanoparticle formed within each RF shell, which could be ascribed to Ostwald ripening, involving the initial dissolution of smaller seeds by oxidative-etching by I^-/O_2 and then re-deposition to the larger seeds.[39] Further growth induced a unique concave structure along the long axis of AuNRs (denoted as cAuNRs thereafter).[91] Depending on the amount of added precursors, the seeds could grow progressively into cAuNRs with highly uniform size and shape with perfect parallel alignment to the Fe_3O_4 nanorods (**Figures 3.9d, 3.9e**). Details of the unique concave structures are shown in **Figure 3.9f** with two typical orientations (side by side and overlapped configurations) of cAuNRs. The hybrid nanostructure is further confirmed by element mapping **(Figure 3.9g)** and energy-dispersive X-ray spectroscopy (EDS) analysis (**Figure 3.9h),** with the latter clearly revealing a side-by-side (left) and overlapping (right) configurations. The growth was isotropic initially and then switched to anisotropic mode, with longitudinal plasmon modes appearing at a longer wavelength and red-shifting continuously to 880 nm (**Figure 3.9i**).

While both transverse and longitudinal peaks became stronger as the seeded growth proceeded, the peak due to the surface concave structure appeared at 630 nm. With more precursors, the growth became faster, resulting in cAuNRs with larger aspect ratios (**Figure 3.9j**). By manipulating the reaction kinetics, we could produce cAuNRs with different aspect ratios (up to 3.8) and correspondingly control their longitudinal resonance wavelengths.

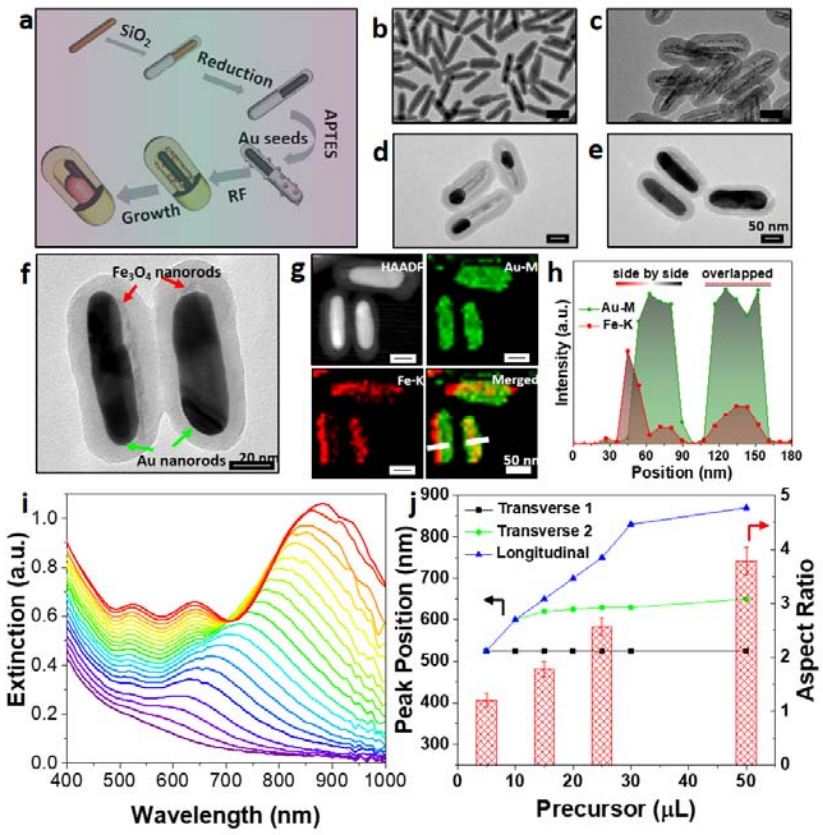

Figure 3.9. Synthesis and characterization of plasmonic-magnetic hybrid nanostructures. (a) Scheme of the confined growth towards magnetic-plasmonic hybrid nanorods. TEM images of nanorods after (b) SiO_2 coating, (c) RF coating, seeded growth with (d) 15 μL, (e) 25 μL of precursor. (f) TEM images showing hybrid nanorods with two typical configurations (left: side by side; right: overlapped). (g) HAADF and EDS mapping images of the hybrid structures. (h) The cross sectional line profile of element distribution. (i) The real-time extinction spectra of cAuNRs with a time interval of 15 s. (j) Dependence of peak positions of surface plasmonic resonance and aspect ratios of cAuNRs on volume of precursor. The reaction kinetics is controlled by adding different number of precursors as indicated.

To understand the plasmonic excitation of anisotropic nanostructures under linearly polarized light, we first derived the analytical equations of plasmonic excitation based on bra-ket notation. **Figure 3.10a** shows an arbitrary configuration of cAuNRs, whose orientation can be mathematically expressed by a ket, |α, Θ>. Under z-polarized light (**Figure 3.10b**), the bra-ket notation of orientation state, |S>, of cAuNRs in **Figure 3.10a** is expressed as A_L|α, Θ> +A_T|90°+α, Θ>, where the first and second terms determine the longitudinal and transverse excitation, respectively. Exciting plasmon resonance of cAuNRs under polarized light could be interpreted as polarizer operator (*P*, |z><z|) operating on the corresponding ket:

$$|A> = P|\psi_L> + P|\psi_T> = A_L cos\alpha|z> - A_T sin\alpha|z> \quad (1)$$

where $A_L$cosα and $A_T$sinα represent longitudinal and transverse excitation coefficients, respectively. The resulted ket, |z>, indicates that the resonance happens along the z-direction. Given an arbitrary orientation ket, the expectation value of excitation can be derived as follows by using the bra-ket theorem:

$$<A(\alpha,\theta)> = <\psi_L|\mathrm{P}|\psi_L> + <\psi_T|\mathrm{P}|\psi_T> = I_L cos^2\alpha + I_T sin^2\alpha \quad (2)$$

It predicts that the expected value of excitation is only dependent on the azimuthal angle, α. We used ratiometric data processing to quantify the correlation between excitation states and azimuthal angle, α, which helps to eliminate signal fluctuation and backgrounds:

$$\frac{<E_L(\alpha,\theta)> - <E_L(90^o,\theta)>}{<E_L(0^o,\theta)> - <E_L(90^o,\theta)>} = cos^2\alpha \quad (3)$$

$$\frac{<E_T(\alpha,\theta)> - <E_T(0^o,\theta)>}{<E_T(90^o,\theta)> - <E_T(0^o,\theta)>} = sin^2\alpha \quad (4)$$

where E is transverse or longitudinal extinction at given orientations.

We experimentally studied the orientation-dependent plasmonic excitation of cAuNRs by measuring the extinction of their colloidal dispersions in different magnetic fields. The perfect parallel alignment between cAuNRs and Fe_3O_4 nanorods, enabled by our unique synthesis, facilitated convenient magnetic control of the plasmon resonance of cAuNRs. Under an ordinary light (**Figure 3.10c**), both transverse and longitudinal modes were excited and consequently, the solutions appeared gray. Under polarized light, selective excitation of transverse or longitudinal mode could be achieved by magnetically aligning cAuNRs to $|90^o, 90^o\rangle$ and $|0^o, 90^o\rangle$, respectively (**Figure 3.10d**). At $|90^o, 90^o\rangle$ configuration, only the transverse mode at 525 nm was excited, and the solution of cAuNRs with different ARs was red (middle panel in **Figure 3.10d**). At $|0^o, 90^o\rangle$ configuration, the color of the solution turned from red to blue, green and finally yellow (bottom panel in **Figure 3.10d**) due to the selective excitation of longitudinal modes and their continuous red-shift. The extinction spectra of cAuNRs with an aspect ratio of 2.5 are shown in **Figures 3.10e** and **3.10f** under normal and polarized light, respectively. As shown in **Figures** 3.10g, the dependence of plasmonic excitation on α from experimental measurements and simulation is consistent with the analytical solution.

To quantitatively describe the color brightness of the dispersions, we introduce the tunability factor, $f(\alpha) = E_L(\alpha)/E_T(\alpha)$, where $E_L(\alpha)$ and $E_T(\alpha)$ are the longitudinal and transverse extinction, respectively. As summarized in **Figure 3.10h**, the highest contrast under ordinary light is 1.25, which is of high consistency with the gray/brown color in the aqueous solutions (bottom panel in **Figure 3.10c**). Under polarized light, the factor can be modulated in a much broader range, from 0.5 to 2.7 (**Figure 3.10i**), giving rise to obvious

color changes in the aqueous solutions once aligning the cAuNRs from y-axis to z-axis via a magnetic field (**Figure 3.10c**).

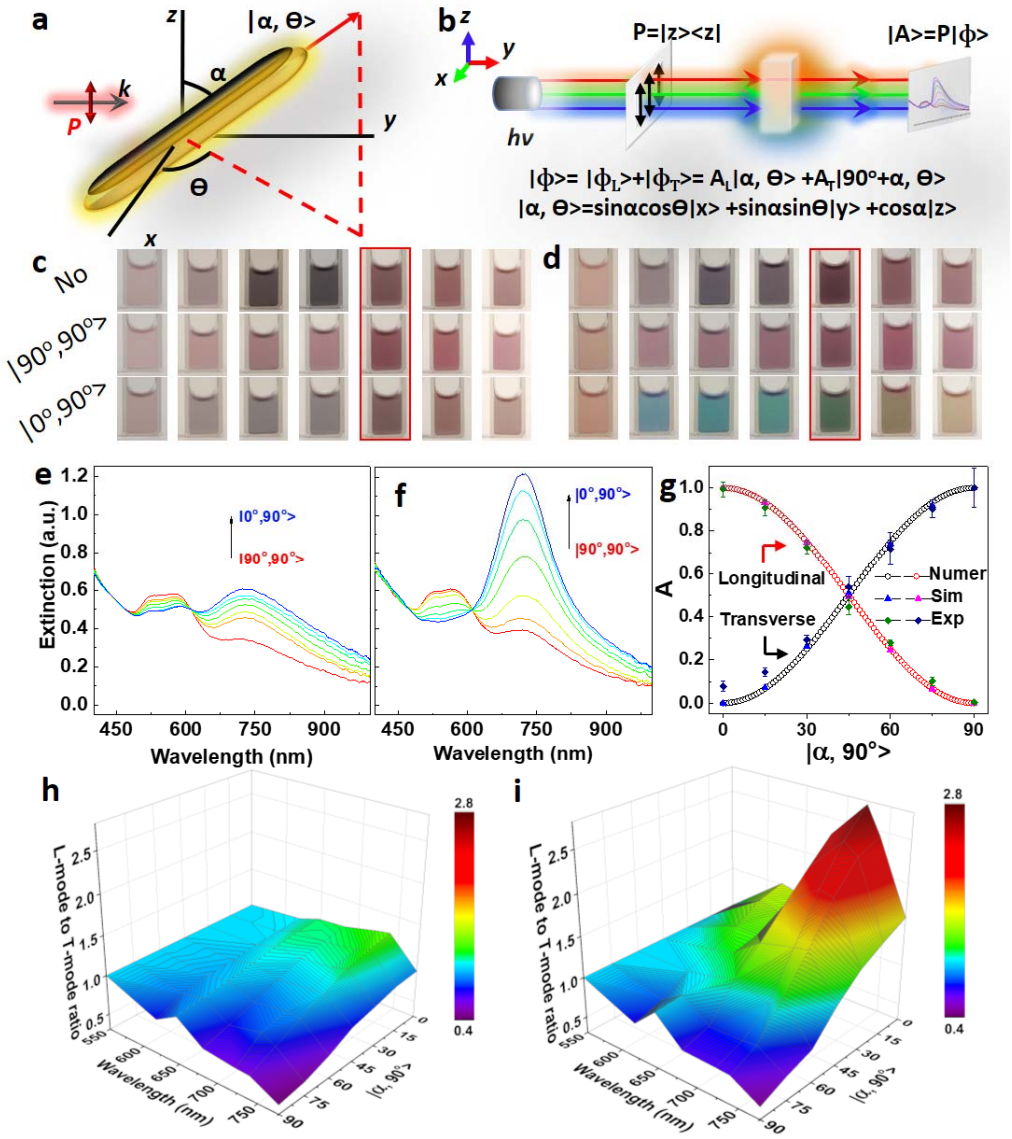

Figure 3.10. Optical tunability of cAuNRs suspension. (a) Schematic illustration of cAuNRs under the orientational state |α, Θ> with respect to the polarization of light. (b) Tuning plasmonic extinction of cAuNRs under polarized light and the corresponding mathematical interpretation by bra-ket notation. Digital images of cAuNRs dispersion under normal, (c) and polarized light, (d) In both (c) and (d), the highlighted columns are used for plots in **Figure 3.10e and 3.10f**. Tuning extinction of cAuNRs under (e) normal

and (f) polarized light. (e) and (f) share the same y-axis. (g) Correlation between excitation modes and orientational states of cAuNRs, whose fine spectra tunability is shown in (f). Summary of L-mode to T-mode ratio of different dispersions in c and d achieved by varying α under (h) normal and (i) polarized light. The azimuth angle, Θ, was set at 90°.

The dependence of plasmonic excitation of cAuNRs on their orientation offers a reliable tool for fabricating mechanochromic devices. To this end, we prepared a cAuNRs/polymer composite film with nanorods aligned along a given direction by UV-curing an aqueous dispersion of cAuNRs and acrylamide under a uniform magnetic field. **Figure 3.11a** shows the extinction spectra of the film with aligned cAuNRs. The preferential parallel alignment of cAuNRs with the magnetic fields was confirmed by the good agreement between the measured and theoretical values. Our statistical analysis revealed a narrow normal distribution of cAuNRs orientation along the directions of magnetic fields (SD=2.8^o). To analyze the mechanochromic sensitivity of plasmonic films, we calculated the first derivative of the E_L-α function. As plotted in **Figure 3.11b**, it approaches maximum and then decreases dramatically as α increases from 0^o to 90^o, suggesting that [30^o, 60^o] (slope threshold of 0.9) is the optimal range for engineering mechanochromic film with high sensitivity. To verify this hypothesis, we prepared three plasmonic films, in which cAuNRs were aligned randomly, 0^o, and 30^o to the surface normal. When the films were subjected to various pressures, their plasmonic excitation was monitored *in-situ* in real time. The embedded cAuNRs tended to rotate to a horizontal position due to the elastic deformation of the polymer under vertical pressures. In **Figure 3.11c**, as the pressure increased from 0 to 67.7 kPa, the intensity of longitudinal modes of cAuNRs gradually increased. Interestingly, the change under 30^o was significantly larger than that of 0^o or random orientation (**Figure 3.11d**). This observation is consistent with our theoretical prediction of sensitivity and experimentally verifies the proposed working principle for designing highly sensitive mechanochromic films. We further investigated the mechanochromic

response of the films under stretching. The extinction spectra were systematically measured by stretching the film along different directions relative to the rod orientation. Under unidirectional strains (ε), the film elongates along the axial direction and narrows due to the Poisson effect. Therefore, the cAuNRs realign to the axial direction as evidenced by the gradual increase of the longitudinal excitation (**Figure 3.11e**). **Figure 3.11f** reveals a linear correlation between ΔE and ε, the fitting slopes of which are highly dependent on the initial alignment (α) of cAuNRs. As summarized in the inset of **Figure 3.11f**, the film exhibits anisotropic mechanochromic responses as enabled by magnetic alignment. More specifically, we observe the maximum slope at 45°, and when α deviates from this angle, the slope decays to a negligible value (**Figure 3.11g**). The dependence on α can be predicted by the first derivative of the longitudinal excitation in **Figure 3.11b**, indicating the general applicability of the mechanochromic film for stress sensing. By utilizing the nonlinear dependence of colorimetric response on α, we prepared a film with programmable mechanochromic responses to stress. Differential chromatic responses could be produced by patterning cAuNRs with different orientations within the film. In the specific example shown in **Figure 3.11h**, cAuNRs were magnetically aligned vertically (90°) in the red stars, and 45° in other parts to the stretching direction. During stretching, the change of extinction (ΔE) of cAuNRs in the red stars was negligible, while in other areas, ΔE gradually increased with strains, resulting in enhanced longitudinal plasmonic excitation and a complementary blue color. Therefore, the plasmonic film exhibited a changing contrast as the strain increased, providing a highly sensitive and vivid colorimetric response.

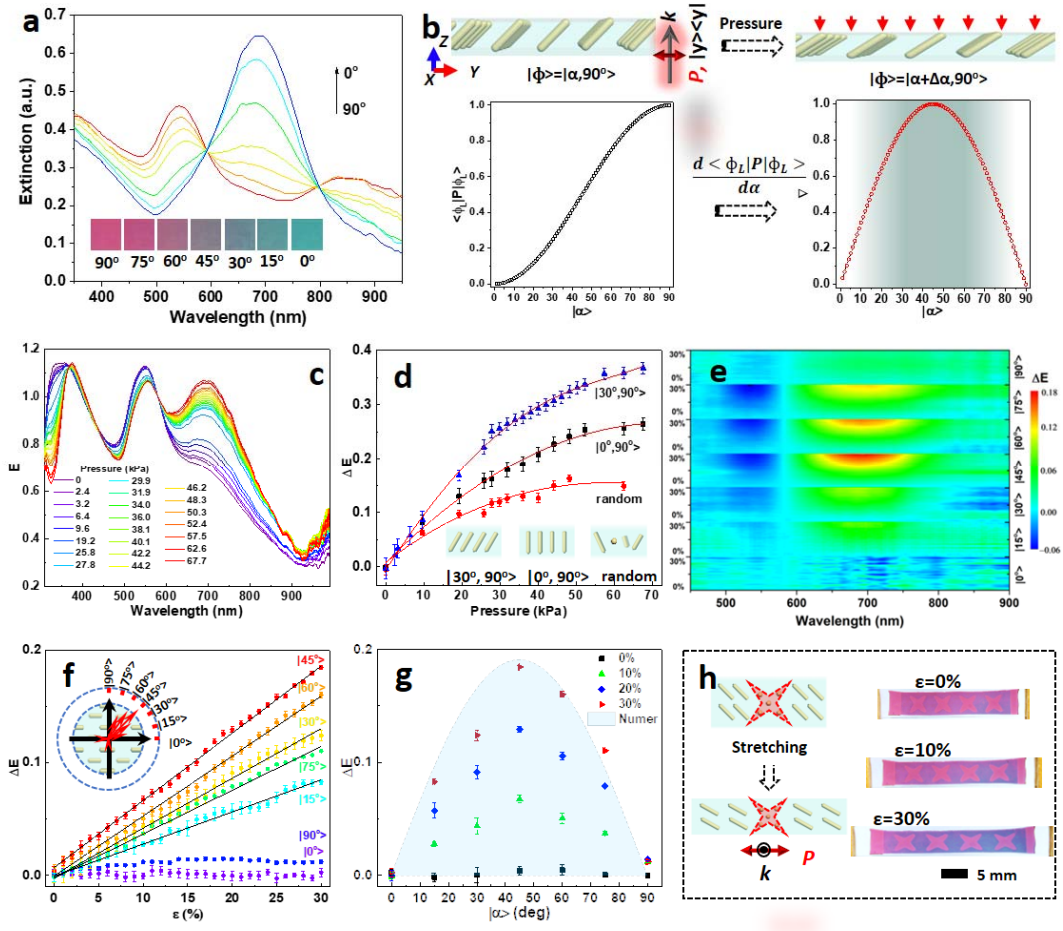

Figure 3.11. Programming the mechanochromic response by magnetic alignment. (a) Extinction spectra of plasmonic film at different rotational angles. Insert shows its corresponding colors. (b) The design principles of mechanochromic response of plasmonic films upon pressing and stretching. (c) Extinction spectra of the plasmonic films under different pressures with cAuNRs aligned along 30° to the surface normal. (d) Intensity changes of longitudinal modes when the plasmonic films were subject to different pressures. (e) Color contour of intensity changes of the film extinction (ΔE) upon stretching. The stretching angle (labeled on the right y-axis), α, is defined as the angle between

stretching directions and the long axes of cAuNRs collectively aligned inside the films. (f) Summary of intensity changes of cAuNRs under different strains. Arrows in inset indicate the slopes of mechanochromic response. (g) Anisotropic mechanochromic response of the plasmonic films enabled by magnetic alignment. (h) Orientation-dependent mechanochromic response of plasmonic films enabled by magnetically aligning cAuNRs along pre-designated directions.

In addition to simple pressing and stretching, we further demonstrate the versatility of the magnetic alignment approach for preparing mechanochromic devices with programmable colorimetric responses to linear rotation, bending, and nonlinear twisting. **Figure 3.12a** illustrates the alignment of cAuNRs along 45° out of plasmonic films, notated as |45°, 90°> under y-polarization. When the film was rotated by 45°, the orientation of cAuNRs became 0°. Consequently, the films turned to red as only the transverse mode of cAuNRs was excited (**Figure 3.12b**). At -45°, the plasmonic excitation of cAuNRs transited to |90°, 90°>. The complementary green color of the longitudinal mode was observed in the films. To confirm the predicted plasmon modes against rotation, we measured the extinction spectra at various rotation angles. As α increased, transverse extinction was enhanced while longitudinal excitation was suppressed. The relative extinction was derived and plotted against the transverse mode angle (ϕ_T) in **Figure 3.12c**, which further confirms the trigonometric prediction of the bra-ket theorem. An excellent agreement was also found between the derived ϕ_T-α correlation from experiments and theoretical prediction, which explicitly demonstrated the linear nature of rotation.

In contrast to uniform color changes upon rotating, bending induced different colors at the two ends of the film due to the separation of the excitation states. For example, bending the film by 45° downwards realigned cAuNRs into vertical, |0°, 90°>, and horizontal, |90°, 90°>, orientations, which further induced selective transverse (left end) and longitudinal (right end) excitation correspondingly and exerted uniform red and green colors at the two ends (**Figure 3.12d**).

By comparing rotating and bending, a critical principle became clear: symmetry-breaking along the active axis of mechanical perturbations induces separation of plasmon modes of cAuNRs during that motion . In order to verify this hypothesis, we have constructed a three-dimensional model with cAuNRs aligned 45^{o} within the films (top-view in **Figure 3.12e**). For both left- and right-handed helices formed upon 540^{o} twisting, the aligned cAuNRs were re-configured into a helical form (**Figure 3.12f**). Our further interpretation of the twisting perturbation revealed that the helical configuration was induced by localized rotation effect. More specifically, twisting the film along its long axis implied localized rotational perturbations with a continuously increased rotating angle (γ), which can be visualized by configuring the three-dimensional orientation of representative rods (highlighted by the red dashed rectangle in **Figure 3.12e**). The rods tend to rotate around y-axis by the twisting perturbation. In this case, whereas the angle between their orientation and y-axis remained at 45^{o}, γ varied as a function of positions, whose dependence can be described as $\omega * y/L$, where ω is the twisting angles, y is the coordinates of one arbitrary position in the films, and L represents their total length.

The alignment of cAuNRs was achieved by applying magnetic fields at the designated angle followed by UV fixation. The successful alignment was evidenced by the uniform red and green color across the films under perpendicular and parallel polarization, respectively (**Figure 3.12g**). When the film was twisted, its initial uniform color turned into alternating red and green segments. Due to the symmetric orientation of cAuNRs against the x-y plane, the same changes of plasmon modes were observed during left-handed and right-handed twisting, thus inducing a handedness-independent

mechanochromic response. When the polarizer was rotated by 90^{o} in the x-y plane, the initial colors of the twisted film turned to the opposite ones. To understand the intrinsic dependence of optical properties on twisting, we measured the space-resolved extinction spectra of twisted films, whose transverse mode was extracted. The resulted extinction-local rotation correlation was plotted in **Figure 3.12h**. The plasmon resonance of cAuNRs gradually switched from longitudinal mode to transverse mode as the twisting propagated from 0^{o} to 180^{o} inside the helical film. The helical configuration of cAuNRs was evidenced by the appearance of significant circular dichroism (CD) signals in **Figure 3.12i**, and further confirmed by the localized surface electric fields excited at 800 nm and Poynting vectors excited at 630 nm, which represented the strength of longitudinal and transverse resonance, respectively (**Figure 3.12j**). We examined the quantitative correlation of γ-ϕ_T from two independently measured quantities, the y-coordinates of the films and the transverse extinction and found that such dependence could be well predicted by the theoretical calibration curve . During each 180^{o} twisting, one node was formed, which separated two regions with orthogonally aligned cAuNRs as evidenced by the clear color contrast. More importantly, twisting exerted nonlinear perturbations to the excitation states of cAuNRs as the dependence of transverse mode angle (ϕ_T) on local rotation angle (γ) was nonlinear.

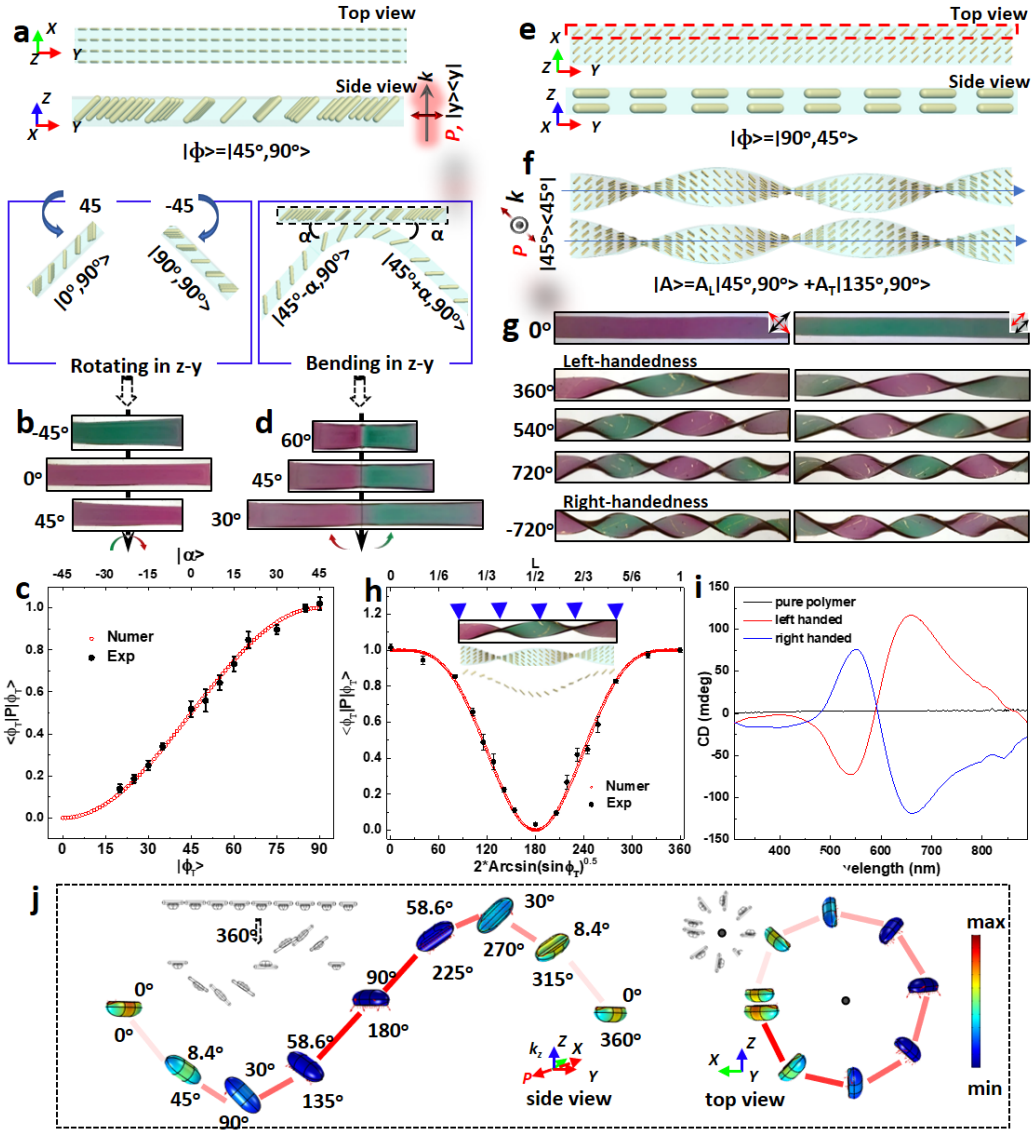

Figure 3.12. Motion-active plasmonic films. (a) Schematics of the specific arrangement of cAuNRs in the plasmonic film. (b) Top views of the plasmonic films under different rotation angles. (c) The transverse excitation of cAuNRs under different transverse phase angles (ϕ_T). (d) Top views of the plasmonic films under different bending angles. (e) Schematics showing the in-plane 45° arrangement of cAuNRs inside the plasmonic film at top (top) and side view (bottom). (f) Schematics of left-handed twist (top) and right-handed

twist states (bottom). The twisting angle is set at 540°. (g) Digital images of the plasmonic film at initial (top panel), left-handed (middle panel) and right-handed twisting states (bottom panel). The polarization direction and orientation of cAuNRs are illustrated by red and black arrows correspondingly. (h) Dependence of transverse excitation on localized rotation angle and y-coordinates by analyzing the superposition of intensity of transverse and longitudinal resonances to the overall lineshape. Insets: a picture of the twisted plasmonic film and the helical configuration of cAuNRs. (i) CD spectra of pure polymer and plasmonic films under twisted configuration. (j) Electric filed distribution (at 800 nm) and Poynting vectors (at 630 nm), *S*, on the surface of cAuNRs under a twisted configuration. In the side view, the numbers under and above the cAuNRs are γ and ϕ_T, respectively. The arrows and colors indicate the strength of transverse and longitudinal modes, respectively.

More complex colorimetric responses to mechanical motions can be programmed by patterning differently aligned cAuNRs at different locations of the films. As shown in **Figure 3.13a**, the alignment of cAuNRs in the rhombus and background regions was 45° to the top and 45° to the bottom, respectively. Primary gray/brown was observed as both transverse and longitudinal modes were excited in the two regions. When the film was rotated left-hand to 30° and 45°, the rhombus area turned blue, and the background appeared red. Interestingly, the colors switched when the film was rotated to -30° and -45°. The plasmonic excitation of cAuNRs in the two regions diverged from each other as rotation increased, thereby exhibiting the pre-designed images with high contrast. In the case of bending (**Figure 3.13b**), the asymmetric mechanochromic response was observed in the regions separated by the bending axis due to the opposite effect of bending to the plasmonic excitation of cAuNRs with the same orientation in the two regions. Thanks to its solution processability, the fabrication can be easily scaled up to produce centimeter-sized films with programmable mechanochromic responses to bending and rotating.

We further demonstrate the versatility of the system by constructing a mechanochromic film with readable and asymmetric colorimetric responses to pressure change in an air chamber (**Fig, 3.13c**). The chamber was made by polysiloxane and glass, with the top opening sealed by a plasmonic film containing cAuNRs uniformly aligned 45° to the surface normal in a "butterfly" pattern. At ambient pressure, the flat film was gray as both transverse and longitudinal modes were excited (**Figure 3.13d**). When air was injected into the chamber, a positive pressure pushed the top layer outward and displayed an asymmetric colorimetric response in the two wings, showing blue on the left and red on the right. In

contrast, the color switched in the two wings under negative pressure when air was extracted from the chamber. While this device may find potential use as a simple colorimetric pressure indicator, more complex patterns can be designed based on the convenient magnetic alignment to provide readable colorimetric responses that allow qualitative estimation of the applied pressure.

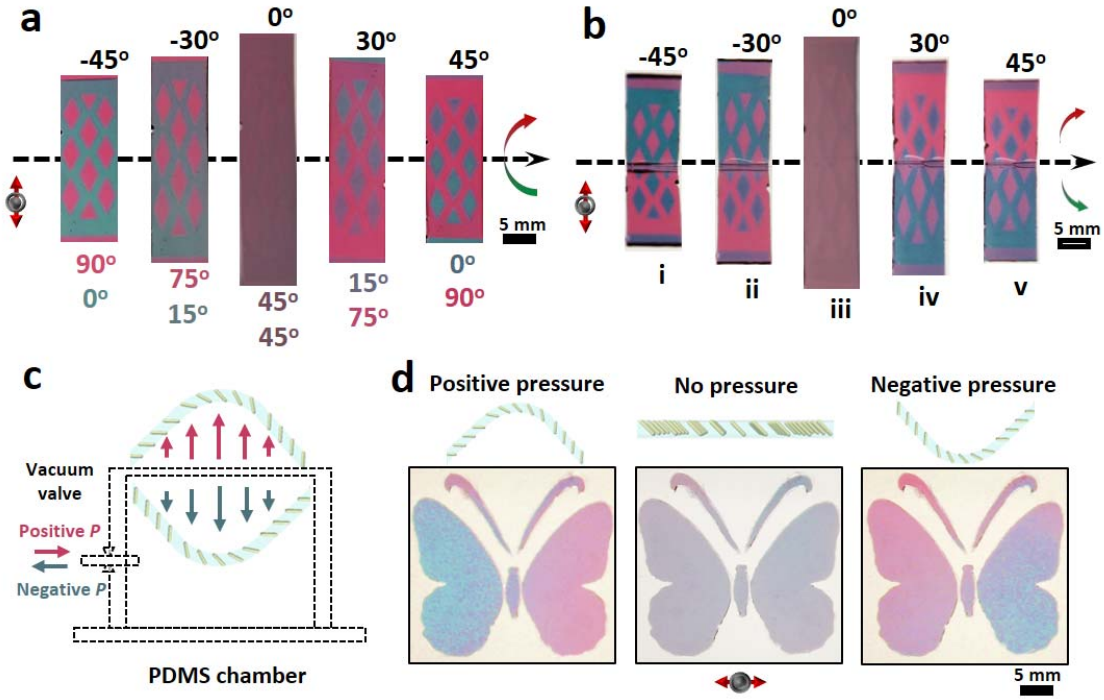

Figure 3.13. Mechanochromic devices. Top views of the plasmonic films under (a) rotation and (b) bending. The angles above the images are rotation angles. And, numbers below the images in (a) indicate the excitation angle of longitudinal modes (α) of cAuNRs imbedded in the regions with same colors. In (a), the plasmonic film was rotated in a left-handed manner. In (b), negative bending angle indicates bending backwards while positive angles indicate bending forwards. (c) The scheme of the mechanochromic devices. The top plasmonic film will expand upwards or downwards when subject to positive or negative pressures, respectively. (d) The cAuNRs were 45° aligned to the surface normal in the butterfly patterns (middle panel). When subject to pressure, the film exhibited different colors in the two wings of the butterfly due to the excitation of different plasmon modes of cAuNRs.

3.5 Magnetically Tunable Plasmon Coupling of Au shells Enabled by Confined Growth in Deformable Shells

Resonant scattering of colloidal plasmonic particles induced by the localized surface plasmon resonance (LSPR) has recently attracted ever-increasing attention in a variety of applications, including flexible transparent displays, optical metasurfaces, smart windows, wearable electronics and color holograms.[92-98] These applications rely on the sharp and strong resonance of plasmonic structures that can efficiently scatter light of a particular wavelength while being "transparent" at off-resonance wavelength. As the plasmonic properties of metallic nanostructures are highly dependent on the size, morphology, anisotropy and the chemical surrounding, lots of research efforts have been exerted on exploiting plasmonic structures with large scattering cross-sections and tailorable resonant wavelengths.[80, 99-100] It has been recognized in earlier studies that large plasmonic nanospheres, particularly of Au and Ag, have scattering-dominant LSPR, whose resonant wavelength can be tuned from visible to near-infrared (NIR) regions by simply increasing the particle size.[101-102] However, since the LSPR of metallic particles decreases with greater depths, the scattering cross-sections and atomic scattering efficiency of large particles decrease significantly. For example, the skin depth of plasmonic structures of Au was estimated to be only tens of nanometers, resulting in low plasmonic activities of inner Au atoms and the associated low scattering efficiency.

Compared with solid nanospheres, previous theoretical studies have predicted that plasmonic shells of Ag coated on dielectric cores have much higher scattering efficiency

and wavelength selectivity in plasmonic resonance.[92-93] Unfortunately, their further advancement to practical applications is highly limited by the poor chemical and structural stability of Ag particles against changeable chemical environments.[42, 103] In addition, Ag plasmonic nanostructures are also quite lossy in the visible spectrum due to their strong LSPR-induced absorption, which causes significant decay of transparency. Compared with Ag, plasmonic shells of Au have similar scattering properties but much better colloidal stabilities and higher tolerance of environmental perturbation.[21, 42] The challenge of practical implementation, however, lies in large-scale production of high-quality Au shells with tunable resonant scattering while exhibiting considerably low absorption away from the resonance. A conventional approach is to directly grow Au shells on organic or inorganic cores that are firstly immobilized with small seeds.[104-105] Although the Au shells with tunable optical properties were produced, these existing methods are still facing critical challenges when advancing to practical applications. For example, the free growth of multiple grains in seeded growth usually produces thick Au shell with poor control over thickness.[40, 105] To form complete Au shell, multi-step seeded growth was required, which hinders reproducibility of synthesis and large-scale production.[106] Also, the as-prepared Au shells are typically formed by the fusion of individual large Au grains, resulting in poor optical properties as evidenced by the coupling-induced broadband absorption in most literature reports,[10, 106-108] which adds additional limitations on fully exploiting the potentials of Au shells in resonant scattering-based applications.

By simply increasing the core size, their scattering can be tuned from visible to NIR regions with tailorable scattering and absorption. Instead of the direct seeded growth methods as

reported elsewhere, a soft, deformable and highly permeable polymer shell is employed to mediate and confine the seeded growth of metallic Au within the hard-soft interface between magnetic core and polymer coating into well-defined shell structures. In general, the solid magnetic core similarly acts as a support to the deposition of Au atoms as normally occurred in conventional seeded growth. The key point in this method lies in the deformable features of polymer shells, which enables the growth of Au without the need for creating a pre-designed limiting space or gap in templated synthesis. While the elasticity of polymer shells suppresses the deposition of Au atoms along the radical directions, their high deformability can afford enough spaces for the formation of complete metallic shells. This synthesis approach is general and robust to produce a variety of core-shell nanostructures independent of size, morphology, components and surface properties.

Our approach toward the active tuning over the scattering of Au shells is based on the fact that it can selectively scatter light at a particular wavelength due to the LSPR while being almost "transparent" at off-resonance wavelengths. As shown in **Figures 3.14a**, the resonant scattering of Au shells red-shifted from 590 nm to 980 nm when their core size increased from 20 to 70, 125 and 150 nm. Compared with solid nanoparticles of the same diameters (**Figure 3.14b**), they exhibit more remarkable scattering characteristics due to the increased electron scattering at the multiple interfaces and much broader tuning range due to hybridized plasmon in dielectric-metal core-shell structures.[109] On one hand, the low energy symmetric bonding plasmon band is very sensitive to the size of the metal shells and surroundings, giving rise to a remarkable shift in peak positions by simply increasing core sizes. On the other hand, the primary resonant scattering is far away from the strongest

resonant absorption in Au shell (**inset of Figure 3.14c**), which facilitates the scattering-based application and lowers optical loss at the resonant frequency by minimizing unexpected interference between the two plasmon bands. Also, the merit figure of resonant scattering, which is defined by the ratio between scattering efficiency and maximum absorption efficiency, of Au shell increases gradually as core sizes with a value greater than one in a broad spectrum. As shown in **Figure 3.14c**, the Au shell exhibits scattering-dominant plasmonic resonance when the core size reaches 30 nm. The arrows in the left panels in **Figure 3.14d** represent the surface scattering profiles of the Au shell, which indicates the strong scattering of Au shells around the entire surface. The electric field distribution (right panels in **Figure 3.14d**) indicates much lower magnitudes in Au shell with larger core size, further confirming its lower absorption at the on-resonance wavelength. In principle, the plasmonic shell of Au has tunable plasmonic resonance from visible to NIR regions, which can strongly scatter light at the resonant wavelength while maintaining considerably low absorption over the entire spectrum of interest.

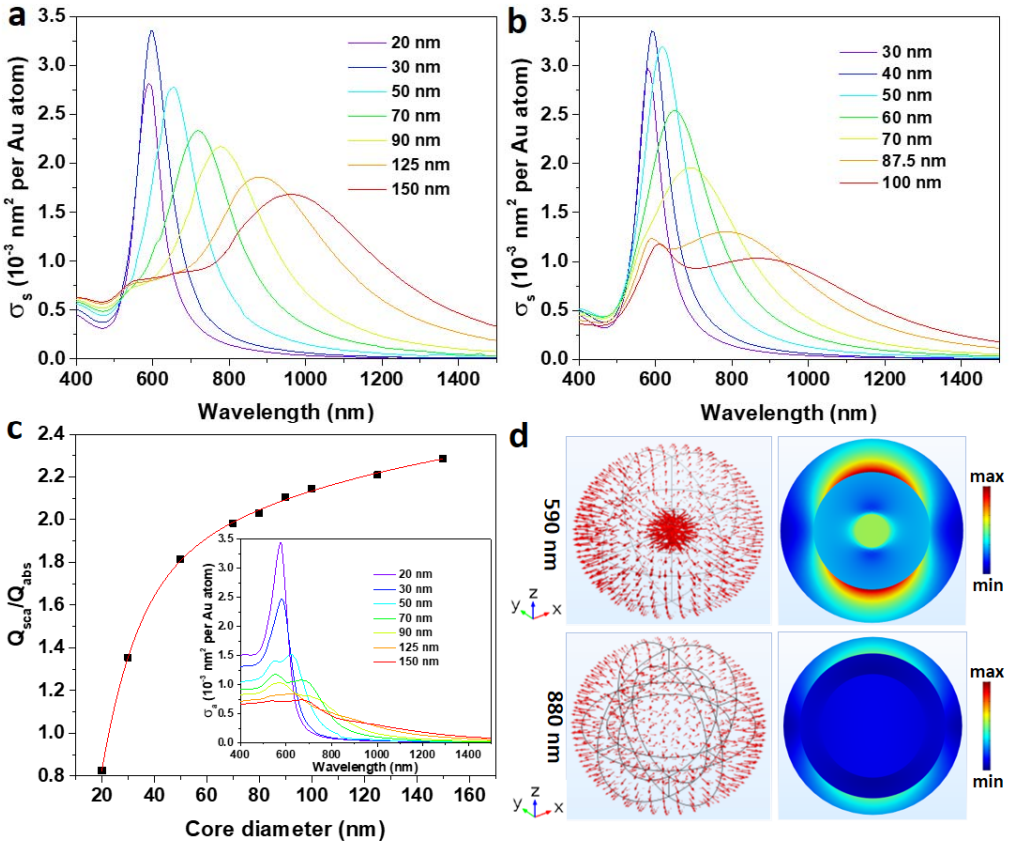

Figure 3.14. Concept design. Simulated atomic scattering cross sections of (a) Au shells and (b) Au nanoparticles with different diameters. The Au shells of 25 nm thickness were used for simulations. (c) Merit figure of scattering of Au shells. Inset: Simulated atomic absorption cross sections of Au shell. (d) Near-field electric field distribution (left) and Poynting vectors (right) of Au shell excited at the resonant wavelength.

The unconventional confined synthesis of Au shell on magnetic nanoparticles is depicted in **Figure 3.15a**. Magnetic particles of different sizes from 20 nm to 150 nm were first synthesized by previously reported methods.[29] A typical TME image of the synthesized colloidal nanocrystal clusters (CNCs) was shown in **Figure 3.15b** with uniform size (125 nm) and good dispersibility. They exhibited superparamagnetic properties due to the unique cluster feature and small magnetic grain size.[29] Based on electrostatic interaction, branched polyethylenimine (PEI) was modified on PAA-capped CNCs surface by simply mixing them at ambient condition, which was confirmed by a significant change in zeta-potential of Fe_3O_4 nanoparticles from -70 mV to +90 mV. Then, negatively charged Au nanoparticles (~2 nm) were immobilized on the surface of CNCs by electrostatic adsorption, which serves as seeds for further deposition of Au atoms. Afterward, highly permeable and soft phenolic resins were coated based on based-catalyzed step-growth polymerization of resorcinol and formaldehyde (RF) at elevated temperature, which functions as confining shell to modulate the seeded growth of Au shell.[110] A typical TEM image of Fe_3O_4/Aus@RF is shown in **Figure 3.15c** and the thickness of RF is 30 nm. Notably, the small Au seeds are randomly distributed inside RF shells without any noticeable aggregation.

During the seeded growth of Au shell, the key point is the homogeneous deposition of reduced Au to multiple seeds while maintaining the reaction at a reasonably slow reduction rate to minimize self-nucleation. Previous studies have demonstrated that reaction kinetics of seeded growth of Au nanostructures could be effectively reduced by adding strong coordinating anions of metal precursors in the growth solution. In general, the formed metal

complex has a lower reduction potential compared with the initial precursor salt, thus regulating the overall reaction in a more controllable manner. However, these coordinating anions are also good etchant to less stable metal crystals, particularly small seeds, thus inducing Ostwald ripening through first oxidative etching of seeds under the presence of dissolved oxygen and then selective deposition of Au atoms into larger ones. The oxidative etching has been well established by previous studies and is found to play key roles in breaking the growth symmetry of anisotropic noble-metal nanostructures by etching away less stable shape impurities.[39, 111-112] Also, our previous studies revealed that Ostwald ripening enables selective deposition of Au atoms to one particular seed inside a well-defined gap and is critical to producing high-crystallinity Au nanorods by templated synthesis. This strategy is, however, not applicable to the seeded growth of Au shells due to the undesirable etching of homogeneously distributed seeds. Therefore, when KI as a strong coordinating agent of Au^{3+} was involved in seeded growth, we observed irregular large Au crystals located randomly at the core-shell interfaces in the control experiment. Instead of the coordination chemistry, an alternative approach towards minimizing self-nucleation is to find a mild reducing agent, which is "strong" enough to overcome the elastic potential of deformed RF shell during seeded growth. To this end, we report the use of H_2O_2 as a reliable reductant to support the seeded growth of Au shell while maintaining the whole reaction free of self-nucleation. H_2O_2 has been found of great importance in the formation of Ag nanoplates by removing less stable non-twinned seeds.[16] In a more general sense, its powerful oxidizing strength has been well recognized with pH-dependent standard potential: 1.763 V in acidic solution and 0.867 V in alkaline solution.[16, 113]

Therefore, to get rid of etching of Au seeds by H_2O_2, the pH of the growth solution needs to be adjusted to slight above 7 by adding sodium oleate. Under this scenario, H_2O_2 has lower reduction potential than $AuCl_4^-$ (+0.93 V) and the Au seeds can remain stable for further deposition of reduced Au atoms onto multiple sites. Considering the slight difference in the reduction potentials, H_2O_2 may also help to minimize self-nucleation by etching away unstable free Au monomers. In addition to an oxidant, previous studies have also revealed the reductant role of H_2O_2 in alkaline condition due to the formation of anion HO_2^-, which has a standard reduction potential of +0.08 V.[113-114] The weak reducing power of H_2O_2 could afford a slow deposition of Au atoms to the multiple seeds, which potentially facilitates the formation of uniform and smooth shell structures. More importantly, by harnessing the oxidative etching/reducing equilibrium of H_2O_2, we could achieve exclusively deposition of Au toms to multiples seeds without noticeable Ostwald ripening and self-nucleation. Overall, the seeded growth of Au shell in alkaline conditions occurs in the following course:

$$H_2O_2 + OH^- = HO_2^- + H_2O \quad (5)$$

$$3HO_2^- + AuCl_4^- = Au + 3HO_2\cdot + 4Cl^- \quad (6)$$

The morphology of the Au shell after seeded growth was shown in **Figure 3.15d**. A complete coating of Au with a thickness of ~ 25 nm was observed at the interface between Fe_3O_4 core and soft RF shell. It is worth noting that the thickness of the RF shell decreased from an initial 35 nm to 18 nm during seeded growth, clearly demonstrating the expansion

caused by continuous deposition of Au atoms. It remains as an intact shell even under the surface strain of approximate 20%, which further confirms the good elasticity of RF shell.

The growth of the Au shell was companied by a gradual change in the optical properties as revealed in the real-time extinction spectra (**Figure 3.15e**). Within 1 min, one plasmon band appeared at 810 nm, indicating the start of Au shell formation as metallic shell structures have lower resonant frequency compared with solid particles. As the reaction preceded, the band first red- and then blue-shifted to 880 nm, which is consistent with the growth process from thin to thick Au shell. Notably, another plasmon peak appeared at 675 nm in addition to the initial plasmon band at 545 nm. The calculated spectra indicate that the plasmon band at 810 nm originated from the strong scattering of the Au shells while the two located at shorter wavelengths have dominant resonant absorption. When Fe_3O_4 of 20 nm was used as the core, we observed a continuous redshift of a single plasmon band from 525 to 600 nm (**Figure 3.15f**). The absence of the plasmon band at 530 nm suggests the high yield of Au shells without obvious exitance of spheres.

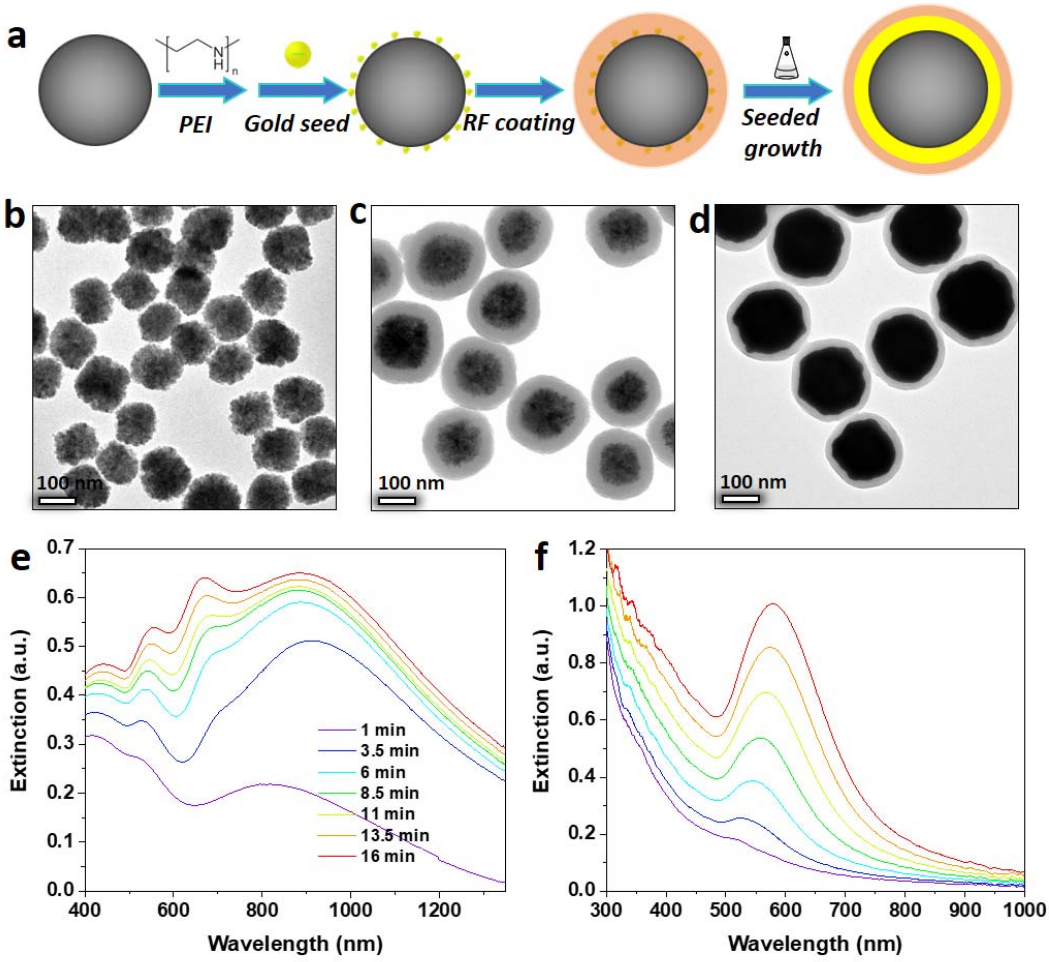

Figure 3.15. Confined growth of Au shells at the hard Fe_3O_4 and deformable polymer interfaces. (a) Schematic illustration of the seed-mediated growth of Au shells on CNCs. TEM images of (b) CNC, (c) CNC/Aus@RF and (d) CNC@Au@RF nanospheres. Evolution of plasmonic peaks during seeded growth of Au shells on **(e)** 125 nm and **(f)** 20 nm Fe_3O_4 as cores.

This unique method can be readily extended for synthesizing Au shells with different inner diameters from 20 to 70, 125 and finally 150 nm. The Fe_3O_4@Au@RF is shown in TEM images in **Figure 3.16a to 3.16d**. After seeded growth, the initial magnetic cores are fully covered by Au, thus suggesting the formation of a conformal Au shell outside the cores. The diameter of particles within the RF shell increased from 60 to 110, 165 and 200 nm from **Figure 3.16a to 3.16d**, indicating shell thickness of 20, 20, 20 and 25 nm, respectively. In their extinction spectra (**Figure 3.16e**), we observed a redshift of the hybridized bonding plasmon band from 585 to 730, 875 and 960 nm.[115] Accordingly, the colors of the colloidal dispersion of the Au shells changed from blue to green and brown, which could be accurately predicted by the complementary color of the maximum extinction wavelength. Besides, the measured extinction profile of Au shell is consistent with the simulated spectra of Au shells in **Figure 3.16g**, further confirming the high-quality and well-defined plasmonic properties.

Given the specific requirements of surface properties in plasmonic-based applications, particularly in biosensing, imaging, and SERS, we developed a reliable way to etch away the cross-linked RF layer while maintaining the well-defined plasmonic properties of Au shell. This was achieved by incubating Fe_3O_4@Au@RF colloidal particles in a high-concentration NaOH solution at elevated temperature. As shown in **Figure 3.16h**, the plasmon band of Au shell with 20 nm core blue-shifted from 585 to 540 nm because the refractive index of the surrounding environment decreased from ca. 1.5 of RF to 1.33 of water. Notably, the peak became sharper without any appearance of new plasmon bands, indicating that RF was completely removed, and Au remained as an intact shell with good

dispersibility. The colloidal solution turned from blue to red during etching, which was in good agreement with the measured peak shift (**inset in Figure 3.16h**). Due to the presence of the magnetic core, the Fe_3O_4@Au particles could be magnetically separated from the solution as indicated by the concentration gradient in the inset of **Figure 3.16h**. Similarly, we observed a blueshift from 730 to 685 nm in the plasmon band of Au shell with a core of 70 nm when RF was removed (**Figure 3.16i**). Under bright background, the perceived color in the colloidal dispersion was complementary to the plasmonic extinction and therefore the color turned from green to light blue (left two panels in the inset of **Figure 3.16i**). Conversely, both the solutions before and after removing RF shell appeared red under dark background (right two panels in **Figure 3.16i**), which is ascribed to their strong scattering of red light between 622 and 770 nm.

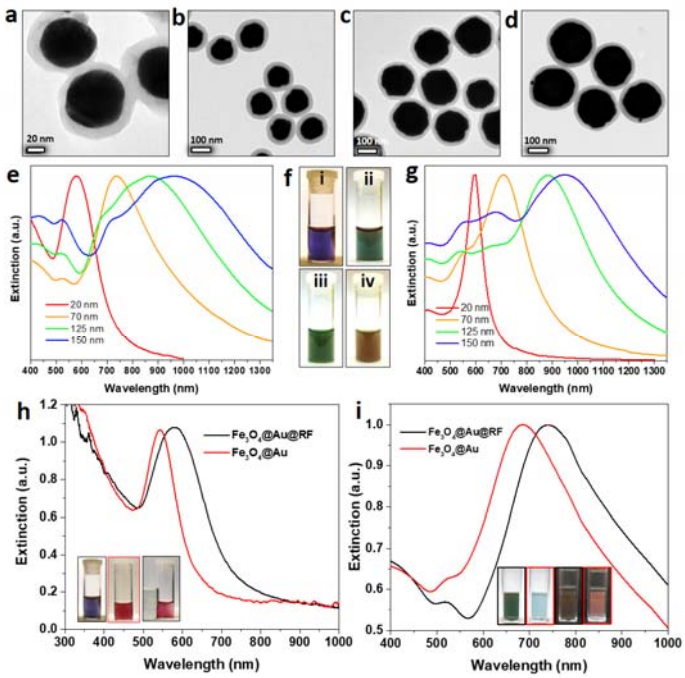

Figure 3.16. Tailorable resonant scattering of Au shells. TEM images of Fe_3O_4@Au@RF nanospheres synthesized by using CNCs with diameter of (a) 20 nm, (b) 70 nm, (c) 125 nm and (d) 150 nm as core materials. The UV-Vis spectra of Fe_3O_4@Au@RF nanospheres with different core diameters based on (e) experimental measurement and (g) simulation. f) Digital pictures of colloidal dispersion of Fe_3O_4@Au@RF nanospheres with core diameter of (i) 20 nm, (ii) 70 nm, (iii) 125 nm and (iv) 150 nm. UV-Vis spectra of as-synthesized Au shell before and after etching away RF. The diameters of CNCs in (h) and (i) are 20 nm and 70 nm, respectively. Inset images in (h) from left to right: Fe_3O_4@Au@RF, Fe_3O_4@Au and Fe_3O_4@Au solution exposed to a magnetic field. Inset images in (i): solutions of Fe_3O_4@Au@RF and Fe_3O_4@Au under bright and dark fields. The Au shell thickness from (a) to (d): 20 nm, 25 nm, 20 nm and 25 nm.

To take advantage of the strong scattering of the Au shells, we first prepared transparent display by incorporating Au shells into PVA films. Their scattering properties were first investigated by finite element analysis. As shown in **Figure 3.17a**, the peak position of the measured spectra of Fe_3O_4@Au with 70 nm core agrees well with the calculated cross-section. The slight discrepancy at off-resonance wavelength is probably due to the broad-band absorption of iron oxides. The calculated cross-sections confirm that the resonant scattering of Au shells is much stronger than the absorption, thus confirming that Au shells are ideal for transparent displays as they only scatter light at a particular wavelength while maintaining "transparent" elsewhere. Under p-mode (**Figure 3.17b**), we observed a similar scattering pattern as the Lambertian distribution of an ideal diffusely reflecting surface. In the case of s-mode, however, the scattering occurred in a broader scope, indicating that the scattering of the Au shell can be viewed from a wide-angle. The Poynting vectors and localized electric field distribution are shown in **Figure 3.17c**, which further confirms the wide-angle scattering of Au shells. To incorporate Au shells into a transparent polymer matrix, 10% weight of PVA aqueous solution was added into Au shell dispersion with a final concentration of ~ 0.005 mg/mL. The mixture was spin-casted on a PDMS film and left at the ambient condition to remove bubbles and dry out (**Figure 3.17d**). The digital picture of the film shown in **Figure 3.17e** indicates the high transparency of the fabricated film as the details of behind landscape could be observed with only slight changes in their appearance color and brightness. In **Figure 3.17f**, a transparent film was shown at work with red letters projected on the screen. The projected image showed up clearly and can be viewed from all directions. Conversely, the pure polymer film without Au shell appeared

dark and the image can barely be observed under the same laser projector due to the lack of scattering (**Figure 3.17g**).

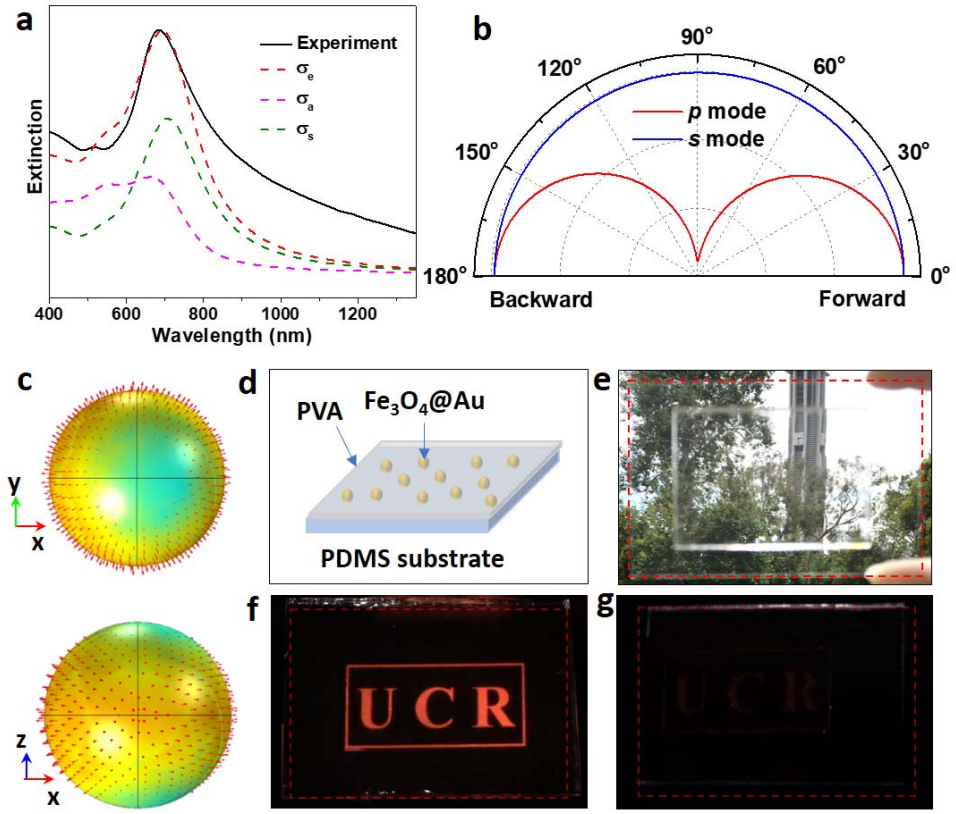

Figure 3.17. Resonant scattering of single Au shell. (a) Optical properties of Au shells prepared by using 70 nm CNCs as cores. (b) Polar plot showing the angular distribution of scattered light of Au shells at 738 nm under *p*- and *s*-mode excitation. (c) The corresponding surface Poynting vector and electric field distribution of Au shells. (d) The fabrication of PVA/Au composite film for transparent displays. (e) Photograph of fabricated film under natural light. Photographs showing the transparent displays made of (f) PVA/Au composite film and (g) pure PVA film .

Relying on the coupled magnetic and plasmonic properties of core-shell structures, we then proposed a new scheme for active tuning of the plasmon coupling of Au shells by the magnetic assembly of Fe_3O_4@Au@RF into 1D nanochains. We first calculated the optical cross-sections of the assembled chains under different interparticle separations and orientations by the finite element method. As shown in **Figure 3.18a**, the extinction spectra of plasmonic chains containing Au shells with 50-nm core reveals a redshift of the coupling band from 690 to 750 nm as the interparticle separation decreases from 40 to 5 nm. Meanwhile, we observe a great increase in the enhancement of localized electric fields inside the gaps, which confirms the coupling between neighboring Au shells (**Figure 3.18b**). More explicitly, there is a 90-times enhancement of electric fields within the gap of 40 nm, which approaches about 400-times within the 5-nm gaps. Such filed enhancement represents an anisotropic plasmon coupling of Au shells within 1D chains, whose strength is highly dependent on the polarization of incident light. As confirmed in **Figure 3.18c**, the intensity of coupling peaks at 695 nm for an interparticle separation of 30 nm decreases when the angles between chain orientation and polarization changes from 0° to 90°. Notably, the plasmon band at 535 nm only shifts slightly due to the overlap with the coupling band, indicating that this band is from the resonance of Au shells rather than the coupling effect. Under the excitation of polarized light at 695 nm, we observe a strong coupling between Au shells at 0° and then a gradual attenuation of coupling strength when the polarization switches to 90° (**Figure 3.18d**). To verify the plasmonic coupling of Au shells, we measured the extinction spectra of Fe_3O_4@Au@RF under different magnetic fields. It was found that the peak position of coupling bands could be well controlled by

the strength of magnetic fields: continuous redshift caused by the reduced interparticle separation as strength increases (**Figure 3.18e**). Such the coupling-induced redshift is consistent with the well-documented literature that is focused on the assembly of plasmonic nanospheres, particularly of Au and Ag.[7, 116-118] In our system, for the first time, we demonstrated that the plasmon coupling of Au shells within 1D plasmon chains could be readily tuned by magnetically aligning the chains along different directions. As shown in **Figure 3.18f**, the coupling peak reached the maximum value when a parallel magnetic field to the polarization of incident light (0^o) was applied. Gradual increasing the angle gave rise to weak coupling strength and hence the reduced peak intensity of the coupling band at 700 nm. As a result, the colloidal dispersion of Au shells under different magnetic fields exhibited slightly different colors (**insets in Figure 3.18f**).

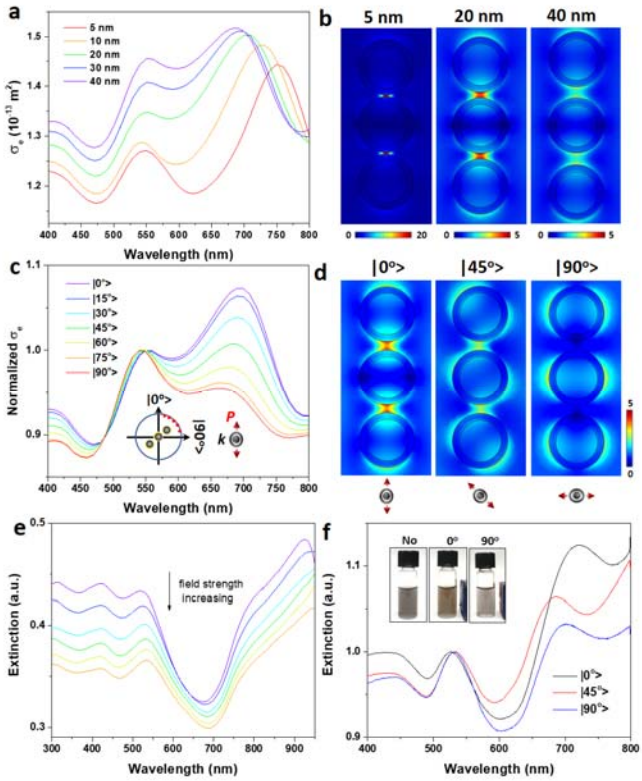

Figure 3.18. Plasmonic coupling of Au shells enabled by magnetic assembly of Fe_3O_4@Au into plasmonic chains. (a) Simulated extinction spectra of the plasmonic chain under different particle separation. (b) The corresponding localized electric field distribution at separation of 5 nm, 20 nm and 40 nm. The excitation wavelength from left to right is 750, 710 and 690 nm, respectively. (c) Simulated extinction spectra of plasmonic chain under different orientations. The interparticle separation was set to be 30 nm. (d) The localized electric field distribution of plasmonic chains under orientations of 0°, 45° and 90°. (e) Measured extinction spectra of plasmonic chains under different field strength. (f) Measured extinction spectra of the plasmonic chains under different orientations. Inset: digital pictures of the colloidal dispersion under different magnetic fields.

The magnetically tunable plasmon coupling of Au shells affords a reliable way to actively regulate the coupled resonant scattering of Au shells. As shown in the optical microscopic images in **Figure 3.19a**, we only observed bright dots due to the scattering of individual particles under the absence of magnetic fields. When a magnetic field was applied, however, 1D chain-like structures formed with parallel alignment to the field direction. 1D chains with bright red color formed immediately when a magnetic field parallel to light polarization was applied. The extremely fast response is ascribed to high magnetic saturation of CNCs, which were fully investigated in our previous studies.[29, 119-120] When magnetic fields were removed, the chains disassembled into individual particles due to strong electrostatic repulsion originating from the abundant surface charges of RF shells, which enables the reversible and dynamic tuning of the plasmonic coupling of Au shells. Interestingly, it was found that the apparent color of the 1D chains was dependent on their orientations under linearly polarized light. When the orientation of the chain was parallel to the polarization of light, a bright and uniform red color was observed in the 1D structures. Under the other two perpendicular orientations, however, they turned from red to pale yellow. To further confirm the physical origin of the color, we carried out control experiments by using Fe_3O_4/Aus@RF before seeded growth as building blocks. Conversely, as shown in **Figure 3.19b**, no obvious color was observed under three typical orientations. It is, therefore, reasonable to conclude that the perceived colors of 1D chains under polarized light is originating from the resonant scattering of the coupled plasmonic Au shells.

On one hand, compared with the previous methods for active tuning of resonant scattering of plasmonic nanostructures, such as changing the surrounding dielectrics by chemical and electronic doping,[94, 121] the magnetic assembly approach has much faster response and is fully reversible. On the other hand, the coupled magnetic and plasmonic properties of 1D plasmonic chains facilitate the control over the orientation of the assemblies, which enables a variety of plasmonic-based applications, particularly for those that are not attainable by conventional plasmonic assemblies. As schematically shown in **Figure 3.19c,** it is realized by combining lithography of photocurable polymer with the magnetic assembly of Au shells. Fe_3O_4@Au@RF was first dispersed in the EG solution of acrylamide and then sandwiched between a glass coverslip and a glass slide to form a thin liquid film. A photomask with a pre-designed pattern was placed atop the sample, followed by applying a magnetic field (B_1). After the first UV exposure, 1D plasmonic chains with parallel alignment to external fields were fixed in the uncovered areas. The photomask was then removed, and the second UV was applied to polymerize the remaining parts of the film under a horizontal magnetic field (B_2). **Figure 3.19d** displays the optical microscopic images of the as-prepared films under different polarization conditions. These images accentuate the alignment of plasmonic chains at the boundary (dashed lines) of horizontal (left) and vertical (right) orientations. Under a vertical polarizer, the right parts appeared red due to the coupling-induced resonant scattering of Au shells within the chains while the left parts were brown. When rotating the polarizer to a horizontal position, we observed a color switch in the two regions. Moreover, the color contrast in the two regions disappeared under 45^o or no polarizer as the excitation of the plasmonic resonance in 1D

chains was the same in both cases. **Figure 3.19e** and **3.19f** exhibit two patterns created by multiple lithography methods. Switching the polarization from horizontal to vertical directions reverses the observed patterns while almost no contrast is observed under 45^{o} polarization.

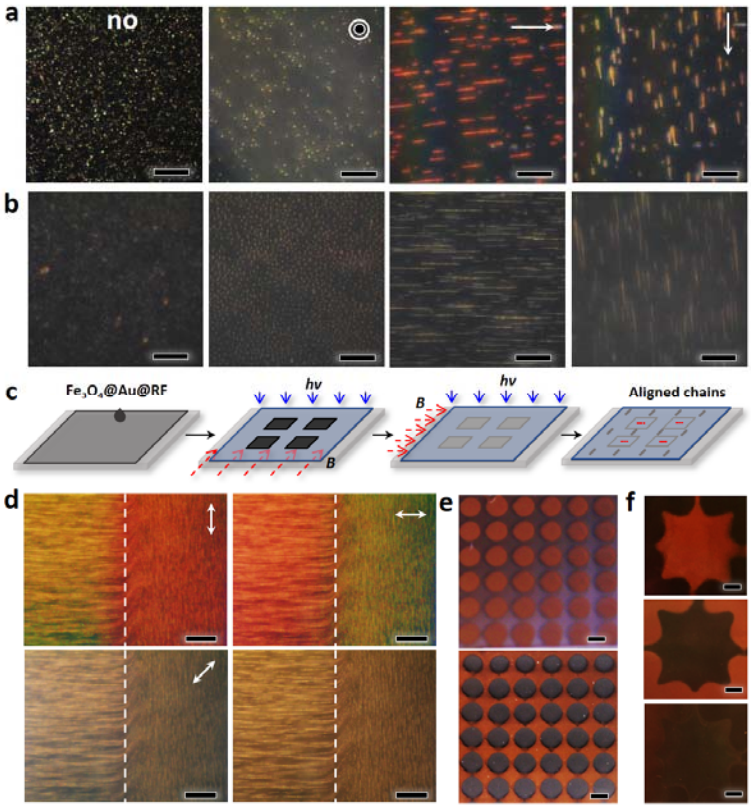

Figure 3.19. Coupled resonant scattering of Au shells enabled by magnetic assembly of Fe_3O_4@Au into plasmonic chains. (a) Polarized optical macroscopic (POM) images of Fe_3O_4@Au@RF under different magnetic fields. (b) POM images of Fe_3O_4/Aus@RF under different magnetic fields. (c) Schematic illustration of the lithography process for the fabrication of thin films with different chain orientations. (d) Normal and polarized optical macroscopic images of boundary areas with horizontal (left regions) and vertical (right regions) plasmonic nanochains. (e) Digital pictures of pattern I under horizontal (top) and vertical polarization (bottom). (f) Digital images of pattern II under horizontal (top), vertical (middle) and 45° polarization (bottom). Scale bars: (a), (b) and (d) 10 μm; (e) and (f) 500 μm.

3.6 Conclusion

In summary, an unconventional templated synthesis of hybrid magnetic-plasmonic nanorods were developed here. By confining the seeded growth of Au within the well-defined gap between inside magnetic nanorods and outside permeable polymer shells, rather than a central cavity as commonly being created against colloidal templates in conventional templated synthesis, this method not only shares the advantages of conventional template synthesis, such as robust, cost-effective and scalable production of metallic nanostructures, but also provides additional degree of freedoms to tailor the structures and physical properties of the hybrid nanostructures. The presence of magnetic nanorods within RF shells created unique concavity at the surface of Au nanorods, whose curvature and dimension were easily tuned by the size of FeOOH nanorods and the silica thickness. These concave Au nanorods are far from thermodynamic equilibrium but favored by the reduction kinetics during seeded growth due to the presence of high-energy facets, shape edges and crystal defects. Such surface cavity exerted negligible influence on the classic transverse plasmon band but surprisingly produced another structure-dependent transverse cavity band at long wavelength. Our simulation results further revealed that the plasmonic resonance of the cavity band was localized at the surface concavity with dominant scattering effects. The thermodynamic instability and structure-dependent plasmonic properties of cAuNRs afford us an ideal model to investigate the reconstruction dynamics and kinetics of Au nanostructures under mild and controllable conditions, which is rarely reported in previous research in contrast to the case of Ag as Au is generally more stable against physical and chemical stimuli. The as-prepared Au nanorods with energetic

surface concavity and associated novel localized cavity plasmonic resonance are expected to provide new opportunities in high-performance catalysts, high-sensitive chemical, thermal and biological sensors. More importantly, the unconventional templated synthesis and "backward" aging method may pave new ways for discovering new materials with integrated functionalities and structural diversities, particularly the ones that are not attainable by conventional templated methods or ligand-directed colloidal synthesis.

Second, we have developed novel mechanochromic films with well-controllable colorimetric responses towards linear and nonlinear mechanical motions and deformations by magnetically aligning the magnetic-plasmonic hybrid nanorods along pre-designed directions within polymer films. The asymmetric alignment of anisotropic plasmonic nanostructures about the active axis of external mechanical stimuli induces the excitation of different resonance modes, enabling readable color changes. The incorporation of hybrid nanostructures and their magnetic alignment are compatible with the current fabrication processes of soft actuators, robots, and biomimetic systems. In addition, the contactless, fast and reversible magnetic interactions allow colloidal nanoparticles to be efficiently aligned and patterned in polymer matrices, making them potentially useful for various applications, such as displays, sensors and actuators, anti-counterfeiting devices, and biomimetic systems with simultaneous shape and color changes

In the last part, we have developed an unconventional synthesis approach toward plasmonic shells by confining the seeded growth of Au within the hard-soft interfaces between Fe_3O_4 core and a deformable polymer shell. The growth of Au shell does not require limiting gap

or space but rather relies on the elastic deformation of cross-linked RF shell. It is found that H_2O_2 plays a key role in controlling the reduction kinetics to minimizing the self-nucleation of Au while maintaining the smooth Au deposition to the multiple seeds by avoiding the use of coordinating anions and the Ostwald ripening in the growth solution. The as-prepared Au shells have well-defined plasmon bands, which can be readily tuned from visible to NIR regions simply by increasing the core sizes. The synthesis represents an alternative method for preparing Au shells with uniform morphology, well-controlled optical properties and can be potentially extended for synthesizing other plasmonic shell structures. Relying on the well-defined, highly tailorable optical properties of the Au shells, we then prepared transparent display based on their resonant scattering in a simple and cost-effective way. In the last part, we have proposed a new approach to actively tune the resonant scattering of coupled Au shells by the magnetic assembly of Fe_3O_4@Au@RF into plasmonic chains. Compared with previous reports on active plasmonics, magnetic assembly has several advantages, including instantaneous response, remote control, and fully reversible tuning. Therefore, it is expected that this unique synthesis and convenient tuning of plasmonic coupling via magnetic fields can enable many plasmonic-based applications.

3.7 References

1. Hentschel, M.; Schäferling, M.; Duan, X.; Giessen, H.; Liu, N., Chiral plasmonics. *Science advances* **2017,** *3* (5), e1602735.

2. Jiang, N.; Zhuo, X.; Wang, J., Active plasmonics: principles, structures, and applications. *Chem. Rev.* **2017,** *118* (6), 3054-3099.

3. Kristensen, A.; Yang, J. K.; Bozhevolnyi, S. I.; Link, S.; Nordlander, P.; Halas, N. J.; Mortensen, N. A., Plasmonic colour generation. *Nature Reviews Materials* **2017,** *2* (1), 16088.

4. Stewart, M. E.; Anderton, C. R.; Thompson, L. B.; Maria, J.; Gray, S. K.; Rogers, J. A.; Nuzzo, R. G., Nanostructured plasmonic sensors. *Chem. Rev.* **2008,** *108* (2), 494-521.

5. Han, X.; Liu, Y.; Yin, Y., Colorimetric stress memory sensor based on disassembly of gold nanoparticle chains. *Nano Lett.* **2014,** *14* (5), 2466-2470.

6. Brongersma, M. L.; Halas, N. J.; Nordlander, P., Plasmon-induced hot carrier science and technology. *Nat. Nanotechnol.* **2015,** *10* (1), 25.

7. Liu, L.; Gao, Z.; Jiang, B.; Bai, Y.; Wang, W.; Yin, Y., Reversible assembly and dynamic plasmonic tuning of Ag nanoparticles enabled by limited ligand protection. *Nano Lett.* **2018,** *18* (8), 5312-5318.

8. Feng, J.; Yang, F.; Wang, X.; Lyu, F.; Li, Z.; Yin, Y., Self-Aligned Anisotropic Plasmonic Nanostructures. *Adv. Mater.* **2019**, 1900789.

9. Lee, K.-S.; El-Sayed, M. A., Gold and silver nanoparticles in sensing and imaging: sensitivity of plasmon response to size, shape, and metal composition. *The Journal of Physical Chemistry B* **2006,** *110* (39), 19220-19225.

10. Li, Z.; Yin, S.; Cheng, L.; Yang, K.; Li, Y.; Liu, Z., Magnetic targeting enhanced theranostic strategy based on multimodal imaging for selective ablation of cancer. *Adv. Funct. Mater.* **2014,** *24* (16), 2312-2321.

11. Wiley, B.; Sun, Y.; Mayers, B.; Xia, Y., Shape-controlled synthesis of metal nanostructures: the case of silver. *Chemistry–A European Journal* **2005,** *11* (2), 454-463.

12. Skrabalak, S. E.; Chen, J.; Sun, Y.; Lu, X.; Au, L.; Cobley, C. M.; Xia, Y., Gold nanocages: synthesis, properties, and applications. *Acc. Chem. Res.* **2008,** *41* (12), 1587-1595.

13. Wiley, B.; Sun, Y.; Xia, Y., Synthesis of silver nanostructures with controlled shapes and properties. *Acc. Chem. Res.* **2007,** *40* (10), 1067-1076.

14. Sun, Y.; Xia, Y., Shape-controlled synthesis of gold and silver nanoparticles. *Science* **2002,** *298* (5601), 2176-2179.

15. Sun, Y.; Gates, B.; Mayers, B.; Xia, Y., Crystalline silver nanowires by soft solution processing. *Nano Lett.* **2002,** *2* (2), 165-168.

16. Zhang, Q.; Li, N.; Goebl, J.; Lu, Z.; Yin, Y., A systematic study of the synthesis of silver nanoplates: is citrate a "magic" reagent? *J. Am. Chem. Soc.* **2011,** *133* (46), 18931-18939.

17. Zhou, Y.; Yu, S. H.; Wang, C. Y.; Li, X. G.; Zhu, Y. R.; Chen, Z. Y., A novel ultraviolet irradiation photoreduction technique for the preparation of single-crystal Ag nanorods and Ag dendrites. *Adv. Mater.* **1999,** *11* (10), 850-852.

18. Xia, Y.; Yang, P.; Sun, Y.; Wu, Y.; Mayers, B.; Gates, B.; Yin, Y.; Kim, F.; Yan, H., One-dimensional nanostructures: synthesis, characterization, and applications. *Adv. Mater.* **2003,** *15* (5), 353-389.

19. Brolo, A. G., Plasmonics for future biosensors. *Nat. Photon.* **2012,** *6* (11), 709.

20. Mulvihill, M. J.; Ling, X. Y.; Henzie, J.; Yang, P., Anisotropic etching of silver nanoparticles for plasmonic structures capable of single-particle SERS. *J. Am. Chem. Soc.* **2009,** *132* (1), 268-274.

21. Zhang, Q.; Ge, J.; Pham, T.; Goebl, J.; Hu, Y.; Lu, Z.; Yin, Y., Reconstruction of silver nanoplates by UV irradiation: tailored optical properties and enhanced stability. *Angew. Chem. Int. Ed.* **2009,** *48* (19), 3516-3519.

22. Zhang, S.; Zhang, L.; Liu, K.; Liu, M.; Yin, Y.; Gao, C., Digestive ripening in the formation of monodisperse silver nanospheres. *Materials Chemistry Frontiers* **2018,** *2* (7), 1328-1333.

23. Link, S.; Burda, C.; Mohamed, M.; Nikoobakht, B.; El-Sayed, M. A., Laser photothermal melting and fragmentation of gold nanorods: energy and laser pulse-width dependence. *The Journal of Physical Chemistry A* **1999,** *103* (9), 1165-1170.

24. Link, S.; Burda, C.; Nikoobakht, B.; El-Sayed, M. A., Laser-induced shape changes of colloidal gold nanorods using femtosecond and nanosecond laser pulses. *The Journal of Physical Chemistry B* **2000,** *104* (26), 6152-6163.

25. Zhang, J.; Langille, M. R.; Personick, M. L.; Zhang, K.; Li, S.; Mirkin, C. A., Concave cubic gold nanocrystals with high-index facets. *J. Am. Chem. Soc.* **2010,** *132* (40), 14012-14014.

26. Jin, M.; Zhang, H.; Xie, Z.; Xia, Y., Palladium concave nanocubes with high-index facets and their enhanced catalytic properties. *Angew. Chem. Int. Ed.* **2011,** *50* (34), 7850-7854.

27. Wang, X.; Vara, M.; Luo, M.; Huang, H.; Ruditskiy, A.; Park, J.; Bao, S.; Liu, J.; Howe, J.; Chi, M., Pd@ Pt core–shell concave decahedra: a class of catalysts for the oxygen reduction reaction with enhanced activity and durability. *J. Am. Chem. Soc.* **2015,** *137* (47), 15036-15042.

28. Gilroy, K. D.; Elnabawy, A. O.; Yang, T.-H.; Roling, L. T.; Howe, J.; Mavrikakis, M.; Xia, Y., Thermal stability of metal nanocrystals: An investigation of the surface and bulk reconstructions of Pd concave icosahedra. *Nano Lett.* **2017,** *17* (6), 3655-3661.

29. Ge, J.; Hu, Y.; Biasini, M.; Beyermann, W. P.; Yin, Y., Superparamagnetic magnetite colloidal nanocrystal clusters. *Angew. Chem. Int. Ed.* **2007,** *46* (23), 4342-4345.

30. Gao, C.; Zhang, Q.; Lu, Z.; Yin, Y., Templated synthesis of metal nanorods in silica nanotubes. *J. Am. Chem. Soc.* **2011,** *133* (49), 19706-19709.

31. Finkelstein, N.; Hancock, R. D., A new approach to the chemistry of gold. *Gold Bulletin* **1974,** *7* (3), 72-77.

32. Wang, X.; Wang, C.; Cheng, L.; Lee, S.-T.; Liu, Z., Noble metal coated single-walled carbon nanotubes for applications in surface enhanced Raman scattering imaging and photothermal therapy. *J. Am. Chem. Soc.* **2012,** *134* (17), 7414-7422.

33. Li, T.; Cao, M.; Liang, J.; Xie, X.; Du, G., Mechanism of Base-Catalyzed Resorcinol-Formaldehyde and Phenol-Resorcinol-Formaldehyde Condensation Reactions: A Theoretical Study. *Polymers* **2017,** *9* (9), 426.

34. Zhang, G.; Ni, C.; Liu, L.; Zhao, G.; Fina, F.; Irvine, J. T., Macro-mesoporous resorcinol–formaldehyde polymer resins as amorphous metal-free visible light photocatalysts. *J. Mater. Chem. A* **2015,** *3* (30), 15413-15419.

35. Gao, C.; Lu, Z.; Liu, Y.; Zhang, Q.; Chi, M.; Cheng, Q.; Yin, Y., Highly stable silver nanoplates for surface plasmon resonance biosensing. *Angew. Chem. Int. Ed.* **2012,** *51* (23), 5629-5633.

36. Yin, Y.; Alivisatos, A. P., Colloidal nanocrystal synthesis and the organic–inorganic interface. *Nature* **2004,** *437* (7059), 664.

37. Baghalha, M., The leaching kinetics of an oxide gold ore with iodide/iodine solutions. *Hydrometallurgy* **2012,** *113*, 42-50.

38. Qi, P.; Hiskey, J. B., Dissolution kinetics of gold in iodide solutions. *Hydrometallurgy* **1991,** *27* (1), 47-62.

39. Chen, L.; Ji, F.; Xu, Y.; He, L.; Mi, Y.; Bao, F.; Sun, B.; Zhang, X.; Zhang, Q., High-yield seedless synthesis of triangular gold nanoplates through oxidative etching. *Nano Lett.* **2014,** *14* (12), 7201-7206.

40. Wang, X.; Feng, J.; Yu, H.; Jin, Y.; Davidson, A.; Li, Z.; Yin, Y., Anisotropically shaped magnetic/plasmonic nanocomposites for information encryption and magnetic-field-direction sensing. *Research* **2018,** *2018*, 7527825.

41. Tang, Y.; Ouyang, M., Tailoring properties and functionalities of metal nanoparticles through crystallinity engineering. *Nature materials* **2007,** *6* (10), 754.

42. Gao, C.; Hu, Y.; Wang, M.; Chi, M.; Yin, Y., Fully alloyed Ag/Au nanospheres: combining the plasmonic property of Ag with the stability of Au. *J. Am. Chem. Soc.* **2014,** *136* (20), 7474-7479.

43. Zhang, Q.; Zhou, Y.; Villarreal, E.; Lin, Y.; Zou, S.; Wang, H., Faceted gold nanorods: nanocuboids, convex nanocuboids, and concave nanocuboids. *Nano Lett.* **2015,** *15* (6), 4161-4169.

44. An, J.; Tang, B.; Zheng, X.; Zhou, J.; Dong, F.; Xu, S.; Wang, Y.; Zhao, B.; Xu, W., Sculpturing effect of chloride ions in shape transformation from triangular to discal silver nanoplates. *The Journal of Physical Chemistry C* **2008,** *112* (39), 15176-15182.

45. Métraux, G. S.; Mirkin, C. A., Rapid thermal synthesis of silver nanoprisms with chemically tailorable thickness. *Adv. Mater.* **2005,** *17* (4), 412-415.

46. Jin, R.; Cao, Y. C.; Hao, E.; Métraux, G. S.; Schatz, G. C.; Mirkin, C. A., Controlling anisotropic nanoparticle growth through plasmon excitation. *Nature* **2003,** *425* (6957), 487.

47. Bin, D.-S.; Chi, Z.-X.; Li, Y.; Zhang, K.; Yang, X.; Sun, Y.-G.; Piao, J.-Y.; Cao, A.-M.; Wan, L.-J., Controlling the compositional chemistry in single nanoparticles for functional hollow carbon nanospheres. *J. Am. Chem. Soc.* **2017,** *139* (38), 13492-13498.

48. Tsung, C.-K.; Kou, X.; Shi, Q.; Zhang, J.; Yeung, M. H.; Wang, J.; Stucky, G. D., Selective shortening of single-crystalline gold nanorods by mild oxidation. *J. Am. Chem. Soc.* **2006,** *128* (16), 5352-5353.

49. Kim, F.; Song, J. H.; Yang, P., Photochemical synthesis of gold nanorods. *J. Am. Chem. Soc.* **2002,** *124* (48), 14316-14317.

50. Chan, E. P.; Walish, J. J.; Urbas, A. M.; Thomas, E. L., Mechanochromic photonic gels. *Adv. Mater.* **2013,** *25* (29), 3934-3947.

51. Ge, J.; Yin, Y., Responsive photonic crystals. *Angew. Chem. Int. Ed.* **2011,** *50* (7), 1492-1522.

52. Li, Z.; Yin, Y., Stimuli-Responsive Optical Nanomaterials. *Adv. Mater.* **2019**, 1807061.

53. Chi, Z.; Zhang, X.; Xu, B.; Zhou, X.; Ma, C.; Zhang, Y.; Liu, S.; Xu, J., Recent advances in organic mechanofluorochromic materials. *Chem. Soc. Rev.* **2012,** *41* (10), 3878-3896.

54. Kim, Y.; Yeom, B.; Arteaga, O.; Yoo, S. J.; Lee, S.-G.; Kim, J.-G.; Kotov, N. A., Reconfigurable chiroptical nanocomposites with chirality transfer from the macro-to the nanoscale. *Nature materials* **2016,** *15* (4), 461.

55. Millstone, J. E.; Park, S.; Shuford, K. L.; Qin, L.; Schatz, G. C.; Mirkin, C. A., Observation of a quadrupole plasmon mode for a colloidal solution of gold nanoprisms. *J. Am. Chem. Soc.* **2005,** *127* (15), 5312-5313.

56. Gramotnev, D. K.; Bozhevolnyi, S. I., Plasmonics beyond the diffraction limit. *Nature photonics* **2010,** *4* (2), 83-91.

57. Kristensen, A.; Yang, J. K.; Bozhevolnyi, S. I.; Link, S.; Nordlander, P.; Halas, N. J.; Mortensen, N. A., Plasmonic colour generation. *Nature Reviews Materials* **2016,** *2*, 16088.

58. Grigorenko, A.; Geim, A.; Gleeson, H.; Zhang, Y.; Firsov, A.; Khrushchev, I.; Petrovic, J., Nanofabricated media with negative permeability at visible frequencies. *Nature* **2005,** *438* (7066), 335-338.

59. Nicholls, L. H.; Rodríguez-Fortuño, F. J.; Nasir, M. E.; Córdova-Castro, R. M.; Olivier, N.; Wurtz, G. A.; Zayats, A. V., Ultrafast synthesis and switching of light polarization in nonlinear anisotropic metamaterials. *Nature Photonics* **2017,** *11*, 628.

60. Maity, S.; Wu, W.-C.; Xu, C.; Tracy, J. B.; Gundogdu, K.; Bochinski, J. R.; Clarke, L. I., Spatial temperature mapping within polymer nanocomposites undergoing ultrafast photothermal heating via gold nanorods. *Nanoscale* **2014,** *6* (24), 15236-15247.

61. Maity, S.; Wu, W.-C.; Tracy, J. B.; Clarke, L. I.; Bochinski, J. R., Nanoscale steady-state temperature gradients within polymer nanocomposites undergoing continuous-wave photothermal heating from gold nanorods. *Nanoscale* **2017,** *9* (32), 11605-11618.

62. Shen, Y.; Zhou, J.; Liu, T.; Tao, Y.; Jiang, R.; Liu, M.; Xiao, G.; Zhu, J.; Zhou, Z.-K.; Wang, X., Plasmonic gold mushroom arrays with refractive index sensing figures of merit approaching the theoretical limit. *Nature communications* **2013,** *4*, 2381.

63. Zhu, X.; Vannahme, C.; Højlund-Nielsen, E.; Mortensen, N. A.; Kristensen, A., Plasmonic colour laser printing. *Nature nanotechnology* **2016,** *11* (4), 325-329.

64. Wurtz, G. A.; Pollard, R.; Hendren, W.; Wiederrecht, G.; Gosztola, D.; Podolskiy, V.; Zayats, A. V., Designed ultrafast optical nonlinearity in a plasmonic nanorod metamaterial enhanced by nonlocality. *Nature nanotechnology* **2011,** *6* (2), 107-111.

65. Ellenbogen, T.; Seo, K.; Crozier, K. B., Chromatic plasmonic polarizers for active visible color filtering and polarimetry. *Nano Lett.* **2012,** *12* (2), 1026-1031.

66. Shafiei, F.; Wu, C.; Wu, Y.; Khanikaev, A. B.; Putzke, P.; Singh, A.; Li, X.; Shvets, G., Plasmonic nano-protractor based on polarization spectro-tomography. *Nature Photonics* **2013,** *7* (5), 367-372.

67. Shafiei, F.; Monticone, F.; Le, K. Q.; Liu, X.-X.; Hartsfield, T.; Alù, A.; Li, X., A subwavelength plasmonic metamolecule exhibiting magnetic-based optical Fano resonance. *Nature nanotechnology* **2013,** *8* (2), 95-99.

68. Yang, S.; Ni, X.; Yin, X.; Kante, B.; Zhang, P.; Zhu, J.; Wang, Y.; Zhang, X., Feedback-driven self-assembly of symmetry-breaking optical metamaterials in solution. *Nature nanotechnology* **2014,** *9* (12), 1002-1006.

69. Liu, Q.; Cui, Y.; Gardner, D.; Li, X.; He, S.; Smalyukh, I. I., Self-alignment of plasmonic gold nanorods in reconfigurable anisotropic fluids for tunable bulk metamaterial applications. *Nano Lett.* **2010,** *10* (4), 1347-1353.

70. Khatua, S.; Chang, W.-S.; Swanglap, P.; Olson, J.; Link, S., Active modulation of nanorod plasmons. *Nano Lett.* **2011,** *11* (9), 3797-3802.

71. Liu, Q.; Yuan, Y.; Smalyukh, I. I., Electrically and optically tunable plasmonic guest–host liquid crystals with long-range ordered nanoparticles. *Nano Lett.* **2014,** *14* (7), 4071-4077.

72. Franklin, D.; Chen, Y.; Vazquez-Guardado, A.; Modak, S.; Boroumand, J.; Xu, D.; Wu, S.-T.; Chanda, D., Polarization-independent actively tunable colour generation on imprinted plasmonic surfaces. *Nature communications* **2015,** *6*, 7337.

73. Zhang, Y.; Liu, Q.; Mundoor, H.; Yuan, Y.; Smalyukh, I. I., Metal nanoparticle dispersion, alignment, and assembly in nematic liquid crystals for applications in switchable plasmonic color filters and E-polarizers. *Acs Nano* **2015,** *9* (3), 3097-3108.

74. Dirix, Y.; Bastiaansen, C.; Caseri, W.; Smith, P., Oriented pearl-necklace arrays of metallic nanoparticles in polymers: A new route toward polarization-dependent color filters. *Adv. Mater.* **1999,** *11* (3), 223-227.

75. Wilson, O.; Wilson, G. J.; Mulvaney, P., Laser writing in polarized silver nanorod films. *Adv. Mater.* **2002,** *14* (13-14), 1000-1004.

76. de León, A. G.; Dirix, Y.; Staedler, Y.; Feldman, K.; Hähner, G.; Caseri, W. R.; Smith, P., Method for fabricating pixelated, multicolor polarizing films. *Appl. Opt.* **2000,** *39* (26), 4847-4851.

77. Jung, I.; Ih, S.; Yoo, H.; Hong, S.; Park, S., Fourier Transform Surface Plasmon Resonance of Nanodisks Embedded in Magnetic Nanorods. *Nano Lett.* **2018,** *18* (3), 1984-1992.

78. Jung, I.; Yoo, H.; Jang, H. J.; Cho, S.; Lee, K.; Hong, S.; Park, S., Fourier Transform Surface Plasmon Resonance (FTSPR) with Gyromagnetic Plasmonic Nanorods. *Angew. Chem.* **2018,** *130* (7), 1859-1863.

79. Wang, M.; Yin, Y., Magnetically responsive nanostructures with tunable optical properties. *J. Am. Chem. Soc.* **2016,** *138* (20), 6315-6323.

80. Wang, M.; Gao, C.; He, L.; Lu, Q.; Zhang, J.; Tang, C.; Zorba, S.; Yin, Y., Magnetic tuning of plasmonic excitation of gold nanorods. *J. Am. Chem. Soc.* **2013,** *135* (41), 15302-15305.

81. Zhang, M.; Magagnosc, D. J.; Liberal, I.; Yu, Y.; Yun, H.; Yang, H.; Wu, Y.; Guo, J.; Chen, W.; Shin, Y. J., High-strength magnetically switchable plasmonic nanorods assembled from a binary nanocrystal mixture. *Nature nanotechnology* **2017,** *12* (3), 228.

82. Jiang, N.; Zhuo, X.; Wang, J., Active Plasmonics: Principles, Structures, and Applications. *Chem. Rev.* **2017**.

83. Wang, M.; He, L.; Xu, W.; Wang, X.; Yin, Y., Magnetic assembly and field-tuning of ellipsoidal-nanoparticle-based colloidal photonic crystals. *Angew. Chem. Int. Ed.* **2015,** *54* (24), 7077-7081.

84. Piao, Y.; Kim, J.; Na, H. B.; Kim, D.; Baek, J. S.; Ko, M. K.; Lee, J. H.; Shokouhimehr, M.; Hyeon, T., Wrap–bake–peel process for nanostructural transformation

from β-FeOOH nanorods to biocompatible iron oxide nanocapsules. *Nature materials* **2008,** *7* (3), 242-247.

85. Xu, W.; Wang, M.; Li, Z.; Wang, X.; Wang, Y.; Xing, M.; Yin, Y., Chemical Transformation of Colloidal Nanostructures with Morphological Preservation by Surface-Protection with Capping Ligands. *Nano Lett.* **2017,** *17* (4), 2713-2718.

86. Li, N.; Zhang, Q.; Liu, J.; Joo, J.; Lee, A.; Gan, Y.; Yin, Y., Sol–gel coating of inorganic nanostructures with resorcinol–formaldehyde resin. *Chem. Commun.* **2013,** *49* (45), 5135-5137.

87. Fang, X.; Liu, S.; Zang, J.; Xu, C.; Zheng, M.-S.; Dong, Q.-F.; Sun, D.; Zheng, N., Precisely controlled resorcinol–formaldehyde resin coating for fabricating core–shell, hollow, and yolk–shell carbon nanostructures. *Nanoscale* **2013,** *5* (15), 6908-6916.

88. Pekala, R., Organic aerogels from the polycondensation of resorcinol with formaldehyde. *Journal of materials science* **1989,** *24* (9), 3221-3227.

89. Al-Muhtaseb, S. A.; Ritter, J. A., Preparation and properties of resorcinol–formaldehyde organic and carbon gels. *Adv. Mater.* **2003,** *15* (2), 101-114.

90. Zhang, Q.; Zhang, T.; Ge, J.; Yin, Y., Permeable silica shell through surface-protected etching. *Nano Lett.* **2008,** *8* (9), 2867-2871.

91. Gilroy, K. D.; Elnabawy, A. O.; Yang, T.-H.; Roling, L. T.; Howe, J.; Mavrikakis, M.; Xia, Y., Thermal Stability of Metal Nanocrystals: An Investigation of the Surface and Bulk Reconstructions of Pd Concave Icosahedra. *Nano Lett.* **2017**.

92. V. Besteiro, L.; Kong, X.-T.; Wang, Z.; Rosei, F.; Govorov, A. O., Plasmonic glasses and films based on alternative inexpensive materials for blocking infrared radiation. *Nano Lett.* **2018,** *18* (5), 3147-3156.

93. Hsu, C. W.; Zhen, B.; Qiu, W.; Shapira, O.; DeLacy, B. G.; Joannopoulos, J. D.; Soljačić, M., Transparent displays enabled by resonant nanoparticle scattering. *Nature communications* **2014,** *5*, 3152.

94. Peng, J.; Jeong, H.-H.; Lin, Q.; Cormier, S.; Liang, H.-L.; De Volder, M. F.; Vignolini, S.; Baumberg, J. J., Scalable electrochromic nanopixels using plasmonics. *Science advances* **2019,** *5* (5), eaaw2205.

95. Lal, S.; Link, S.; Halas, N. J., Nano-optics from sensing to waveguiding. *Nat. Photon.* **2007,** *1* (11), 641.

96. Byers, C. P.; Zhang, H.; Swearer, D. F.; Yorulmaz, M.; Hoener, B. S.; Huang, D.; Hoggard, A.; Chang, W.-S.; Mulvaney, P.; Ringe, E., From tunable core-shell nanoparticles to plasmonic drawbridges: Active control of nanoparticle optical properties. *Science advances* **2015,** *1* (11), e1500988.

97. Montelongo, Y.; Tenorio-Pearl, J. O.; Williams, C.; Zhang, S.; Milne, W. I.; Wilkinson, T. D., Plasmonic nanoparticle scattering for color holograms. *Proc. Natl. Acad. Sci* **2014,** *111* (35), 12679-12683.

98. Chen, T.; Reinhard, B. M., Assembling color on the nanoscale: multichromatic switchable pixels from plasmonic atoms and molecules. *Adv. Mater.* **2016,** *28* (18), 3522-3527.

99. Yang, D.; Pang, X.; He, Y.; Wang, Y.; Chen, G.; Wang, W.; Lin, Z., Precisely size-tunable magnetic/plasmonic core/shell nanoparticles with controlled optical properties. *Angew. Chem.* **2015,** *127* (41), 12259-12264.

100. Pang, X.; He, Y.; Jung, J.; Lin, Z., 1D nanocrystals with precisely controlled dimensions, compositions, and architectures. *Science* **2016,** *353* (6305), 1268-1272.

101. Gao, C.; Vuong, J.; Zhang, Q.; Liu, Y.; Yin, Y., One-step seeded growth of Au nanoparticles with widely tunable sizes. *Nanoscale* **2012,** *4* (9), 2875-2878.

102. Liu, X.; Yin, Y.; Gao, C., Size-tailored synthesis of silver quasi-nanospheres by kinetically controlled seeded growth. *Langmuir* **2013,** *29* (33), 10559-10565.

103. Jiang, X.; Zeng, Q.; Yu, A., Thiol-frozen shape evolution of triangular silver nanoplates. *Langmuir* **2007,** *23* (4), 2218-2223.

104. Brinson, B. E.; Lassiter, J. B.; Levin, C. S.; Bardhan, R.; Mirin, N.; Halas, N. J., Nanoshells made easy: improving Au layer growth on nanoparticle surfaces. *Langmuir* **2008,** *24* (24), 14166-14171.

105. Levin, C. S.; Hofmann, C.; Ali, T. A.; Kelly, A. T.; Morosan, E.; Nordlander, P.; Whitmire, K. H.; Halas, N. J., Magnetic− plasmonic core− shell nanoparticles. *ACS nano* **2009,** *3* (6), 1379-1388.

106. Zhang, Q.; Ge, J.; Goebl, J.; Hu, Y.; Sun, Y.; Yin, Y., Tailored synthesis of superparamagnetic gold nanoshells with tunable optical properties. *Adv. Mater.* **2010,** *22* (17), 1905-1909.

107. Kim, J.; Park, S.; Lee, J. E.; Jin, S. M.; Lee, J. H.; Lee, I. S.; Yang, I.; Kim, J. S.; Kim, S. K.; Cho, M. H., Designed fabrication of multifunctional magnetic gold nanoshells

and their application to magnetic resonance imaging and photothermal therapy. *Angew. Chem. Int. Ed.* **2006,** *45* (46), 7754-7758.

108. Shen, J.; Zhu, Y.; Yang, X.; Zong, J.; Li, C., Multifunctional Fe_3O_4@ Ag/SiO_2/Au core–shell microspheres as a novel SERS-activity label via long-range plasmon coupling. *Langmuir* **2012,** *29* (2), 690-695.

109. Jain, P. K.; El-Sayed, M. A., Universal scaling of plasmon coupling in metal nanostructures: extension from particle pairs to nanoshells. *Nano Lett.* **2007,** *7* (9), 2854-2858.

110. Liu, J.; Qiao, S. Z.; Liu, H.; Chen, J.; Orpe, A.; Zhao, D.; Lu, G. Q., Extension of the Stöber method to the preparation of monodisperse resorcinol–formaldehyde resin polymer and carbon spheres. *Angew. Chem. Int. Ed.* **2011,** *50* (26), 5947-5951.

111. Xiong, Y.; Chen, J.; Wiley, B.; Xia, Y.; Aloni, S.; Yin, Y., Understanding the role of oxidative etching in the polyol synthesis of Pd nanoparticles with uniform shape and size. *J. Am. Chem. Soc.* **2005,** *127* (20), 7332-7333.

112. Long, R.; Zhou, S.; Wiley, B. J.; Xiong, Y., Oxidative etching for controlled synthesis of metal nanocrystals: atomic addition and subtraction. *Chem. Soc. Rev.* **2014,** *43* (17), 6288-6310.

113. Yu, H.; Zhang, Q.; Liu, H.; Dahl, M.; Joo, J. B.; Li, N.; Wang, L.; Yin, Y., Thermal synthesis of silver nanoplates revisited: a modified photochemical process. *ACS nano* **2014,** *8* (10), 10252-10261.

114. Weiss, J., The catalytic decomposition of hydrogen peroxide on different metals. *Trans. Faraday Society* **1935,** *31*, 1547-1557.

115. Prodan, E.; Radloff, C.; Halas, N. J.; Nordlander, P., A hybridization model for the plasmon response of complex nanostructures. *Science* **2003,** *302* (5644), 419-422.

116. Lin, S.; Li, M.; Dujardin, E.; Girard, C.; Mann, S., One-dimensional plasmon coupling by facile self-assembly of gold nanoparticles into branched chain networks. *Adv. Mater.* **2005,** *17* (21), 2553-2559.

117. Sönnichsen, C.; Reinhard, B. M.; Liphardt, J.; Alivisatos, A. P., A molecular ruler based on plasmon coupling of single gold and silver nanoparticles. *Nat. Biotechnol.* **2005,** *23* (6), 741.

118. Jain, P. K.; Huang, W.; El-Sayed, M. A., On the universal scaling behavior of the distance decay of plasmon coupling in metal nanoparticle pairs: a plasmon ruler equation. *Nano Lett.* **2007,** *7* (7), 2080-2088.

119. Ge, J.; Hu, Y.; Yin, Y., Highly tunable superparamagnetic colloidal photonic crystals. *Angew. Chem. Int. Ed.* **2007,** *46* (39), 7428-7431.

120. Kim, H.; Ge, J.; Kim, J.; Choi, S.-e.; Lee, H.; Lee, H.; Park, W.; Yin, Y.; Kwon, S., Structural colour printing using a magnetically tunable and lithographically fixable photonic crystal. *Nat. Photon.* **2009,** *3* (9), 534.

121. Jiang, N.; Shao, L.; Wang, J., (Gold nanorod core)/(polyaniline shell) plasmonic switches with large plasmon shifts and modulation depths. *Adv. Mater.* **2014,** *26* (20), 3282-3289.

Chapter 4 Confined Growth of Fe_3O_4@Au Nanorods for Unconventional Background-free Bioimaging

4.1 Introduction

In contrast to the great success in the treatment of heart and cerebrovascular diseases or Pneumonia, we do not win in the war against cancer yet[1] as the mortality only decreases by 5.2% from 1950 to 2005 provided by NCHS, despite the intensive advancements in surgery and medication. Under this scenario, early-stage diagnosis is a still reliable way to survive in the fight, which is heavily based on imaging techniques. Recent progress in nanomedicine have provided promising imaging probes for cancer diagnoses, such as QDs,[2-3] magnetic,[4-5] plasmonic nanoparticles,[6-7] and UCNPs.[8-9] Their novel optical, magnetic, and electric properties have been intensively exploited in engineering nano agents for cancer theranostic.[10] The functionalities of nanoparticles in various imaging modalities, however, are suffering from the inherent limitations.[11] Optical imaging, for example, is well-known for high sensitivity, high spatial resolution, and multiple color capability but frequently questioned by the penetration issues of light (limited to millimeters). MRI features perfect tissue penetration by offering 3D tomography images but is not sensitive compared with optical imaging. One approach to overcome this limitation is engineering nanoparticles of different functionalities within small size for multimodality imaging. However, contrast agents in conventional integrated platforms passively form separate imaging modality without synergetic interference and active control over the imaging signals. Whereas they provide more diagnostic details by analyzing images acquired from different modalities, the suffering, like strong background

noises and poor delineation between tumor and normal tissues, still exists. In the case of magnetic-plasmonic contrast agents, like Fe_3O_4@Au core-shell nanoparticles, they offer both high-resolution MRI and highly sensitive PA imaging as reported in previous work.[12] But, most invariably, they cannot get rid of strong acoustic noises arising from the optical absorption of endogenous molecules in tissues, like hemoglobin and melanin.[13] Therefore, it is still desirable to develop next-generation coupled multimodality imaging platforms to simultaneously suppress background noises and enhance signal specificity through modulating imaging signals actively.

Engineering multifunctionalities within a nanometer scale is of long-lasting interests to the research areas of nanomedicine and biotechnology and has brought broad impacts in both the fundamental biology and clinic medications.[12, 14-16] By taking advantage of nanotechnology, various functional nanoparticles have been reported as molecular imaging probes or theranostic platform for the treatment of life-threatening diseases, such as cancer, with overwhelming advantages compared with conventional molecular form probes or drugs. The easy access to and on-demand programmable functionalities of various nanoscale probes, including magnetic nanoparticles (MNPs),[17] quantum dots (QDs),[2, 18] plasmonic nanoparticles and upconversion nanoparticles (UCNPs),[19-21] have promoted a broad spectrum of biomedical applications. Relying on their unique magnetic, optical or electric properties, ultrasensitive-detection, high resolution molecular imaging and synergistic theranostic are among the most promising advancements in biotechnology. For example, nano components with distinct properties can be integrated into multimodality imaging probes to overcome the limitations of each component. Optical imaging is well-

known for high sensitivity, high resolution, and capability of multi-color imaging but suffers significantly from limited penetration of light in living organisms.[22-24] Magnetic resonance imaging (MRI) features unlimited tissue penetration. It is, however, not as sensitive as optical imaging techniques.[25-27] By coupling magnetic nanoparticles with optical ones, like plasmonic, fluorescence or Raman, these concerns have been addressed to produce biological imaging probes, which provide unlimited tissue penetration while featuring high sensitivity and resolution. For example, Fe_3O_4@Au nanoparticles have been extensively exploited in multimodality imaging to enhance the signal specificity in tumors by high sensitive photoacoustic (PA) imaging and provide deep tissue physiological information by MRI.[28-29] However, conventional multimodality imaging probes most invariably form separate imaging mode by each component without any synergistic interference between integrated functionalities. One of the striking limitations is the significant unavoidable background noises, in forms of random optical scattering, auto-fluorescence or acoustic wave due to endogenous molecular absorption.[30-32] Therefore, developing next-generation multimodality probes is still of great challenges for not only enhancing the signal intensity of tumors or tissues by conventional imaging techniques but also suppressing the background noises by coupled functionalities that are not achievable from each component.

Background-free imaging represents one pioneering research attempt towards advanced imaging techniques. Each component of different functionalities serves as conventional imaging contrast agent but most importantly couple mutually for active modulation of signal intensities through external stimuli, like magnetic field or ultrasound.[33-34] Gao et al.

developed a coupled contrast agent for magnetomotive photoacoustic imaging based on Fe_3O_4@Au core/shell nanoparticles.[11] However, due to the small size of the Fe_3O_4 nanoparticles, they didn't have well-defined and tunable plasmonic resonance in NIR regions. It has also been shown that tuning the plasmonic absorption of small spherical nanostructures into NIR range is quite difficult as their plasmonic response is normally located in the visible range and scattering will dominate their extinction when the thickness of Au shell increases. Further advancement of these nanomaterials into in vivo or clinic background-free imaging is challenged by lack of versatile synthesis approaches toward multifunctional nanomaterials, limited tunability in their optical properties in terms of both peak positions and extinction, slow or irreversible response of optical properties and imaging signals to external stimuli.

In **Chapter 4**, we focus on background-free optical imaging in the two near-infrared (NIR) windows by using Fe_3O_4@Au nanorods. An unconventional polymer-confined, seeded growth method is used to prepare nanorods with desirable physical properties. It enables the confined growth of metal shells without the need of creating a space. More importantly, the confined growth occurs at the hard-soft interfaces between core and shell, enabling the precise control over the shell thickness and plasmonic properties of the core-shell nanorods. Therefore, we expect that this method can provide an efficient and robust way to produce high-quality core-shell structures. More specifically, in **Section 4.3**, by using this advanced confined growth method, we report the growth of thin Au shell on small Fe_3O_4 nanorods and use them as integrated contrast agent in photoacoustic imaging. On the basis of the magnetic modulation of the physical properties of nanorods and fast Fourier-transformed

(FFT) data processing, a background-free photoacoustic imaging is developed in the first tissue optical transparency window, referred as NIR-I located between 700 nm and 950 nm. In **Section 4.4**, we extend this novel imaging technique to background-free OCT imaging in the second tissue optical transparency window, referred to NIR-II located between 1000 nm and 1700 nm. In this section, the flexibility of this unique synthesis methodology is proved by producing thick Au shells with the scattering-dominated optical properties that is highly desired in OCT imaging.

4.2 Materials and Methods

Materials. All chemicals are used directly without further purification. Ethanol was purchased from Decon Labs. Iron chloride (III) hexahydrate, polyacrylic acid (PAA, MW=1800), sodium hydroxide, polyvinylpyrrolidone (PVP, MW=10000), resorcinol (R), formaldehyde (F) were bought from Sigma-Aldrich. Hydrogen peroxide (H_2O_2) was purchased from Fisher Scientific. Chloroauric (III) acid trihydrate ($HAuCl_4 \cdot 3H_2O$) was from Acros Organics. Oleic acid sodium salt (NaOL) was purchased from TCI AMERICA. 3-aminopropyl-triethoxysilane ($C_9H_{23}NO_3Si$, APTES) w purchased from Sigma-Aldrich. Ammonium hydroxide ($NH_3 \cdot H_2O$) and potassium iodide (KI) were purchased from Fisher Scientific. Ethylene glycol (EG) and diethylene glycol (DEG) was from Acros Organics.

Background-free PA imaging. In both the in vitro and in vivo imaging, imaging contrast agents, such as Au nanorods as control group and Fe_3O_4@Au nanorods as experimental group, were injected into a mouse or a biological tissue. Normal PA mode was acquired under the absence of a magnetic field. To actively modulate the PA signals from

Fe_3O_4@Au nanorods, external magnetic fields with direction parallel and perpendicular to light incidence were used to acquire deactivated and bright imaging mode, respectively.

Background-free OCT imaging. In both the ex vivo imaging, imaging contrast agents, such as FeOOH@Au nanorods as control group and Fe_3O_4@Au nanorods as experimental group, were injected into a chicken or pork tissue. Different imaging modes were acquired by using the same method as described in the background-free PA imaging.

Data processing: To remove the noises from background, pixel from deactivated imaging mode needs to be subtracted from pixel from bright mode. A background-free image is created by using the resulted pixel. In FFT-processed imaging, the pixel at the same imaging point is extracted from a time sequence of PA images and plotted against time. The time-domain plot is transformed into frequency-domain plot. By applying frequency threshold, background fluctuation is removed, leaving signal with periodic intensity in coherence with applied alternating magnetic fields. A background-free PA image is created. The date processing is achieved by coding in matlab.

4.3 Magnetically Modulated, FFT-processed Background-free PA Imaging

The unconventional seeded growth of ultrathin Au shell is depicted in **Figure 4.1a**, and we choose FeOOH nanorods with length of 110 nm (**Figure 4.1b**) as primary template because it can support strong LSPR at the two bioimaging windows while maintaining considerably small size. After being converted into Fe_3O_4 nanorods by surface-protected reduction, Cystamine is grafted on rod surface through Fe-amino coordination, which is further used for planting Au seeds through Au-S coordination. The TEM images in **Figure 4.1c** indicates homogeneous distribution of Au seeds (~2 nm). Then, a highly deformable phenolic resin is coated through based-catalyzed step-growth polymerization. A soft-hard RF-Fe_3O_4 interfaces forms, wrapping the Au seeds between conformal RF coating (~ 30 nm in **Figure 4.1d**) and oxides cores. Because of the excellent permeability and deformability of RF resins, we propose that it can sustain smooth, continuous deposition of Au atoms by using the confined growth method without the needs of creating confining spaces.

Smooth Au atom deposition on individual seed is critical to the growth of uniform Au shells of controllable thickness. Therefore, it requires delicate control over the reaction kinetics to get rid of self-nucleation. In conventional seeded growth, particular molecules are needed to coordinate with metal precursor, which slow down reactions by reducing the reduction potential. As the coordinating molecules simultaneously promote the oxidation of small seeds by forming more stable metal complex in classic Ostwald ripening, this method is not suitable for growing uniform Au shell. Instead, we maintain the reduction reaction at a considerable low rate by introducing a weak reducing agent, H_2O_2. Our

previous study has demonstrated that H_2O_2 has a standard reduction potential of +0.08 V under the presence of a weak base sodium oleate. In a typical reduction reaction, PVP is used as stabilizer, and the growth of Au shells takes 20 min. The growth intermediates at 10 min and 20 min were examined by TEM images in **Figures 4.1e** and **4.1f**, respectively. Thanks to the proper reaction condition, we observed homogeneous deposition of Au atoms to seeds without noticeable ripening and self-nucleation. At first few minutes, the size of Au gradually increases to a close contact, and the plasmon coupling between neighbouring Au domains induces broad-band absorption (extinction at 2.5 min in **Figure 4.1g**). Due to radical confinement of RF shells, at 15 min, we observed elongated growth of Au structures between the soft-hard interfaces of Fe_3O_4@RF, which fuses neighbouring Au to form single domain. These seeded growth and domain fusion are evidenced by the plasmon band appeared at long wavelength (**Figure 4.1g)**. As reduction reaction proceeds, this band gradually blueshifts to a final wavelength at 1300 nm, indicating formation of complete Au shell. The morphology of Fe_3O_4@Au@RF nanostructures is shown in TEM in **Figure 4.1f**. The cross-linked RF shells can be etched away by NaOH at elevated temperature while the Au shell can be well maintained. A TEM image of the obtained Fe_3O_4@Au rods indicates a ~9 nm conformal coating of Au outside low-contrast magnetic cores (**Figure 4.1h**). Due to decrease of refractive index of surrounding dielectrics from RF (n=1.65) to water (n=1.333), we observed a 50-nm blueshift of the longitudinal band from NIR-II to NIR-I biological imaging window (**Figure 4.1i**). Meanwhile, in the colloidal dispersion, the color changes from green to purple due to the blueshift of high-frequency plasmon band from 600 nm to 550 nm.

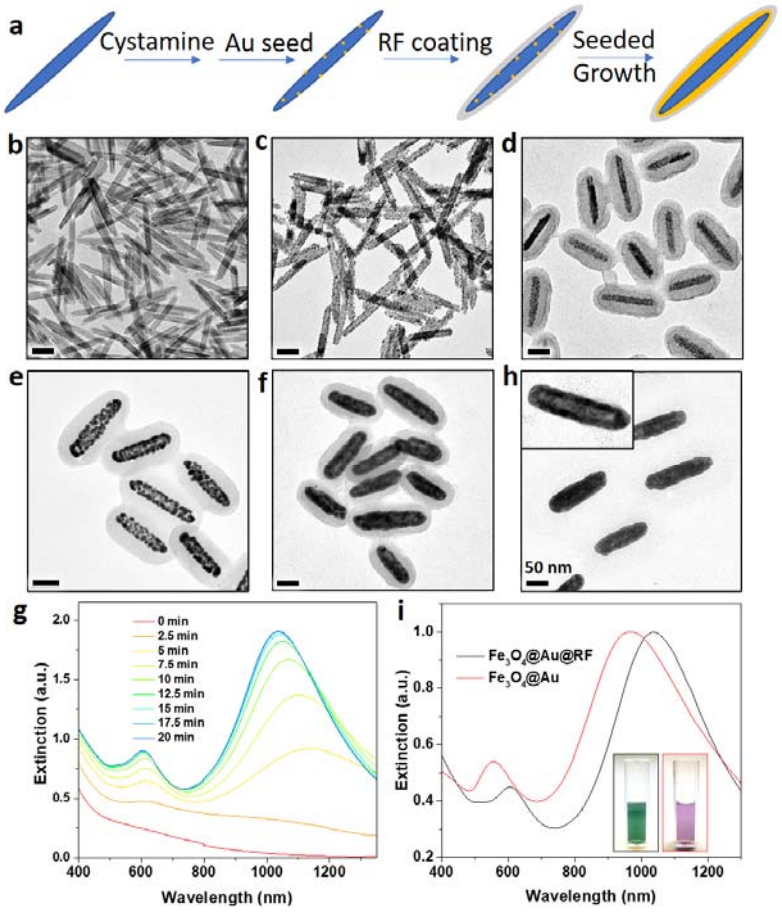

Figure 4.1. Synthesis of coupled PA contrast agent. (a), Schematic illustration of the seed-mediated growth of Au shell on Fe_3O_4 nanorods. (b-f), TEM images of (b) FeOOH, (c) Fe_3O_4/Aus, (d) Fe_3O_4/Aus@RF, Fe_3O_4/Aus@RF after seeded growth for (e) 10 min and (f) 20 min. (g) Real-time extinction spectra during seeded growth process. (h) TEM image of Fe_3O_4@Au nanorods. (i) Extinction spectra of coupled nanorods before and after etching away RF shells. Inset: Digital pictures of colloidal dispersions of Fe_3O_4@Au@RF (left) and Fe_3O_4@Au nanorods (right).

To confirm the radical confinement of RF shells, we examine the growth mode of Au on Fe_3O_4/Aus nanorods. As shown in **Figures 4.2a and 4.2b**, the deposition of Au atoms still occurs on multiple seeds but favors homogeneous growth on each seed. It thus produces isolated big Au particles of dozens of nanometers instead of fusing each domain. It could be possible to form conformal Au shell by further growth. In practical, it produces thick Au shells, rough surface, and scattering-dominated extinction. In another control experiment, we used conventional growth methods by adding coordinating reagent (KI) to the growth solution. After 10-min growth, the number of Au seeds at the soft-hard interfaces decreased and seeded growth preferentially occurred at few seeds (**Figures 4.2c and 4.2d**). These observations suggestion an Ostwald ripening, which etches away unstable seeds and favors growth on more stable ones. These experiments come to appreciate the critical role of RF shell: it confines the radical deposition of Au and thus locally regulates the seeded growth into an elongated mode at the soft-hard interfaces, producing thin, conform Au shell at the properly prepared reduction reaction.

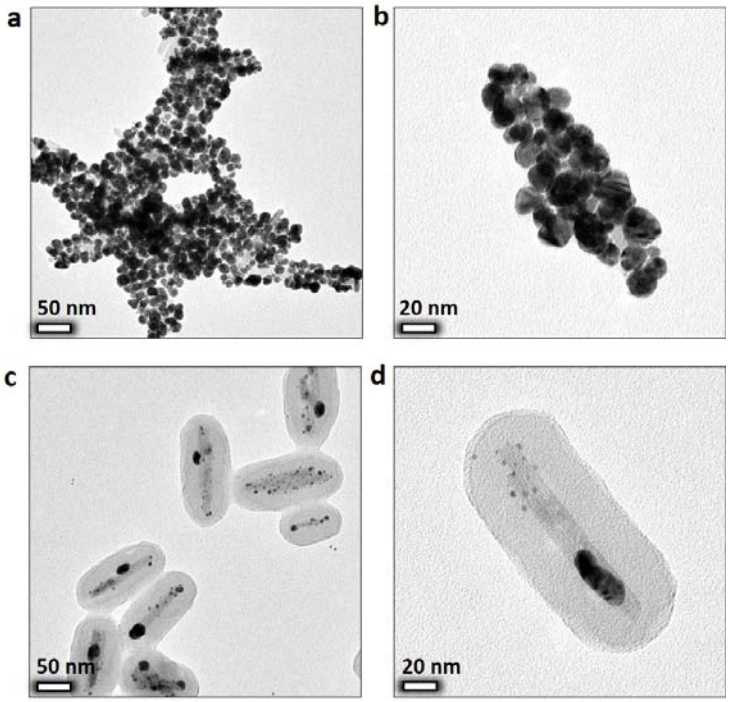

Figure 4.2. (a-b), TEM images of seeded growth of Au without the confinement of RF shells. (c-d), TEM images of nanostructures grown by using KI as coordinating agents and AA reducing agents.

To analyze the plasmon mode of each band, we calculate the extinction cross section of Fe_3O_4@Au@RF NRs by using finite element method. In **Figure 4.3a**, the plasmon band at 930 nm and 530 nm excited when NRs are parallel and perpendicular to the wave polarization, which indicates longitudinal and transverse plasmon bands, respectively. We observed gradual suppression of longitudinal band when NRs are aligned from 0^o to 90^o. After carefully examining their correlation, we find the strength of longitudinal, transverse plasmon bands of Au shell can be accurately described by $\cos^2$- and $\sin^2$-function, respectively. The electric field distributions in **Figure 4.3b** further reveal that the two bands originate from a dipole resonance of Au shell to electromagnetic wave. The tip LSPR is tenfold stronger than transverse mode, both of which are highly dependent on orientation of Au shell. Our calculation suggests that LSPR of Au shell can be actively modulated on demand by controlling its orientation. To confirm this proposal, we measured the extinction of Fe_3O_4@Au NRs by applying a magnetic field. As shown in **Figure 4.3c**, peak intensity at 930 nm is boosted to its maximum when the field direction is parallel to polarization of incident light ($|0^o>$). Switching to a perpendicular field ($|90^o>$) deactivates this band as the peak at 930 nm disappears completely. An inverse tuning is observed on transverse plasmon band, which gives rise to slight color change. The promising results inspire us to further examine the magnetically regulated photothermal conversion of Fe_3O_4@Au NRs. The temperature (T) and its change (ΔT) of colloidal NRs dispersion were measured by applying different magnetic fields relative to the polarization of a 980 nm laser. In **Figure 4.3d**, T was promoted to ~ 50^oC. When field parallel to laser polarization was applied ($|0^o>$). At $|90^o>$, T was reduced to less than 30^oC from a normal 35^oC (random). The

magnetically modulated physical properties of Fe_3O_4@Au NRs are summarized in **Figures 4.3e** and **4.3f**. Specifically, we achieve active tunibility between ±45% for optical extinction and from -12% to +30% for photothermal conversion by simply applying a particular magnetic field.

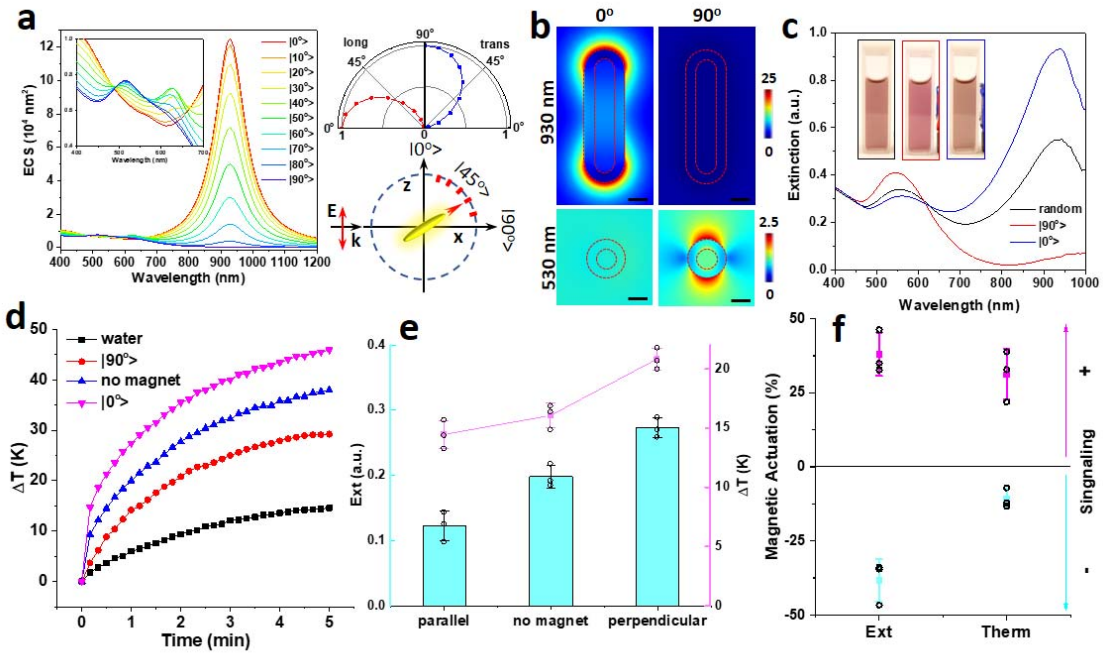

Figure 4.3. Magnetic modulation of the physical properties of Fe_3O_4@Au nanorods. (a) Calculated extinction spectra of Fe_3O_4@Au nanorods under different orientations. (b) Electric field distribution of orientated nanorods under excitation of particular wavelength. Scale bars: 20 nm. (c) Extinction spectra of nanorods dispersion under different magnetic field directions. (d) Temperature changes of rods dispersion measured under different field directions. Summary of changes (e) and tunability (f) of optical extinction and temperature.

To specify coordination limit of NRs to magnetic fields, we tracked the signal changes of longitudinal mode under an alternating magnetic field with ever-creasing frequency. In **Figure 4.4a**, we observed periodic signals between 1 Hz and 3 Hz. Further increasing the alternating frequency attenuates the periodic signal, setting a limit at 3Hz for NRs dispersed in water. We observed high-intensity peaks corresponding to fields of each frequency when converting the signal from time domain to frequency domain (**Figure 4.4b**). Interestingly, the FFT-processed signal frequency is exactly twice of the applied frequency (**Figure 4.4c**). As magnetic field rotate in one circle, it generates same plasmon band twice. The highly linear correlation indicates perfect coherence of Fe_3O_4@Au NRs to applied magnetic fields within the frequency limits. The recycling performance is illustrated in **Figure 4.4d**, and the signal maintains periodic coherent oscillation to applied field without any noticeable decay and maladjustment.

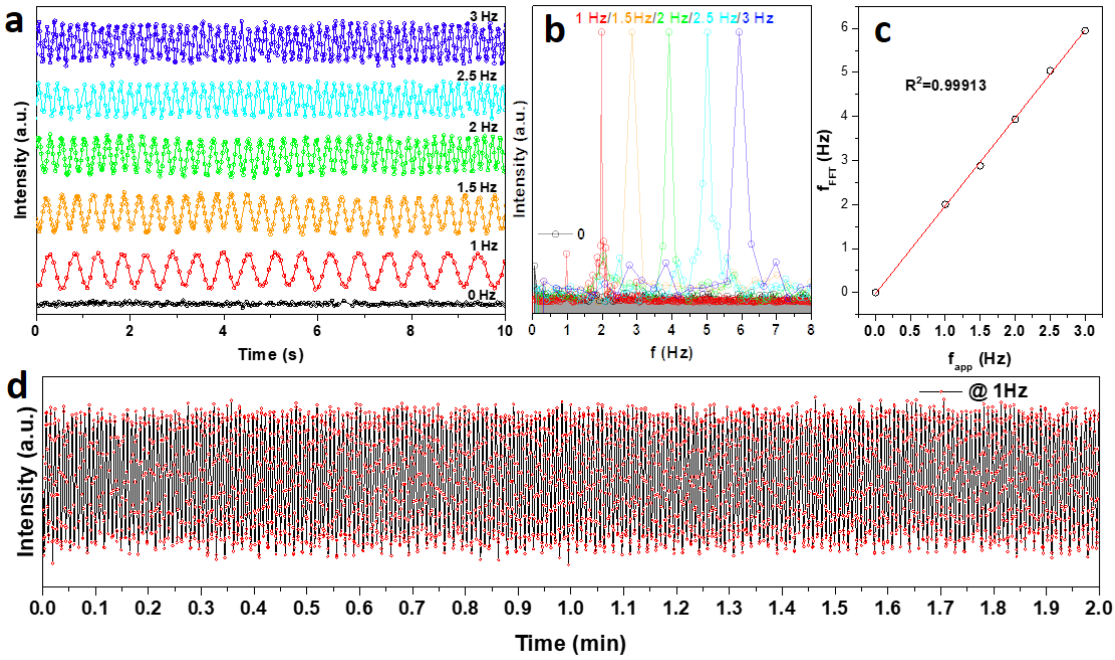

Figure 4.4. Magnetic modulation of the physical properties of Fe_3O_4@Au nanorods. (a) Extinction modulation of rods dispersion under alternating magnetic fields. FFT of magnetically modulated signals (b) and its correlation with applied frequency (c). (d) Stability of signal modulation at 1 Hz.

Magnetically modulated photon-phonon conversion. The working principle of magnetically modulated background-free PA imaging is depicted in **Figure 4.5a**. In normal imaging mode, real-time PA images are acquired after administration of Fe_3O_4@Au NRs. In this mode, the longitudinal plasmon is not excited to the maximum strength considering the random orientation of NRs in the imaging areas. By applying perpendicular magnetic fields to the imaging laser, Fe_3O_4@Au NRs in imaging areas will be realigned parallelly to local field direction. It thus generates a bright PA mode that is boosted by the promoted photothermal and photon-phonon conversion efficiency. In a typical imaging sequence, the magnetic field will be then switched to be parallel to laser incidence. Consider the coherent re-orientation of NRs to applied field. The longitudinal plasmon will be suppressed, generating deactivated PA mode, whose imaging contrast and specificity should be much weaker than the previous two modes. Notably, in these imaging modes, PA background contrast from endogenous biological sources always exists, such as blood vessels and tissue interfaces. Although the bright PA mode is expected to have higher contrast than that in normal PA mode, it still suffers from the interference of background PA signals. By subtracting pixels of deactivated mode from pixels of bright mode, we propose that the background PA signals can be totally removed, generating background-free imaging with greatly enhanced contrast and specificity.

To access the ability of Fe_3O_4@Au NRs to produce dynamic PA signals, we started with acquiring PA images of the colloidal dispersion of AuNRs as control experiment and Fe_3O_4@Au NRs by applying different magnetic fields. As shows in **Figure 4.5b**, AuNRs can produce considerable PA intensity but rather only exhibiting randomly fluctuating

signals (**Figure 4.5c**) under magnetic fields. In the case of Fe_3O_4@Au NRs, we observed a remarkable modulation of PA signals in accordance with applied magnetic fields (**Figures 4.5d and 4.5e**). More especially, PA signals were coherently enhanced or suppressed with twofold tunability when perpendicular and parallel magnetic fields were applied. These observations are consistent with the optical extinction and photothermal conversion changes under an identical magnetic field. More importantly, they suggest that the integrated imaging contrast agent enables us to dynamically, reversibly tune PA signals by simply applying a magnetic field, a stimulus source that is non-invasively feasible to implement and provides precise control, unlimited tissue penetration, instant signaling, and highly reversible modulation. To examine the PA tunability of Fe_3O_4@Au in a biological tissue, we acquired PA images of a subcutaneous tumor of a mouse after intra-tumor (i. t.) injection of AuNRs (**Figure 4.5f**) and Fe_3O_4@Au NRs (**Figure 4.5g**). In the case of AuNRs, they generate field-independent PA signal, which was completely removed after the pixel-wise imaging processing. When the integrated agents were used, PA signals can still be dynamically modulated by external magnetic fields in the high viscous microenvironments of biological tissues. A simple subtraction of pixel of deactivated mode from bright mode produce considerably high PA intensity and diminish PA noise from tissue backgrounds. Due to the rapid response of integrated agents to external magnetic fields, PA signals can be modulated multiple times and the created background-free PA image does not exhibit significant intensity decay (**Figure 4.5h**).

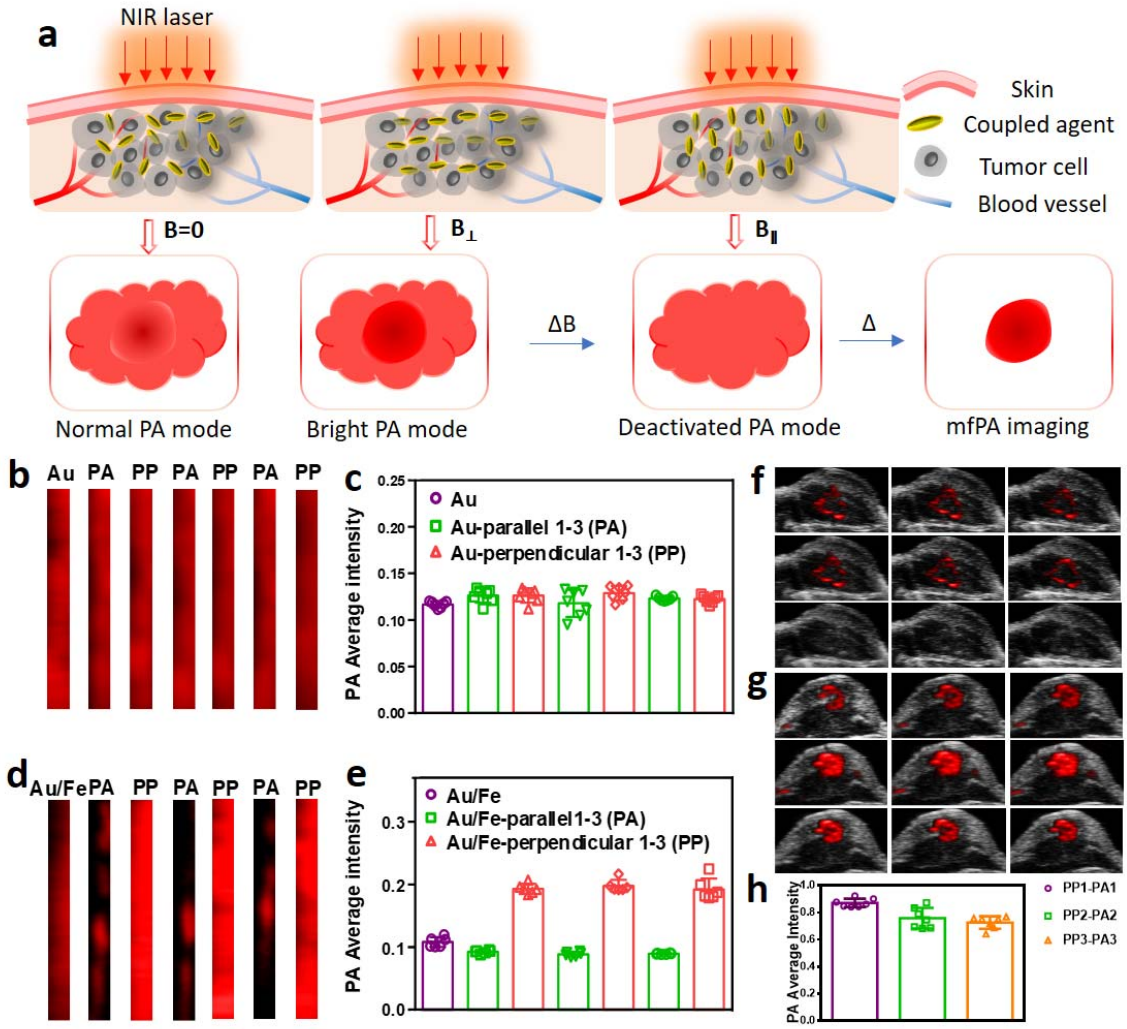

Figure 4.5. Actively Modulating PA signals by external magnetic fields. (a) Working principle of background-free PA imaging based on magnetic signal modulation. PA imaging (b) and signal (c) of AuNRs under different magnetic fields. PA imaging (d) and signal (e) of AuNRs under different magnetic fields. Magnetically modulated PA imaging of tumors after i.t. injection of AuNRs (f) and coupled rods (g). (h) PA signal changes modulated by magnetic fields in the PA images of (g).

In vivo magnetically modulated background-free PA imaging. For in vivo imaging studies, we first use muscle tissue of a mouse as model system. In three experiment groups in **Figure 4.6a** from top to bottom panel, they were injected with AuNRs, Fe_3O_4@Au NRs, both of them, respectively. It is found that only PA signals from Fe_3O_4@Au NRs can be modulated coherently by external magnetic fields. In the bottom panel, two NRs were injected in the neighborhood, where the AuNRs mimic PA noises. In a sequence of two PA images under parallel and perpendicular fields, PA signals of Fe_3O_4@Au NRs exhibited significant enhancement while signals of AuNRs only randomly fluctuate. Interestingly, by pixel-wise subtraction, "noise" signal of AuNRs was completely removed and interested areas administrated with Fe_3O_4@Au NRs is thus emphasized with high imaging contrast and specificity (**Figure 4.6b**). The in vivo tumor PA imaging was carried out on a subcutaneous tumor model. Fe_3O_4@Au NRs were intravenously injected and directed specifically to tumor via enhanced permeability and retention (EPR) effect. The PA images in **Figure 4.6c** indicate excellent tumor passive targeting of NRs 24h after injection. When perpendicular magnetic field was applied, PA signals of Fe_3O_4@Au NRs can be remarkably enhanced, which was twofold higher than that under parallel magnetic fields (**Figure 4.6d**). By using the pixel-wise data processing, we showed that noises from any biological backgrounds is removed, forming a background-free PA imaging mode as mediated by external magnetic fields.

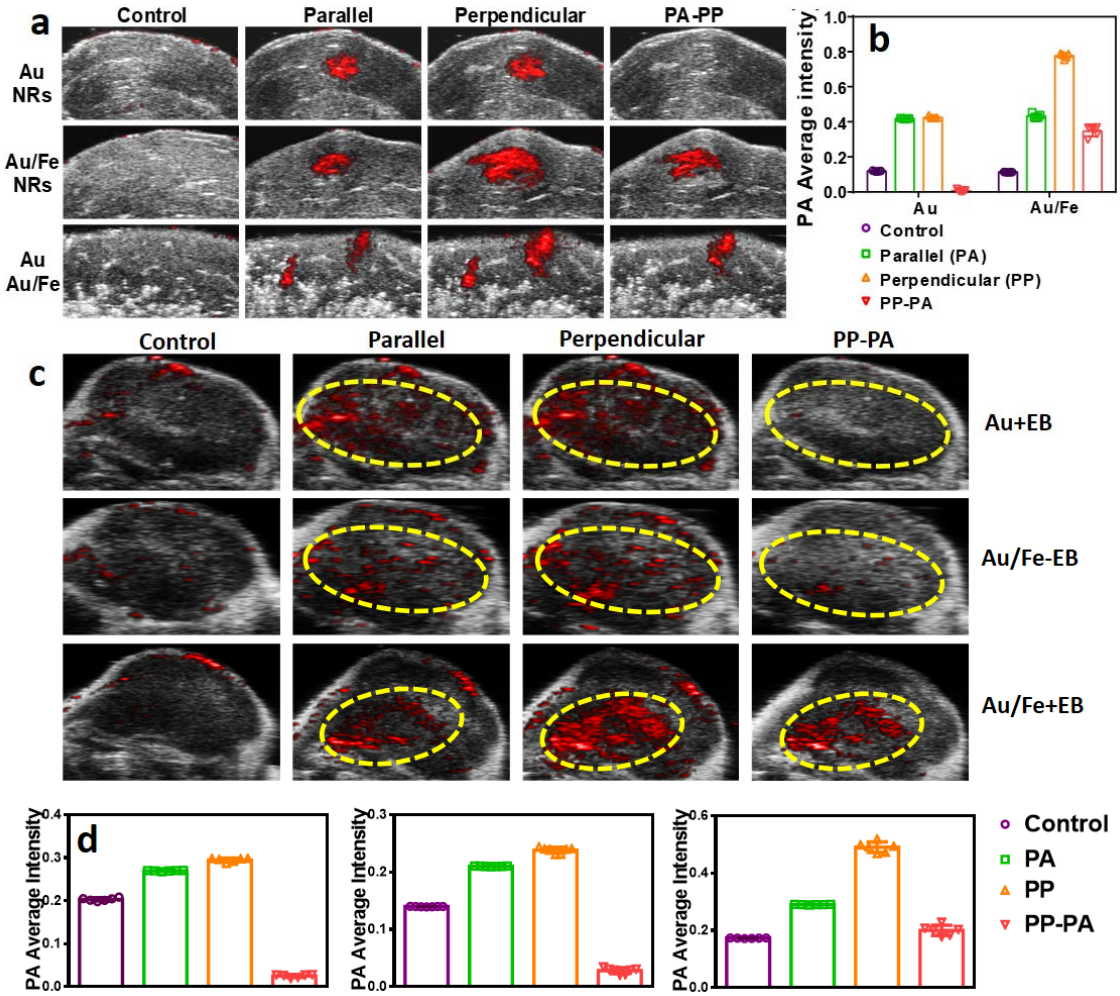

Figure 4.6. Magnetically Modulated Background-free PA imaging. (a) PA imaging of muscles after injection with AuNRs and Fe_3O_4@Au NRs. (b) Their signal changes mediated by magnetic fields. (c) Background-free tumor imaging after i.v. injection of AuNRs and Fe_3O_4@Au NRs. (d) The signal changes of PA imaging before and after data processing: left panel (AuNRs); middle panel (Fe_3O_4@Au NRs without EB); right panel (Fe_3O_4@Au NRs with EB).

Magnetically modulated and FFT-processed background-free PA imaging. One character of PA imaging is that endogenous PA noise can vary in a broad range in intensity, distribution, and depth. Hence, achieving PA images with high specificity and contrast by using low dosage of contrast agent is still challenging. The magnetically modulated background-free imaging developed here holds the potential for solving this challenge but still possibly suffers when noises are so strong that makes data processing unsolvable. To this end, we further hypothesize magnetically modulated and FFT-processed background-free PA imaging methodology. The data processing is illustrated in **Figure 4.7**. Instead of direct pixel-wise subtraction, we take advantage of the coherent periodic PA signal changes of Fe_3O_4@Au NRs in accordance with applied alternating magnetic field. In the acquired PA images in a properly chosen time sequence, the signal changes of each pixels in the imaging area are extracted and plotted in real-time fashion. Thus, in the time-domain plot, pixel generated by PA signals of Fe_3O_4@Au NRs features perfect periodic changes against time while noise pixel from backgrounds only show random fluctuation within a constantly small range. The FFT is then applied to the signal-time plot for each pixel to convert the time domain to frequency domain. One critical rule of this working principle is that only periodic signals will generate sharp peaks at the resonant frequency. Therefore, signals from noises can be readily and reliably removed by applying a frequency threshold that isolates noise signals from signals of contrast agent. A PA images need to be further recovered by using peak intensity in the frequency-domain plot. The PA imaging before and after FFT are shown in the bottom panel of **Figure 4.7**, which clearly demonstrates the disappearance of background noises.

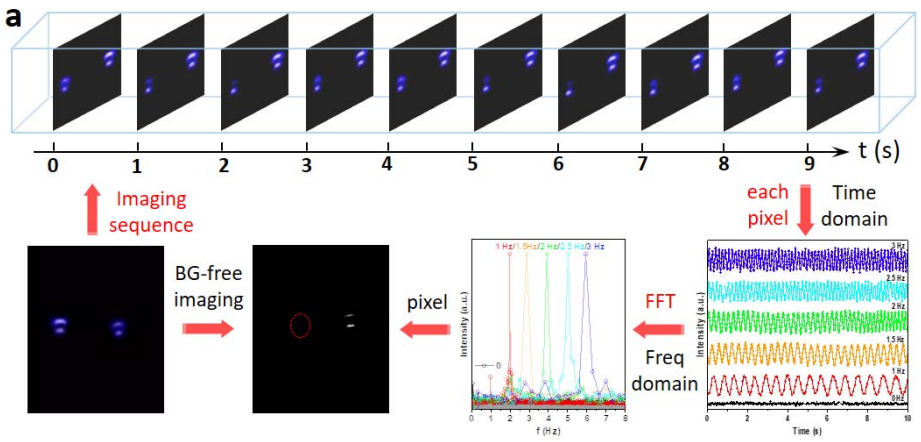

Figure 4.7. FFT-processed Background-free Photoacoustic Bioimaging. (a) Data processing of the magnetically modulated and FFT-processed background-free PA imaging.

4.4 Background-Free Optical Coherence Tomography Imaging

Optical coherent tomography (OCT) is an optical imaging technique for acquiring sub-surface images of tissues and organs at near-microscopic resolution. It collects and processes a small portion of incident optical beam that is reflected light from biological tissues for tissue morphology imagery. OCT allow for the imaging of fine structures within tissue based on inherent contrast from heterogeneity of optical refractive index. However, use of a contrast agent can aid in visualization of a target of interest when the intrinsic contrast in a sample makes such identification difficult. Here, we demonstrate the use of magnetically responsive gold-coated nanorods selectively tuned for use with a 1310 nm-centered spectral domain OCT system to nearly eliminate this background noise from non-responsive tissue surrounding the nanorods. By varying the intensity of light reflected from the nanorods using varying magnetic field orientation, it is possible to remove the unchanging background noise from tissue even if the intensity of light from the tissue is higher than from the nanorods themselves, revealing structures hidden within the tissue.

Magnetically-responsive nanorods for OCT imaging were synthesized from Fe_3O_4 nanorods uniformly coated with gold (Au). Non-responsive rods for comparison were synthesized from FeOOH. Nanorods were then uniformly coated with Au to form the final nanorods tuned to highly excite at approximately 1300 nm wavelength light. Magnetically responsive nanorods were suspended in water and were imaged using spectral domain OCT (SD-OCT) centered at 1310 nm under no magnet, parallel magnetic field to the laser, and perpendicular magnetic field to the laser. Magnetically responsive and non-responsive nanorods were then injected into tubing wrapped in pork tissue to demonstrate differing

responses to magnetic field. Background tissue noise was removed by subtracting parallel frames from matching perpendicular frames. Finally, magnetically responsive nanorods were injected into pork tissue and then subjected to perpendicular and parallel magnetic fields to the imaging laser. Again, background noise was removed through subtraction of parallel frames from perpendicular frames

The FeOOH nanorods are 200 nm in length and 30 min in width (**Figure 4.8a**). By using the unconventional seeded growth methods, Au shell can be homogeneously grown at the hard-soft interfaces between Fe_3O_4 cores and deformable RF shells. As shown in TEM image in **Figure 4.8b**, magnetic cores are completely covered by Au shells of 25 nm in thickness as confined by the RF shells, forming Fe_3O_4@Au@RF nanostructures. The extinction spectra of a colloidal dispersion of Fe_3O_4@Au@RF were measured by applying magnetic fields with different directions. The longitudinal plasmon band is located at 1250 nm. The transverse plasmon band has multiple resonance to the external electromagnetic fields due to hybridization of sphere and cavity plasmon modes. Interestingly, switching the direction of applied magnetic field can actively modulate the plasmonic excitation of Au shells. Under ordinary light (**Figure 4.9a**), the longitudinal mode of Au shell is suppressed when the applied magnetic field is parallel to the incident light. Under this scenario, only transverse mode at 615 nm is excited. When switching the field direction to be perpendicular, we observe an enhancement of longitudinal mode. Meanwhile, the color of the measured solutions changes from blue to green. If measured in polarized light, it was found that the extinction spectra can be magnetically modulated over a broader range. As shown in **Figure 4.9b**, the extinction of longitudinal mode can be enhanced by 7 times

when the Fe_3O_4@Au@RF NRs are aligned from parallel to perpendicular configuration. Such large tunability is attributed to the strong magnetic properties of the Fe_3O_4 NRs coupled with perfect plasmonic properties of Au shells, which enables the instant, reversible modulation of the optical properties.

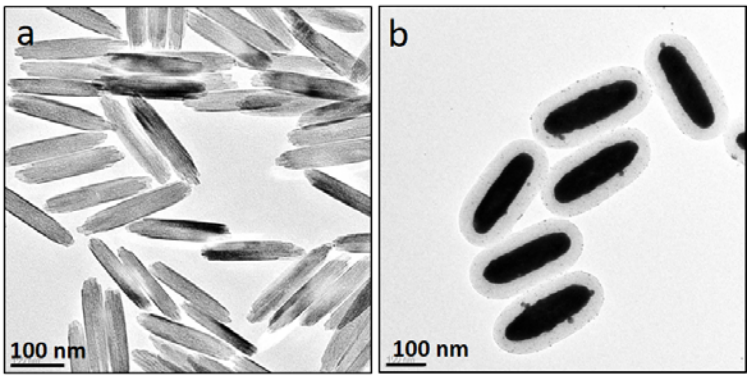

Figure 4.8. TEM images of FeOOH and Fe_3O_4@Au@RF nanorods

As contrast in OCT image is produced by light scattering, a good imaging contrast agent should have high scattering at the incident wavelength. To study the possibility of using Fe_3O_4@Au@RF NRs as contrast agent and their signal tunability under external magnetic fields, we performed OCT imaging on the colloidal dispersion of NRs by applying different magnetic fields. As shown in **Figure 4.9c**, water is quite transparent to light at 1300 nm due to the low absorption and scattering at the NIR-II window. In the colloidal dispersion of NRs, we observed strong scattering signals with gradually decayed intensity along the image depth, demonstrating the good scattering properties of Fe_3O_4@Au@RF NRs. As beam is incident along the surface normal of water-air interface, its intensity will be attenuate by the scattering of homogenously dispersed NRs, which in turn gives rise to a signal gradient in OCT imaging. More interestingly, when applying external magnetic fields, we found that OCT signals can be immediately modulated. When a parallel magnetic field was applied, the OCT signal was reduced on the basis of two observations. First, a direct evidence is that image brightness ("parallel" panel in **Figure 4.9c**) and SNR decrease at the water-air interface compared with the case under the absence of magnetic fields. Second, image gradient increased with better beam penetration when parallel magnetic fields were applied (**Figure 4.9d**). It indicates an associated decrease in NRs scattering so that incident beam can reach a deeper region. When the magnetic field was switched to perpendicular configuration, however, OCT signals can be greatly enhanced ("perpendicular" panel **Figure 4.9c**). Our real-time measurement and quantitative analysis in **Figure 4.9e** further elucidate that OCT signals of Fe_3O_4@Au@RF NRs can be reversibly, rapidly modulated by controlling the direction of an external magnetic field.

The SNR of OCT images can be regulated between 25 and 65 with more than three times enhancement (top panel in **Figure 4.9e**) while its decay rate along depth can be regulated between -70 and -5 dB/mm (bottom panel in **Figure 4.9e**). Based on these analyses, we conclude that Fe_3O_4@Au@RF NRs is perfect OCT contrast agent due to the scattering-dominated extinction of Au shell and their OCT signals can be modulated by ±40% (**Figure 4.9f**) when an external magnetic field is used to control the orientation of NRs in colloidal dispersion.

We then start with an artificial phantom to investigate the ex vivo background-free OCT imaging in NIR-II window. As depicted in **Figure 4.10a**, two capillary tubes are implanted into a piece of pork that mimics biological noise in OCT imaging. Into the right capillary tube, FeOOH@Au@RF NRs without any magnetic responses were injected to serve as the synthetic noises. Magnetically responsive Fe_3O_4@Au@RF NRs were injected into the left capillary tube as positive imaging contrast agent. During OCT imaging, a parallel and perpendicular magnetic field were applied in sequence. As shown in **Figure 4.10b**, both the biological noise from pork and the synthetic noises from non-responsive FeOOH@Au@RF NRs only exhibited random signal fluctuation under different magnetic fields. In contrast, we observed remarkably increase in imaging contrast when perpendicular magnetic field was applied (**Figure 4.10c**). In recognition of the difference between the sequential images, we applied pixel-wise data processing to create the background-free OCT images. It is achieved by subtracting the pixel of "parallel" image from that of "perpendicular" image. As reconstructed in **Figure 4.10b**, the noises from both biological and synthetic backgrounds were successfully removed, only leaving few random

signals in OCT images. Instead, OCT image that is free of noises is created, showing high imaging contrast and specificity. When comparing the SNR before and after data processing, a 400-fold enhancement of SNR is reported in OCT imaging. This strategy can be extended to 3D OCT imaging with much enhanced performances. In typical imaging methodology, 2D B-scan images are acquired in a time sequence. A static magnetic field will be applied to modulate the signal in the 2D OCT images. The pixel subtraction is performed according between the two positive and negative OCT images acquired at the same cross-section. The negative and positive 3D volume rendering of the OCT images was shown in the left and middle panel in **Figure 4.10e**. We found that all the signals from both the responsive and nonresponsive NRs were immersed into the background noises, making the analysis of the interested regions very difficult. Surprisingly, on the basis of proposed data processing, we can reconstruct 3D background-free OCT imaging based on volume rendering of the subtracted 2D images. The capillary tube can be fully recovered and background noises from both the biological and synthetic noises were removed completely.

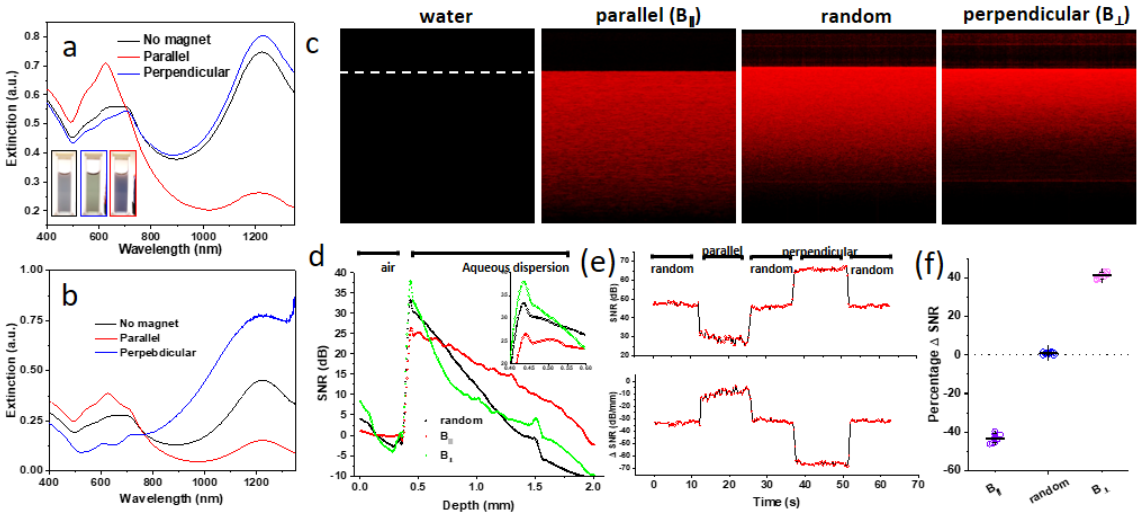

Figure 4.9. Extinction spectra of Fe_3O_4@Au@RF nanorods measured under (a) ordinary and (b) polarized light. (c) OCT images of water and colloidal dispersions of Fe_3O_4@Au@RF nanorods with without magnetic fields. (d) Line profile of SNR of the OCT images modulated by different magnetic fields. (e) Tunability (top panel) and changes (bottom panel) of SNR modulated by magnetic fields. (f) Percentage of SNR changes.

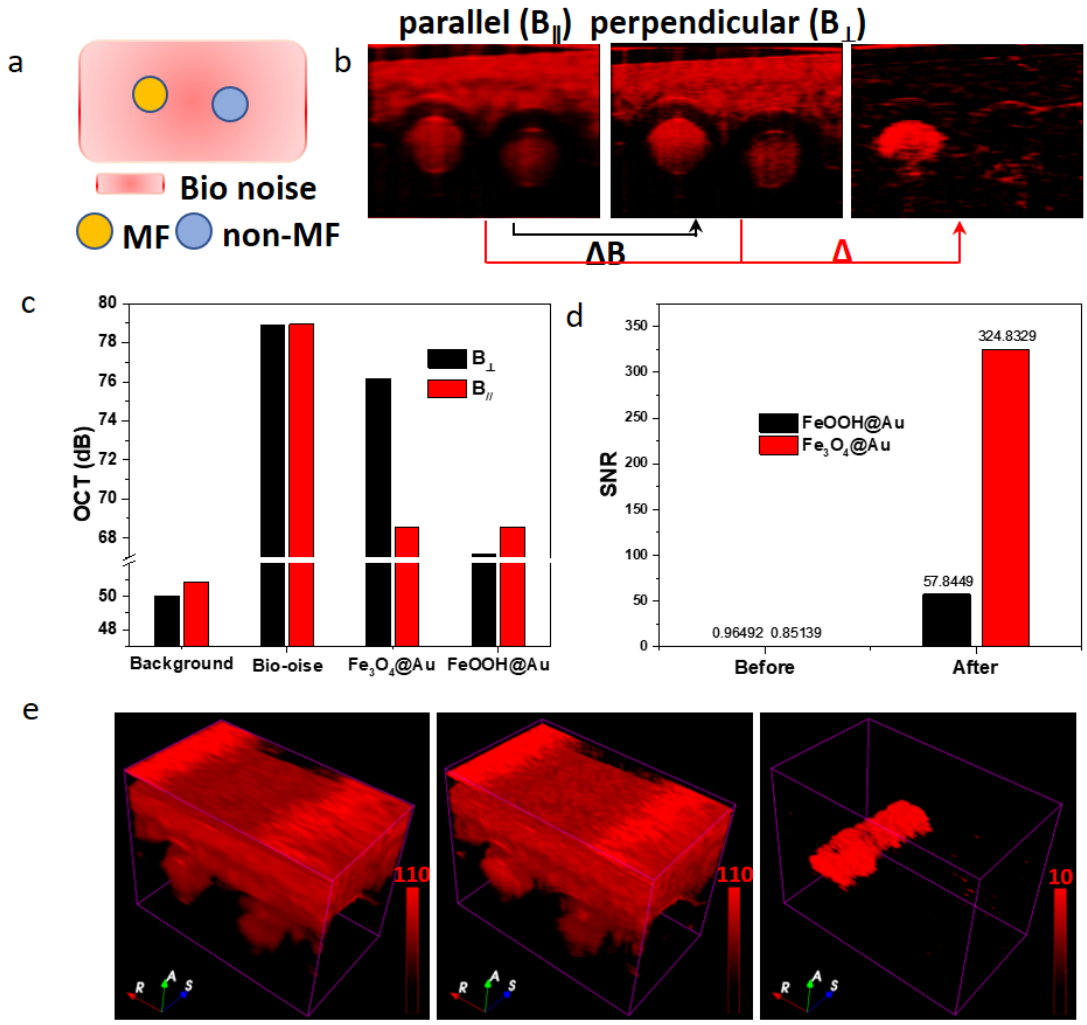

Figure 4.10. **(a)** Scheme of ex vivo phantom used for biological imaging. (b) Ex vivo OCT imaging. (c) OCT signal changes modulated by magnetic fields. (d) Enhancement of SNR in OCT imaging enabled by magnetic alignment. (e) 3D rendering of OCT imaging before and after data processing.

Compared with imaging in aqueous dispersion, the application of nanorods has several challenges. First, the rotational resistance in biological tissue is much higher than that in water, making coherent modulation of rods orientation more difficult. Second, the random diffusion of nanorods inside biological tissues can attenuate the imaging intensity due to the diluting effect. Therefore, to further demonstrate the feasibility of Fe_3O_4@Au@RF NRs as tunable imaging contrast agent and the proposed data processing in biological OCT imaging, we focus the imaging performance by directly injecting as-synthetized NRs into pork tissues in the following section. The administration of nanorods is illustrated in **Figure 4.11a**. In a similar way, responsive and nonresponsive nanorods ware injected into the right and left side of a pierce of pork. Bright and deactivated mode will be performed by applying perpendicular and parallel magnetic field to the incident beam, respectively, to acquire the positive and negative OCT images. The 2D B-scan images with different magnetic fields are shown in **Figure 4.11b**. We observed enhanced OCT signals in the area that was injected with Fe_3O_4@Au@RF NRs. On the right side where the FeOOH@Au@RF NRs were injected, there is no any observable changes in the OCT images. However, it has to be noted that specifying the imaging areas of interest is still impossible as the signals from imaging contrast agent are totally mixed with background noises. By using the pixel-wise data processing, we demonstrate that this issue can be successfully solved, and background-free OCT image could be created by the differentiated pixels. By extending this strategy to 3D volume rendering, we further reconstructed 3D volume where the noises from biological backgrounds can be removed (**Figure 4.11c**). In addition to enhance the OCT imaging contrast, this method is expected to greatly improve

the imaging specificity as the regions that are targeted by active imaging contrast agents can be recognized with high resolution (**Figure 4.11d**).

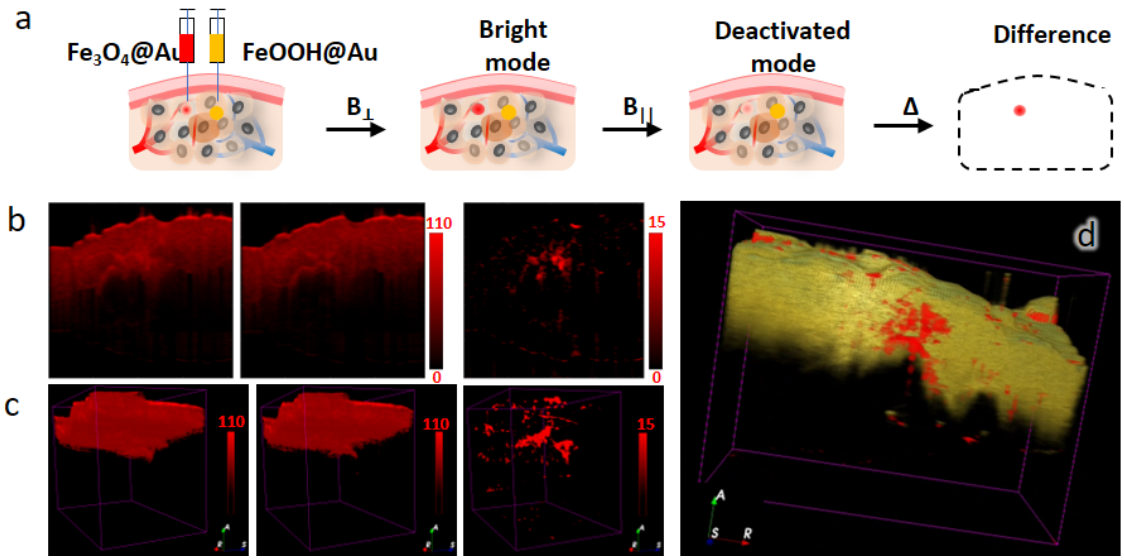

Figure 4.11. (a), Schematic illustration of NIR-II background-free OPT imaging. (b) In vivo 2D OCT imaging. (c) 3D rendering. (d) Created OCT images. Signal from imaging contrast agent is in red while background OCT noises are in yellow.

4.5 Conclusion

In this chapter, we have developed an unconventional background-free bioimaging modality. The unique imaging is achieved on the basis of our new synthetic strategy in the production of Fe_3O_4@Au rods. The space-free confined growth method is able to produce high-quality Au shell with controllable thickness and LSPR. It does not need a pre-designed gap or hollow interior for the growth of a second structure, thus providing a cost-effective, timesaving growth methodology. In the first part, by using small rods as initial templates, we synthesized Fe_3O_4@Au rods with compact structures and integrated functionalities. Thanks to the magnetic properties of Fe_3O_4 core, the physical properties of Au shell, including plasmon band, perceived color, photothermal conversion, and photoacoustic signals are reversibly tuned by changing the directions of applied magnetic fields. If these rods are used as imaging contrast in PA imaging, we demonstrate that PA signals from injected nanorods can be effectively tuned by applying an alternating magnetic field. By applying a data processing, including pixel subtraction or FFT, we create a method to remove the random PA signals form biological and synthetic background noises, generating a background-free PA image with remarkably enhanced imaging contrast and specificity.

In the second part, we develop a reliable and robust strategy for background-free OCT imaging in the second NIR window. A smart imaging contrast agent, whose scattering can be actively tuned by changing the direction of applied magnetic field, was synthesized by using an unconventional seeded growth method. In the first part, we demonstrate that uniform Au shell with controllable thickness and tailorable plasmonic properties can be

conformably coated on magnetic nanorods relying on the elastic deformation and radical confinement of RF shells. This method has the ability to produce various metal nanostructures without the need of creating a pre-designed confining gap. Thanks to the strong magnetic properties of Fe_3O_4 nanorods and the well-defined plasmonic extinction of Au shell, the scattering and the OCT signals of the rods can be magnetically modulated in an instant, remote, and reversible way. In the last pat, we report a reliable data processing to diminish any noises from biological backgrounds. Our results have demonstrated that this strategy is promising for achieving 2D and 3D background-free OCT imaging in the second NIR window with high imaging contrast, resolution, and specificity.

4.6 References

1. Leaf, C., Why we're losing the war on cancer (and how to win it). *FORTUNE-EUROPEAN EDITION-* **2004,** *149* (5), 42-55.

2. Gao, X.; Cui, Y.; Levenson, R. M.; Chung, L. W.; Nie, S., In vivo cancer targeting and imaging with semiconductor quantum dots. *Nature biotechnology* **2004,** *22* (8), 969.

3. Dubertret, B.; Skourides, P.; Norris, D. J.; Noireaux, V.; Brivanlou, A. H.; Libchaber, A., In vivo imaging of quantum dots encapsulated in phospholipid micelles. *Science* **2002,** *298* (5599), 1759-1762.

4. Le Sage, D.; Arai, K.; Glenn, D.; DeVience, S.; Pham, L.; Rahn-Lee, L.; Lukin, M.; Yacoby, A.; Komeili, A.; Walsworth, R., Optical magnetic imaging of living cells. *Nature* **2013,** *496* (7446), 486.

5. Laurent, S.; Forge, D.; Port, M.; Roch, A.; Robic, C.; Vander Elst, L.; Muller, R. N., Magnetic iron oxide nanoparticles: synthesis, stabilization, vectorization, physicochemical characterizations, and biological applications. *Chemical reviews* **2008,** *108* (6), 2064-2110.

6. Fan, Z.; Shelton, M.; Singh, A. K.; Senapati, D.; Khan, S. A.; Ray, P. C., Multifunctional plasmonic shell–magnetic core nanoparticles for targeted diagnostics, isolation, and photothermal destruction of tumor cells. *ACS nano* **2012,** *6* (2), 1065-1073.

7. Huang, P.; Lin, J.; Li, W.; Rong, P.; Wang, Z.; Wang, S.; Wang, X.; Sun, X.; Aronova, M.; Niu, G., Biodegradable gold nanovesicles with an ultrastrong plasmonic coupling effect for photoacoustic imaging and photothermal therapy. *Angewandte Chemie* **2013,** *125* (52), 14208-14214.

8. Cheng, L.; Yang, K.; Li, Y.; Chen, J.; Wang, C.; Shao, M.; Lee, S. T.; Liu, Z., Facile preparation of multifunctional upconversion nanoprobes for multimodal imaging and dual-targeted photothermal therapy. *Angewandte Chemie* **2011,** *123* (32), 7523-7528.

9. Cheng, L.; Wang, C.; Liu, Z., Upconversion nanoparticles and their composite nanostructures for biomedical imaging and cancer therapy. *Nanoscale* **2013,** *5* (1), 23-37.

10. Kircher, M. F.; De La Zerda, A.; Jokerst, J. V.; Zavaleta, C. L.; Kempen, P. J.; Mittra, E.; Pitter, K.; Huang, R.; Campos, C.; Habte, F., A brain tumor molecular imaging strategy using a new triple-modality MRI-photoacoustic-Raman nanoparticle. *Nature medicine* **2012,** *18* (5), 829.

11. Jin, Y.; Jia, C.; Huang, S.-W.; O'donnell, M.; Gao, X., Multifunctional nanoparticles as coupled contrast agents. *Nature communications* **2010,** *1*, 41.

12. Li, Z.; Yin, S.; Cheng, L.; Yang, K.; Li, Y.; Liu, Z., Magnetic targeting enhanced theranostic strategy based on multimodal imaging for selective ablation of cancer. *Advanced Functional Materials* **2014,** *24* (16), 2312-2321.

13. Cheng, L.; Liu, J.; Gu, X.; Gong, H.; Shi, X.; Liu, T.; Wang, C.; Wang, X.; Liu, G.; Xing, H., PEGylated WS2 nanosheets as a multifunctional theranostic agent for in vivo dual-modal CT/photoacoustic imaging guided photothermal therapy. *Advanced materials* **2014,** *26* (12), 1886-1893.

14. Smith, B. R.; Gambhir, S. S., Nanomaterials for in vivo imaging. *Chemical reviews* **2017,** *117* (3), 901-986.

15. Louie, A., Multimodality imaging probes: design and challenges. *Chemical reviews* **2010,** *110* (5), 3146-3195.

16. Li, Z.; Wang, C.; Cheng, L.; Gong, H.; Yin, S.; Gong, Q.; Li, Y.; Liu, Z., PEG-functionalized iron oxide nanoclusters loaded with chlorin e6 for targeted, NIR light induced, photodynamic therapy. *Biomaterials* **2013,** *34* (36), 9160-9170.

17. Ge, J.; Hu, Y.; Biasini, M.; Beyermann, W. P.; Yin, Y., Superparamagnetic magnetite colloidal nanocrystal clusters. *Angew. Chem. Int. Ed.* **2007,** *46* (23), 4342-4345.

18. Michalet, X.; Pinaud, F.; Bentolila, L.; Tsay, J.; Doose, S.; Li, J.; Sundaresan, G.; Wu, A.; Gambhir, S.; Weiss, S., Quantum dots for live cells, in vivo imaging, and diagnostics. *science* **2005,** *307* (5709), 538-544.

19. Wang, X.; Wang, C.; Cheng, L.; Lee, S.-T.; Liu, Z., Noble metal coated single-walled carbon nanotubes for applications in surface enhanced Raman scattering imaging and photothermal therapy. *Journal of the American Chemical Society* **2012,** *134* (17), 7414-7422.

20. Park, Y. I.; Lee, K. T.; Suh, Y. D.; Hyeon, T., Upconverting nanoparticles: a versatile platform for wide-field two-photon microscopy and multi-modal in vivo imaging. *Chemical Society Reviews* **2015,** *44* (6), 1302-1317.

21. Wang, C.; Cheng, L.; Liu, Z., Drug delivery with upconversion nanoparticles for multi-functional targeted cancer cell imaging and therapy. *Biomaterials* **2011,** *32* (4), 1110-1120.

22. Ntziachristos, V., Going deeper than microscopy: the optical imaging frontier in biology. *Nature methods* **2010,** *7* (8), 603.

23. Smith, A. M.; Mancini, M. C.; Nie, S., Bioimaging: second window for in vivo imaging. *Nature nanotechnology* **2009,** *4* (11), 710.

24. Chen, J.; Saeki, F.; Wiley, B. J.; Cang, H.; Cobb, M. J.; Li, Z.-Y.; Au, L.; Zhang, H.; Kimmey, M. B.; Li, X., Gold nanocages: bioconjugation and their potential use as optical imaging contrast agents. *Nano letters* **2005,** *5* (3), 473-477.

25. Louie, A. Y.; Hüber, M. M.; Ahrens, E. T.; Rothbächer, U.; Moats, R.; Jacobs, R. E.; Fraser, S. E.; Meade, T. J., In vivo visualization of gene expression using magnetic resonance imaging. *Nature biotechnology* **2000,** *18* (3), 321.

26. Jun, Y. W.; Lee, J. H.; Cheon, J., Chemical design of nanoparticle probes for high-performance magnetic resonance imaging. *Angewandte Chemie International Edition* **2008,** *47* (28), 5122-5135.

27. Jun, Y.-w.; Huh, Y.-M.; Choi, J.-s.; Lee, J.-H.; Song, H.-T.; Kim, S.; Kim, S.; Yoon, S.; Kim, K.-S.; Shin, J.-S., Nanoscale size effect of magnetic nanocrystals and their utilization for cancer diagnosis via magnetic resonance imaging. *Journal of the American Chemical Society* **2005,** *127* (16), 5732-5733.

28. Li, J.; Zheng, L.; Cai, H.; Sun, W.; Shen, M.; Zhang, G.; Shi, X., Facile one-pot synthesis of Fe_3O_4@ Au composite nanoparticles for dual-mode MR/CT imaging applications. *ACS applied materials & interfaces* **2013,** *5* (20), 10357-10366.

29. Zhou, T.; Wu, B.; Xing, D., Bio-modified Fe 3 O 4 core/Au shell nanoparticles for targeting and multimodal imaging of cancer cells. *Journal of materials chemistry* **2012,** *22* (2), 470-477.

30. Wang, L. V.; Hu, S., Photoacoustic tomography: in vivo imaging from organelles to organs. *science* **2012,** *335* (6075), 1458-1462.

31. De La Zerda, A.; Zavaleta, C.; Keren, S.; Vaithilingam, S.; Bodapati, S.; Liu, Z.; Levi, J.; Smith, B. R.; Ma, T.-J.; Oralkan, O., Carbon nanotubes as photoacoustic molecular imaging agents in living mice. *Nature nanotechnology* **2008,** *3* (9), 557.

32. Larson, D. R.; Zipfel, W. R.; Williams, R. M.; Clark, S. W.; Bruchez, M. P.; Wise, F. W.; Webb, W. W., Water-soluble quantum dots for multiphoton fluorescence imaging in vivo. *Science* **2003,** *300* (5624), 1434-1436.

33. Lu, G. J.; Farhadi, A.; Szablowski, J. O.; Lee-Gosselin, A.; Barnes, S. R.; Lakshmanan, A.; Bourdeau, R. W.; Shapiro, M. G., Acoustically modulated magnetic resonance imaging of gas-filled protein nanostructures. *Nature materials* **2018,** *17* (5), 456.

34. Huynh, E.; Leung, B. Y.; Helfield, B. L.; Shakiba, M.; Gandier, J.-A.; Jin, C. S.; Master, E. R.; Wilson, B. C.; Goertz, D. E.; Zheng, G., In situ conversion of porphyrin microbubbles to nanoparticles for multimodality imaging. *Nature nanotechnology* **2015,** *10* (4), 325.

Chapter 5 Concluding Remarks

5.1 Conclusion of this Dissertation

This dissertation includes our efforts in exploiting new colloidal synthesis and self-assembly methods for smart nanomaterials based on nanoscale magnetic assembly. On the basis of a number of well-documented methodologies, we have developed several new approaches towards smart optical materials through the colloidal synthesis of hybrid magnetic-plasmonic nanostructures and magnetic assembly of anisotropic nanostructures. The results in this dissertation have pointed out the possibilities and research opportunities by combining colloidal synthesis and magnetic assembly with new chemical processes, engineering, and fabrication methods. It is expected that the methodologies developed in this dissertation will inspire further developments in smart optical materials.

In Chapter 2, we outline a set of concepts in the magnetic assembly of anisotropic nanostructures, including cubes, rods, and plates, and have developed several approaches toward photonic crystals with new optical properties. In the case of magnetic nanocubes, it is found that they tend to self-assembly into 1D photonic crystals in an "edge-to-edge" manner due to the interacting interference between dipole-dipole coupling and Zeeman coupling. Such the completing effect of magnetic interactions of different physical origins results in a tilted packing, instead of hard contact, between nanocubes. The structural color of 1D photonic chains can be readily tuned by changing the directions of the applied magnetic field. When the symmetry of building blocks is further reduced to nanoplates, the magnetic field can direct the formation of a 2D photonic sheet in their colloidal dispersions. More specifically, nanoplates self-assembled into a centered rectangular phase in the 2D

lattice. Our analysis indicates that the magnetic attractions between interacting plates equilibrate the interaction repulsion force at an offset position. A similar bonding manner is also observed in the magnetic assembly of nanorods. As discussed in the last part of this chapter, the offset packing of nanorods results in highly ordered 3D photonic crystals. The different phase behavior between rods and plates is because of their distinct shape-induced magnetic anisotropy: rods have higher radial symmetry when assembling along the direction of long axes. It thus provides additional bonding sites in the lateral direction of nanorods to support the crystallization of 3D photonic crystals. Instead, plates favor magnetization along their radical directions. As thus, their offset self-assembly occurs along radical directions, the represented axis symmetry of which is different from the long axis of rod magnetization. Plates experience weak magnetic interactions when approaching the assembled 2D photonic sheet. The stronger steric and/or electrostatic repulsion between them will dominate, making lateral packing and 3D structures energetically unfavorable. Overall, our systematical studies over the self-assembly of anisotropic nanostructures under magnetic fields come to appreciate that magnetic interactions between anisotropic building blocks can efficiently break the dense packing fate of a number of colloidal particles in entropy-dominated aggregates. The characterization methods, force analysis, and multi-scale computational methods are universal to understand dynamic interactions between colloidal particles. From an application perspective, photonic crystals of anisotropic building blacks offer us an additional degree of freedom to actively tuning their photonic bands and structural colors. The remarkable advantages of orientational control over distance control in tuning the structural colors of photonic crystals include that it does

not require high charge density and enables whole-visible-spectrum tunability of the fixed photonic structures.

In chapter 3, we extend the conventional templated synthesis methodology to produce a number of hybrid magnetic-plasmonic nanostructures. It is inspired by our new understanding of the high permeability and elasticity of phenolic resins: the resorcinol-formaldehyde resins. Compared with the typical silica prepared by the Stöber process in reported literature, RF represents highly porous polymeric shells that have an efficient mass transfer to support the seeded growth, the robustness of which has been demonstrated by the successful production of various emerging plasmonic nanostructures. The use of polymeric shells also diversifies our engineering strategies for preparing more complicated structures, such as the hybrid nanostructures with conventional physical morphology but highly integrated chemical components. It is achieved by using silica as a "transforming layer" and RF as a confining layer. The first strategy in this chapter describes the synthesis of hybrid Fe_3O_4-Au nanorods by controlling the reaction thermodynamics and ripening of seeds. Au seed-mediated growth of uniform Ag nanorods is challenging as Ag is less stable and prefers homogeneous deposition to form shell structures. To achieve the selection deposition of Ag on Au seeds, we propose a kinetic control. This method can produce high-quality hybrid Fe_3O_4-Ag nanorods with excellent optical properties and tunability. Seeded growth is also extended to Cu for preparing hybrid Fe_3O_4-Cu nanorods, which has advantages of high abundance and low cost for large-scale production in practical applications. Considering the deformability of soft RF shells, we further report an unconventional confined growth method that does not need pre-designed confining space.

In this space-free method, the growth of secondary metal nanostructures occurs at the hard-soft interface between the inorganic core and RF shell. The deformability of the phenolic shell can afford enough space for a conformal coating of the metal layer while the polymer elasticity confines the metal deposition along radical directions. As seed-mediated growth is confined in an interface rather than a gap, it is expected to solve several concerns in conventional templated synthesis, including time-consuming and high cost. More importantly, it opens a door to various complex nanostructures, including core/shell structures. Thanks to the unique magnetic and plasmonic properties of as-prepared nanostructures, our efforts are further focused on developing smart optical materials that exhibit colorimetric changes in response to external stimuli. On the basis of the coupled magnetic and plasmonic anisotropy of Fe_3O_4/Au nanorods, we have developed programmable mechanochromic films. Combining the orientational control of nanorods with lithography has produced mechanochromic devices, which change colors in a programmable manner in response to a number of linear and nonlinear mechanical perturbations, including rotating, bending, twisting, stretching, and pressing. For Fe_3O_4@Au nanospheres, we propose a new method to actively tune their coupled resonant scattering by the magnetic assembly of superparamagnetic Au shell into the 1D plasmonic chain.

In chapter 4, highly integrated contrast agents are synthesized relying on the unconventional space-free confined growth method. In the first part, a magnetically modulated and FFT-processed background-free PA imaging is achieved in NIR-I. It can remarkably improve imaging contrast and specificity by removing any background noises

by easy data processing. Compared with conventional PA imaging, this probe provides reversible tuning of PA signals, which is highly desirable for long-term cancer theranostic. If the size and thickness of Au shells are engineered to support strong LSPR in NIR-II, the background-free imaging concept can be extended to other optical imaging techniques, such as OCT.

5.2 Outlook and Future Work

The past two decades have witnessed remarkable progress in colloidal synthesis and self-assembly. With these developments in nanotechnology, one may expect to prepare smart materials with desirable responses to external stimuli. Standing on the shoulders of giants, we need to continue our efforts in these popular research fields and devote to developing next-generation smart materials. As always, the first and critical challenge of practical implementation of these conceptual designs and emerging materials is low-cost, large-scale production. While researchers and scientists are devoting tremendous efforts to more complicated materials and devices for lab-scale conceptual developments, investors are raising ever-increasing concerns about the stability, scalability, and reproducibility of nanomaterials, particularly nanostructures of highly integrated functionalities. The synthesis of hybrid nanorods, for example, involves multi-step chemical transforms that occur at the nanoscale. It will increase the production cycle and need a complex facility for factory-scale production. The use of noble metals, like Au and Ag, will induce cost issues, limiting their applications in specific uses. In general sense, typical chemical reactions occur on a scale from microliters to liters, which means the scalability is the first issue facing commercialization use of nanoparticles. Particularly, in a reaction that is sensitive to pressure, temperature, and water content, enlarging the reaction by several times in an inorganic lab is sometimes found to produce products with size variation. It has been long recognized that organic-inorganic interfaces play an important role in determining the reaction dynamics and kinetics. To solve these existing challenges requires continuous research input in understanding the fundamentals of nanoscale chemical reactions. Beyond

the cost and scalability issues, the methodologies described in this dissertation and well documented in reported literature are expected to make life easier by providing more intelligent materials.

Therefore, from the perspective of fundamental science, understanding the nanoscale chemical and physical transformations is central to solving the challenges facing commercial use of smart nanomaterials. Exploiting noble metal-free plasmonic nanomaterials with proper electron properties and dielectric functions to support strong LSPR represents a practical route to reduce the cost of smart materials. To the fundamental aspects of nanomaterials, synthesis of uniform building blocks with good crystallinity and uniform size is of particular importance for colloidal assembly. As current magnetic self-assembly relies on post-reduction methods, it is difficult to interpret the underlying forces in an atom scale. Anisotropic magnetic nanostructures experiencing post-reduction features polycrystalline, wide grain size distribution, and irregular crystal grains in a protecting shell, thus making it difficult to accurately estimate anisotropic magnetic interaction and vdW interaction between inorganic cores.

To this end, we will continue our efforts in exploiting new colloidal synthesis and self-assembly approaches. A properly prepared solid-state reduction is possible to produce highly crystalline building blocks, which is expected to update our understanding of nanoscale magnetic assembly. Extending present methodologies to materials of different shapes and chemical components is a simple but effective way to exploit new functionalities and phase behaviors. For example, the 1D, 2D, and 3D assembled structures from anisotropic building blocks are ideal models for studying a number of the physical

and chemical processes from space-resolved plasmonic coupling to mass and energy transportation in energy storage and conversion. To this end, continuous experimental and computational inputs are required to delineate the blueprint of the phase diagram of colloidal self-assembly. In colloidal synthesis, our primary goal is boosting the performances of anisotropic plasmonic nanostructures in various research fields. This can be achieved by magnetically aligning them along a particular direction to prepare fully excited plasmon in case studies of sensing and energy conversion. In conclusion, the commercialization of present techniques and exploiting new fundamental concepts are two primary goals in the future development.